EMISSIONS FROM SAVANNA FIRES IN SOUTHERN AFRICA

Parikhit Sinha

A dissertation submitted in partial fulfillment of the
requirements for the degree of

Doctor of Philosophy

University of Washington
2004

Program Authorized to Offer Degree:
Department of Atmospheric Sciences

University of Washington

Graduate School

This is to certify that I have examined this copy of a doctoral dissertation by

Parikhit Sinha

and have found that it is complete and satisfactory in all respects,
and that any and all revisions required by the final
examining committee have been made.

Chair of Supervisory Committee:

Peter V. Hobbs

Peter V. Hobbs

Reading Committee:

Peter V. Hobbs

Peter V. Hobbs

Lyatt Jaeglé

R H Gammon

Richard H. Gammon

Date: August 9, 2004

In presenting this dissertation in partial fulfillment of the requirements for the doctoral degree at the University of Washington, I agree that the Library shall make its copies freely available for inspection. I further agree that extensive copying of the dissertation is allowable only for scholarly purposes, consistent with "fair use" as prescribed in the U.S. Copyright Law. Requests for copying or reproduction of this dissertation may be referred to Proquest Information and Learning, 300 North Zeeb Road, Ann Arbor, MI 48106-1346, to whom the author has granted "the right to reproduce and sell (a) copies of the manuscript in microform and/or (b) printed copies of the manuscript made from microform."

Signature 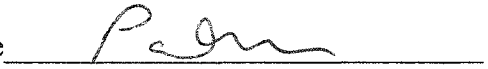

Date August 9, 2004

University of Washington

Abstract

Emissions from Savanna Fires in Southern Africa

Parikhit Sinha

Chair of the Supervisory Committee:
Professor Peter. V. Hobbs
Department of Atmospheric Sciences

Airborne measurements are presented of emissions from savanna fires in southern Africa during the dry season. Measurements were obtained aboard the University of Washington Convair-580 research aircraft during the SAFARI 2000 field project in August and September 2000. Savanna fires in southern Africa emit a wide range of gaseous and particulate species including carbon, sulfur, nitrogen, halogen, and oxygenated compounds. Emission factors, emission ratios, and regional emissions of fifty trace gas and particulate species were derived, including eight species not previously reported in the literature (dimethyl sulfide, methyl nitrate, five species of hydrocarbons, and particles with diameters from 0.1-3 μm diameter). The physical, chemical, and radiative properties of the plume from a large savanna fire in South Africa are characterized, including plume dimensions, secondary formation of ozone and organic acids, oxidation of hydrocarbons, coagulation of particles, and gas-to-particle conversion in aged smoke. Numerous fires, thermodynamically stable layers aloft, and large-scale anticylonic flow result in high concentrations of air pollution distributed throughout the lower troposphere over southern Africa during the dry season. Average regional concentrations of CO (261±81 ppbv), SO_2 (2.5±1.6 ppbv), O_3 (64±13 ppbv), black particulate carbon (2.3±1.9 μg m^{-3}), organic particulate carbon (6.2±5.2 μg m^{-3}), total particle mass (26.0±4.7 μg m^{-3}) are comparable to those found in polluted urban environments. The GEOS-CHEM model of tropospheric chemistry is used to characterize the transport of biomass burning emissions from southern Africa to the neighboring Atlantic and Indian Oceans during the dry season (May–October) of 2000. A large quantity of biomass burning emissions from southern Africa is transported westward over the latitudes 0-20°S to the southern Atlantic Ocean (~40 Tg CO from May-October), contributing to a pollution anomaly in the south Atlantic

Ocean. However, most of this material is transported back eastward over higher latitudes to the south (21-60°S) eventually reaching the southern Indian Ocean. As a result, ~60 Tg of CO from biomass burning in southern Africa is transported eastward to the Indian Ocean across the latitude band 0-60°S from May-October, enhancing background CO concentrations by ~4-13 ppbv per month over the southern subtropical Indian Ocean during the dry season.

TABLE OF CONTENTS

LIST OF FIGURES

LIST OF TABLES

Table Number Page

ACKNOWLEDGEMENTS

I wish to express my appreciation to my mentors, family, and friends. I would like to thank my graduate adviser, Professor Peter Hobbs, for giving me the opportunity to take part in his aircraft research program, and for his excellent mentorship in the interpretation and publication of results. I would also like to thank Dr. Robert Yokelson for his extensive collaboration in my research, providing complementary data and insightful reviews. I would like to acknowledge Dr. Lyatt Jaegle for collaborating with me to utilize chemical transport modeling in conjunction with field observations. I wish to also thank Dr. Richard Gammon and Dr. Daniel Jaffe for their guidance in instrument calibration and for serving on my graduate committee.

I want to acknowledge my parents, Mita and Provat Sinha, my sister, Paramita Sinha, my wife, Amanda Sinha, and my wife's parents, Royal and Barbara Moses, for their love and encouragement. I also have to thank my colleagues at the Department of Atmospheric Sciences, particularly the members of the Cloud and Aerosol Research Group, for their friendship and good conversation.

DEDICATION

To my parents, Provat and Mita Sinha.

CHAPTER 1
INTRODUCTION

1.1. Importance of Biomass Burning

Biomass burning, the combustion of vegetation, is an ancient practice that has been used by humans for clearing land, hunting, controlling pests and weeds, and for domestic cooking and heating for tens of thousands of years [*Andreae*, 1991]. Biomass burning is the leading source of air pollution in the tropics, and for some compounds (e.g., nitrogen oxides and black carbon) it rivals fossil fuel combustion as a global source of atmospheric pollution [*Crutzen and Andreae*, 1990]. Savanna fires are the most common type of biomass burning emissions, and tropical Africa contains about two thirds of the world's savanna [*Hao and Liu*, 1994; *Andreae et al.*, 1996].

The Cloud and Aerosol Research Group (CARG) at the University of Washington (UW) has measured emissions from biomass fires since the 1960's. Early measurements of smoke from biomass burning focused on cloud condensation nuclei (CCN) emitted from forest fires in Washington State [*Hobbs and Radke*, 1969; *Hobbs and Locatelli*, 1969] and their effects on cloud droplet size distributions downwind of fires [*Eagan et al.*, 1974]. Airborne measurements of traces gases and particles from forest fires in Washington State were later used to determine emission factors for these species [*Radke et al.*, 1978]. Emission factors from a number of biomass fires in North America were used to estimate regional and global fluxes of trace gases and particles from biomass burning [*Hegg et al.*, 1990; *Laursen et al.*, 1992]. The physical and chemical evolution of aged smoke was later characterized in the plume of a large prescribed biomass burn in Washington State [*Hobbs et al.*, 1996].

In August and September 1995, the UW CARG participated in the Smoke, Clouds, and Radiation-Brazil (SCAR-B) experiment in the Amazon and cerrado regions of Brazil, one of the major biomass burning regions of the world. In addition to determining emission factors for trace gases and particles from biomass fires in Brazil [*Ferek et al.*, 1998], chemical, physical, and radiative properties of regional haze during

the biomass burning season were characterized [*Reid et al.*, 1998; *Ross et al.*, 1998]. Airborne measurements of biomass smoke during SCAR-B were used to estimate global direct radiative forcing from biomass burning [*Hobbs et al.*, 1997].

Biomass burning is a source of a wide variety of chemical species that are important in global atmospheric chemistry, including carbon monoxide (CO), nitrogen oxides (NO_x), sulfur dioxide (SO_2), hydrocarbons, halocarbons, oxygenated organic compounds, and particles [*Delmas,* 1982; *Crutzen and Andreae*, 1990; *Ward and Hardy,* 1991; *Hurst et al.,* 1994; *Blake et al.,* 1996; *Yokelson et al.,* 1996; *Ferek et al.,* 1998]. Gases with high global warming potentials, such as methane (CH_4) and nitrous oxide (N_2O), are released in globally minor but non-trivial quantities by biomass burning [*Logan et al.,* 1981; *Quay et al.,* 1991; *Hurst et al.,* 1994; *Cofer et al.,* 1996; *Andreae et al.*, 1996]. Methyl chloride (CH_3Cl), methyl bromide (CH_3Br), and other halocarbons released by biomass burning, may contribute to stratospheric ozone (O_3) depletion [*Blake et al.,* 1996; *McKenzie et al.*, 1996]. Organic and black carbon particles emitted from biomass burning play important roles in the earth's radiation balance [*Cachier et al.*, 1996]. Gas-to-particle conversion of organic compounds, NO_x, and SO_2 may alter the radiative and cloud nucleating properties of smoke aerosols [*Reid et al.*, 1998]. Acids in smoke from biomass fires, such as acetic acid (CH_3COOH), formic acid (HCOOH), nitric acid (HNO_3), and sulfuric acid (H_2SO_4), can alter the pH of precipitation [*Lacaux et al.*, 1991; *Yokelson et al.,* 1996]. Organic compounds and CO emitted from biomass fires in Africa have been shown to react photochemically in the presence of nitrogen oxides to produce increases in ozone mixing ratios. Ozone is an important greenhouse gas, and O_3 and oxygenated compounds are key precursors of the hydroxyl radical (OH), which is the primary oxidant in the troposphere and is responsible for the removal of reactive pollutants released into the atmosphere by anthropogenic and natural processes [e.g., *Seinfeld and Pandis*, 1998].

As emissions from biomass burning age, they are physically and chemically transformed. In studies of smoke from cerrado and rain forest regions of Brazil, *Reid et al.* [1998] found that the properties of aged gases and particles in regional hazes dominated by biomass burning were significantly different from those of young smoke,

due to particle coagulation and mass growth by secondary species, and condensation and gas-to-particle conversion of inorganic and organic vapors. As the smoke aged the excess non-methane hydrocarbons (C<11) ratioed to excess CO dropped by about one-third, and the aerosol mass to CO ratio increased by ~20-40% with one-third to one-half of the mass growth likely occurring in the first few hours of aging. Changes in particle sizes and compositions during aging have a large impact on the optical properties of the aerosols. *Hobbs et al.* [1996] obtained airborne measurements in a smoke plume from a prescribed biomass burn on the Pacific coast of Washington State. Measurable decreases in the CO_2-normalized concentrations of NO and NO_x were documented over about 35 min of aging due to formation of nitric acid. In 1.8 h, the CO_2-normalized concentration of SO_2 decreased by about 60% due to formation of sulfate, and the peak in the CO_2-normalized particle number concentration decreased dramatically while the particle number mode shifted from 0.16 to 0.28 μm and the particle volume mode from 0.25 to 0.38 μm due to coagulation. The mixing ratio of O_3 was below ambient very close to the fire due to titration by NO, but it rose quickly and peaked after about half-hour of aging as a result of oxidation of non-methane organic carbon in the presence of NO_x. *Goode et al.* [2000] reported that the ratio of excess O_3 to excess CO rose to as much as 8.9% within 2 h of aging near the top of an Alaskan smoke plume. On the same time scale, the ratio of excess NH_3 to excess CO fell by about two-thirds due to conversion to ammonium, and both formic and acetic acid doubled with respect to CO as a result of oxidation of alkenes by O_3 and OH.

After an hour or two of aging, biomass smoke is generally visually indistinguishable from the ambient regional haze [*Magi and Hobbs*, 2003]. Regional hazes also age photochemically, and are sometimes present in distinct layers that have been transported from different source regions [*Hobbs*, 2003]. Measurements of CO and hydrocarbons [*Blake et al.*, 1996], ozone [*Diab et al.*, 1996, *Thompson et al.*, 2002], and aerosols [*Anderson et al.*, 1996] have been made in ambient hazes over southern Africa during the dry season. Meteorological conditions, such as vertically stable layers and anticyclonic circulations, influence the distribution of trace gases and aerosols over

southern Africa during the dry season [*Garstang et al.*, 1996; *Jury*, 2000; *Freiman et al.*, 2002].

Long-range transport of pollutants from savanna burning in southern Africa produces elevated concentrations of O_3 over the southern Atlantic Ocean [*Fishman et al.*, 1991, 1996; *Thompson et al.*, 1996]. Biomass burning emissions have also been observed in the southern Pacific Ocean [*Hoell et al.*, 1999]. Using a global chemical model in tandem with the PEM-Tropics A observations, *Staudt et al.* [2002] found that southern Africa and South America make comparable contributions to biomass burning pollution in the southern Pacific Ocean. The spatial scale of the transport of smoke from biomass burning observed in PEM-Tropics A was ~10,000 km, making it a planetary-scale phenomenon (called the southern "subtropical global plume" by *Chatfield et al.* [2002]). In order for emissions from biomass burning in southern Africa to reach the southern Pacific Ocean, the emissions must first be transported across the Indian Ocean. In early September 2000, a meteorological event, termed the "river of smoke" by *Annegarn et al.* [2002], transported smoke southeastward from southern Africa to the Indian Ocean, resulting in a week-long period of heavy haze and reduced visibility over the region.

1.2. SAFARI 2000 Field Project

In August and September 2000, the Cloud and Aerosol Research Group (CARG) from the University of Washington (UW), with its Convair-580 research aircraft, participated in the Southern African Regional Science Initiative 2000 (SAFARI 2000) field project, a multinational, multiplatform study of the southern African biogeochemical system [*Swap et al.*, 2003]. The goals of SAFARI 2000 were to characterize, quantify and understand the processes driving biogenic, pyrogenic and anthropogenic emissions in southern Africa, to extend understanding of the transport, transformations, and deposition of these emissions, and to determine their impacts on climatic, hydrological, and ecosystem processes.

The field study was carried out from August 10 to September 18, 2000, during the dry season in southern Africa (May-October) when biomass burning is widespread.

From August 10 to September 9, the UW Convair-580 research aircraft was based in Pietersburg (since renamed "Polokwane"), South Africa. During this period twenty-five research flights were carried out over South Africa, Botswana, Zambia and Mozambique. From September 10 to 18, 2000, the Convair-580 was based in Walvis Bay, Namibia, where five flights were made over Namibia and off the west coast of southern Africa. Fifty gaseous and particulate species were measured aboard the CV-580 research aircraft in initial smoke (a few minutes old) and aged smoke (< 1 hr old) from ten active savanna fires in southern Africa. Six of these fires were prescribed, allowing for the characterization of vegetation and combustion properties by scientists on the ground. During thirty research flights, sixty-four vertical profiles in the lower troposphere (< 5 km above mean sea level) over southern Africa were obtained in ambient haze outside of smoke plumes.

1.3 Objectives and Organization

The objective of this dissertation is to characterize the emissions, evolution, distributions, and transport of trace gases and particles emitted by savanna fires in southern Africa during the dry season. Chapter 2 describes the measurement and modeling methods used in this work. Chapter 3 presents emission ratios and emission factors for smoke from savanna fires in southern Africa for a wide range of gaseous and particulate species including carbon, sulfur, nitrogen, halogen, and oxygenated compounds following *Sinha et al.* [2003a]. Emission factors are combined with estimates of the amounts of biomass burned to obtain regional emissions of trace gases and particles from savanna fires in southern Africa during the dry season based on *Sinha et al.* [2004a]. In chapter 4, the chemical and physical transformations of aged smoke downwind of an active savanna fire in the Timbavati Game reserve in South Africa (hereafter referred to as the Timbavati fire) are described following *Hobbs et al.* [2003], including secondary formation of ozone and organic acids, coagulation of particles, and gas-particle conversion. Chapter 5 describes the cumulative effect of savanna fire emissions on tropospheric air quality over southern Africa during the dry season based on *Sinha et al.* [2003b]. The long-range transport of savanna fire

emissions from southern Africa to the neighboring Atlantic and Indian Oceans is characterized in chapter 6 following *Sinha et al.* [2004b]. A summary of results and recommendations for future work are given in chapter 7.

CHAPTER 2
METHODS

2.1. Instrumentation

Instrumentation aboard the UW Convair-580 research aircraft provided measurements of navigational and aircraft flight characteristics; meteorological state parameters (temperature, humidity, winds); comprehensive measurements of aerosol concentrations and size spectra (from 0.01 to 47 μm diameter); light scattering, absorption and extinction; aerosol humidographs; aerosol shape and elemental composition; cloud condensation nuclei (for flights based out of Walvis Bay only); aerosol composition and mass; aerosol optical depths; cloud and precipitation size distributions; cloud liquid water content and cloud droplet effective radius; concentrations of SO_2, O_3, CO_2, CO, NO, NO_x, hydrocarbons, reactive and stable gaseous combustion emissions; column water vapor and ozone; upwelling and downwelling broadband visible, near-infrared, and ultraviolet radiation; solar spectral irradiances and radiances; and, albedos and the bidirectional reflection distribution function (BRDF) of surfaces and clouds. Instruments relevant to the present study are described below.

2.1.1 Continuous Measurements

Continuous measurements of SO_2 were made using a Teco model 43S pulsed-fluorescence analyzer (precision of 7%, detection limit of 0.1 ppbv). Calibration of this instrument, both in flight and on the ground, was carried out prior to, during, and following the field project with a commercial standard mixture (Scott-Marrin) of 180 ± 9 ppbv SO_2 in ultra pure air. The instrument was zeroed using ultra pure air (SO_2 <1 ppbv). Continuous measurements of O_3 were obtained with a Teco model 49C UV photometric analyzer (precision of 2%, detection limit of 3 ppbv). Calibration of this instrument was carried out prior to and following the field project using a Columbia Scientific Instruments Photocal 3000 Version 080 ozonator. The total concentration of

particles (CN) in the size range ~0.003-3 μm diameter was measured continuously with a TSI 3025A ultrafine condensation particle counter (precision of 10%). Continuous measurements of particle size spectra from 0.5-3.0 μm diameter were measured with a TSI 3320 aerodynamic particle sizer. The light-scattering coefficient of particles were measured continuously with an MS Electron nephelometer.

Ambient air temperatures were measured with an in-house built temperature sensor enclosed in a reverse-flow housing to eliminate dynamic heating. Total temperature was measured with a Rosemount platinum resistance thermometer, and the ambient temperature derived from this by correcting for dynamic heating. The ambient dewpoint temperature, from which the ambient relative humidity (RH) could be derived, was measured with a Cambridge chilled-mirror device.

The NASA Ames Solar Spectral Flux Radiometer (SSFR) was used to measure irradiance over the wavelength range 300-1700 nm [*Pilewskie et al.*, 2003]. Spectral resolution is 9 to 12 nm over the spectra range. The dynamic resolution is 15 bits full range. Integration time was nominally 100 ms and spectral sampling rate was approximately 1 Hz. The SSFR was calibrated for wavelength response, angular response, and absolute spectra power. The SSFR was calibrated before and after flights using a LI-COR field calibration unit, which allowed monitoring of the stability of the SSFR over the duration of the experiment. Absolute accuracy of spectral irradiance was estimated to be 3% across the spectrum. Precision was estimated to be 0.1% over one day and 1% over one month.

2.1.2 AFTIR

An airborne Fourier transform infrared spectrometer (AFTIR) was used aboard the Convair-580 aircraft. The AFTIR had a dedicated inlet that directed ram air through a Pyrex multipass cell with an exchange time of 4-5 s. During plume penetrations, the AFTIR was used to grab smoke samples and to detain them for 2-3 min of signal averaging. This allowed measurements of the major reactive and stable trace gases present above 5-20 ppbv. The species measured were water vapor (H_2O), carbon dioxide (CO_2), CO, nitric oxide (NO), nitrogen dioxide (NO_2), methane (CH_4), ethene

(C_2H_4), acetylene (C_2H_2), formaldehyde (HCHO), methanol (CH_3OH), acetic acid (CH_3COOH), formic acid (HCOOH), ammonia (NH_3), O_3, and hydrogen cyanide (HCN). The AFTIR technique, the precision of the measurements, and many of the results are discussed by *Yokelson et al.* [2003].

2.1.3 Filters and Electron Microscope Grids

Particles were collected for specified time periods on quartz filters (Pallflex 2500 QAT-UP), Teflon filters (Gelman Sciences Teflo membrane, 2.0 μm pore size), and on electron microscope (EM) grids. The Teflon filters were weighed before and after particle sampling in a humidity and temperature controlled chamber (RH = 40%, T = 293 K) to determine the masses of dry total particulate matter (TPM) collected on the filters. From control and field blank filters, the uncertainty of the dry TPM was estimated to be ±6 μg. By comparison, the typical dry TPM loading for the smoke aerosol samples was always greater than 100 μg.

After gravimetric analysis, the Teflon filters were extracted in deionized water (HPLC grade) and analyzed by a standard ion chromatography system. This analysis yielded mass concentrations of the chloride, nitrate and sulfate (Cl^-, NO_3^- and SO_4^{2-}, respectively) to a precision of 5%, as well as several organic species (precision within 20%) such as oxalate ($C_2O_4^{2-}$). An Inductively Coupled Plasma–Atomic Emission Spectrometer was used to measure the mass concentration of the potassium ion (K^+) to a precision of 4%. Each of these measurements was accompanied by field blanks to correct for background signals and to estimate measurement uncertainties and detection limits. Further details on the Teflon filter analyses, and results obtained are given by *Gao et al.* [2003].

Aerosol samples collected intermittently on quartz (Pallflex 2500 QAT-UP) filters were used to determine the concentration of particulate carbon. The quartz filters were baked before use at 800°C for at least 6 h to remove carbonaceous impurities, and then analyzed for total carbon (TC) content using the evolved gas analysis (EGA) method described by *Novakov* [1981, 1982]. In EGA, a portion of the filter is heated at a constant rate (40°C min^{-1} in this case) from 50 to 800°C in an oxygen atmosphere.

The carbon-containing gases that evolve from the sample are converted to CO_2 (over a manganese dioxide catalyst maintained at 800°C) that is subsequently measured with a nondispersive infrared analyzer (Beckman Model 870). A plot of the CO_2 concentration versus temperature is called a thermogram. The area under a thermogram is proportional to the TC content of the analyzed sample. The tandem filter method described by *Turpin et al.* [1994] and *Kirchstetter et al.* [2001] was used to adjust estimates of TC for the positive sampling artifact that results from the adsorption of organic gases on the quartz filters. Black carbon (BC) concentrations were estimated with an optical transmission technique similar to that described by *Rosen and Novakov* [1983]. This method compares the attenuation of white light through a loaded filter relative to that of a blank filter. The relationship between optical attenuation (ATN) and the BC concentration ($\mu g\ cm^{-2}$) is given by $ATN = \sigma \cdot BC$, where $ATN = 100\ln(I_o/I)$, where I_o and I are the transmitted light intensities through the blank and loaded filters, respectively, and σ is the mass absorption cross-section for BC deposited on quartz ($m^2\ g^{-1}$) [*Gundel et al.*, 1984]. A value of 20 $m^2 g^{-1}$ was used for the mass absorption cross-section. This value was derived from comparison of light absorption measurements and BC concentrations (measured by thermal EGA) on many samples [*Gundel et al.*, 1984; *Kirchstetter et al.*, 2003]. Further information on the EGA and optical transmission techniques used here, and the results obtained, are given by *Kirchstetter et al.* [2003].

Since the time that it took the aircraft to cross the width of a smoke plume (~1-2 min) was too short to pass enough smoke through the Teflon filters, quartz filters, and the EM grids for subsequent detailed analyses of the aerosol, a "grab-bag" technique was used. The grab-bag consisted of a 2.5 m^3 electrically conducting plastic (Velostat) bag, which could be filled with a sample of smoke in 12 s when exposed to ram air. The sample in the grab-bag was drawn through the various gas and aerosol measuring instruments aboard the aircraft, through the filters, and onto the EM grids, for subsequent analysis. Particle size measurements could also be made using the bag samples. The grab-bag system had an aerosol 50% cut-off diameter of about 4 μm, as larger particles were lost in the inlet and on the walls of the grab bag. When crossing a plume, the grab-bag was also used to obtain samples for SO_2 measurements using the

Teco 43S pulsed fluorescence analyzer. Grab-bag samples were followed by sampling of the ambient air, allowing determination of excess concentrations of species in a plume.

2.1.4 Canister Samples

Electropolished stainless steel canisters were filled with air samples from smoke plumes, and ambient air just upwind of the fires, using a stainless steel inlet that passed through the aircraft fuselage. The canister samples coincided with the "grab-bag" samples. A typical sampling time for a canister was 30 s. The canister samples were subsequently analyzed for hydrocarbons, halocarbons, dimethyl sulfide (DMS), and methyl nitrate (CH_3ONO_2).

For each canister sample, mixing ratios of C_2-C_9 non-methane hydrocarbons (NMHC), methyl chloride (CH_3Cl), methyl iodide (CH_3I), chloroform ($CHCl_3$), methyl bromide (CH_3Br), bromoform ($CHBr_3$), chlorofluorocarbons (CFCs), hydrochlorofluorocarbons (HCFCs) and hydrofluorocarbons (HFCs) were determined by gas chromatography with flame ionization, electron capture and mass spectrometer detection. The precision of the NMHC, $CHCl_3$, $CHBr_3$ and methyl halide measurements was 3%, and the NMHC detection limit was 3 pptv. Measurements of the longer-lived CFCs, HCFCs, and HFCs were precise to within 1%. Mixing ratios (precisions in parentheses) of CO_2 (3%), CO (5%), and CH_4 (0.1%) were determined using separate instrumentation. A detailed description of the analytical procedure for the canister samples, including quantification of the measurement precision for individual compounds, is given by *Colman et al.* [2001].

2.2. Definitions of Excess Molar Mixing Ratio, Normalized Excess Molar Mixing Ratio, and Combustion Efficiency

The *excess molar (or volume) mixing ratio, ΔX,* of a species X in a smoke plume is defined as:

$$\Delta X = X_{plume} - X_{ambient} \qquad (2.1)$$

where, X_{plume} and $X_{ambient}$ are the molar (or volume) mixing ratios of X in the smoke plume and in the ambient air, respectively.

The *normalized excess molar mixing ratio* of a species X is the excess molar mixing ratio of X in the smoke divided by the excess molar mixing ratio of a simultaneously measured reference gas (such as CO or CO_2). For example, a normalized excess molar emission ratio of species X relative to CO is $\Delta X/\Delta CO$. It is common to refer to $\Delta X/\Delta CO$ as the *excess molar emission ratio*. However, we prefer to use this wording only when ΔX and ΔCO are measured very close to a fire. Since CO is a biomass burning product with a lifetime of ~1 month in the ambient, tropical troposphere, most of the decrease in the excess molar mixing ratio of CO in the smoke plume, at least in the first few hours, is due to mixing with the ambient air. Therefore, by dividing ΔX by ΔCO, the effects of dilution of ΔX due to mixing with the ambient air are largely removed, so that other physical and chemical processes that change ΔX in the plume can be isolated.

The *combustion efficiency* (CE) is the molar ratio of excess carbon (C) emitted as CO_2 from a fire to the total excess carbon emitted [*Ward and Hardy*, 1991]:

$$CE = \frac{\Delta C_{CO_2}}{\Delta C_{CO_2} + \Delta C_{CO} + \Delta C_{CH_4} + \Delta C_{NMOC} + \Delta C_{PC}} \qquad (2.2)$$

where NMOC and PC indicate non-methane organic compounds and particulate carbon, respectively. Thus, CE is the fraction of fuel carbon emitted that is completely oxidized to CO_2.

Although CE is a useful quantity for fire models, it is often difficult to measure all of the individual carbon species in the emissions from a fire. As will be shown in Chapter 3, the emission of CO is closely linked to the emission of CH_4, NMOC, and PC. Therefore, in this study we have chosen to use the *modified combustion efficiency (MCE)* as the principal quantity to describe the relative amounts of flaming and smoldering combustion [*Ward and Hao*, 1992; *Ward and Radke*, 1993], which is defined as:

$$MCE = \frac{\Delta C_{CO_2}}{\Delta C_{CO_2} + \Delta C_{CO}} \qquad (2.3)$$

Since CH_4, NMOC, and PC are emitted in small quantities relative to CO_2 and CO, the difference between CE and MCE is typically only a few percent.

Both CE and MCE are useful as indicators of the relative amounts of flaming and smoldering combustion that generate emissions. In laboratory studies, *Yokelson et al.* [1996] found that pure flaming combustion has an MCE near 0.99 and pure smoldering combustion an MCE near 0.8. Therefore, an MCE <0.9 roughly indicates >50% smoldering combustion, and an MCE >0.9 suggests >50% flaming combustion.

2.3. Model Description

We used the GEOS-CHEM global model of tropospheric chemistry to investigate transport of biomass burning emissions. The GEOS-CHEM model is driven by assimilated meteorological observations from the Goddard Earth Observing System (GEOS) of the NASA Global Modeling and Assimilation Office (GMAO). A full description of the model and a global model evaluation using meteorological fields and field observations for 1994 is given by *Bey et al.* [2001]. Meteorological fields for 2000 (GEOS-Terra) are used in this study with horizontal resolution of 1° latitude by 1° longitude and 48 sigma levels in the vertical, from the surface up to 0.01 hPa. For computational efficiency, we regrid these fields to 2° latitude by 2.5° longitude and 30 vertical levels. The model includes 80 chemical species and carries 24 tracers to describe tropospheric O_3-NO_x-hydrocarbon chemistry. Model version 5.05 (http://www-as.harvard.edu/chemistry/trop/geos) is used here.

Incorporation of biomass burning emissions in the model follow the methodology of *Duncan et al.* [2003], which incorporates a climatological inventory of fuel consumption from J. Logan and R. Yevich as described in *Lobert et al.* [1999]. Fuel consumption is combined with emission factors from *Andreae and Merlet* [2001] to obtain emissions. The Total Ozone Mapping Spectrometer (TOMS) Aerosol Index

(AI) and Along Track Scanning Radiometer (ATSR) fire counts are used to obtain seasonal and interannual variability in biomass burning emissions.

Model emissions of CO in subequatorial Africa during the dry season from fossil fuels, biomass burning, and domestic biofuels are given in Table 2.1 for the year 2000 and for a climatological average dry season. Fossil fuel and biofuel emissions occur evenly throughout the year, whereas biomass burning emissions are concentrated during the dry season, accounting for ~90% of CO emissions from May to October. On an annual basis, biomass burning also dominates CO emissions, accounting for ~83% of annual modeled CO emissions from subequatorial Africa in 2000. Biomass burning emissions in 2000 are comparable to the climatological average, except for September and October which are ~25% lower and ~40% higher than average, respectively. Rainfall conditions in 2000 were above-average due to the moist La Nina phase of the El Nino-Southern Oscillation (ENSO) [*Swap et al.*, 2003].

We also use in this study a GEOS-CHEM tagged CO simulation [*Liu et al.*, 2001] to resolve source regions of CO (Africa, South America, Asia, and Australia) and source types (biomass burning, fossil fuel/biofuel, and oxidation of methane and biogenic volatile organic compounds). The tagged CO simulation uses meteorological fields for 1994–2000 and climatological average biomass burning emissions (Table 2.1). Concentrations of total CO, CO from biomass burning in southern Africa, and CO from biomass burning in South America will be referred to as CO, CO_{BBAF}, and CO_{BBSAM}, respectively.

Table 2.1. Dry season and annual model emissions of CO (Tg) in subequatorial Africa (10-40°E, 0-40°S) by source in 2000. For biomass burning, model emissions are provided for 2000 and for a climatological average year.

	May	June	July	August	September	October	May–October	Annual
Industry	0.51	0.50	0.50	0.51	0.49	0.51	3.0	16.0
Domestic biofuels	0.95	0.92	0.95	0.95	0.92	0.95	5.6	11.2
Biomass burning								
Year 2000	3.7	10.0	18.0	15.3	17.1	15.7	79.8	86.4
Climatology	3.6	10.9	17.0	16.0	23.1	11.0	81.6	94.3

CHAPTER 3
EMISSIONS OF TRACE GASES AND PARTICLES FROM SAVANNA FIRES IN SOUTHERN AFRICA

3.1. Vegetative Types and Sampling of Smoke

In this chapter we describe measurements obtained in the smoke from ten fires covering a variety of vegetation types in several regions of southern Africa (Table 3.1): four fires in South Africa, two in Zambia, one in Mozambique, and three on the Botswana/South Africa border. The nature of the vegetative fuel plays an important role in determining emissions from biomass fires [e.g., *Ward and Hardy*, 1991]. Vegetation types vary from lowvelds and highvelds in South Africa, to dambo and miombo woodlands in Zambia, to east African coastal mosaic in Mozambique. The lowveld fires studied here were located in and around the Kruger National Park in South Africa. Vegetation in the lowvelds varied from south Zambezian undifferentiated woodland to Tongaland-Pondoland bushland [*White,* 1981, 1983]. The bushveld fires were located on the Botswana/South Africa border, in a Zambezian vegetation zone that transitions from undifferentiated woodland to Acacia deciduous bushland and wooded grassland. The miombo woodland fires in Zambia were in a Zambezian woodland vegetation zone dominated by species of Brachystegia and related genera. The dambo grassland fire in Zambia was in a seasonally flooded region covered with a medium-dense, uniform grass mat. The Mozambique fire was located in a transition zone between miombo woodland dominated by Brachystegia and a Zanzibar-Inhambane east African coastal mosaic of woodland habitats [*White*, 1981, 1983].

More than 60 aircraft penetrations were made through the smoke plumes of the ten fires. Penetrations were determined both visually and using concentrations of condensation nuclei. However, since emission factors rely on source measurements, we use only the results for smoke samples less than a few minutes old acquired directly (typically ~500 m) above the fires, which we term "initial" smoke. Canisters were filled and grab-bag samples acquired during 16 penetrations of initial smoke.

Table 3.1. Savanna fires in southern Africa from which measurements were obtained in this study.

Name of Fire and/or General Location	Latitude (deg. S)	Longitude (deg. E)	Date (mm:dd:yy)	Time (UTC)	Number of Samples GC/C, AFTIR	Country	Vegetation Type	Type of Fire	Modified Combustion Efficiency (MCE, %)*
Skukuza 1 (Kruger National Park, South Africa)	25.46	31.58	08:17:00	1002	1, 3	South Africa	Lowveld	Fire of opportunity	93.8
Skukuza 2 (Kruger National Park, South Africa)	24.43	31.83	08:17:00	1110	1, 3	South Africa	Lowveld	Fire of opportunity	97.9
Madikwe 1 (Limpopo River valley, South Africa)	24.67	26.41	08:18:00	916	1, 5	South Africa, Botswana border	Bushveld	Prescribed fire	89.7
Madikwe 2 (Limpopo River valley, South Africa)	24.74	26.24	08:20:00	1253	1, 2	South Africa, Botswana border	Bushveld	Prescribed fire	98.0
Madikwe 3 (Limpopo River valley, South Africa)	24.66	26.29	08:20:00	1328, 1354	2, 3	South Africa, Botswana border	Bushveld	Prescribed fire	93.7, 92.1
Kruger National Park (South Africa)	25.10	31.46	08:29:00	1410, 1417	2, 2	South Africa	Lowveld	Fire of opportunity	92.7, 90.0
Beira (Mozambique)	21.00	34.74	08:31:00	1119, 1133	2, 3	Mozambique	Miombo woodland/ E. African Coastal Mosaic	Fire of opportunity	94.8, 92.4
Kaoma 1 (Zambia)	14.81	24.48	09:01:00	0902, 0908	2, 6	Zambia	Miombo woodland	Prescribed fire	93.6, 93.8
Kaoma 2 (Zambia)	14.84	24.43	09:05:00	1156, 1208	2, 5	Zambia	Dambo grassland	Prescribed fire	96.1, 96.7
Timbavati (Near Kruger National Park, South Africa	24.37	31.22	09:07:00	0842, 0857	2, 4	South Africa	Lowveld	Prescribed fire	93.8, 92.9

*Derived from the canister/gas chromatograph measurement

3.2 Emission Ratios

The excess molar mixing ratio of each species was regressed against the excess molar mixing ratio of CO or CO_2 to obtain the emission ratio of that species. The slope of the regression line gives the molar emission ratio (hereafter abbreviated to "*emission ratio*") of the species with respect to the reference tracer (CO or CO_2). Since NO_x, SO_2, and CO_2 are mainly emitted in flaming combustion, excess values of NO_x and SO_2 were regressed against excess CO_2. Other compounds are mainly emitted with CO during smoldering combustion, so their excess mixing ratios were regressed against excess CO.

Figure 3.1 shows the excess mixing ratios of several species plotted against excess mixing ratios of CO (or CO_2). Slopes and correlation coefficients for these and all the other species we measured are listed in Table 3.2 (for the canister samples) and in Table 3.3 (for the AFTIR samples). For emission ratios obtained from the gas chromatography measurements (Table 3.2), an average emission ratio for a given species was derived using the sixteen canister samples from the ten fires. For the AFTIR measurements (Table 3.3), there were often several measurements close to the fire in each of the smoke plumes. For these cases, we give an average emission ratio for each measured species for each fire. The average emission ratios of CO, CH_4, and acetylene in Table 3.2 are not significantly different from the corresponding values listed in Table 3.3. An exception is that the average emission ratio for ethene determined from the AFTIR is about 50% greater than that determined from gas chromatography. In section 3.4, we compare and discuss measurements obtained by gas chromatography with those obtained by AFTIR. Emission ratios are not given here for O_3 since it is not emitted directly from a fire, although O_3 develops downwind in smoke plumes,. The time evolution of O_3 in one of the smoke plumes we studied is described in chapter 4.

For comparison with our measurements, we also show in Table 3.2 the emission ratios for smoke from savanna fires in southern Africa and agricultural fires in Brazil reported by *Blake et al.* [1996], and for smoke from grass, cerrado and forest fires in Brazil given by *Ferek et al.* [1998]. The analysis techniques used in these two studies

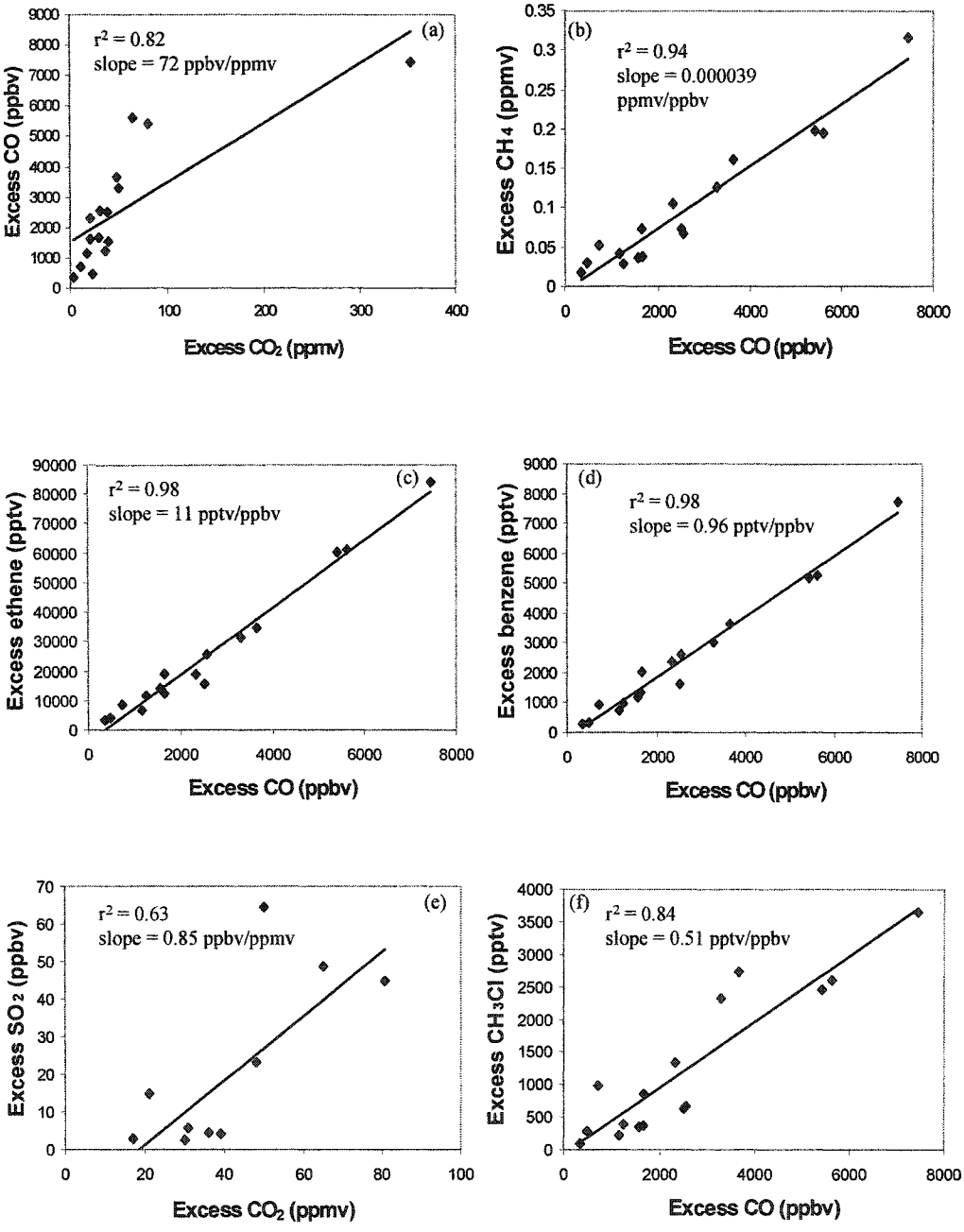

Figure 3.1. Excess mixing ratios of selected trace gases (measured in canisters) versus excess mixing ratios of CO_2 or CO in the smoke from savanna fires in southern Africa. The correlation coefficient is given by r^2.

Table 3.2. Average molar emission ratios (with respect to CO or CO_2) measured in this study for young smoke from savanna fires in southern Africa for which the correlation coefficients (r^2) of the excess mixing ratios of the species versus the excess mixing ratio of CO or CO_2 was greater than or equal to 0.5, and which were therefore considered to be emitted by the fires. Shown for comparison are results from *Blake et al.* [1996] for mainly aged smoke from savanna fires in southern Africa and from grass, cerrado, and forest fires in Brazil, and from *Ferek et al.* [1998] for young smoke from grass, cerrado, and forest fires in Brazil.*

Species	Technique Used for Measure-ment in this study†	Southern Africa (This Study)		Southern Africa [*Blake et al.*, 1996]		Brazil [*Blake et al.*, 1996]		Brazil [*Ferek et al.*, 1998]	
		Molar Emission Ratio	r^2	Molar Emission Ratio	r^2	Molar Emission Ratio	r^2	Molar Emission Ratio	r^2
Carbon monoxide (CO)	GC/C	0.072 ±0.009	0.82	—	—	—	—	—	—
Methane (CH_4)	GC/C	0.039 ±0.003	0.94	0.078 ±0.004	0.91	0.094 ±0.013	0.70	0.12	0.90
Sulfur dioxide (SO_2)	Teco 43S (via bag house)	0.00085 ±0.0002	0.63	—		—		—	
Dimethyl sulfide (CH_3SCH_3)	GC/C	0.0000087 ±0.0000011	0.86	—		—		—	
Methyl bromide (CH_3Br)	GC/C	0.0000036 ±0.0000006	0.69	0.0000060 ±0.0000005	0.78	0.0000106 ±0.0000008	0.88	—	—
Methyl chloride (CH_3Cl)	GC/C	0.00051 ±0.00006	0.84	0.00057 ±0.00003	0.92	0.00085 ±0.00006	0.88	—	—
Methyl iodide (CH_3I)	GC/C	0.00000084 ±0.00000023	0.50	0.0000012 ±0.0000002	0.70	0.0000012 ±0.0000002	0.57	—	—
Methyl nitrate (CH_3ONO_2)	GC/C	0.0000025 ±0.0000004	0.74	—	—	—	—	—	—
Ethane (C_2H_6)	GC/C	0.0026 ±0.00022	0.93	0.0052 ±0.0002	0.96	0.0083 ±0.0003	0.97	0.0052	0.85
Ethene (C_2H_4)	GC/C	0.0110 ±0.0005	0.98	0.0083 ±0.0006	0.78	0.0061 ±0.0004	0.87	0.011	0.83
Propane (C_3H_8)	GC/C	0.00048 ±0.00006	0.81	0.00097 ±0.00004	0.94	0.0016 ±0.001	0.95	0.0010	0.82
Propene (C_3H_6)	GC/C	0.0028 ±0.0002	0.94	0.001 ±0.0001	0.56	0.0004 ±0.0001	0.62	0.0039	0.87
Acetylene (C_2H_2)	GC/C	0.0032 ±0.0003	0.92	0.0045 ±0.0001	0.98	0.0033 ±0.0001	0.97	0.0024	0.63
i-butane (C_4H_{10})	GC/C	0.000031 ±0.000004	0.82	0.000043 ±0.000004	0.77	0.000055 ±0.000010	0.55	—	—
n-butane (C_4H_{10})	GC/C	0.000087 ±0.0000074	0.92	0.00016 ±0.00001	0.88	0.00021 ±0.00002	0.86	0.00021	0.79
t-2-butene (C_4H_8)	GC/C	0.00012 ±0.0000098	0.92	—	—	—	—	0.00026	0.89

Table 3.2 continued

Species	Technique Used for Measure-ment in this study[†]	Southern Africa (This Study)		Southern Africa [*Blake et al.*, 1996]		Brazil [*Blake et al.*, 1996]		Brazil [*Ferek et al.*, 1998]	
		Molar Emission Ratio	r^2	Molar Emission Ratio	r^2	Molar Emission Ratio	r^2	Molar Emission Ratio	r^2
1-butene (C_4H_8)	GC/C	0.00042 ±0.000036	0.91	—	—	—	—	0.00066	0.90
c-2-butene (C_4H_8)	GC/C	0.000086 ±0.0000071	0.92	—	—	—	—	0.00022	0.89
n-pentane (C_5H_{12})	GC/C	0.000017 ±0.0000046	0.51	0.000053 ±0.000005	0.80	0.000051 ±0.000005	0.80	0.000059	0.73
1,3-butadiene (C_4H_6)	GC/C	0.00048 ±0.000044	0.90	—	—	—	—	—	—
3-methyl-l-butene (C_5H_{10})	GC/C	0.000033 ±0.000003	0.94	—	—	—	—	—	—
t-2-pentene (C_5H_{10})	GC/C	0.000032 ±0.0000027	0.92	—	—	—	—	—	—
2-methyl-2-butene (C_5H_{10})	GC/C	0.000026 ±0.0000025	0.90	—	—	—	—	—	—
2-methyl-1-butene (C_5H_{10})	GC/C	0.000033 ±0.0000022	0.95	—	—	—	—	—	—
c-2-pentene (C_5H_{10})	GC/C	0.000021 ±0.0000014	0.95	—	—	—	—	—	—
n-hexane (C_6H_{14})	GC/C	0.000055 ±0.0000042	0.94	—	—	—	—	—	—
Isoprene (C_5H_8)	GC/C	0.00017 ±0.000043	0.53	—	—	—	—	0.000069	0.73
2-methyl-1-pentene (C_6H_{12})	GC/C	0.000026 ±0.0000022	0.92	—	—	—	—	—	—
n-heptane (C_7H_{16})	GC/C	0.000025 ±0.0000024	0.90	—	—	—	—	—	—
Benzene (C_6H_6)	GC/C	0.00096 ±0.00004	0.98	0.00130 ±0.00004	0.96	0.00129 ±0.00005	0.97	0.0015	0.89
Toluene(C_7H_8)	GC/C	0.00072 ±0.000074	0.87	0.00049 ±0.00003	0.85	0.00057 ±0.00003	0.93	0.00094	0.81
Sum of all NMHC listed above	GC/C	0.024 ±0.001	0.98	0.022	—	0.022	—	0.027	—
Total particulate matter (TPM)	F/GB	200 ±66	0.69	—	—	—	—	—	—
Organic carbon (OC)	F/GB	32 ±12	0.56	—	—	—	—	—	—
Black carbon (BC)	F/GB	6 ±2.2	0.55	—	—	—	—	—	—
Total carbon (TC)	F/GB	40 ±12	0.60	—	—	—	—	—	—
Chloride (Cl^-)	F/GB	32 ±14	0.58	—	—	—	—	—	—

Table 3.2 continued

Species	Technique Used for Measure-ment in this study[†]	Southern Africa (This Study)		Southern Africa [*Blake et al.*, 1996]		Brazil [*Blake et al.*, 1996]		Brazil [*Ferek et al.*, 1998]	
		Molar Emission Ratio	r^2	Molar Emission Ratio	r^2	Molar Emission Ratio	r^2	Molar Emission Ratio	r^2
Nitrate (NO_3^-)	F/GB	3.3 ±0.63	0.88	—	—	—	—	—	—
Sulfate (SO_4^{2-})	F/GB	4.4 ±1.6	0.66	—	—	—	—	—	—
Potassium (K^+)	F/GB	15 ±3.8	0.79	—	—	—	—	—	—

*Molar emission ratios were obtained from the slope of the excess mixing ratio of a species plotted against the excess mixing ratio of a reference species. For CO and SO_2, the reference species was CO_2; for all other compounds the reference species was CO. Molar emission ratios have no units, except for particles (i.e., TPM and thereafter) for which the units are excess $\mu g/m^3$/excess CO ppmv.

[†]GC/C = gas chromatography via canisters; F/GB = filters via grab bag.

Table 3.3. As for Table 3.2 but for smoke from some of the individual savanna fires sampled by AFTIR in southern Africa in this study. See Table 3.1 for information on each fire.

Species	Skukuza 1,2	Madikwe 1	Madikwe 2,3	Kruger National Park	Beira	Kaoma 1	Kaoma 2	Timbavati	Average ± Standard Deviation From This Study
Carbon monoxide (CO)/CO_2	0.078	0.059	0.046	0.073	0.099	0.063	0.026	0.069	0.064±0.022
Nitric oxide (NO)/CO_2	0.0019	0.0019	0.001	0.0011	—	0.0010	0.0009	0.0008	0.0011±0.0004
Nitrogen dioxide (NO_2)/CO_2	0.0016	0.0020	0.0022	0.0019	0.0030	0.0020	0.0011	0.0018	0.0020±0.0005
Methane (CH_4)/CO	0.059	0.054	0.048	0.070	0.061	0.036	0.038	0.059	0.053±0.012
Ethene (C_2H_4)/CO	0.019	0.015	0.020	0.016	0.016	0.012	0.023	0.016	0.017±0.003
Acetylene (C_2H_2)/CO	0.0033	0.0037	0.0054	0.0043	0.0037	0.0037	0.0072	0.0034	0.0043±0.0013
Formaldehyde (HCHO)/CO	0.016	0.014	0.023	0.010	0.013	0.010	0.012	0.019	0.015±0.004
Methanol (CH_3OH)/CO	0.014	0.016	0.015	0.020	0.014	0.013	0.0093	0.015	0.015±0.003
Acetic acid (CH_3CO_2H)/CO	0.019	0.017	0.017	0.017	0.016	0.015	0.013	0.015	0.016±0.002
Formic acid (HCO_2H)/CO	0.0021	0.0066	0.0087	0.0054	0.0045	0.0051	0.0087	0.0064	0.0059±0.0022
Ammonia (NH_3)/CO	0.0076	0.0081	0.012	0.0027	—	0.0097	—	0.0016	0.0070±0.0046
Hydrogen cyanide (HCN)/CO	0.0094	0.011	0.013	0.0059	0.0056	0.056	0.011	0.0072	0.0085±0.0029

were similar to those we used in Africa. The sampling by *Blake et al.* [1996] in Africa was conducted in September-October 1992, similar to the August-September period of SAFARI 2000. However, most of the samples collected by Blake et al. were of aged smoke, whereas, the measurements reported here and those of Ferek et al. are for initial smoke.

Blake et al. reported emission ratios for CH_4 with respect to CO of 0.078 ± 0.004 and 0.094 ± 0.013 for southern Africa and Brazil, respectively. For Brazil, Ferek et al. report a CH_4 emission ratio of 0.12. Our emission ratios for CH_4 in southern Africa are 0.039 ± 0.003 for samples collected in canisters and 0.053 ± 0.012 from the AFTIR measurements. It appears from the average of these measurement that the CH_4 emission ratio with respect to CO from biomass burning in Brazil (0.11 ± 0.02) may be greater than that for savanna burning in southern Africa (0.057 ± 0.013). This could be due to high CH_4 emissions for downed woody material [*Bertschi et al.,* 2003].

We found a stronger correlation between excess CH_3Br and excess CO (r^2 = 0.69) than between excess CH_3I and excess CO ($r^2 = 0.50$) (Table 3.2). The emission ratios for CH_3Br, CH_3Cl and CH_3I reported here are 10-40% lower than those reported by *Blake et al.* [1996] for African biomass fires, and 30-66% lower than those reported by Blake et al. for Brazilian fires. *Mano and Andreae* [1994] estimated that CH_3Br emissions from biomass burning worldwide range from 10 to 50 Gg per year, which is comparable to that from oceans and pesticide use. Their value was obtained using a methyl bromide-to-methyl chloride emission ratio of 6×10^{-3} to 9×10^{-3}. Based on the measurements reported here for savanna burning in southern Africa, the emission ratio of methyl bromide with respect to methyl chloride is $(7.5 \pm 0.6)\times10^{-3}$ (Figure 3.2), which lies within the range used by Mano and Andreae.

Meinardi et al. [2003] detected emissions of dimethyl sulfide (CH_3SCH_3 or DMS) from bush fires in Australia. Their molar emission ratio of DMS to CO was 6.3 $\times 10^{-6}$ to 17×10^{-6}. The mixing ratios of DMS in southern Africa smoke plumes are strongly correlated with CO (Table 3.2 and Figure 3.3). This confirms that biomass burning is a source of DMS, which derives from the decomposition of amino acids such as methionine in plants. Using our value for the molar emission ratio of DMS with

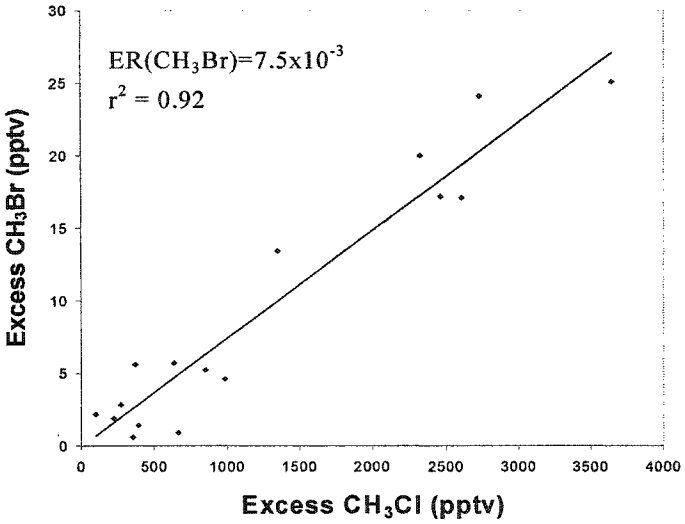

Figure 3.2. Excess mixing ratio of methyl bromide versus excess mixing ratio of methyl chloride. The molar emission ratio (ER) for methyl bromide with respect to methyl chloride obtained from the slope of the plot is shown. The correlation coefficient is given by r^2.

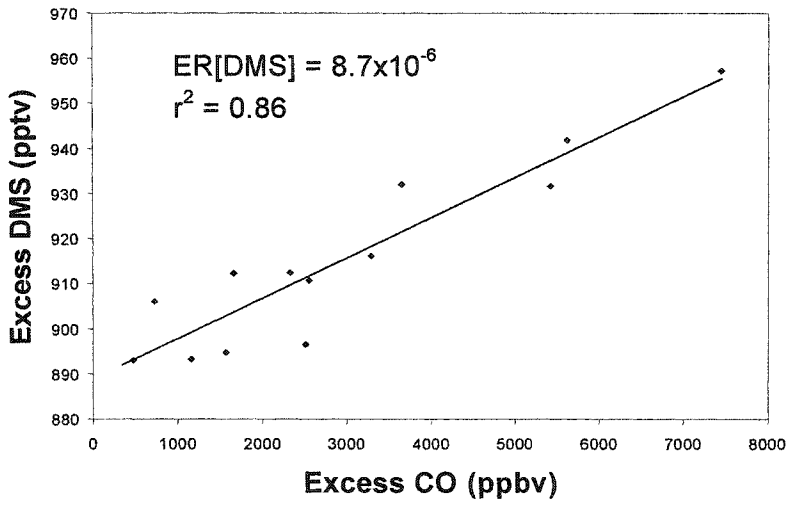

Figure 3.3. Excess mixing ratios of DMS versus excess mixing ratios of CO. The molar emission ratio (ER) for DMS with respect to CO obtained from the slope of the plot is shown. The correlation coefficient is given by r^2.

respect to CO [$(8.7 \pm 1.1)\times10^{-6}$], together with an estimate for the annual emission of CO worldwide from savanna and grassland burning (206 Tg yr^{-1}; *Andreae and Merlet* [2001]), yields an annual flux of DMS from savanna and grassland burning of 2.9 ± 0.4 Gg yr^{-1}. For comparison, the annual flux of DMS from the world's oceans is 30-50 Tg yr^{-1} [*Seinfeld and Pandis*, 1998]. However, there are large uncertainties associated with this type of extrapolation, in which a small number of data points from a specific region and season are used as a surrogate for DMS emissions from global savanna and grassland burning throughout the year. Also, there are significant uncertainties in the global CO emission estimates, which are known to within only about ±50% [*Blake et al.,* 1996].

Although small in relation to marine sources, DMS from biomass burning could be an important source of sulfur in non-industrial, continental interiors, even though direct emissions of sulfur as SO_2 from biomass burning (0.43 ± 0.30 g kg^{-1} for savanna burning in southern Africa) dominates over that of DMS (0.0013 ± 0.0011 g kg^{-1}). Oxidation of DMS by OH leads to the formation of SO_2. The lifetime of DMS with respect to OH oxidation is ~2 days [*Warneck,* 2000]. On the other hand, the lifetime of SO_2 with respect to removal by dry deposition is only ~1 day [*Seinfeld and Pandis,* 1998]. Therefore, DMS will be transported over somewhat larger distances after which, following oxidation by OH, it will serve as a source of SO_2.

The AFTIR aboard the Convair-580 in SAFARI 2000 provided the first quantitative measurements of oxygenated organic compounds in smoke from savanna fires (Table 3.3). The emission ratios of these compounds show that 3 of the top 5 organic compounds emitted by savanna fires are oxygenated. These compounds are discussed further in section 3.3 and by *Yokelson et al.* [2003].

Many other species measured in this study show potentially interesting results, but are not included in our tabulations or discussion because they did not satisfy our criteria for being emitted from the biomass fires (i.e., a correlation coefficient $\geq$0.5 for the excess mixing ratio of the species against the excess mixing ratio of CO or CO_2). For example, based on our measurements, the emission ratio of *i*-pentane with respect to excess CO in the smoke was about a factor of 5 below that reported by *Ferek et al.*

[1998]. However, the correlation coefficient for the excess mixing ratio of *i*-pentane against the excess mixing ratio of CO was 0.43.

3.3 Emission Factors

All of the emission factors (EF) reported here are based on airborne measurements made in smoke directly over, or within a few kilometers of the fire, that is, in initial smoke. As smoke ages, species within it are removed and others are generated by chemical and physical processes. Various effects of the aging of smoke are discussed in chapter 4.

As mentioned previously, if the correlation coefficient (r^2) for the excess molar mixing ratio of a species against the excess molar mixing ratio of CO (or CO_2) was $\geq$ 0.5, biomass burning was considered to be a significant source of that species. The emission factors for all such species from the present study are given in Table 3.4.

Figure 3.4 shows the EF of several gases plotted against the modified combustion efficiency (MCE) based on gas chromatography analysis of the sixteen canister samples obtained in the ten fires reported here. The slope of the regression of EF versus MCE indicates the importance of the combustion processes (flaming or smoldering) in determining the emission factor: the steeper the slope, the greater the dependence on the combustion process. A positive slope indicates that emission of the species is favored by flaming combustion (Figure 3.4a), and a negative slope that it is favored by smoldering combustion (Figures 3.4b-3.4f). The effectiveness of the MCE as an independent variable for determining EF is given by the correlation coefficient between EF and MCE. For species that have a high correlation coefficient between EF and MCE, measurements of CO and CO_2 alone (which together determine the MCE) may be used to estimate EF. Similar plots to Figure 3.4, but for the oxygenated compounds measured by the AFTIR, are given by *Yokelson et al.* [2003].

Table 3.5 lists slopes, intercepts, and correlation coefficients for the emission factors regressed against MCE for various species collected in the stainless steel canisters and by AFTIR. For many of the species listed in Table 3.5 (except CO_2 of course, see equation (5)), the emission factor decreases with increasing MCE (indicated

Table 3.4. Emission factors of species in young smoke from savanna fires in southern Africa measured in this study. Also listed are the corresponding values given by *Andreae and Merlet* [2001] for savanna and grassland burning. Emission factors have units of grams of species emitted per kilogram of fuel burned, except for CN and $CN_{0.1\text{-}3\mu m}$ which have units of number of particles emitted per kilogram of fuel burned. See Table 3.1 for information on each fire and Tables 3.2 and 3.3 for techniques used for measurements. When emission factors were measured by both GC/C and AFTIR, the GC/C values are given here. See Figure 3.8 for comparison of the two techniques.

Species	Skukuza 1	Skukuza 2	Madikwe 1	Madikwe 2	Madikwe 3	Kruger National Park	Beira	Kaoma 1	Kaoma 2	Timbavati	Average Value ± Standard Deviation From This Study	Average Value ± Standard Deviation [*Andreae and Merlet*, 2001]
Carbon dioxide (CO_2)	1692	1789	1611	1770	1681	1616	1686	1705	1759	1690	1700±60	1613±95
Carbon mon-oxide (CO)	71	24	120	23	82	97	73	73	42	76	68±30	65±20
Methane (CH_4)	3.0	0.6	3.3	0.8	1.7	2.5	1.1	1.4	0.5	1.8	1.70±0.98	2.3±0.9
Non-methane hydrocarbons (NMHC)	3.4	0.7	4.2	3.7	3.0	8.9	4.4	1.7	1.1	2.9	3.4±2.3	3.4±1.0
Nitrogen Oxides (NO_x)	3.8	—	5.4	5.2	—	4.7	5.2	4.8	3.1	3.8	4.50±0.83	3.9±2.4
Sulfur dioxide (SO_2)	—	—	—	—	—	0.87	0.33	0.22	0.30	—	0.43±0.30	0.35±0.16
Dimethyl sulfide (C_2H_6S)	0.0036	0.00048	—	—	0.0013	0.0012	0.0018	0.00049	0.00016	0.0017	0.0013± 0.0011	—

(Cont.)

Table 3.4 continued

Species	Skukuza 1	Skukuza 2	Madikwe 1	Madikwe 2	Madikwe 3	Kruger National Park	Beira	Kaoma 1	Kaoma 2	Timbavati	Average Value ± Standard Deviation From This Study	Average Value ± Standard Deviation [*Andreae and Merlet*, 2001]
Methyl bromide (CH_3Br)	0.0015	0.00027	0.0025	0.00091	0.0010	0.0015	0.00040	0.00048	0.00010	0.0016	0.0010± 0.0008	0.0021± 0.0010
Methyl chloride (CH_3Cl)	0.18	0.021	0.063	0.081	0.085	0.096	0.033	0.029	0.020	0.10	0.070± 0.048	0.075± 0.029
Methyl iodide (CH_3I)	0.00081	0.00014	0.00085	—	—	0.0010	0.00055	0.000084	0.000055	0.00058	0.00045± 0.00039	0.0005± 0.0002
Methyl nitrate (CH_3ONO_2)	0.00019	0.00011	0.0012	0.00079	0.00083	0.00026	0.00040	0.00028	0.00023	0.00075	0.00051± 0.00037	—
Ethane (C_2H_6)	0.42	0.08	0.29	0.13	0.25	0.33	0.096	0.19	0.078	0.25	0.21±0.12	0.32±0.16
Ethene (C_2H_4)	0.83	0.27	1.1	0.21	0.90	0.77	0.78	0.43	0.38	0.73	0.64±0.30	0.79±0.56
Propane (C_3H_8)	0.14	0.020	0.088	0.029	0.056	0.086	0.0014	0.048	0.016	0.064	0.054± 0.041	0.09±0.03
Propene (C_3H_6)	0.35	0.11	0.51	0.070	0.29	0.31	0.11	0.17	0.10	0.27	0.23±0.14	0.26±0.14
Acetylene (C_2H_2)	0.28	0.063	0.27	0.097	0.30	0.29	0.35	0.16	0.16	0.23	0.220± 0.095	0.29±0.27
i-butane (C_4H_{10})	0.012	0.0016	0.0092	0.0028	0.0051	0.0072	0.0007	0.0040	0.0010	0.0067	0.0050± 0.0037	0.006± 0.003
n-butane (C_4H_{10})	0.032	0.0047	0.029	0.0076	0.014	0.022	—	0.013	0.0048	0.018	0.016± 0.010	0.019± 0.090

(Cont.)

Table 3.4 continued

Species	Skukuza 1	Skukuza 2	Madikwe 1	Madikwe 2	Madikwe 3	Kruger National Park	Beira	Kaoma 1	Kaoma 2	Timbavati	Average Value ± Standard Deviation From This Study	Average Value ± Standard Deviation [*Andreae and Merlet*, 2001]
t-2-butene (C_4H_8)	0.023	0.0063	0.027	0.0023	0.015	0.022	0.0096	0.010	0.0038	0.016	0.013± 0.009	0.024± 0.014
1-butene (C_4H_8)	0.067	0.021	0.090	0.012	0.057	0.057	0.0052	0.034	0.019	0.050	0.041± 0.027	0.09±0.06
c-2-butene (C_4H_8)	0.017	0.0046	0.0202	0.0020	0.011	0.0160	0.0042	0.0072	0.0028	0.012	0.0097± 0.0065	0.021± 0.011
n-pentane (C_5H_{12})	—	0.00060	0.0106	0.0021	0.0045	0.0069	—	0.0041	0.0019	0.0050	0.0045± 0.0032	0.005± 0.004
1,3-butadiene (C_4H_6)	0.066	0.023	0.11	0.011	0.067	0.067	0.055	0.039	0.027	0.055	0.052± 0.028	0.07± 0.05
3-methyl-1-butene (C_5H_{10})	0.0089	0.0026	0.012	0.0013	0.0066	0.0064	0.0016	0.0038	0.0022	0.0063	0.0051± 0.0034	—
t-2-pentene (C_5H_{10})	0.0085	0.0021	0.0081	0.0004	0.0050	0.0073	0.0032	0.0033	0.0015	0.0052	0.0045± 0.0028	—
2-methyl-2-butene (C_5H_{10})	0.010	0.0017	0.0090	0.00031	0.0046	0.0087	0.0029	0.0040	0.0013	0.0058	0.0048± 0.0035	0.008± 0.004
2-methyl-1-butene (C_5H_{10})	0.010	0.0021	0.011	—	—	0.0083	0.0028	0.0044	0.0016	0.0066	0.0059± 0.0037	0.008± 0.004
c-2-pentene (C_5H_{10})	0.0045	0.0014	0.0047	—	—	0.0043	0.0012	0.0019	0.00094	0.0032	0.0025± 0.0018	—

(Cont.)

Table 3.4 continued

Species	Skukuza 1	Skukuza 2	Madikwe 1	Madikwe 2	Madikwe 3	Kruger National Park	Beira	Kaoma 1	Kaoma 2	Timbavati	Average Value ± Standard Deviation From This Study	Average Value ± Standard Deviation [*Andreae and Merlet*, 2001]
n-hexane (C_6H_{14})	—	0.0033	0.0284	—	0.013	0.0155	0.0126	0.0101	0.0071	0.0133	0.013± 0.0074	0.039± 0.045
Isoprene (C_5H_8)	0.077	0.011	0.069	0.0095	0.031	0.037	0.055	0.053	0.036	0.037	0.042± 0.022	0.02± 0.012
2-methyl-1-pentene (C_6H_{12})	0.0049	0.0020	0.0077	—	0.0029	0.0040	0.0029	0.0028	0.0003	0.0043	0.0035± 0.0021	—
n-heptane (C_7H_{16})	—	0.00015	0.023	—	0.0014	0.0090	0.0058	0.0056	0.0040	0.0065	0.0070± 0.0072	—
Benzene (C_6H_6)	0.26	0.069	0.28	0.047	0.22	0.25	0.23	0.13	0.089	0.20	0.18±0.09	0.23±0.11
Toluene (C_7H_8)	0.017	0.00056	0.33	0.06	0.19	0.0057	0.17	0.15	0.11	0.067	0.13±0.10	0.13±0.06
Formal-dehyde (HCHO)	1.4	1.4	0.96	1.2	1.2	0.87	1.4	0.75	0.39	1.5	1.1±0.38	0.26-0.44
Methanol (CH_3OH)	1.4	1.4	1.2	0.86	0.86	1.8	1.6	1.0	0.32	1.2	1.20±0.46	1.3
Acetic acid (CH_3CO_2H)	3.4	3.4	2.3	1.8	1.8	2.8	3.6	2.2	0.80	2.3	2.4±0.89	1.3
Formic acid (HCO_2H)	0.29	0.29	0.70	0.73	0.73	0.69	0.76	0.57	0.43	0.79	0.62±0.18	0.7
Ammonia (NH_3)	0.39	0.39	0.32	0.38	0.38	0.13	—	0.40	—	0.070	0.26±0.14	0.6-1.05
Hydrogen cyanide (HCN)	0.76	0.76	0.67	0.64	0.64	0.44	0.55	0.37	0.31	0.52	0.53±0.15	0.028

(Cont.)

Table 3.4 continued

Species	Skukuza 1	Skukuza 2	Madikwe 1	Madikwe 2	Madikwe 3	Kruger National Park	Beira	Kaoma 1	Kaoma 2	Timbavati	Average Value ± Standard Deviation From This Study	Average Value ± Standard Deviation [*Andreae and Merlet, 2001*]
Total particulate matter (TPM)	11	1.7	—	3.5	14	—	—	13	4.8	23	10.0±7.5	8.3±3.2
Organic particulate carbon (OC)	3.5	0.68	—	1.3	3.3	2.2	1.7	3.0	0.70	4.0	2.3±1.2	3.4±1.4
Black carbon (BC)	0.45	0.081	—	—	0.63	0.41	0.25	0.47	0.24	0.68	0.39±0.19	0.48±0.18
Total particulate carbon (TC)	4.0	0.76	—	1.6	3.9	2.6	2.0	3.5	0.94	4.7	2.7±1.4	3.7±1.3
Chloride (Cl^-)	0.57	0.18	—	0.087	1.9	—	—	0.26	0.0093	3.8	0.97±1.40	—
Nitrate (NO_3^-)	0.099	0.013	—	0.25	0.29	—	—	0.19	0.050	0.26	0.16±0.11	—
Sulfate (SO_4^{2-})	0.027	0.003	—	—	0.26	—	—	0.14	0.09	0.48	0.17±0.18	—
Potassium (K^+)	0.17	0.092	—	0.22	—	—	—	0.38	0.12	1.4	0.50±0.53	0.34±0.15
Condensation nuclei (CN)	—	—	—	—	—	2.0×10^{16}	2.7×10^{16}	5.9×10^{16}	1.7×10^{16}		$(3.0\pm1.7)\times10^{16}$	3.4×10^{15}
$CN_{0.1\text{-}3\mu m}$	5.3×10^{14}	1.8×10^{13}	—	2.4×10^{14}	8.9×10^{13}	2.7×10^{14}	1.6×10^{14}	2.1×10^{14}	1.5×10^{14}		$(2.0\pm1.5)\times10^{14}$	—

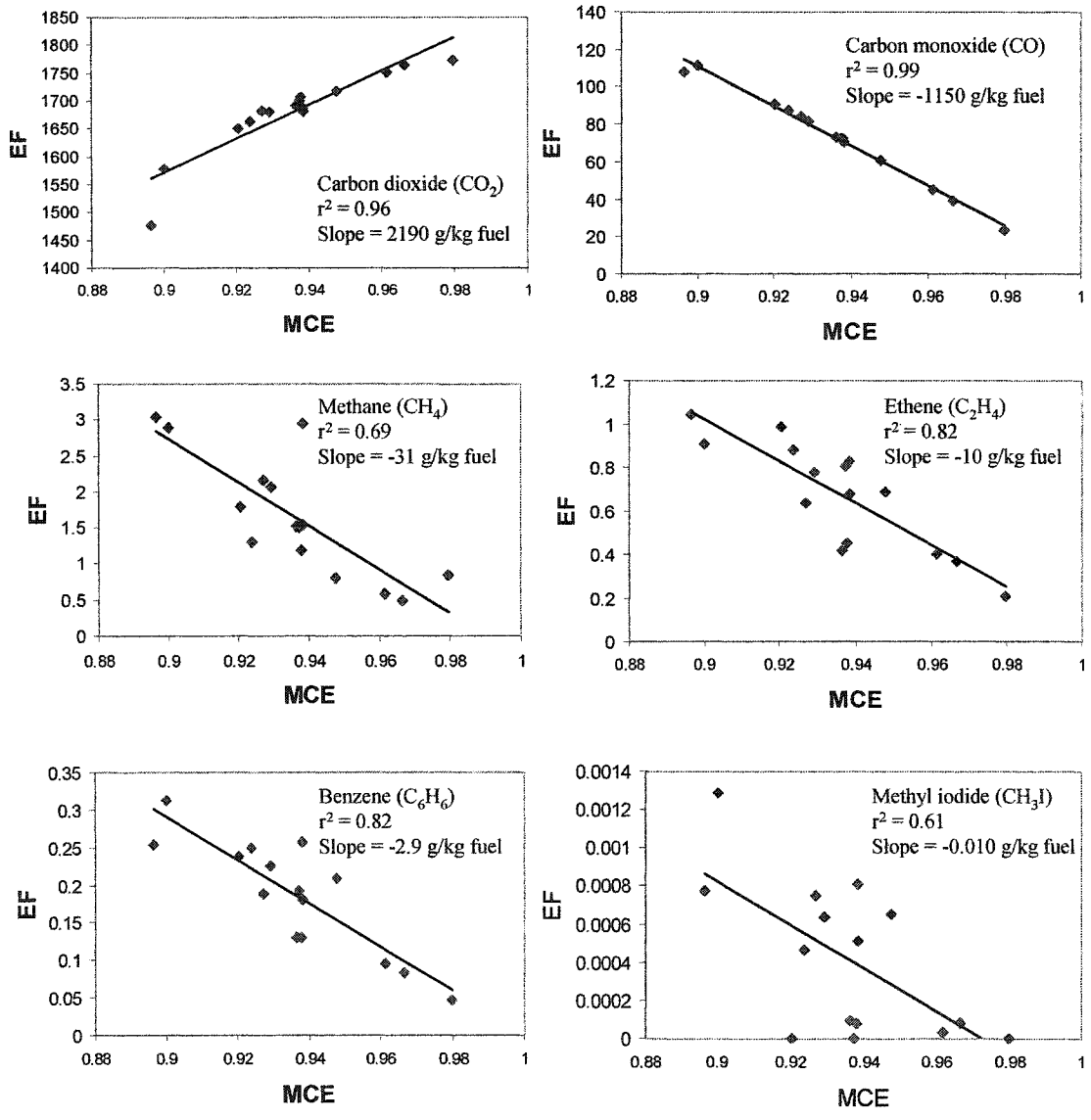

Figure 3.4. Emission factors (grams of species emitted per kilogram of fuel burned) versus modified combustion efficiency (MCE) for various trace gases in each of sixteen canister samples. The correlation coefficient is given by r^2.

Table 3.5. Average values of regression slopes, regression intercepts, and correlation coefficients (r^2) for emission factors (EF, in g per kg of fuel burned) versus modified combustion efficiency (MCE) for young smoke from savanna fires sampled in southern Africa in this study.

Species	Technique Used for Measurement*	Slope	Intercept	r^2
Carbon dioxide (CO_2)	GC/C	2190	-357	0.96
Carbon monoxide (CO)	GC/C	-1150	1150	0.99
Methane (CH_4)	GC/C	-31	31	0.69
Non-methane organic compounds (NMOC)	GC/C	-50	50	0.33
Nitric oxides (NO_x)	GC/C	-10	14	0.10
Sulfur dioxide (SO_2)	Teco 43S (via "grab bag")	-11	10	0.56
Dimethyl sulfide (CH_3SCH_3)	GC/C	-0.020	0.021	0.16
Methyl bromide (CH_3Br)	GC/C	-0.020	0.020	0.54
Methyl chloride (CH_3Cl)	GC/C	-0.52	0.56	0.08
Methyl iodide (CH_3I)	GC/C	-0.010	0.011	0.61
Methyl nitrate (CH_3ONO_2)	GC/C	-0.006	0.006	0.18
Ethane (C_2H_6)	GC/C	-2.9	2.9	0.44
Ethene (C_2H_4)	GC/C	-10	10	0.82
Propane (C_3H_8)	GC/C	-0.87	0.87	0.31
Propene (C_3H_6)	GC/C	-4.5	4.4	0.72
Acetylene (C_2H_2)	GC/C	-2.8	2.8	0.62
i-butane (*i*-C_4H_{10})	GC/C	-0.090	0.087	0.39
n-butane (*n*-C_4H_{10})	GC/C	-0.28	0.28	0.62
t-2-butene (C_4H_8)	GC/C	-0.28	0.28	0.77
1-butene (C_4H_8)	GC/C	-0.80	0.79	0.61
c-2-butene (C_4H_8)	GC/C	-0.20	0.20	0.70
i-pentane (*i*-C_5H_{12})	GC/C	-0.03	0.03	0.86
n-pentane (*n*-C_5H_{12})	GC/C	-0.10	0.098	0.89
1,3-butadiene (C_4H_6)	GC/C	-1.0	0.99	0.88
3-methyl-1-butene (C_5H_{10})	GC/C	-0.10	0.10	0.62
t-2-pentene (C_5H_{10})	GC/C	-0.090	0.087	0.69
2-methyl-2-butene (C_5H_{10})	GC/C	-0.10	0.10	0.66
2-methyl-1-butene (C_5H_{10})	GC/C	-0.11	0.11	0.65
c-2-pentene (C_5H_{10})	GC/C	-0.050	0.047	0.58
n-hexane (C_6H_{14})	GC/C	-0.26	0.26	0.86
Isoprene (C_5H_8)	GC/C	-0.57	0.58	0.47
2-methyl-1-pentene (C_6H_{12})	GC/C	-0.07	0.68	0.65
n-heptane (C_7H_{16})	GC/C	-0.21	0.21	0.61
Benzene (C_6H_6)	GC/C	-2.9	2.9	0.82
Toluene(C_7H_8)	GC/C	-2.1	2.1	0.31
Formaldehyde (HCHO)	AFTIR	-13.94	19.17	0.48
Methanol (CH_3OH)	AFTIR	-21.28	21.17	0.80
Acetic acid (CH_3CO_2H)	AFTIR	-45.33	45.03	0.93
Formic acid (HCO_2H)	AFTIR	-7.51	7.77	0.15
Ammonia (NH_3)	AFTIR	-3.71	3.75	0.12
Hydrogen cyanide (HCN)	AFTIR	-3.07	3.42	0.15
Total particulate matter (TPM)	F/BH	-292	288	0.75
Total carbon (TC)	F/BH	-43	43	0.49

(Cont.)

Table 3.5 continued

Species	Technique Used for Measurement*	Slope	Intercept	r^2
Organic carbon (OC)	F/GB	-37	38	0.47
Black carbon (BC)	F/GB	-5.8	5.8	0.47
Chloride (Cl^-)	F/GB	-39	38	0.38
Nitrate (NO_3^-)	F/GB	-2.4	2.5	0.24
Sulfate (SO_4^{2-})	F/GB	-5.4	5.3	0.39
Potassium (K^+)	F/GB	-16	16	0.45

*GC/C = gas chromatography via canister; F/GB = filters via grab bag; AFTIR = Airborne Fourier Transform Infrared

by negative slopes in Table 3.5). This shows that these species are preferentially released during smoldering combustion. However, for those species whose emission factors are weakly correlated with MCE (indicated by low values of r^2 in Table 3.5), the emissions are not strongly dependent on the combustion process. Our results for SO_2 show a negative slope for EF versus MCE and a reasonably high r^2 value (0.56, Table 3.5), even though laboratory studies indicate that SO_2 is preferentially released in flaming combustion [*Crutzen and Andreae,* 1990; *Yokelson et al.,* 1996]. This could result from fires with low values of MCE occurring by chance in fuels with high sulfur content.

Figure 3.5 compares the emission factors of CO_2, CO, CH_4, and NMOC reported here for the burning of savanna in southern Africa with those reported by *Ferek et al.* [1998] for the burning of grassland in Brazil, and with the global compilation of emission factors for savanna burning by *Andreae and Merlet* [2001]. Taking into account the standard deviations of the measurements, the mean emission factors for CO_2, CO, CH_4, and NMHC provided by these three studies are similar.

Figure 3.6 compares the emission factors reported here for total particulate matter, total particulate carbon, organic carbon, and black carbon with those given by *Ferek et al.* [1998] for the burning of grassland in Brazil and with the compilation by *Andreae and Merlet* [2001]. In view of the standard deviations of the measurements, the mean emission factors for total particulate matter, total carbon, organic carbon, and black carbon given in these three studies are also similar.

The single-scattering albedo of smoke emitted from biomass fires depends on the ratio of organic carbon to black carbon [*Mazurek et al.,* 1991]. The ratio of the emission factors of black carbon to organic carbon in this study is 0.17 ± 0.12. The corresponding value given by *Andreae and Merlet* [2001] for savanna and grassland burning is 0.14 ± 0.08.

The emission factors of several compounds reported here (Table 3.4 and Figure 3.7) differ significantly from those reported by *Andreae and Merlet* [2001]. For example, the average emission factor for NH_3 measured in this study is 0.26 ± 0.15 g

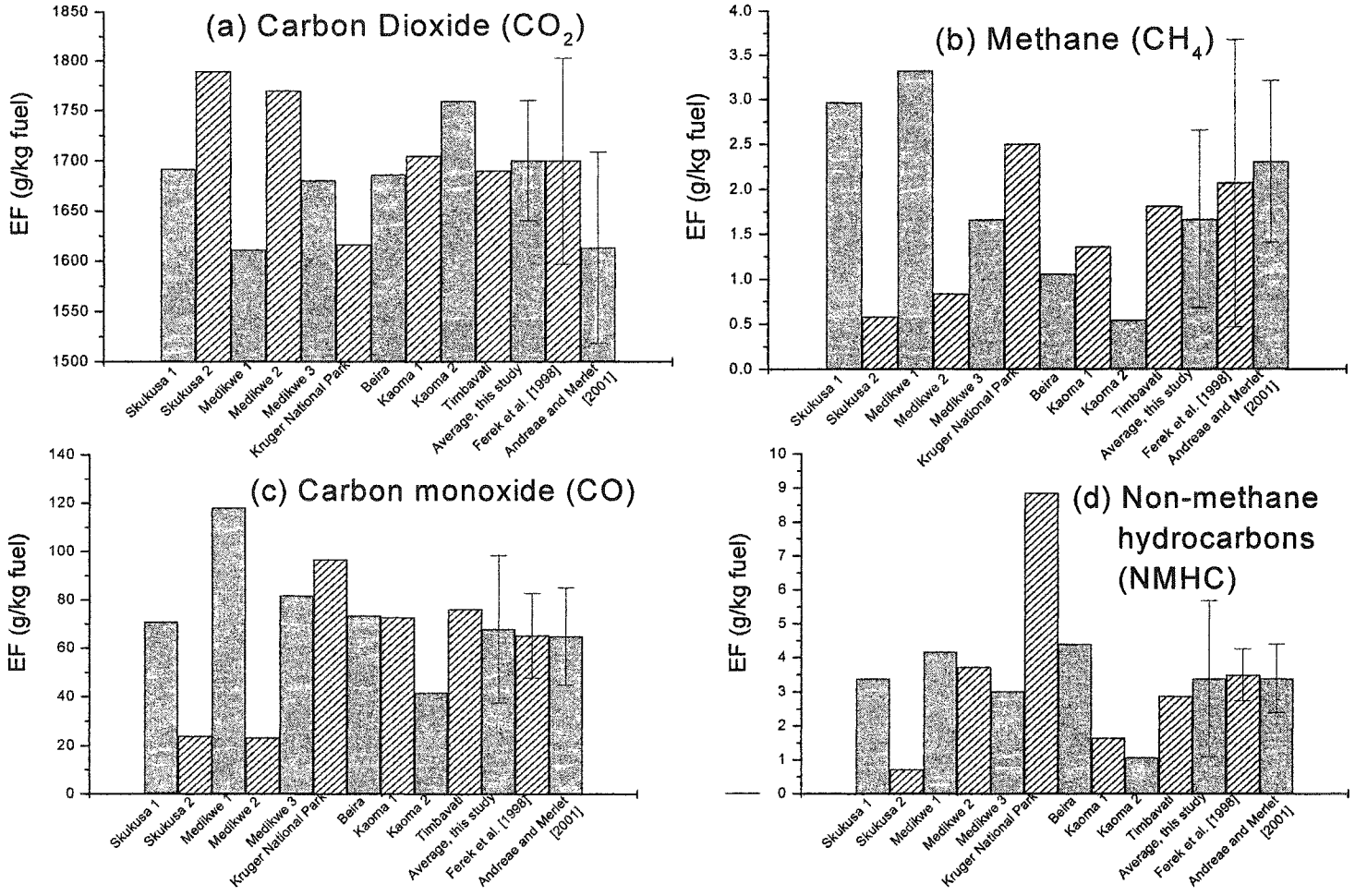

Figure 3.5. Emission factors (EF) for CO_2, CO, CH_4, and NMHC, derived from canister measurements, for the burning of savanna in southern Africa (this study), grassland in Brazil [*Ferek et al.,* 1998], and global savanna burning [*Andreae and Merlet,* 2001].

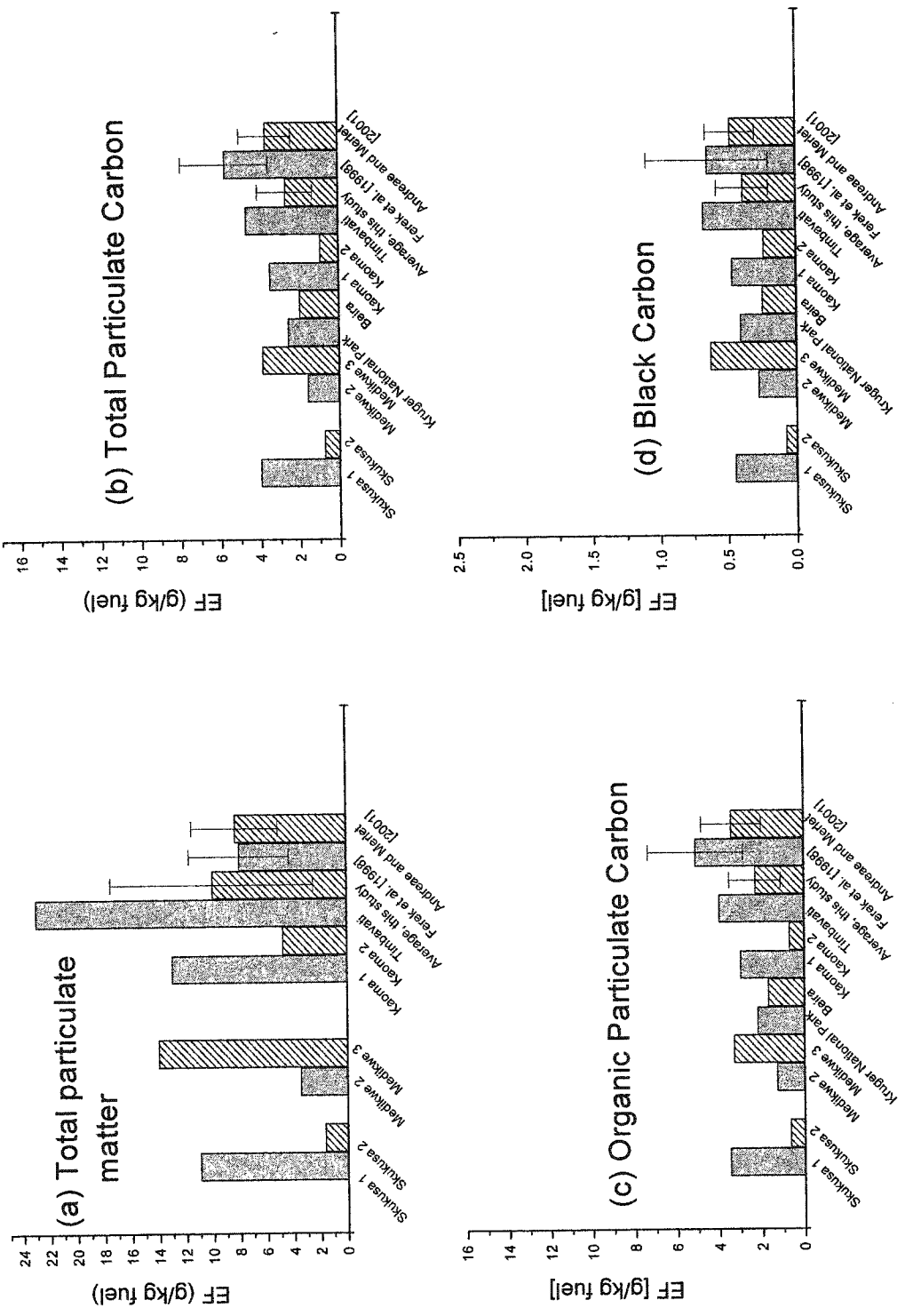

Figure 3.6. As for Figure 3.5 but for total particulate matter, total particulate carbon, organic particulate carbon and black carbon.

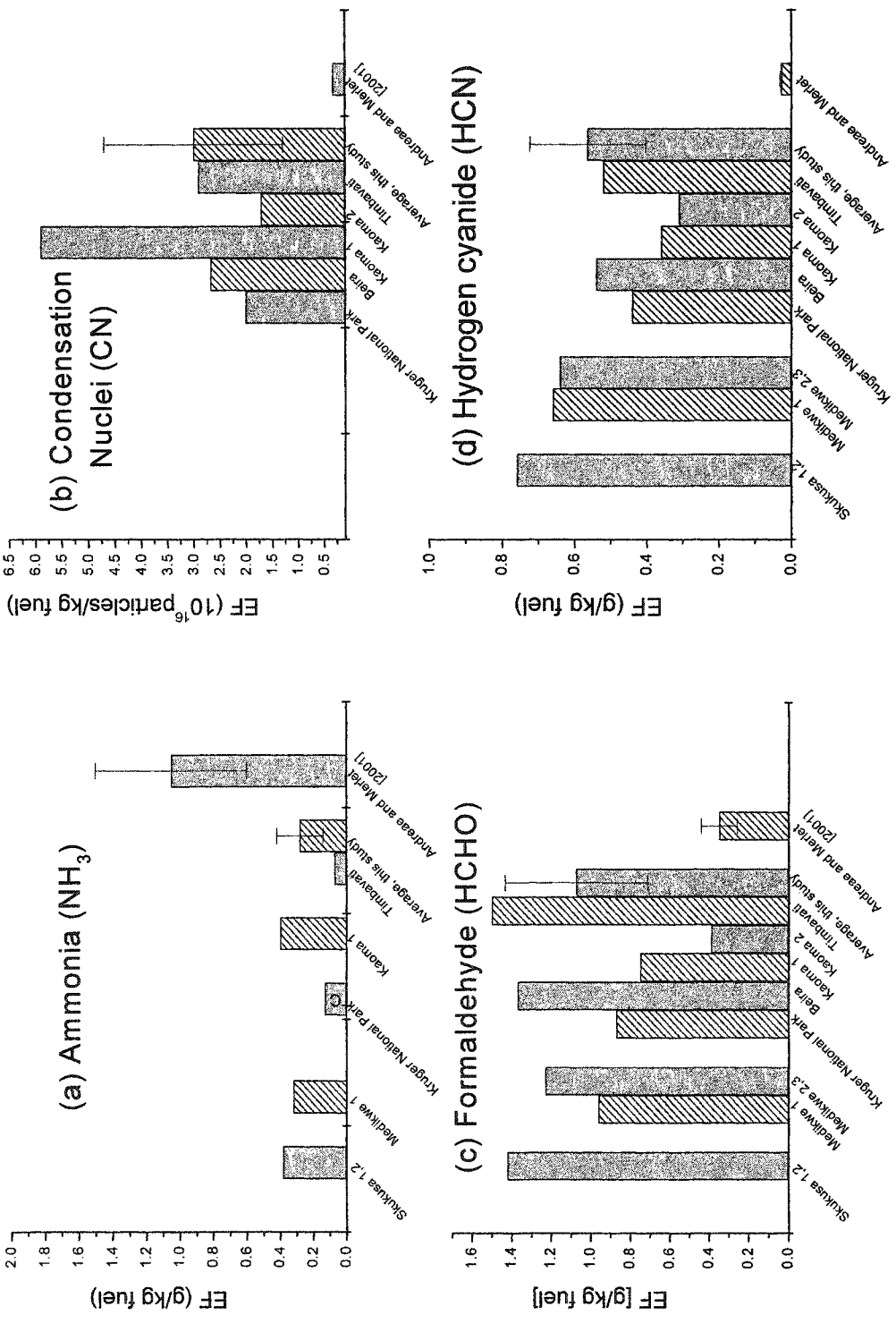

Figure 3.7. Emission factors (EF) for ammonia, condensation nuclei, formaldehyde, and hydrogen cyanide from the burning of savanna in southern Africa measured in this study compared to those given for global savanna burning by *Andreae and Merlet* [2001].

kg^{-1} compared to 0.6-1.5 g kg^{-1} given by Andreae and Merlet. Multiplying the average NH_3 emission factor for savanna fires in southern Africa given here by an estimate for savanna burned in Africa (1600 Tg yr^{-1}; *Hao and Liu* [1994]) yields 0.34 ± 0.27 Tg yr^{-1} of NH_3 emitted by African savanna fires. Since the emission of ammonia from all sources worldwide is believed to be ~55 Tg yr^{-1} [*Seinfeld and Pandis*, 1998], savanna burning in Africa makes only a small contribution to global NH_3 emissions. Boreal forest fires have a large emission factor for NH_3 and may produce more total NH_3 emissions [*Goode et al.*, 2000].

As mentioned earlier, AFTIR samples obtained in this study showed that oxygenated organic compounds were a major component of smoke from young savanna fires. While NMHC dominate organic emissions on a carbon basis, oxygenated emissions dominate on a mass basis. The oxygenates have important effects on chemical reactions in a smoke plume, as described by *Mason et al.* [2001]. On a mass basis, acetic acid is the major initial organic emission (EF = 2.4 ± 0.9 g/kg), and its concentration rapidly increases downwind [*Yokelson et al.*, 2003]. Methanol and formaldehyde are the other two major oxygenates emitted by fires. Methanol is a source of HO_2 and HCHO in the atmosphere. The average emission factor for the direct emission of HCHO given here is 1.1 ± 0.38 g kg^{-1} (Table 3.4), compared to 0.26-0.44 g kg^{-1} given by *Andreae and Merlet* [2001]. Multiplying our average HCHO emission factor for savanna burning by the estimate of 1600 Tg yr^{-1} for savanna burned in Africa, yields ~1.8 ± 0.62 Tg yr^{-1} of HCHO emitted from savanna fires in Africa. Photolysis of HCHO produces HO_2, which leads to conversion of NO to NO_2 and subsequent ozone formation. Therefore, HCHO emissions from savanna burning may lead to increased initial ozone formation rates [*Yokelson et al.*, 1999]. The oxygenated organic compounds were strongly affected by cloud processing [*Yokelson et al.*, 2003].

Our average emission factor for HCN is 0.53 ± 0.15 g kg^{-1} (Table 3.4), compared to 0.025-0.03 g kg^{-1} given by *Andreae and Merlet* [2001]. Since the major global source for HCN is biomass burning, and since this species can be monitored

from space, HCN has been proposed as a tracer for biomass burning [*Li et al.*, 2000]. The abundance of HCN emitted by African savanna fires lends support to this proposal.

The emission factor for aerosols (i.e., Aitken nuclei or CN) given by *Andreae and Merlet* [2001], namely 3.4×10^{15} particles per kilogram of fuel burned, is based on laboratory measurements. Taking into account the uncertainty in the measurements, our CN emission factor for savanna burning in southern Africa is ~3-14 times greater than the value given by *Andreae and Merlet* (Table 3.4 and Figure 3.7). Multiplying our average CN emission factor, $(3.0 \pm 1.7) \times 10^{16}$ particles per kilogram of fuel burned, by Hao and Liu's estimate of 1600 Tg yr^{-1} for savanna burned in Africa, yields 2×10^{28} to 8×10^{28} CN emitted per year from African savanna fires. This estimate is about an order of magnitude greater than an earlier estimate by *Le Canut et al.* [1996] of ~3×10^{27} to 8×10^{27} particles emitted per year worldwide by savanna fires which assumed 3690 Tg yr^{-1} of savanna burned worldwide. Since ~30-100% of submicron biomass smoke particles can act as cloud condensation nuclei [*Rodgers et al.*, 1991], the particles emitted by African savanna fires could have important effects on regional cloud microstructures.

Table 3.4 lists emission factors for eleven species that do not appear in the compilation of emission factors for biomass burning given by *Andreae and Merlet* [2001]. These species are DMS, methyl nitrate, five hydrocarbons (3-methyl-1-butene, *c*-2-pentene, *t*-2-pentene, 2-methyl-1-pentene, and *n*-heptane), the particulate anions Cl^-, SO_4^{2-} and NO_3^-, and particles in the size range 0.1 to 3 μm diameter ($CN_{0.1\text{-}3\mu m}$). For all these species, the correlation coefficient (r^2) of the excess mixing ratio versus the excess mixing ratio of CO was ≥0.5, indicating that they were emitted by biomass burning. Except for Cl^-, SO_4^{2-}, and NO_3^-, which are discussed by *Andreae et al.* [1998], these species have not been previously reported for biomass burning of savanna in southern Africa. These species are discussed in turn below.

The oxidation of DMS to SO_2 can lead subsequently to the formation of sulfate particles. Average emission factors for DMS, SO_2 and SO_4^{2-} from this study are,

respectively, 0.0013 ± 0.001, 0.43 ± 0.30, and 0.17 ± 0.18 grams per kilogram of fuel burned (Table 3.4). The large standard deviations in these values reflect the high variability in the emissions of these species, which is not surprising since fuel sulfur content varies greatly. Nevertheless, the average value of the emission factor for DMS is about a factor of 100 below that of SO_2 and SO_4^{2-}. Therefore, on average, the direct emission of SO_4^{2-} from the fires probably dominated over the subsequent production of SO_4^{2-} through DMS oxidation, but not over SO_4^{2-} production due to the oxidation of SO_2 emitted directly from the fires.

Methyl nitrate (CH_3ONO_2), which is produced photochemically from CH_4 and NO_x, and the thermal decomposition of PAN, can serve to redistribute NO_2 in regions distant from its source, which can then lead to O_3 formation [*Warneck,* 2000]. The average emission factor for CH_3ONO_2 measured in this study of young smoke is only 0.00051 ± 0.00037 grams per kilogram of fuel burned, compared to 4.50 ± 0.83 g kg^{-1} for NO_x (Table 3.4). However, CH_3ONO_2 and NO_x could have comparable mixing ratios in older smoke.

The five new hydrocarbons we detected in the smoke over the fires are reactive alkanes and alkenes. Because the OH radical is a major oxidant for these five hydrocarbons, their presence will reduce the concentration of OH, and therefore oxidation by OH, downwind in smoke plumes. All five hydrocarbons decreased significantly as the smoke aged (see Chapter 4).

The emission factors for Cl^-, NO_3^- and SO_4^{2-} reported here, namely, 0.97 ± 1.4, 0.16 ± 0.11 and 0.17 ± 0.18 g kg^{-1}, respectively, can be compared with the corresponding values given for savanna, forest and agricultural fires in southern Africa by *Andreae et al.* [1998], namely, 1.40 ± 0.35, 0.37 ± 0.20 and 0.59 ± 0.24, respectively. The values given by Andreae et al. may be larger because of higher nutrient content in agricultural fuels and/or because they sampled older smoke than we did.

Emission factors for the particulate ionic species can be compared to their most abundant corresponding gaseous species. For example, the molar ratio of the emission factors of NO_3^- to NO_x is 0.022, and the molar ratio of the emission factors of SO_4^{2-} to SO_2 is 0.26. These ratios indicate that most of the nitrogen released from the fires was in gaseous form as NO_x, and about four times as much SO_2 was released as was SO_4^{2-}. Furthermore, chemical transformations from NO_x to nitrate, and from SO_2 to sulfate, could have occurred even in the young smoke. However, the latter transformation must have occurred more rapidly than the former. The molar ratio of the emission factor of Cl^- to CH_3Cl is 20, which suggests that most of the chlorine released was in particulate form as Cl^-.

The emission factors for Cl^-, NO_3^- and SO_4^{2-} can be compared with those for K^+ and NH_3, to check the balance between emissions of positive and negative ions. The emission factors for K^+ and Cl^- are 0.50 ± 0.53 and 0.97 ± 1.4 g kg^{-1} (or 0.013 ± 0.014 and 0.027 ± 0.039 mol kg^{-1}), respectively, which are not significantly different (K^+ and Cl^- can form the neutral KCl). Ammonia is the primary basic gas in the atmosphere, which can neutralize HNO_3 and H_2SO_4. The emission factor for NH_3 is 0.26 ± 0.15 g kg^{-1} (or 0.015 ± 0.009 mol kg^{-1}), while the sum of the emission factors for NO_3^- and SO_4^{2-} is 0.33 ± 0.21 g kg^{-1} (or 0.0044 ± 0.0026 mol kg^{-1}). These comparisons indicate that, on average and within the variability of the measurements, the positive and negative ions emitted by the fires were in charge balance.

Aerosol surface area is one of the main factors that determines the rates of heterogeneous reactions. Most of the surface area of aerosols in the atmosphere is associated with accumulation mode particles, which have peak concentrations at a diameter of about 0.1 μm. Since accumulation mode particles are not removed very efficiently from the atmosphere, they have relatively long residence times (~weeks) [e.g., *Hobbs,* 2000]. As shown in Table 3.4, the average emission factor of particles with diameters from 0.1 to 3 μm (i.e., accumulation-mode particles) from savanna

burning in southern Africa measured in this study was $(2.0 \pm 1.5) \times 10^{14}$ particles per kilogram of fuel burned, compared to $(3.0 \pm 1.7) \times 10^{16}$ total (CN) particles emitted per kilogram of fuel burned. If it is assumed that all particles in the accumulation mode have a diameter of 0.1 μm, the emission factor for the surface area of these particles is (1.6 ± 1.2) m^2 per kilogram of fuel.

Based on the $CN_{0.1\text{-}3\ \mu m}$ and CN emission factors, only ~1% by number of the particles in the initial smoke were in the accumulation mode. Particle size spectra measured with the DMPS showed that the particle mode diameter in the initial smoke was ~0.01 μm, with most of the particles ranging from ~0.01-0.03 μm. As smoke ages, particle coagulation and gas-to-particle conversion increase the particle mode diameter (see Chapter 4).

3.4. Comparisons of Measurements Using Gas Chromatography and Fourier Transform Infrared Spectroscopy

In laboratory studies, *Goode et al.* [1999] obtained excellent agreement for the concentrations of a number of gaseous species measured in the same biomass smoke by gas chromatography on canister samples (GC/C) and by Fourier transform infrared spectroscopy. In the field studies described in the present paper, five species (CO_2, CO, CH_4, C_2H_2 and C_2H_4) were measured by both GC/C and by AFTIR. This provides a unique opportunity to compare measurements from these two independent techniques under field conditions. However, in doing so it should be pointed out that in the present study the GC/C and AFTIR measurements were not made on exactly the same smoke samples. Also, whereas a single ambient GC/C sample was obtained for each fire, multiple ambient AFTIR measurements were obtained.

Shown in Table 3.6 are comparisons of both emission factors and MCEs derived from the GC/C and AFTIR measurements for the ten fires described in this paper. The emission factors derived from these two independent measuring techniques are in good agreement for the Madikwe 2, 3, Kruger National Park, Kaoma 1, and Kaoma 2, and the Timbavati fires. For these fires, the MCE derived from the GC/C and AFTIR

Table 3.6. Modified combustion efficiency (MCE) and emission factors (grams of species emitted per kilogram of fuel burned) measured by gas chromatography on canister samples (GC/C) and by airborne Fourier Transform Infrared Spectroscopy (AFTIR). A total of sixteen GC/C samples and thirty-six AFTIR samples were obtained for the ten fires listed.

Measurement	Technique Used for Measurement	Skukuza 1, 2*	Madikwe 1	Madikwe 2, 3*	Kruger National Park	Beira	Kaoma 1	Kaoma 2	Timbavati	Study Average
MCE	GC/C	0.96	0.90	0.96	0.93	0.95	0.94	0.96	0.94	0.94 ± 0.02
	AFTIR	0.93	0.94	0.96	0.93	0.91	0.94	0.97	0.94	0.94 ± 0.02
Emission Factor										
Carbon dioxide	GC/C	1741	1611	1726	1616	1686	1705	1759	1690	1700 ± 51
	AFTIR	1678	1715	1738	1688	1643	1711	1779	1696	1706 ± 38
Carbon monoxide	GC/C	48	120	53	97	73	73	42	76	68 ± 24
	AFTIR	84	64	51	78	103	69	30	75	69 ± 21
Methane	GC/C	1.8	3.3	1.3	2.5	1.1	1.4	0.5	1.8	1.7 ± 0.8
	AFTIR	2.8	2.0	1.4	3.1	3.6	1.4	0.6	2.5	2.2 ± 0.9
Ethene	GC/C	0.55	1.1	0.56	0.77	0.78	0.43	0.38	0.73	0.64 ± 0.22
	AFTIR	1.61	0.97	1.02	1.22	1.60	0.82	0.69	1.19	1.14 ± 0.31
Acetylene	GC/C	0.17	0.27	0.20	0.29	0.35	0.16	0.16	0.23	0.22 ± 0.07
	AFTIR	0.26	0.22	0.26	0.31	0.36	0.24	0.20	0.24	0.26 ± 0.05

* Measurements for Skukuza 1 and 2 are averaged together since they were obtained on similar fires located close together on the same day; similarly for Madikwe 2 and 3.

measurements are either identical or similar, indicating that similar smoke was sampled by both techniques. For the Skukuza 1, 2 and Beria fires, the smoke sampled for the GC/C measurements had higher average MCEs than the smoke sampled by the AFTIR. Consistent with this, the emission factor for CO_2 was greater, and the emission factors for the smoldering products (CO, CH_3, C_2H_2 and C_2H_4) were lower, from the GC/C measurements than from the AFTIR. The reverse was true for the Madikwe 1 fire, where the smoke sampled for the GC/C measurements had a lower MCE than the smoke sampled by the AFTIR. We conclude from these results that the GC/C and AFTIR provided similar results when they sampled similar smoke.

Comparisons of study-average emission ratios and emission factors for CO_2, CO, CH_4, C_2H_2 and C_2H_4 derived from the GC/C and AFTIR are shown in Figure 3.8. The values obtained from the two techniques are in good agreement, with the exception of C_2H_4 (ethene). The average emission ratios for C_2H_4 from GC/C and AFTIR are 0.0110± 0.0005and 0.017 ± 0.003, respectively. *Ferek et al.* [1998] reported a C_2H_4 emission ratio of 0.011 obtained by GC/C for young smoke from grass, cerrado, and forest fires in Brazil. *Blake et al.* [1996] reported C_2H_4 emission ratios from GC/C of 0.0083 ± 0.0006 and 0.0061 ± 0.0004 for young and aged smoke (with depleted C_2H_4) from savanna fires in southern Africa and from agricultural fires in Brazil, respectively. Hence, the C_2H_4 emission ratios measured by several workers using GC/C are lower in magnitude than those obtained in this study using AFTIR, although *Goode et al.* [1999] did not observe a significant difference between the two measurement techniques.

The study-average emission factors for C_2H_4 from the GC/C and AFTIR are 0.64 ± 0.22 and 1.14 ± 0.31 grams per kilogram of fuel burned, respectively. If these two average values are weighted by the number of samples obtained for the GC/C and AFTIR measurements (16 and 36, respectively), and then combined to yield an overall study-average for the emission factor of C_2H_4, the value obtained is 0.99 ± 0.28 grams per kilogram of fuel burned. *Andreae and Merlet* [2001] give a value of (0.79 ± 0.56) g/kg for the emission factor of C_2H_4 from savanna and grassland fires.

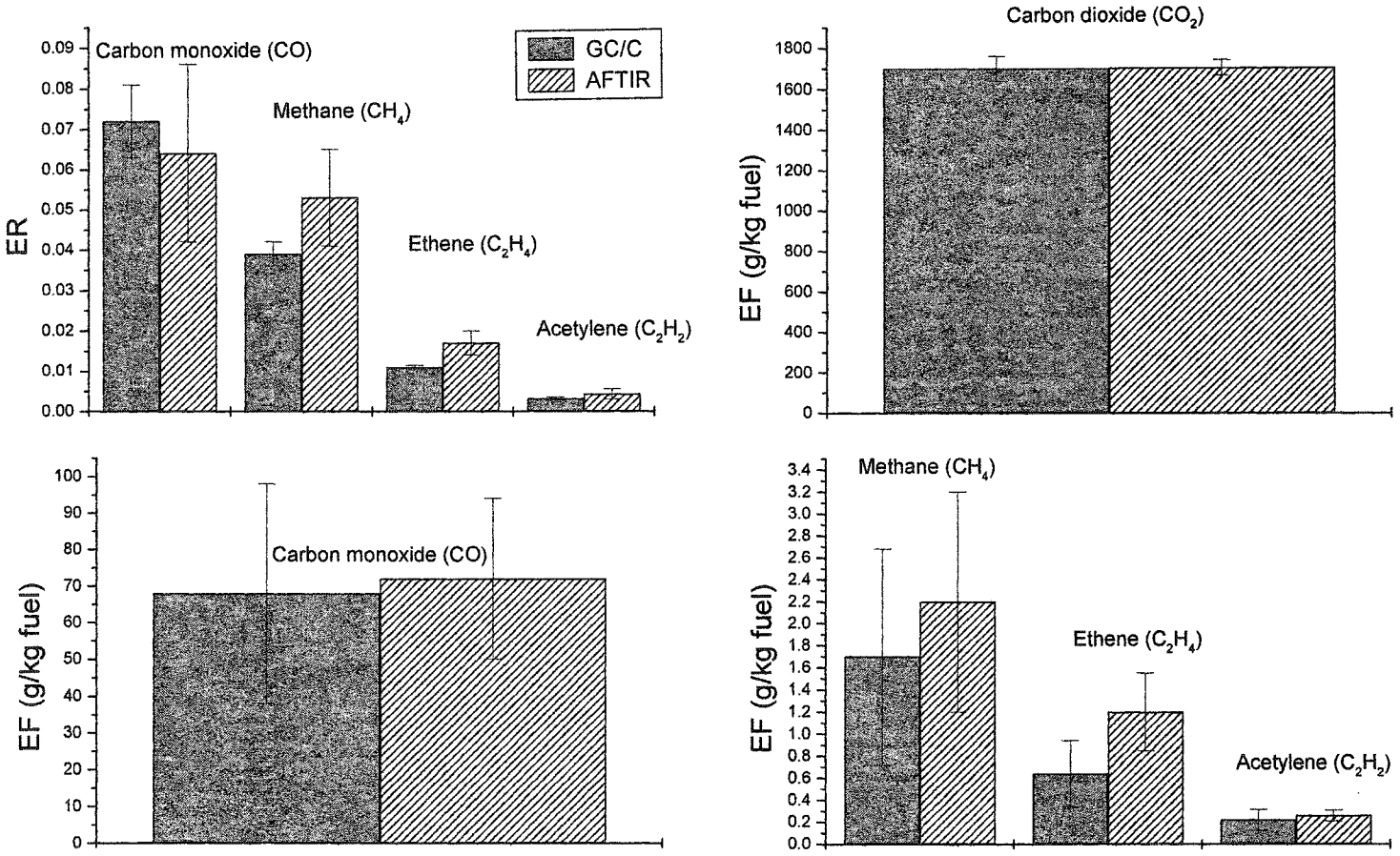

Figure 3.8. Comparisons of molar emission ratios (ER) and emission factors (EF) for savanna fires in southern Africa for carbon monoxide (with respect to CO_2) and methane, ethane and acetylene (with respect to CO), and emission factors for carbon dioxide, carbon monoxide, methane, ethane and acetylene, calculated from two independent measurement techniques: gas chromatography on canister samples and AFTIR.

3.5. Estimates of Regional Emissions

Emission factors for fifty gaseous and particulate species from savanna fires in southern Africa are provided in Table 3.4. Emission factors can be combined with estimates of fuel consumption to obtain regional emissions from savanna fires. Emission factors from the "Kaoma 1" miombo woodland savanna fire and "Kaoma 2" dambo grassland savanna fire (Table 3.4) are used to estimate regional emissions from savanna fires in southern Africa. The miombo woodland ecosystem is the most abundant type of savanna in southern Africa and the largest contiguous block of deciduous tropical woodlands and dry forests in the world, covering ~2.8 million km^2 including much of Africa from 4–17°S. Dambo grasslands are major enclaves within miombo woodlands, covering up to 40% of the landscape in some areas [*IGBP,* 1997]. Combining the emission factors from the miombo woodland and dambo grassland savanna fires (Table 3.4) with estimates of fuel consumed by woodland and grassland savanna fires in southern Africa (Table 3.7), we can obtain estimates of the emissions of trace gases and particles from woodland and grassland savanna fires in southern Africa during the dry season (May–October) of 2000 (Table 3.8).

The fuel consumption values in Table 3.7 were calculated by multiplying burned area by the amount of fuel biomass above ground and by a combustion factor (CF), defined as the fraction of the available fuel biomass above ground combusted in a fire. Burned areas by month and country in southern Africa in 2000 for two broad vegetation types, woodland savanna and grassland savanna, were obtained from the Global Burned Area 2000 Project (GBA2000) satellite burned area retrievals [*Joint Research Centre,* 2003]. The burned area estimates used in our study differ from those reported by *Silva et al.* [2003] due to updates in the SPOT burned area algorithm (see http://www.grid.unep.ch/activities/earlywarning/ preview/ ims/gba/). The amount of biomass fuel loading above ground in plots of miombo woodland and dambo grassland in Zambia were measured by *Shea et al.* [1996], *Hoffa et al.* [1999], and J. M. C. Pereira et al. (unpublished manuscript). These studies yield an average value of 0.87 ± 0.30 kg m^{-2} and 0.34 ± 0.10 kg m^{-2} for miombo woodland and dambo grassland, respectively.

Table 3.7. Biomass combusted* (Gg) by woodland and grassland savanna fires in southern Africa† during the dry season of 2000.

Country	Ecosystem	May	June	July	Aug.	Sept.	Oct.	May-Oct.
Angola	Grassland	89	1260	2015	1182	594	93	5232
Angola	Woodland	309	12904	34092	28165	18182	3460	97112
Botswana	Grassland	24	174	10	29	104	205	546
Botswana	Woodland	89	1878	171	733	3334	8052	14257
D. R. Congo§	Grassland	671	2314	2244	621	93	12	5956
D. R. Congo§	Woodland	1581	16188	25935	10098	1953	311	56066
Lesotho	Grassland	14	15	10	32	13	1	86
Lesotho	Woodland	11	36	40	177	91	6	362
Malawi	Grassland	2	2	34	15	43	16	111
Malawi	Woodland	5	13	458	279	1047	460	2263
Mozambique	Grassland	2	6	145	301	294	181	928
Mozambique	Woodland	12	125	4975	14530	18252	13743	51637
Namibia	Grassland	45	17	18	38	120	34	272
Namibia	Woodland	309	344	613	1788	7326	2547	12927
South Africa	Grassland	189	1275	709	753	1471	332	4729
South Africa	Woodland	118	2356	2164	3236	8126	2241	18242
Swaziland	Grassland	<1	<1	8	2	6	<1	17
Swaziland	Woodland	<1	2	59	26	88	3	178
Tanzania	Grassland	166	983	834	493	348	366	3189
Tanzania	Woodland	342	5989	8390	6982	6328	8139	36170
Zambia	Grassland	39	259	561	294	609	222	1985
Zambia	Woodland	134	2612	9344	6899	18372	8181	45542
Zimbabwe	Grassland	2	3	29	71	220	136	461
Zimbabwe	Woodland	4	19	306	1050	4159	3131	8668

* See section 3.5 for details of how the quantity of biomass combusted was derived in this study.
† "Southern Africa" is defined as the African continent below 4°S, excluding Madagascar.
§ Democratic Republic of Congo.

Table 3.8. Emissions (Gg) of 49 trace gas and particle species from woodland and grassland fires in Zambia and Southern Africa.

Species	Emissions from Woodland Savanna Fires in Southern Africa May-Oct., 2000	Emissions from Grassland Savanna Fires in Southern Africa May-Oct., 2000	Annual Emissions from Savanna Fires Worldwide [*Andreae and Merlet*, 2001]	Emissions from Woodland and Grassland Savanna Fires in Zambia May-Oct., 2000	Annual Emissions from Use of Biofuels in Zambia [*Bertschi et al.*, 2003a]
CO_2	585500	41400	5096000	81100	13100
CO	25100	988	206000	3410	970
CH_4	481	12	7400	65	109
NMHC	584	26	10700	80	
NO_x (as NO)	1202	56	12200	164	14
NH_3	137		3400	18	10
HCN	127	7.3	90	17	
$MeONO_2$	0.096	0.005		0.01	
SO_2	75.6	7.1	1100	10.6	
DMS	0.17	0.004		0.02	
CH_3Br	0.16	0.002	6	0.02	

(Cont.)

Table 3.8 continued)

Species	Emissions from Woodland Savanna Fires in Southern Africa May-Oct., 2000	Emissions from Grassland Savanna Fires in Southern Africa May-Oct., 2000	Annual Emissions from Savanna Fires Worldwide [*Andreae and Merlet*, 2001]	Emissions from Woodland and Grassland Savanna Fires in Zambia May-Oct., 2000	Annual Emissions from Use of Biofuels in Zambia [*Bertschi et al.*, 2003a]
CH_3Cl	9.96	0.47	240	1.36	
CH_3I	0.03	0.001	6	0.004	
Ethane	65.3	1.8		8.8	20
Ethene	148	8.9		20.3	19
Propane	16.5	0.38		2.2	
Propene	58.4	2.4		7.9	10
Acetylene	54.9	3.8		7.6	11.4
i-Butane	1.37	0.02		0.18	
n-Butane	4.46	0.11		0.60	
t-2-Butene	3.43	0.09		0.46	
1-Butene	11.67	0.45		1.59	
c-2-Butene	2.47	0.07		0.33	(Cont.)

Table 3.8 continued

Species	Emissions from Woodland Savanna Fires in Southern Africa May-Oct., 2000	Emissions from Grassland Savanna Fires in Southern Africa May-Oct., 2000	Annual Emissions from Savanna Fires Worldwide [*Andreae and Merlet*, 2001]	Emissions from Woodland and Grassland Savanna Fires in Zambia May-Oct., 2000	Annual Emissions from Use of Biofuels in Zambia [*Bertschi et al.*, 2003a]
i-Pentane	0.38	0.02		0.05	
n-PENTANE	1.41	0.04		0.19	
1,3-Butadiene	13.4	0.63		1.83	
3-Methyl-1-Butene	1.31	0.05		0.18	
t-2-Pentene	1.13	0.04		0.15	
2-methyl-2-butene	1.37	0.03		0.18	
2-methyl-1-butene	1.51	0.04		0.20	
c-2-pentene	0.65	0.02		0.09	
n-Hexane	3.47	0.17		0.47	
Isoprene	18.2	0.85		2.49	
2-Methyl-1-Pentene	0.96	0.01		0.13	
Heptane	1.92	0.09		0.26	(Cont.)

Table 3.8 continued

Species	Emissions from Woodland Savanna Fires in Southern Africa May-Oct., 2000	Emissions from Grassland Savanna Fires in Southern Africa May-Oct., 2000	Annual Emissions from Savanna Fires Worldwide [*Andreae and Merlet*, 2001]	Emissions from Woodland and Grassland Savanna Fires in Zambia May-Oct., 2000	Annual Emissions from Use of Biofuels in Zambia [*Bertschi et al.*, 2003a]
Benzene	44.6	2.1		6.1	
Toluene	51.5	2.6		7.0	
Formaldehyde	258	9.2	1100	35	26
Methanol	343	7.5	3800	46	57
Acetic acid	756	18.8	4200	102	78
Formic acid	196	10.1	2100	27	5
Total particulate matter	4464	113	26200	602	
Total particulate carbon	1202	22	11700	161	
Organic carbon	1030	16.5	10600	138	
Black carbon	161	5.6	1500	22	
Chloride	89.3	0.22		11.9	
Nitrate	65.3	1.2		8.8	

(Cont.)

Table 3.8 continued

Species	Emissions from Woodland Savanna Fires in Southern Africa May-Oct., 2000	Emissions from Grassland Savanna Fires in Southern Africa May-Oct., 2000	Annual Emissions from Savanna Fires Worldwide [*Andreae and Merlet*, 2001]	Emissions from Woodland and Grassland Savanna Fires in Zambia May-Oct., 2000	Annual Emissions from Use of Biofuels in Zambia [*Bertschi et al.*, 2003a]
Sulfate	48.1	2.1		6.6	
Potassium	131	2.8	1090	17.5	
CN*	2.0×10^{28}	4.0×10^{26}	1.1×10^{31}	2.7×10^{27}	

*Units of CN emissions are number of particles.

Since the moisture content of vegetation decreases as the dry season progresses, the CF increases from May to October in southern Africa [*Hoffa et al.,* 1999]. The fuel consumption measurements indicate that for miombo woodland fires, the CF increases fairly linearly from a value of ~0.01 at the beginning of the dry season to ~0.89 near the end of the dry season. For dambo grassland fires, the CF remains relatively high at 0.7 ± 0.2 throughout the dry season, due to the flammability of grasses.

In Figure 3.9, the fuel consumption values in Table 3.7 are summed and plotted by month for the dry season of 2000. These results suggest that the biomass combusted in woodland and grassland savanna fires in southern Africa in 2000 peaked in July and September at a value of ~90 Tg. The July peak was primarily due to burning in Angola and the Democratic Republic of Congo, whereas the September peak is largely attributable to burning in Angola, Mozambique, and Zambia (Table 3.7). *Eck et al.* [2003] report monthly means of aerosol optical depth (at a wavelength of 500 nm) from 1995 to 2000 at Mongu, Zambia. This study showed that as the dry season progresses, aerosol optical depth increases and peaks at a value of ~0.65 in September, the month of highest biomass combustion in Zambia in 2000 (18,372 Gg; Table 3.7). We note also that *Swap et al.* [2003] proposed that biomass combustion in southern Africa during the 2000 dry season was above average due to above average rainfall in the preceding wet season. Above average rainfall would enhance fuel loading, but changes in combustion factors and burned area would also have to be considered to determine interannual variability in biomass combustion. A study of interannual variability of biomass burning emissions constrained by satellite observations [*Duncan et al.,* 2003] found that emissions of CO from biomass burning in southern Africa in 2000 was not above average with respect to the 1979–2000 study period.

In columns 2-3 of Table 3.8 we give estimates of emissions from all woodland and grassland savanna fires in southern Africa from May-October of 2000, the bulk of the southern African dry season. These estimates can be compared with the average annual global emissions from savanna burning worldwide estimated by *Andreae and Merlet* [2001] (Table 3.8, column 4) to obtain rough comparisons of the contributions of

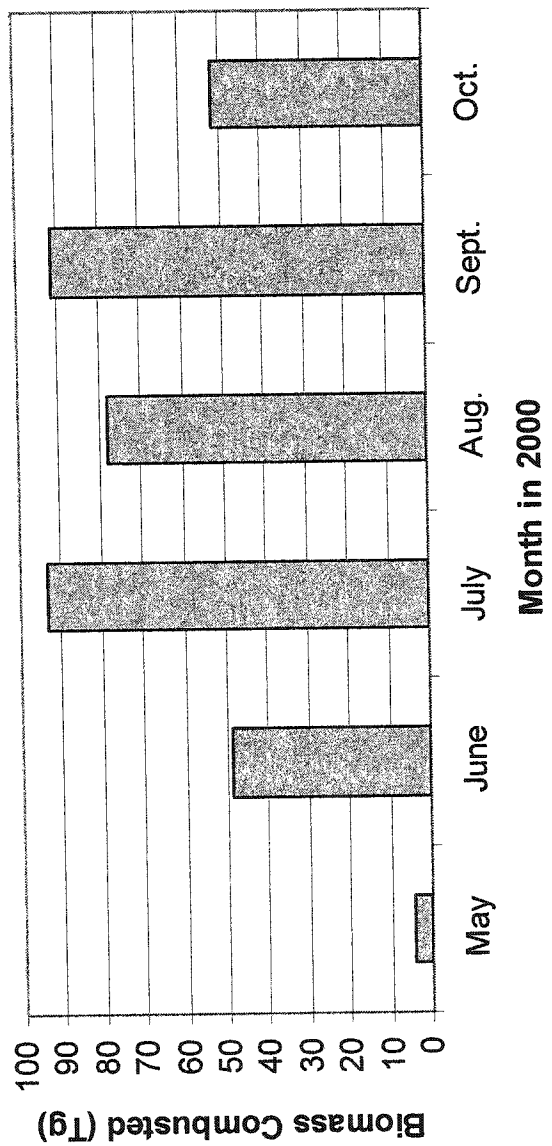

Figure 3.9. Monthly biomass combusted by woodland and grassland savanna fires in southern Africa during the 2000 dry season.

emissions from woodland and grassland savanna fires in the southern African dry season to the annual emissions from savanna burning worldwide. Andreae and Merlet estimated emissions using an estimate of annual global savanna burned of 3160 Tg by Logan and Yevich as reported in *Lobert et al.* [1999]. However, the uncertainty in this total was large enough to make a defensible error analysis impossible. In Table 3.7, we estimate that ~367 Tg of biomass were burned in woodland and grassland savanna fires in southern Africa during the dry season (May-October) of 2000. This is within the (large) range of previous estimates for this region (90–2719 Tg [*Scholes et al.*, 1996]) and would account for ~12% of the biomass that Andreae and Merlet estimated is burned annually by savanna fires worldwide. Uncertainties in these estimates are discussed at the end of this section.

Comparing species emissions from woodland and grassland savanna fires in southern Africa in the dry season of 2000 with those from global annual savanna burning [*Andreae and Merlet*, 2001], we find that the woodland and grassland savanna fires in southern Africa accounted for ~12.3%, 12.6%, 5.9%, 10.3%, 4.0%, and 7.5% of the annual emissions of CO_2, CO, hydrocarbons (CH_4+NMHC), NO_x (as NO), NH_3, and SO_2, respectively, from all types of savanna fires worldwide. For total particulate matter, black carbon, organic carbon, and potassium, the corresponding percentages are ~17.5%, 11.1%, 9.9%, and 12.2%, respectively. For oxygenated species, such as formaldehyde, acetic acid, formic acid, and methanol, the percentages are ~24.2%, 18.4%, 9.8%, and 9.2%, respectively. Percentages for the methyl halides, CH_3Br, CH_3Cl, and CH_3I are ~2.8%, 4.3%, and 0.5%, respectively.

In Table 3.8, our estimate of HCN emissions from woodland and grassland savanna fires in southern Africa (~134 Gg) exceeds Andreae and Merlet's estimate of 90 Gg from global annual savanna burning. However, Andreae and Merlet calculated global annual emissions of HCN from savanna burning using an HCN emission factor of 0.025-0.031 g per kg of fuel burned. If the global annual emissions of HCN from savanna burning are recalculated using the HCN emission factor derived from our measurements (0.31-0.37 g per kg fuel burned), the total HCN emitted by global annual

savanna fires is ~1.1 Tg. In a study of global sources and sinks of HCN, *Li et al.* [2000] estimated an annual source of 2.7–5.6 Tg from all types of biomass burning worldwide.

In column 5 of Table 3.8 we give estimates of emissions from woodland and grassland savanna fires in Zambia alone from May-October of 2000. *Bertschi et al.* [2003a] estimated annual savanna fire emissions from Zambia using emission factors from *Yokelson et al.* [2003] and model estimates of annual biomass burned from *Hao and Liu* [1994]. *Bertschi et al.* [2003a] also estimated annual emissions due to the use of biofuels in Zambia; they found that biofuel emissions are comparable to or exceed those from savanna burning for a number of species, including CH_4, CO, ethane, acetylene, acetic acid, formaldehyde, methanol, and NH_3. Annual biofuel emissions from Zambia reported by *Bertschi et al.* [2003a] are shown in column 6 of Table 3.8. When compared with our estimates of dry season emissions from woodland and grassland savanna fires in Zambia (column 5, Table 3.8), we find that the annual emissions of CH_4, ethane, ethene, acetylene, propene, formaldehyde, methanol, and acetic acid from biofuels are comparable to or exceed dry season emissions from woodland and grassland savanna fires in Zambia.

A similar comparison can be made for the southern African region. Averaging two recent estimates of annual biofuel use in southern Africa [*Yevich and Logan,* 2003; *FAO,* 1999], we estimate that each year ~108 Tg of wood fuel is combusted along with ~4 Tg of charcoal. Combining these estimates with biofuel emission factors measured by *Bertschi et al.* [2003a], we estimate annual biofuel emissions (in Gg) in southern Africa of CO_2, CO, CH_4, NO_x, ethane, ethene, acetylene, acetic acid, formic acid, formaldehyde, and methanol to be 182000, 12300, 1360, 230, 214, 275, 182, 1020, 81, 398, and 569, respectively. Columns 2 and 3 of Table 3.8 show emissions of these species from woodland and grassland savanna fires, respectively, during the dry season of 2000 in southern Africa. Nearly three times as much CH_4 is produced by annual biofuel use in southern Africa than by dry season woodland and grassland savanna fires

in southern Africa. The relative importance of biofuel emissions of the other species is smaller, although still substantial.

Our emission estimates (Table 3.8) are subject to considerable uncertainty, most of which is due to uncertainty in the total area burned by woodland and grassland savanna fires in southern Africa during the 2000 dry season. In addition to the SPOT satellite burned area retrievals used in this paper, preliminary burned area retrievals have been derived from measurements made on the MODIS satellite. In a comparison for September 2000 by *Korontzi et al.* [2004], the burned area derived from MODIS measurements for southern Africa is 55% larger than the SPOT burned area used in the present paper. The values used in the present paper for the available above-ground biomass fuel for miombo woodland and dambo grassland plots are uncertain to ~30%. The combustion factors used in the present paper are uncertain to ~30%, and the emission factors are uncertain to ~10%. Therefore, the emission estimates in Table 3.8 for woodland and grassland savanna fires in southern Africa during the 2000 dry season are uncertain to ~70%.

An additional source of uncertainty is due to emissions from residual smoldering combustion (RSC), which is biomass combustion that produces smoke that is not lofted by strong fire-induced convection. Emissions from RSC are generally not measured from aircraft, and they are not included in the emission factors reported in this paper. Residual smoldering combustion can occur in miombo woodland fires due to the presence of dead/downed logs in the fuel complex. *Bertschi et al.* [2003b] made the first measurements of emission factors from RSC in a miombo woodland. They found that the inclusion of RSC emissions in estimating total emissions from miombo fires had little effect on many compounds, but a significant effect on some. Little data exists on the amount and composition of RSC smoke. Therefore, we will not explore the topic further here except to note that some additional uncertainty due to RSC emissions may occur for some compounds, particularly methane and methanol.

CHAPTER 4
EVOLUTION OF GASES AND PARTICLES FROM A SAVANNA FIRE IN SOUTHERN AFRICA

4.1 Vegetation and Fire

On 7 September 2000 airborne measurements were made above and downwind of an active savanna fire in the Timbavati Private Game Reserve in South Africa (hereafter referred to as the Timbavati fire). The Timbavati fire was a carefully controlled and monitored fire in the lowveld of South Africa [*Landmann,* 2003]. In this region of the lowveld the vegetation varies from south Zambezian undifferentiated woodland to Tongaland-Pondoland bushland [*White,* 1981, 1983]. The fuel for the Timbavati fire was mainly grass, with litter (leaves and twigs) constituting only about 1% of the fuel. The fuel load was ~4800 kg/ha and ~1000 ha were ignited. Since ~80% of the fuel exposed to fire was combusted, ~3.8×10^6 kg of biomass was burned [*Landmann,* 2003]. The fire was ~2 km in width.

The main fire was ignited at 0801 UTC (1001 local time) and the flames reached ~2 m in height. A downwind backfire ignited at 0730 UTC had flames that reached ~0.3-0.5 m in height. Prior to 1100 UTC the fire was predominantly flaming; thereafter, smoldering combustion dominated. The fire was extinct by 1130 UTC, after smoldering samples of wood were put out near the edge of the plot.

Figure 4.1 shows an image of the fire taken at 0829 UTC from the NASA ER-2 aircraft flying at an altitude of ~20 km. The locations of the head fire, back fire, and the ignition point can be seen in Figure 4.1. Figure 4.2 shows a photograph of the fire 7 min later, which was taken from the Convair-580 as it approached the fire from upwind.

4.2 Flight Track

Measurements of the smoke from the Timbavati fire were acquired aboard the Convair-580 from 0842-1036 UTC, which was during the predominantly flaming stage

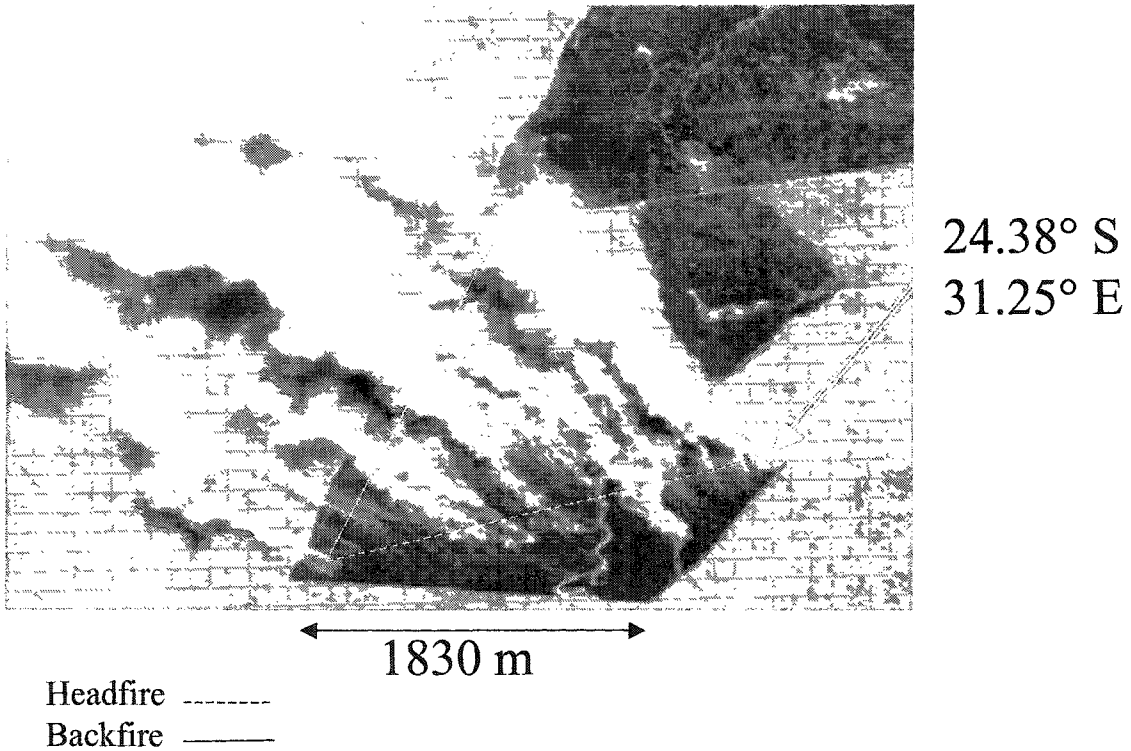

Figure 4.1. Nadir-viewing image at 0829 UTC on September 7, 2000, of the prescribed fire in the Timbavati Private Game Reserve obtained from AirMISR aboard the NASA ER-2 aircraft. The image is a composite constructed from red (672 nm), green (558 nm), and blue (446 nm) bands.

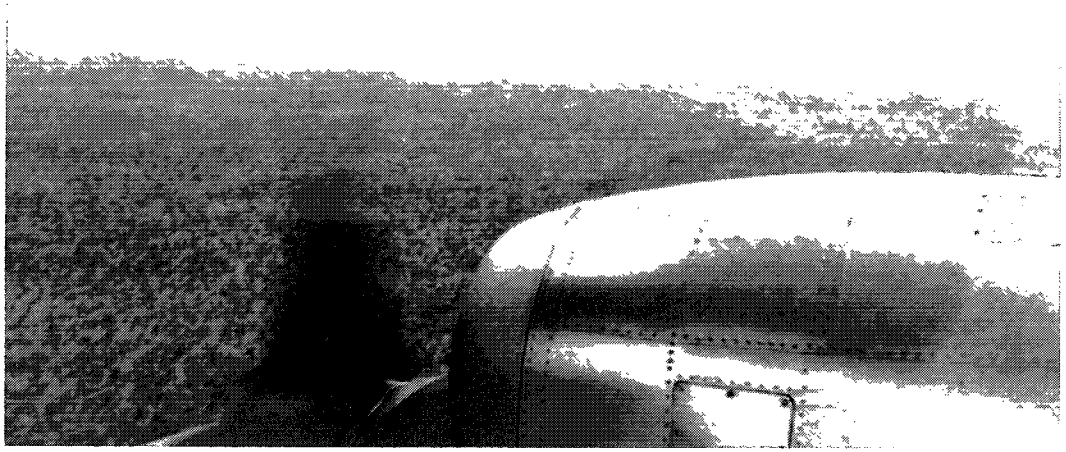

Figure 4.2. Photograph of the Timbavati fire taken at 0836 UTC on September 7, 2000, from the Convair-580 aircraft. (Photo: P. V. Hobbs)

of the fire. Figure 4.3 shows a simplified schematic of the flight track of the Convair-580 during this period. From about 0842 to 1036 UTC samples of smoke were obtained in a series of passes perpendicular to the axis of the plume at various distances and altitudes downwind of the head fire. During these passes, the pilot was instructed to fly the aircraft across the width of the plume.

Table 4.1 summarizes the times and locations of the plume samples, and some of the parameters measured. Using the average wind speed measured aboard the aircraft (11.3 ± 0.9 m s^{-1}), and the distances downwind from the head fire of the various samples, the age of the smoke in each sample was estimated (see Table 4.1). Environmental conditions for each sample (e.g., pressure, temperature, RH, UV flux, etc.) are also given in Table 4.1. Samples 1-5 in Table 4.1 were collected in stainless steel canisters and on Teflon and quartz filters. Samples a-k in Table 4.1 were analyzed by AFTIR.

The time interval between crossing the plume ~0.1 km and 30.1 km downwind of the head fire was 110 min. Therefore, the average speed of the aircraft along the length of the plume was 4.5 m s^{-1}, compared to the average wind speed of 11.3 ± 0.9 m s^{-1}. Hence, the first and last samples were not exactly Lagrangian pairs. However, as mentioned previously, the fire was predominantly flaming and moving into fresh fuel during this period of time (as indicated also by the MCE values in Table 4.1). Therefore, variations in the excess mixing ratio of a species with age of the smoke should primarily reflect effects that occurred downwind.

4.3 Vertical Profiles Upwind of the Fire and Transects Through the Smoke Plume

Figure 4.4 shows vertical profiles of temperature, relative humidity, and SO_2 concentration measured from 0829-0840 UTC just upwind of the Timbavati fire. The strong temperature inversion at ~1.3 km (Figure 4.4a) produced a peak in the SO_2 concentration at this level (Figure 4.4c).

Shown in Figures 4.5 and 4.6 are the light-scattering coefficient due to particles and CN concentrations measured in horizontal tracks across the width of the smoke plume and at various distances downwind of the fire. At 0.2 km downwind, where the

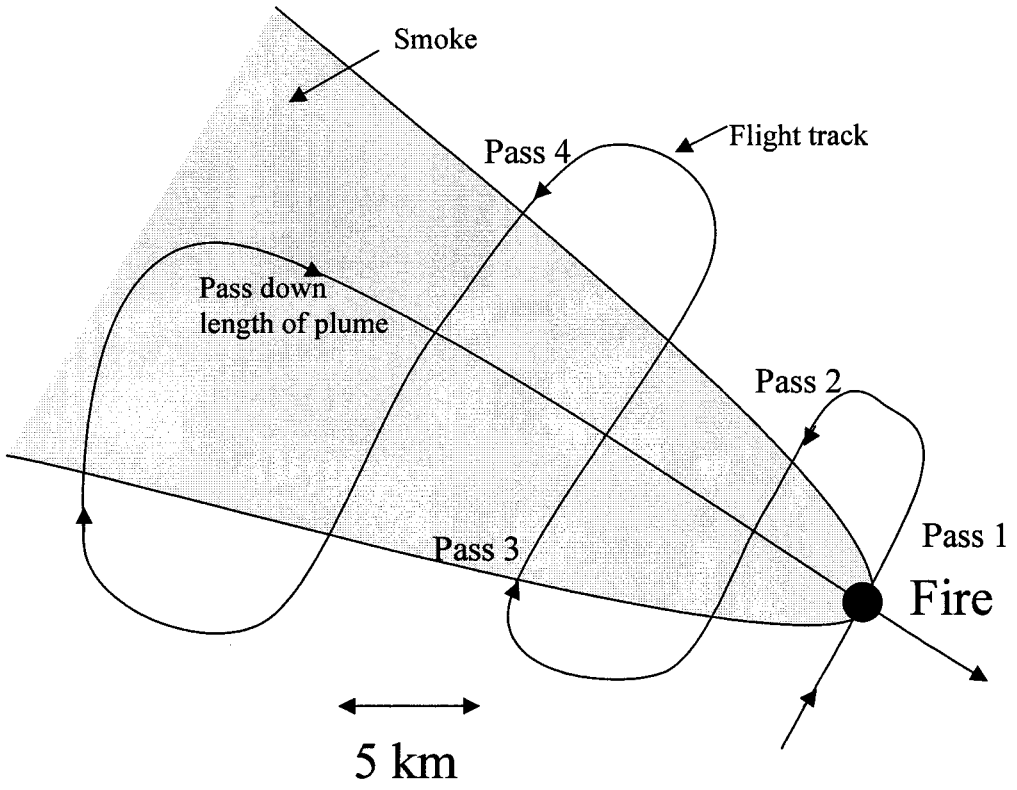

Figure 4.3. Simplified schematic of the Convair-580 flight track in the smoke plume from the Timbavati fire.

Table 4.1. Samples of smoke from the Timbavati fire obtained from the Convair-580. Samples 1-5 were collected in canisters and analyzed by gas chromatography. Samples a-k were measured by AFTIR.

Sample	Time (UTC)	Latitude (deg S)	Longitude (deg E)	Distance From Head Fire (km)	Altitude (m)	Age of Smoke (min)*	Pressure (hPa)	Temperature (°C)	Relative Humidity (%)	Modified Combustion Efficiency (MCE)	Down-welling Ultraviolet (300-390 nm) Flux ($W\ m^{-2}$)	Upwelling Ultraviolet (300-390 nm) Flux ($W\ m^{-2}$)
1	0843	24.37	31.22	1.0	598	1	941	19	35	0.94	37	2.1
2	0857	24.36	31.25	0.2	564	0	942	19	34	0.93	14	2.3
3	0923	24.33	31.25	4.9	896	7 ± 1	909	16	40	0.92	25	3.5
4	0939	24.18	31.12	20.8	1440	31 ± 3	848	14	78	0.91	42	8.3
5	1014	24.16	31.17	26.2	545	39 ± 4	952	21	34	0.93	29	2.3
a	0843	24.37	31.26	1.7	616	3	939	21	38	0.93	26	2.2
b	0846	24.37	31.24	0.1	739	0	920	20	36	0.94	40	3.0

(Cont.)

Table 4.1. continued

Sample	Time (UTC)	Latitude (deg S)	Longitude (deg E)	Distance From Head Fire (km)	Altitude (m)	Age of Smoke (min)	Pressure (hPa)	Temperature (°C)	Relative Humidity (%)	Modified Combustion Efficiency (MCE)	Down-welling Ultraviolet (300-390 nm) Flux ($W\ m^{-2}$)	Upwelling Ultraviolet (300-390 nm) Flux ($W\ m^{-2}$)
c	0855	24.29	31.27	9.5	710	14 ± 1	942	20	34	0.91	33	2.5
d	0921	24.36	31.23	1.9	862	3	903	17	41	0.88	28	2.8
e	0933	24.24	31.28	15.7	1710	23 ± 2	843	16	22	0.93	45	4.7
f	0934	24.21	31.21	17.7	1430	26 ± 3	849	14	32	0.93	44	8.4
g	0940	24.19	31.21	19.9	1440	29 ± 3	846	15	78	0.91	42	8.3
h	0946	24.36	31.25	2.0	564	3	940	21	35	0.91	29	1.5
i	1015	24.18	31.09	26.6	545	39 ± 4	943	22	34	0.92	29	2.3
j	1021	24.17	31.09	27.3	500	40 ± 4	956	23	32	0.91	24	1.6
k	1036	24.15	31.08	30.1	538	44 ± 4	945	23	28	0.94	32	2.4

* Derived from an average measured wind speed of 11.3 ± 0.9 $m\ s^{-1}$.

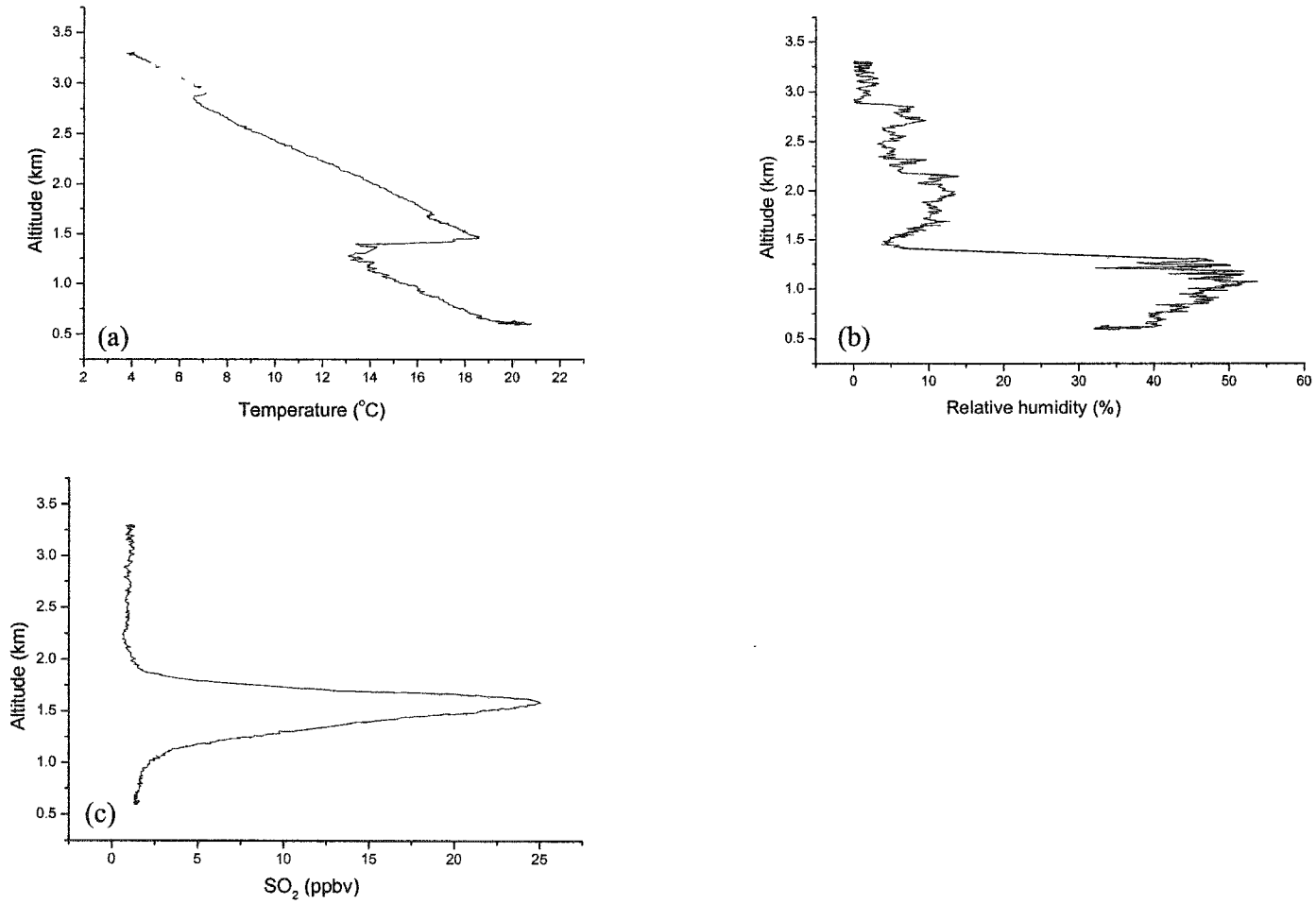

Figure 4.4. Vertical profiles of temperature, relative humidity, and SO_2 concentration measured upwind of the Timbavati fire from 0829-0840 UTC.

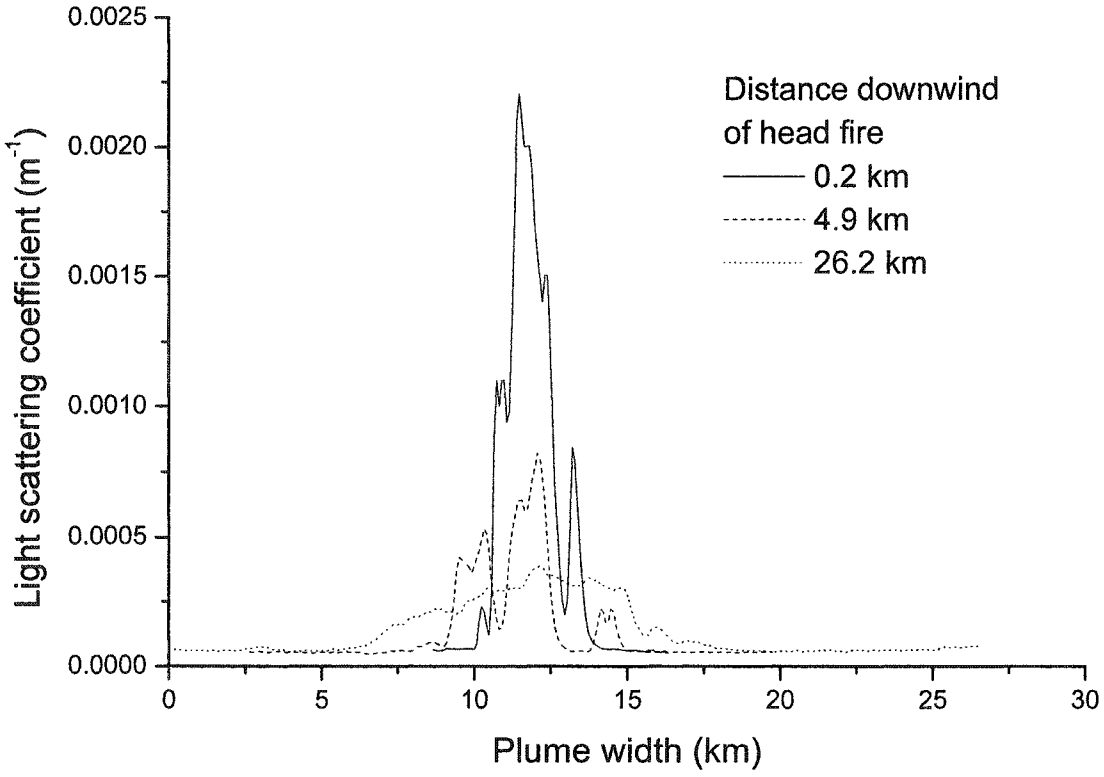

Figure 4.5. Particle light-scattering coefficient across the width of the Timbavati smoke plume at various distances downwind of the fire.

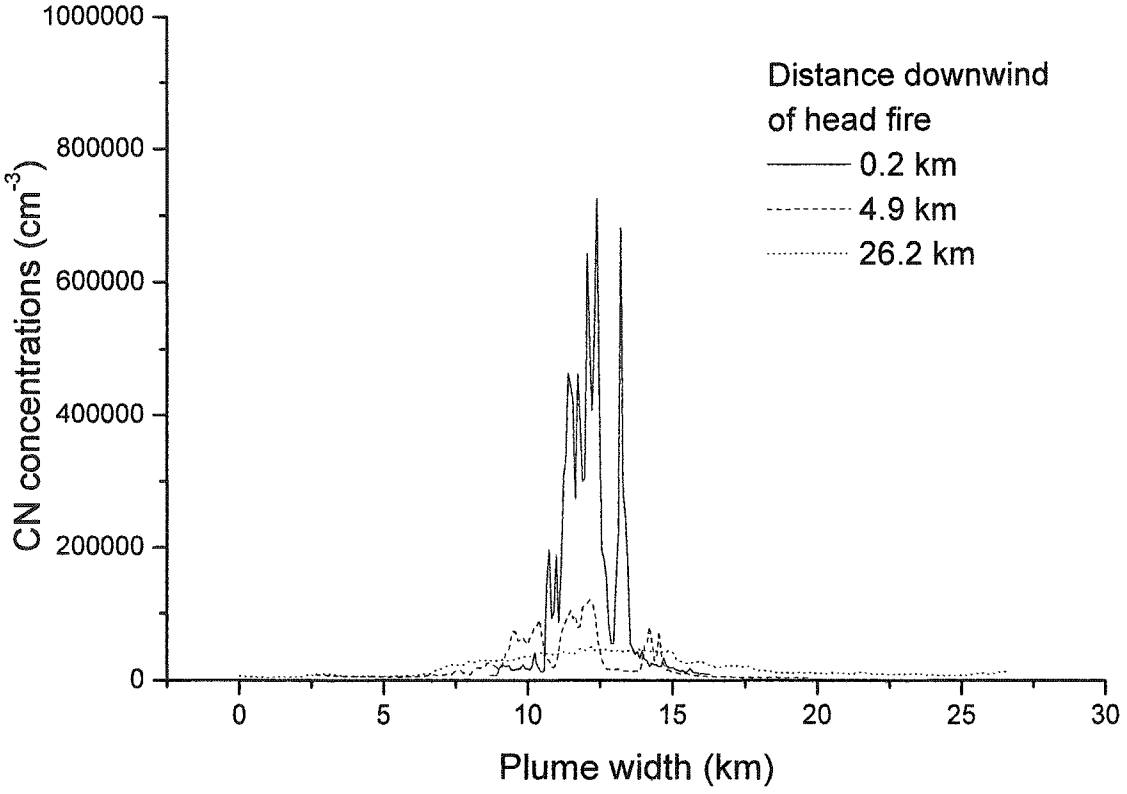

Figure 4.6. Condensation nucleus (CN) concentrations across the width of the Timbavati smoke plume at various distances downwind of the fire.

width of the plume was ~3-4 km, the peak values of the light-scattering coefficient and CN were ~0.0022 m^{-1} and ~7×10^5 cm^{-3}, respectively. The corresponding values at 26.2 km downwind, where the width of the plume was ~10-15 km, were ~0.0004 m^{-1} and ~0.5×10^5 cm^{-3}.

4.4 Attenuation of Solar Radiation by Smoke

Since photochemical reactions in the smoke will depend on the intensity of UV radiation, we show in Figure 4.7 the downwelling UV irradiance in the wavelength band 300-390 nm, measured by the SSFR aboard the Convair-580, in the Timbavati plume from 0842-1036 UTC. Generally, the aircraft was flown at about the vertical center of the plume, but for a brief period of time it was near the top of the plume. Near the center of the plume, the UV flux was about two-thirds of that near the top of the plume.

Figure 4.8(a) shows SSFR-measured upwelling and downwelling irradiance spectra at 0939 UTC (solid curve) and at 1021 UTC (dashed curve), near plume top and approximately 1000 m below plume top, respectively. Both sets of measurements were obtained 20-25 km downwind of the fire. Figure 4.8(b) shows the fractional absorption (obtained by normalizing the absorbed solar radiation in the layer by the solar radiation incident at the top of the layer) in the 1000 m thick smoke layer. The smooth continuum-type absorption is due to the smoke particles; water vapor absorption is evident in the band centered at 940 nm as well as several other smaller bands in the near-infrared. Absolute layer absorption by the smoke was ~91 W m^{-2}, producing an instantaneous heating rate of ~7.4 K day^{-1}.

The spectral behavior of the scattering and absorption by the smoke is similar to that reported by *Pilewskie et al.* [2003] and *Bergstrom et al.* [2003] and is consistent with absorption by elemental carbon [see *Bergstrom et al.,* 2002]. The aerosol single-scattering albedo decreased with increasing wavelength from the near-ultraviolet to near-infrared, but total layer absorption was greatest in the ultraviolet because of the increase in aerosol optical thickness with decreasing wavelength.

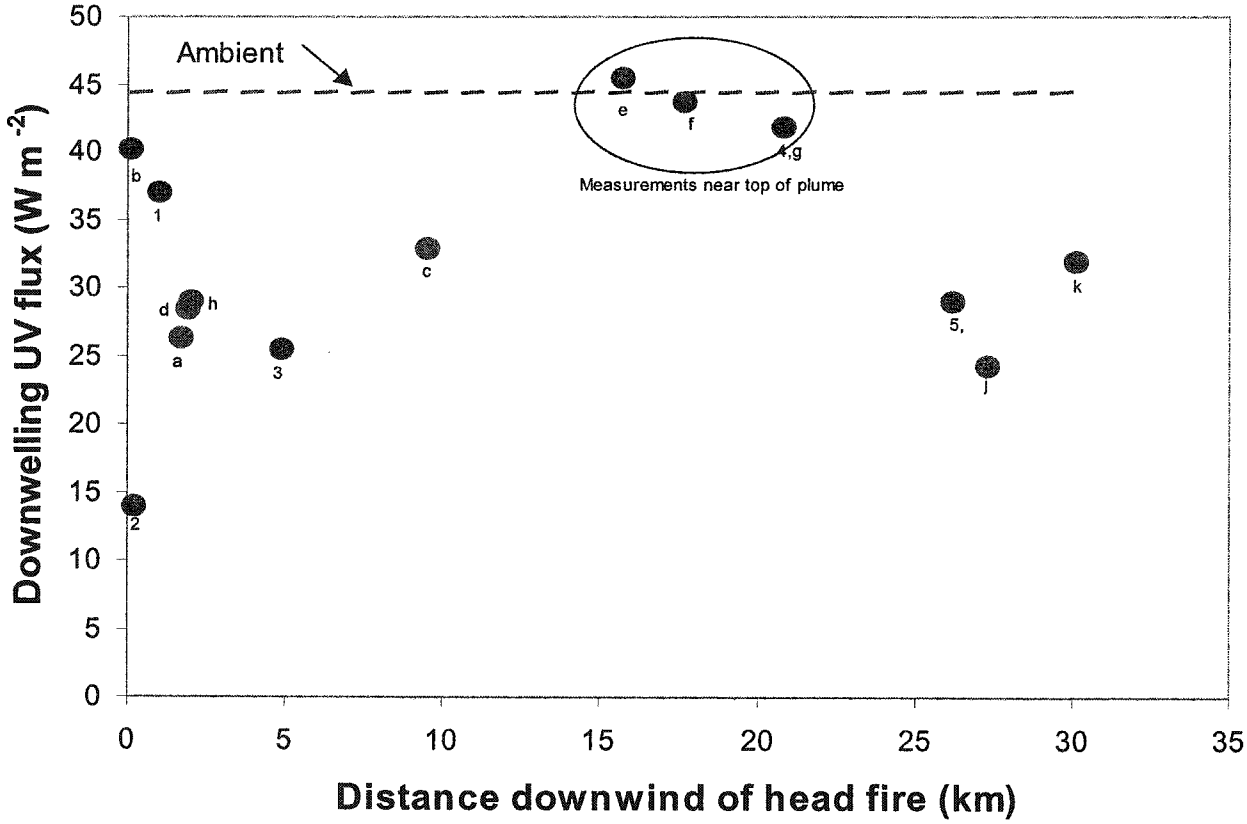

Figure 4.7. Downwelling UV irradiance from 300-390 nm measured along the length of the Timbavati smoke plume. The numbers and letters alongside each data point correspond to those given in the first column of Table 4.1.

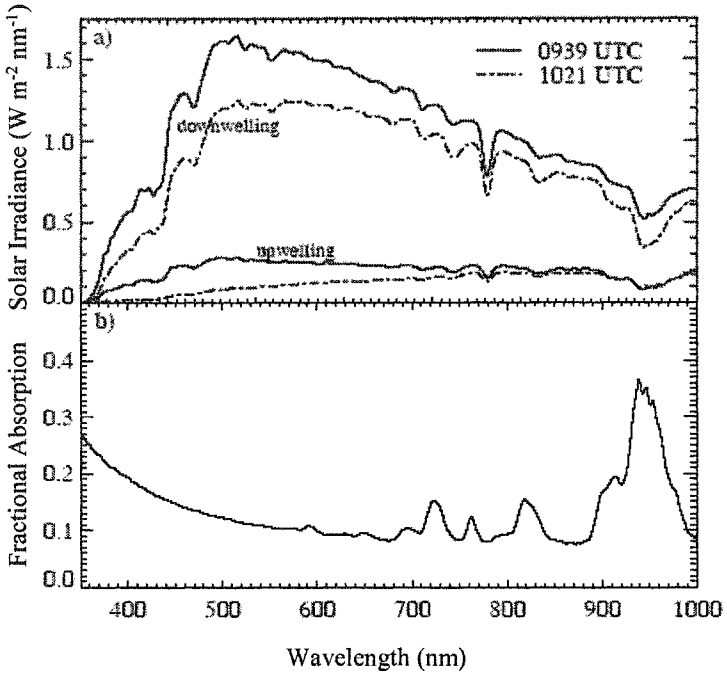

Figure 4.8. (a) Upwelling and downwelling spectral irradiance 20-25 km downwind of the Timbavati fire. The solid curve was obtained at 0939 UTC near plume top, and the dashed curve at 1021 UTC at ~1000 m below plume top. (b) Fractional absorption between plume top and ~1000 m below plume top.

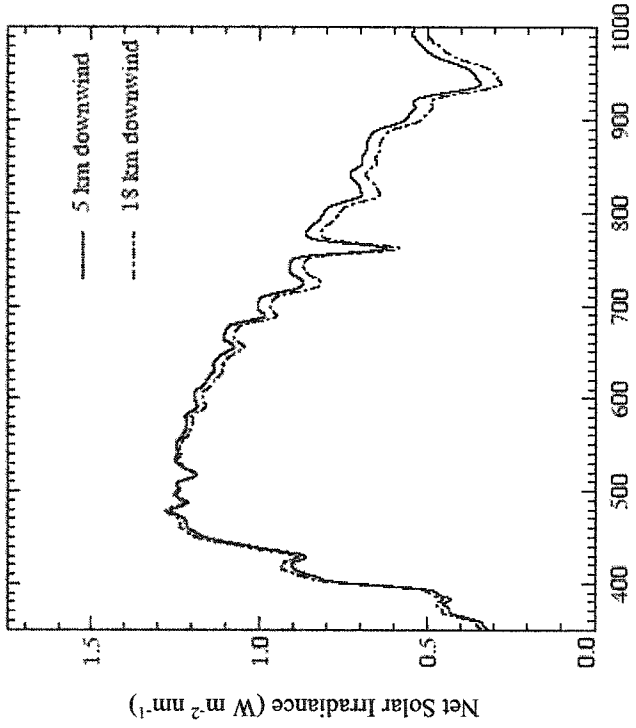

Figure 4.9. Net spectral irradiance in the smoke at 5 km and 18 km downwind of the Timbavati fire. Both measurement sets were made between ~750 and 1000 m below plume top.

We examined the spectral distribution of scattered solar irradiance with plume evolution by comparing spectral irradiance at various distances from the head fire. Figure 4.9 shows the average net solar irradiance (defined as the difference between downwelling and upwelling irradiance) at 5 km and 18 km downwind of the Timbavati fire, at approximately 750 to 1000 m below plume top. In the near-ultraviolet and visible part of the spectrum, where the greatest amount of absorption occurred, the net spectral irradiance is nearly identical at the two distances downwind. The only significant differences occurred in the far visible and near-infrared, which we attribute to changes in surface albedo. Thus, the radiation available to drive photochemical reactions had nearly the same spectral distribution, and was of similar magnitude, 5 km and 18 km downwind of the Timbavati fire.

4.5 Effects of Dilution on Mixing Ratios

Table 4.2 shows mixing ratios of the gases, particulate matter and ions that were measured in the Timbavati plume by gas chromatography (GC/C) and filters (F/GB) and which were considered to derive from biomass burning by the significant correlation of their excess mixing ratios with the excess mixing ratio of CO or CO_2 ($r^2 \geq 0.5$). Table 4.3 lists the excess mixing ratios of gases measured in the smoke plume by AFTIR.

It can be seen from Tables 4.2 and 4.3 that the mixing ratios of many chemical species in the plume changed with distance from the fire. This could be due to chemical reactions, which may produce or consume a species with time. However, even for a species that is not affected by chemical reactions, the mixing ratio in the plume will generally decrease with increasing distance from a fire due to mixing of the smoke with the ambient air. The dilution of a species due to mixing with the ambient air can be removed in large part, at least for the first few hours of travel, by dividing the excess molar mixing ratio of the species by the excess molar mixing ratio of CO.

Isoprene has a daytime lifetime in the ambient tropical atmosphere of only ~60 min due to its reaction with OH [*Mauzerall et al.,* 1998]. Consequently, decreases in the excess mixing ratios of isoprene in young smoke should reflect both its reaction with

Table 4.2. Mixing ratios of gases and mass concentrations of particles and ionic species in samples 1-5 listed in Table 4.1 and in the ambient air. The samples are listed in order of increasing distance from the fire. The measurements were obtained by gas chromatography. bdl indicates that the species was below the detection limit; dashes indicate no data.

Species	Technique Used for Measurement*	Sample					Ambient Air
		2	1	3	4	5	
Gases [in ppbv]							
Carbon dioxide (CO_2)	GC/C	425,000	427,000	391,000	397,000	388,000	377,000
Carbon monoxide (CO)	GC/C	3,900	3,500	1,500	2,300	1,100	220
Sulfur dioxide (SO_2)	Teco 43S†	25	66	15	9.4	8.9	1.7
Methane (CH_4)	GC/C	1,900	1,870	1,790	1,820	1,780	1,740
Dimethyl sulfide (CH_3SCH_3)	GC/C	0.044	0.028	0.012	0.014	0.0051	bdl
Methyl bromide (CH_3Br)	GC/C	0.034	0.030	0.019	0.023	0.014	0.0096
Methyl chloride (CH_3Cl)	GC/C	3.4	3.0	1.7	2.1	1.2	0.68
Methyl iodide (CH_3I)	GC/C	0.0063	0.0054	0.0026	0.0035	0.0019	0.00064
Methyl nitrate (CH_3ONO_2)	GC/C	0.018	0.018	0.013	0.0225	0.0089	0.0057

Table 4.2 continued

Species	Technique Used for Measurement*	Sample					Ambient Air
		2	1	3	4	5	
Gases [in ppbv] (continued)							
Ethane (C_2H_6)	GC/C	13	9.8	4.3	7.2	3.3	0.86
Ethene (C_2H_4)	GC/C	35	32	12	16	6.0	0.32
Propane (C_3H_8)	GC/C	2.3	1.6	0.72	1.2	0.55	0.11
Propene (C_3H_6)	GC/C	8.8	7.4	2.6	2.3	0.83	0.031
Acetylene (C_2H_2)	GC/C	12	12	4.8	7.3	3.1	0.49
i-butane (C_4H_{10})	GC/C	0.18	0.14	0.054	0.084	0.044	0.009
n-butane (C_4H_{10})	GC/C	0.47	0.36	0.15	0.24	0.11	0.023
t-2-butene (C_4H_8)	GC/C	0.42	0.31	0.079	0.097	0.005	bdl
1-butene (C_4H_8)	GC/C	1.3	1.0	0.35	0.27	0.097	0.023
c-2-butene (C_4H_8)	GC/C	0.31	0.23	0.063	0.055	0.0060	bdl
i-pentane (C_5H_{12})	GC/C	0.053	0.037	0.019	0.030	0.012	0.006
n-pentane (C_5H_{12})	GC/C	0.11	0.082	0.037	0.061	0.026	0.009

Table 4.2 continued

Species	Technique Used for Measurement*	Sample					Ambient Air
		2	1	3	4	5	
Gases [in ppbv] (continued)							
1,3-butadiene (C_4H_6)	GC/C	1.4	1.2	0.38	0.086	0.033	bdl
3-methyl-1-butene (C_5H_{10})	GC/C	0.13	0.11	0.036	0.030	0.010	bdl
t-2-pentene (C_5H_{10})	GC/C	0.11	0.084	0.023	bdl	bdl	bdl
2-methyl-2-butene (C_5H_{10})	GC/C	0.12	0.089	0.019	bdl	bdl	bdl
2-methyl-1-butene (C_5H_{10})	GC/C	0.13	0.11	0.031	0.013	0.005	bdl
c-2-pentene (C_5H_{10})	GC/C	0.067	0.052	0.014	bdl	bdl	bdl
n-hexane (C_6H_{14})	GC/C	0.22	0.19	0.067	0.067	0.027	0.007
Isoprene (C_5H_8)	GC/C	0.79	0.64	0.15	0.018	0.015	0.018
2-methyl-1-pentene (C_6H_{12})	GC/C	0.078	0.056	0.016	bdl	bdl	bdl
Heptane (C_7H_{16})	GC/C	0.12	0.074	0.026	0.022	0.01	0.014
Benzene (C_6H_6)	GC/C	3.7	3.1	1.2	1.8	0.73	0.096
Toluene (C_7H_8)	GC/C	3.1	2.2	0.89	1.4	0.47	0.082

Table 4.2 continued

Species	Technique Used for Measurement*	Sample					Ambient Air
		2	1	3	4	5	
Particulates [in $\mu g\ m^{-3}$]							
Total particulate matter (TPM)	F/GB	—	1180	282	—	179	30.1
Organic carbon (OC)	F/GB	—	206	57	—	34	3.6
Black carbon (BC)	F/GB	—	35.0	7.7	—	6.7	0.5
Chloride (Cl^-)	F/GB	—	193	28	—	5.4	bdl
Nitrate (NO_3^-)	F/GB	—	13.6	7.2	—	9.1	0.78
Sulfate (SO_4^{2-})	F/GB	—	25.0	9.2	—	8.1	1.2
Potassium (K^+)	F/GB	—	70.9	9.5	—	3.8	0.74

*GC/C=gas chromatography via canisters; F/GB=filters via grab bag.
†Via grab bag.

Table 4.3. Excess mixing ratios (Δppbv) of some of the chemical species in samples (a) through (k) in Table 4.1. The samples are listed in order of increasing distance from the fire. Measurements were obtained from the AFTIR. bdl indicates that the species was below the detection limit. For a discussion of mixing ratios in background air see *Yokelson et al.* [2003].

Species	Sample										
	b	a	d	h	c	e	f	g	i	j	k
Carbon dioxide (CO_2)	68600	79200	6900	15600	19100	13900	21300	10100	6100	6300	7100
Carbon monoxide (CO)	4024	5738	911	1592	1776	1042	1625	954	549	644	426
Methane (CH_4)	214	345	80	67	109	55	117	60	33	28	21
Ethene (C_2H_4)	58	91	12	20	21	bdl	bdl	bdl	bdl	bdl	bdl
Acetylene (C_2H_2)	14	19	bdl	bdl	6	bdl	bdl	bdl	bdl	bdl	bdl
Formaldehyde (HCHO)	74	109	20	25	16	31	37	31	10	10	20
Methanol (CH_3OH)	55	86	20	19	28	10	bdl	7	bdl	9	5
Acetic Acid (CH_3COOH)	58	75	23	53	14	30	71	36	27	35	32
Formic Acid (HCOOH)	33	33	bdl	6	17	11	bdl	5	bdl	bdl	bdl
Ammonia (NH_3)	13	5	bdl	3	bdl	bdl	bdl	bdl	bdl	bdl	bdl
Nitric oxide (NO)	52	57	bdl	bdl	bdl	bdl	bdl	bdl	bdl	bdl	bdl

(Cont.)

Table 4.3 continued

Species	Sample										
	b	a	d	h	c	e	f	g	i	j	k
Nitrogen dioxide (NO_2)	123	137	bdl	51	51	bdl	bdl	bdl	6	bdl	bdl
Hydrogen cyanide (HCN)	29	37	9	bdl	18	8	18	11	bdl	bdl	bdl
Ozone (O_3)	-52	-52	-12	bdl	22	60	98	86	31	54	19

OH and dilution due to mixing with ambient air. Figure 4.10 shows Δisoprene and Δisoprene/ΔCO as a function of the age of the smoke in the Timbavati plume. Both quantities decline to ambient levels at approximately the same rate, which indicates that chemical reactions were dominant in decreasing the concentration of isoprene in the plume.

Figure 4.11 shows a plot similar to Figure 4.10 but for ethene, which has a significantly longer lifetime than isoprene. In this case, Δethene/ΔCO decreases onlyslightly with age (over ~40 min), but Δethene falls off more rapidly (due to mixing with the ambient air).

4.6 Photochemistry

A value of ΔX/ΔCO measured before any significant post-emission transformations is the emission ratio of compound X for the fire. Changes in ΔX/ΔCO as smoke ages reveal the rate of photochemical and heterogeneous processes in the plume. Tables 4.4 and 4.5 show ΔX/ΔCO values for many species of various ages in the smoke from the Timbavati fire. While ΔX/ΔCO decreases with the age of the smoke for various hydrocarbons, due to reactions with OH (or more slowly with O_3), it should increase for photochemical products. For example, Figure 4.12 shows ΔX/ΔCO for acetic acid (CH_3COOH), O_3, and nitrate increasing as the smoke ages. After 40 min of aging, $\Delta CH_3COOH/\Delta CO$ is about three times its initial value (Figure 4.12(a)). By contrast, it took >2 h for this ratio to double in Alaskan smoke plumes [*Goode et al.*, 2000].

In minutes-old smoke from the Timbavati fire the O_3 mixing ratio was below ambient due to titration by NO and particles, but $\Delta O_3/\Delta CO$ rose to as much as 9% within 30 min (Figure 4.12(b)). In comparison, $\Delta O_3/\Delta CO$ rose to only ~1.5% in 30 min in a smoke plume in the Pacific Northwest of the United States [*Hobbs et al.*, 1996], and required ~2 h to reach 9% in an Alaskan smoke plume [*Goode et al.*, 2000]. These initial bursts of O_3 production may account for a significant portion of the total O_3 production in smoke plumes, since *Yokelson et al.* [2003] report $\Delta O_3/\Delta CO$ of 22% in

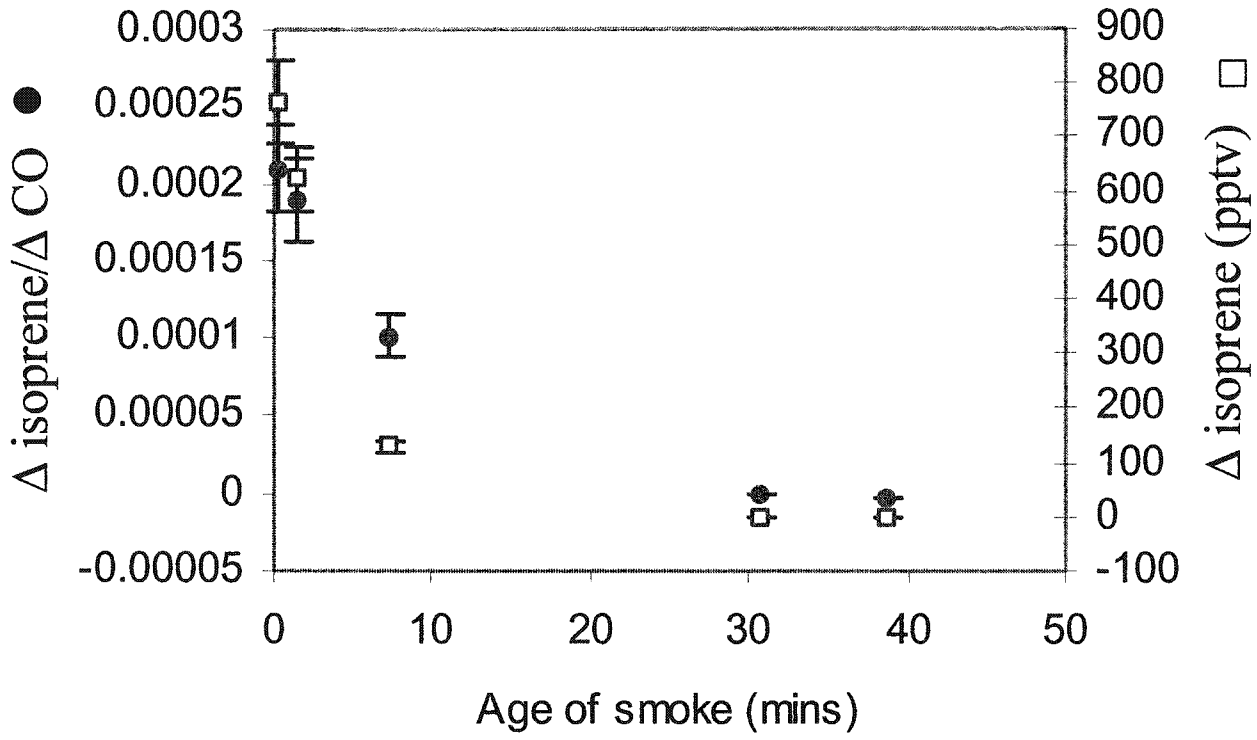

Figure 4.10. Excess volume mixing ratio of isoprene (squares), and the excess volume mixing ratio of isoprene normalized with respect to CO (circles), versus age of the smoke in the Timbavati plume.

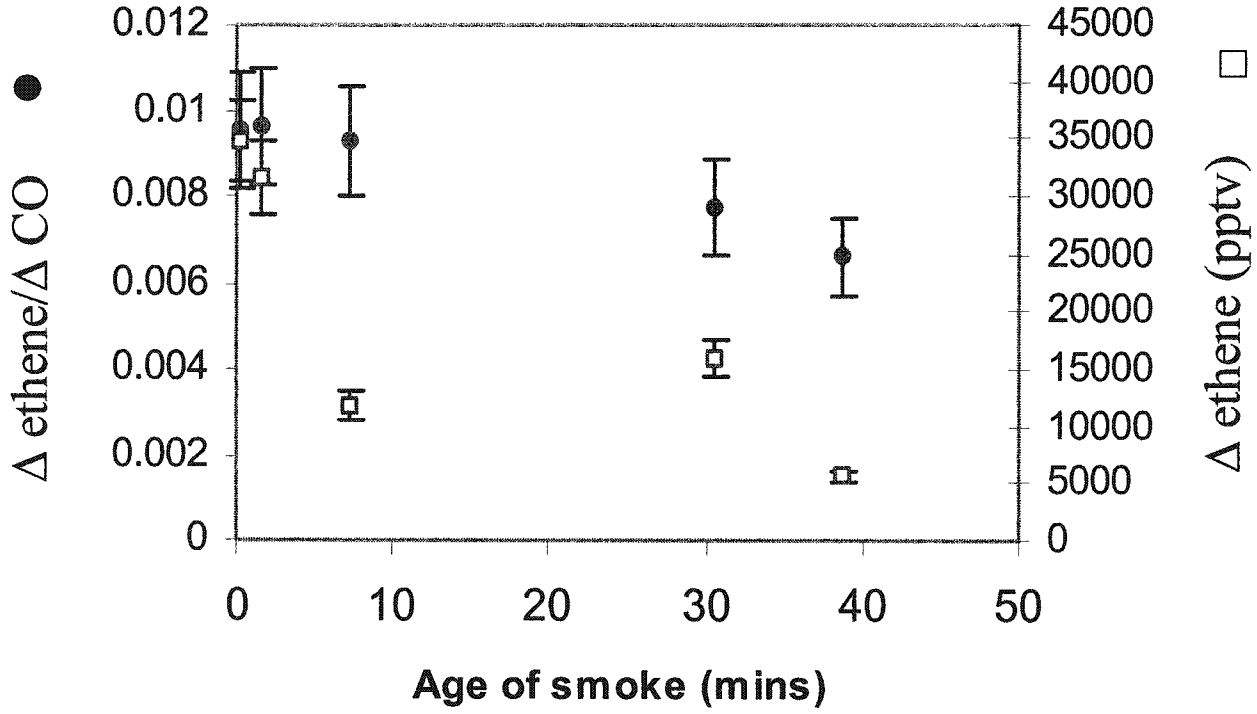

Figure 4.11. As for Figure 4.10 but for ethene.

Table 4.4. Excess mixing ratios of species divided by the excess mixing ratio of CO for Samples 1 Through 5 in Table 1. The samples are listed in order of increasing distance from the fire. See Tables 4.2 and 4.3 for techniques for measurements. bdl indicates that the species was below the detection limit; dashes indicate no data.

Species	Sample					Uncertainty of Each Sample
	2	1	3	4	5	(%)
Gases [in ppbv/ppmv of CO]						
Sulfur dioxide (SO_2)	6.8	20	12	4.6	10	12
Methane (CH_4)	44	38	39	38	40	10
Dimethyl sulfide (C_2H_6S)	1.2×10^{-2}	8.6×10^{-3}	9.2×10^{-3}	6.8×10^{-3}	6.0×10^{-3}	14
Methyl bromide (CH_3Br)	6.6×10^{-2}	6.1×10^{-3}	7.4×10^{-3}	6.5×10^{-3}	5.4×10^{-3}	14
Methyl chloride (CH_3Cl)	0.75	0.71	0.78	0.70	0.59	14
Methyl iodide (CH_3I)	1.2×10^{-2}	8.6×10^{-3}	9.2×10^{-3}	6.8×10^{-3}	6.0×10^{-3}	14
Methyl nitrate (CH_3ONO_2)	6.6×10^{-3}	6.1×10^{-3}	7.4×10^{-3}	6.5×10^{-3}	5.4×10^{-3}	14
Ethane (C_2H_6)	3.3	2.7	2.7	3.1	2.9	14
Ethene (C_2H_4)	9.5	9.6	9.3	7.7	6.6	14
Propane (C_3H_8)	0.59	0.46	0.48	0.55	0.52	14
Propene (C_3H_6)	2.4	2.3	2.0	1.1	0.94	14
Acetylene (C_2H_2)	3.2	3.5	3.4	3.3	3.1	14
i-butane (C_4H_{10})	4.5×10^{-2}	3.9×10^{-2}	3.5×10^{-2}	3.7×10^{-2}	4.1×10^{-2}	14
n-butane (C_4H_{10})	0.12	0.10	0.10	0.11	0.10	14
t-2-butene (C_4H_8)	1.2×10^{-1}	9.3×10^{-2}	6.2×10^{-2}	4.7×10^{-2}	5.9×10^{-3}	14
1-butene (C_4H_8)	0.34	0.31	0.26	0.12	8.65×10^{-2}	14

(Cont.)

Table 4.4 continued

Species	Sample					Uncertainty of Each Sample
	2	1	3	4	5	(%)
c-2-butene (C_4H_8)	8.5×10^{-2}	6.9×10^{-2}	5.0×10^{-2}	2.7×10^{-2}	7.0×10^{-3}	14
i-pentane (C_5H_{12})	1.3×10^{-2}	9.4×10^{-3}	1.0×10^{-2}	1.2×10^{-2}	7.0×10^{-3}	14
n-pentane (C_5H_{12})	2.9×10^{-2}	2.2×10^{-2}	2.2×10^{-2}	2.5×10^{-2}	2.0×10^{-2}	14
1,3-butadiene (C_4H_6)	3.9×10^{-1}	3.6×10^{-1}	3.0×10^{-1}	4.2×10^{-2}	3.9×10^{-2}	14
3-methyl-1-butene (C_5H_{10})	3.5×10^{-2}	3.2×10^{-2}	2.8×10^{-2}	1.5×10^{-2}	1.2×10^{-2}	14
t-2-pentene (C_5H_{10})	2.9×10^{-2}	2.6×10^{-2}	1.8×10^{-2}	bdl	bdl	14
2-methyl-2-butene (C_5H_{10})	3.4×10^{-2}	2.7×10^{-2}	1.5×10^{-2}	bdl	bdl	14
2-methyl-1-butene (C_5H_{10})	3.6×10^{-2}	3.4×10^{-2}	2.4×10^{-2}	6.4×10^{-3}	5.9×10^{-3}	14
c-2-pentene (C_5H_{10})	1.8×10^{-2}	1.6×10^{-2}	1.1×10^{-2}	bdl	bdl	14
n-hexane (C_6H_{14})	5.9×10^{-2}	5.4×10^{-2}	4.7×10^{-2}	2.9×10^{-2}	2.3×10^{-2}	14
Isoprene (C_5H_8)	0.21	0.19	0.10	0	-3.5×10^{-3}	14
2-methyl-1-pentene (C_6H_{12})	2.1×10^{-2}	1.7×10^{-2}	1.3×10^{-2}	bdl	bdl	14
Heptane (C_7H_{16})	2.9×10^{-2}	1.8×10^{-2}	9.4×10^{-3}	3.9×10^{-3}	-4.7×10^{-3}	14
Benzene (C_6H_6)	0.99	0.92	0.89	0.86	0.74	14
Toluene (C_7H_8)	0.84	0.64	0.63	0.62	0.45	14
Particulates [in $\mu g\ m^{-3}$/ppmv of CO]						
Total particulate matter (TPM)	—	350	198	—	174	10
Organic carbon (OC)	—	62	42	—	36	10
Black carbon (BC)	—	10.5	5.6	—	7.2	10

(Cont.)

Table 4.4 continued

Species	Sample					Uncertainty of Each Sample
	2	1	3	4	5	(%)
Chloride (Cl^-)	—	59	22	—	6.3	10
Nitrate (NO_3^-)	—	3.9	5.0	—	9.7	11
Sulfate (SO_4^{2-})	—	7.2	6.3	—	8.1	11
Potassium (K^+)	—	21	6.9	—	3.6	11

Table 4.5. Excess mixing ratio divided by the excess mixing ratio of CO for chemical species for samples (a) through (k) in Table 4.1. The samples are listed in order of increasing distance from the fire. Units are ppbv/ppmv. The excess mixing ratios were measured by AFTIR and are given in Table 4.3. bdl indicates below detection limit. For estimates of the uncertainties in the ratios see *Yokelson et al.* [2003].

Species	Sample										
	b	a	d	h	c	e	f	g	i	j	k
Methane (CH_4)	53	60	88	42	61	52	72	63	60	43	49
Ethene (C_2H_4)	14	16	13	13	12	bdl	bdl	bdl	bdl	bdl	bdl
Acetylene (C_2H_2)	3	3	bdl	bdl	3	bdl	bdl	bdl	bdl	bdl	bdl
Formaldehyde (HCHO)	18	19	22	16	9	30	23	32	18	16	47
Methanol (CH_3OH)	14	15	22	12	16	9	bdl	8	bdl	13	13
Acetic Acid (CH_3COOH)	14	13	25	34	8	29	43	38	49	55	76
Formic Acid (HCOOH)	8	6	bdl	4	10	10	bdl	5	bdl	bdl	bdl
Ammonia (NH_3)	3	1	bdl	2	bdl	bdl	bdl	bdl	bdl	bdl	bdl
Nitric oxide (NO)	13	10	bdl	bdl	bdl	bdl	bdl	bdl	bdl	bdl	bdl
Nitrogen dioxide (NO_2)	31	24	bdl	32	29	bdl	bdl	bdl	11	bdl	bdl
Hydrogen cyanide (HCN)	7	6	10	bdl	10	8	11	12	bdl	bdl	bdl
Ozone (O_3)	-13	-9	13	bdl	12	57	60	90	57	84	46

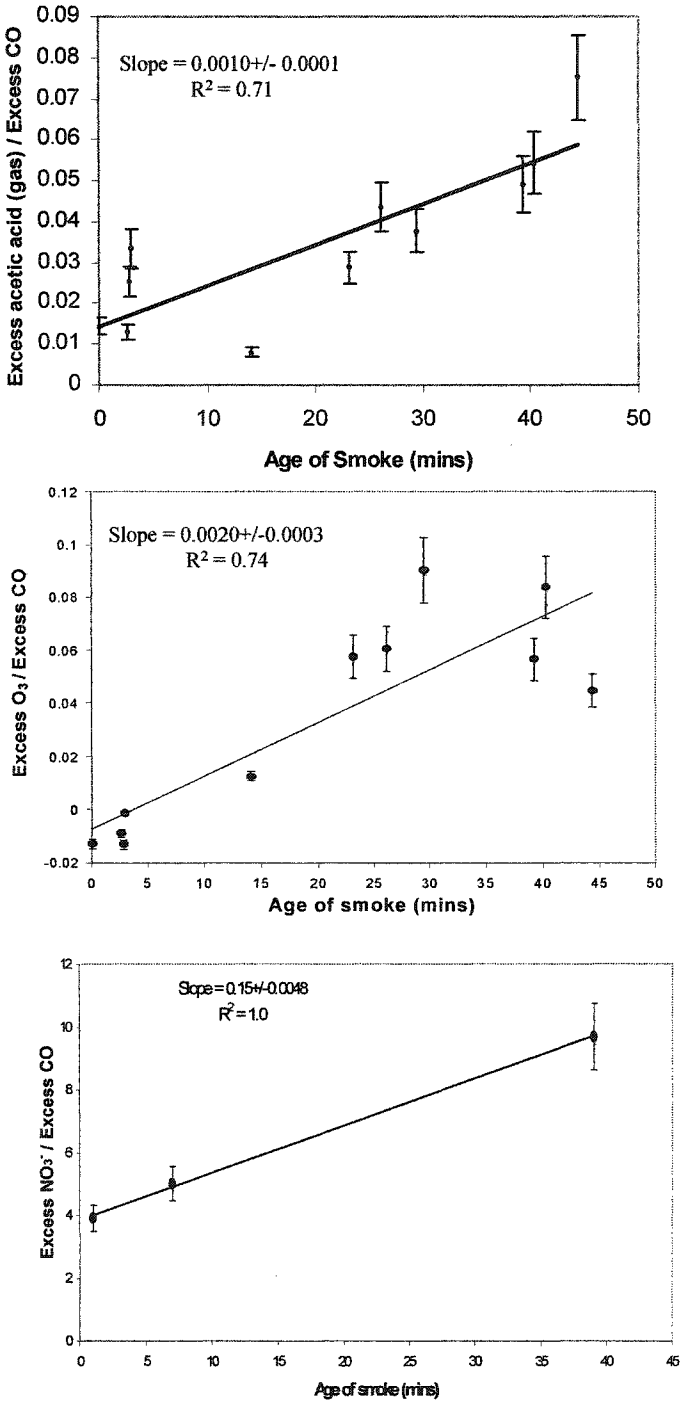

Figure 4.12. Excess mixing ratios normalized with respect to CO as a function of age of smoke in the Timbavati plume of (a) acetic acid and (b) ozone. The ratio of particulate nitrate (in $\mu g\ m^{-3}$) normalized by the excess volume mixing ratio of CO (in ppmv) is shown in (c).

biomass burning haze several days old off the coast of Namibia, and *Andreae et al.* [1994] measured a range of $\Delta O_3/\Delta CO$ values from 20-88% in biomass burning haze estimated to be about 10 days old over the South Atlantic Ocean. Hence, for some species $\Delta X/\Delta CO$ can increase significantly after emission, but the rate of change depends on the species and on local conditions. As expected, faster photochemistry is observed in subtropical Africa than at higher latitudes. Photochemistry should also be faster near the top of a plume where ultraviolet light is more intense. The $\Delta O_3/\Delta CO$ values we measured high in the Timbavati plume (i.e., samples e, f and g in Figure 4.7) lie above the slope in Figure 4.12(b) that gives the average formation rate.

Listed in Table 4.6, and shown in Figures 4.12-4.15, are those gases for which $\Delta X/\Delta CO$ either increased or decreased significantly with aging when modeled as a linear process. ("Significant" refers to a statistical confidence level of at least 95%.) Most of the hydrocarbons in Table 4.6 are alkenes, which react quickly with OH and more slowly with O_3. The oxidation of these hydrocarbons (and other organics, including those entrained in the plume) can lead to the formation of acetic acid, which increased significantly in the aged smoke (Table 4.6 and Figure 4.12 (a)). The fates of several other species listed in Table 4.6 are similarly linked. For example, photolysis of NO_2 yields O_3. Table 4.6 shows that $\Delta O_3/\Delta CO$ increased and $\Delta NO_2/\Delta CO$ decreased to roughly one-third of its initial value in ~40 min. However, this measurement should not be viewed as quantitative, since all of the downwind NO_2 mixing ratios were near or below the detection limit of the AFTIR. Nitrogen dioxide can react with OH to yield gas phase HNO_3, which can then be converted to particulate nitrate; $\Delta NO_3^-/\Delta CO$ increased by a factor of 2.5 in 39 min in the Timbavati plume.

4.7 Estimates of OH Concentrations in the Smoke.

The rate-limiting step for loss of many chemical species in the atmosphere is reaction with the OH radical. We can use this fact to estimate the average concentration of OH in the relatively young smoke from the Timbavati fire.

If the rate of decrease in the CO-normalized excess mixing ratio of species X in a smoke plume is dominated by its reaction with OH, we can write:

Table 4.6. Slope, standard error of slope, and correlation coefficient (r^2) from regression of excess mixing ratio of species divided by excess mixing ratio of CO versus age of smoke. See Tables 2 and 3 for measurement techniques. "Significant" refers to a statistical confidence level ≥95%.

(a) Species for which ΔX/ΔCO increased significantly as smoke aged over ~40-45 min

Species	Slope ± Standard Error of Slope	r^2
Nitrate (NO_3^-)	0.15 ± 0.0048 μg m^{-3} $ppmv^{-1}$ min^{-1}	1.0
Ozone (O_3)	2.0 ± 0.3 ppbv $ppmv^{-1}$ min^{-1}	0.74
Acetic acid (CH_3CO_2H)	1.0 ± 0.1 ppbv $ppmv^{-1}$ min^{-1}	0.71

(b) Species for which ΔX/ΔCO decreased significantly as smoke aged over ~40-45 min

Species	Slope ± Standard Error of Slope (ppbv $ppmv^{-1}$ min^{-1})	r^2
Nitrogen dioxide (NO_2)	$(-4.7 \pm 1.4)\times10^{-1}$	0.79
Ethene (C_2H_4)	$(-7.2 \pm 0.7)\times10^{-2}$	0.97
Propene (C_3H_6)	$(-3.7 \pm 0.2)\times10^{-2}$	0.99
t-2-pentene (C_5H_{10})	$(-7.5 \pm 0.9)\times10^{-4}$	0.96
2-methyl-2-butene (C_5H_{10})	$(-8.0 \pm 1.7)\times10^{-4}$	0.88
c-2-pentene (C_5H_{10})	$(-4.6 \pm 0.6)\times10^{-4}$	0.95
2-methyl-1-pentene (C_6H_{12})	$(-5.2 \pm 0.7)\times10^{-4}$	0.95
1,3-butadiene (C_4H_6)	$(-9.4 \pm 0.9)\times10^{-3}$	0.97
1-butene (C_4H_8)	$(-6.2 \pm 0.5)\times10^{-3}$	0.98
Isoprene (C_5H_8)	$(-5.3 \pm 1.0)\times10^{-3}$	0.91

(Cont.)

Table 4.6 continued

(b) Species for which ΔX/ΔCO decreased significantly as smoke aged over ~40-45 min (continued)

Species	Slope ± Standard Error of Slope (ppbv $ppmv^{-1}$ min^{-1})	r^2
Benzene (C_6H_6)	$(-4.5 \pm 1.3)\times10^{-3}$	0.80
t-2-butene (C_4H_8)	$(-2.2 \pm 0.6)\times10^{-3}$	0.84
c-2-butene (C_4H_8)	$(-1.7 \pm 0.3)\times10^{-3}$	0.92
n-hexane (C_6H_{14})	$(-8.6 \pm 0.7)\times10^{-4}$	0.98
2-methyl-1-butene (C_5H_{10})	$(-7.8 \pm 1.0)\times10^{-4}$	0.95
Heptane (C_7H_{16})	$(-6.4 \pm 1.8)\times10^{-4}$	0.81
3-methyl-1-butene (C_5H_{10})	$(-5.6 \pm 0.4)\times10^{-4}$	0.99

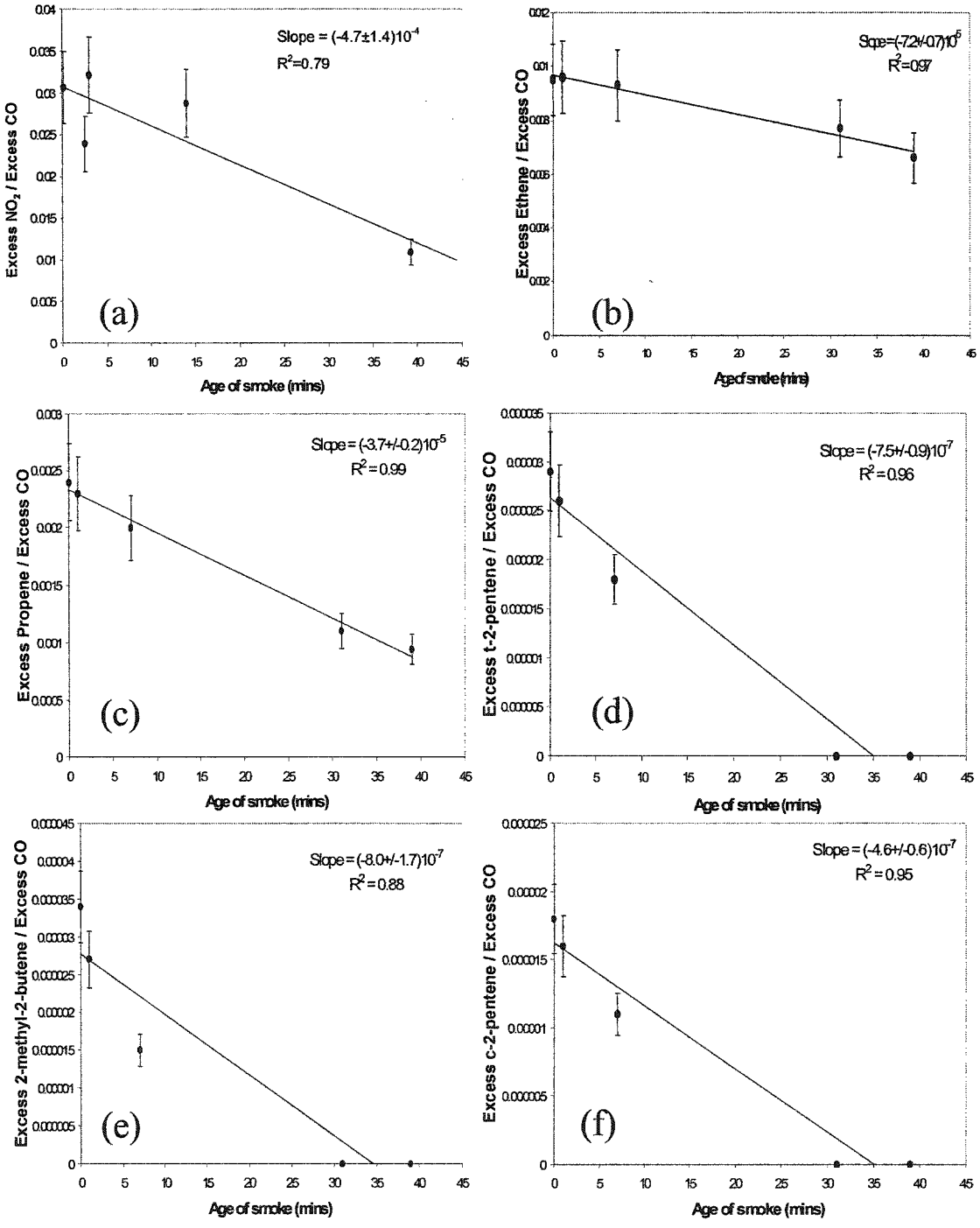

Figure 4.13. As for Figure 4.12 but for (a) nitrogen dioxide (NO_2), (b) ethene (C_2H_4), (c) propene (C_3H_6), (d) *t*-2-pentene (C_5H_{10}), (e) 2-methyl-2-butene (C_5H_{10}), and (f) *c*-2-pentene (C_5H_{10}).

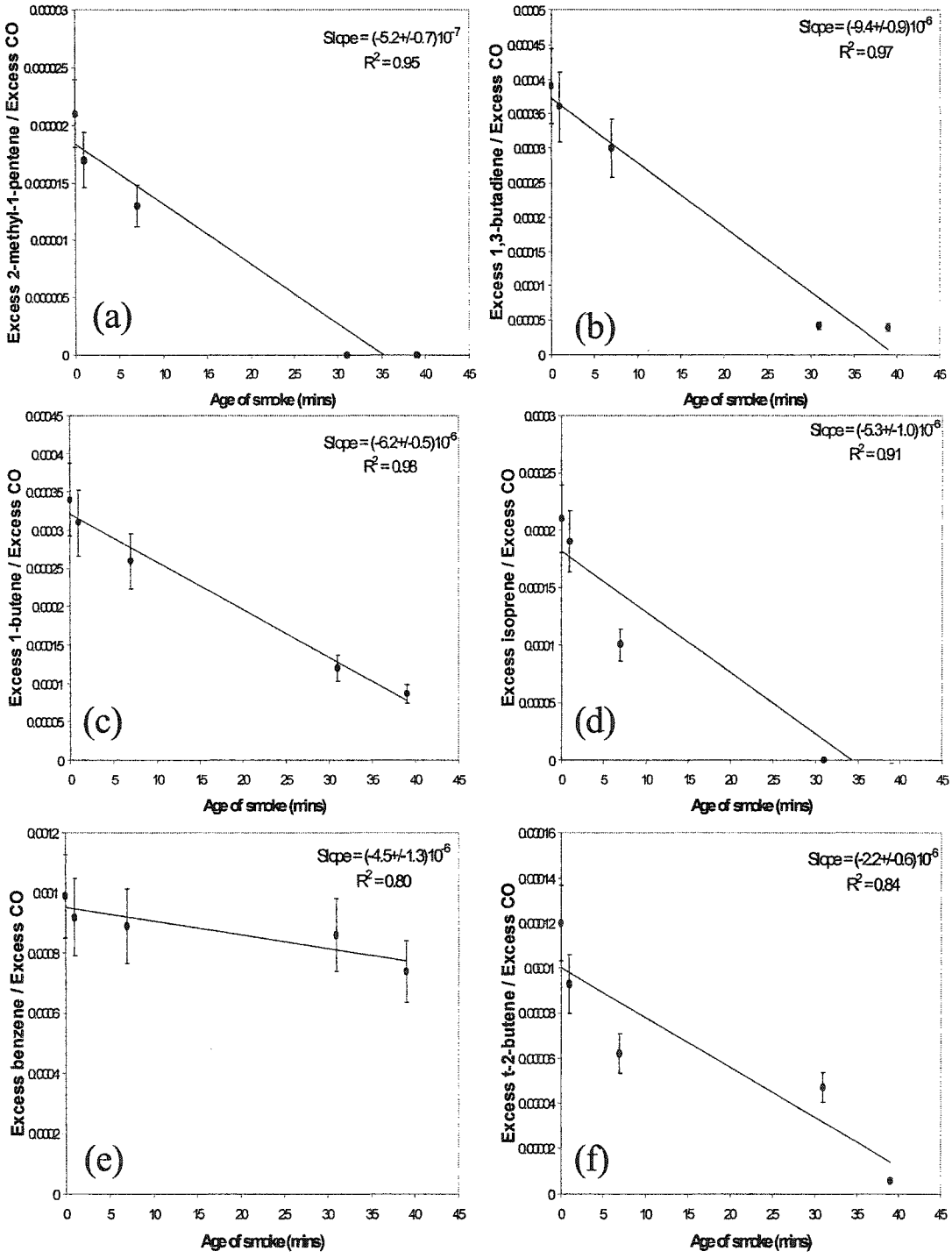

Figure 4.14. As for Figure 4.12 but for (a) 2-methyl-1-pentene (C_6H_{12}), (b) 1,3-butadiene (C_4H_6), (c) 1-butene (C_4H_8), (d) isoprene (C_5H_8), (e) benzene (C_6H_6), and (f) *t*-2-butene (C_4H_8).

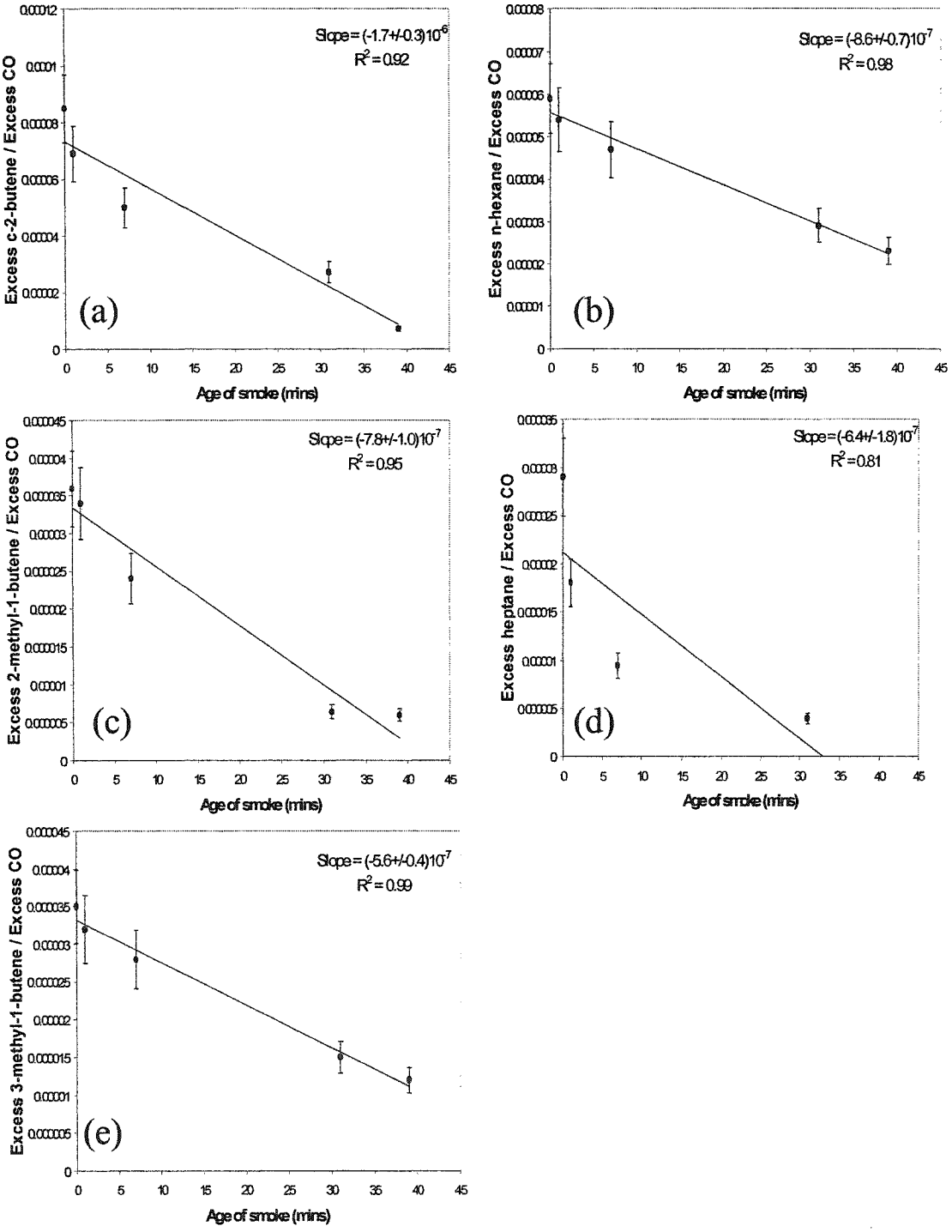

Figure 4.15. As for Figure 4.12 but for (a) *c*-2-butene (C_4H_8), (b) *n*-hexane (C_6H_{14}), (c) 2-methyl-1-butene (C_5H_{10}), (d) heptane (C_7H_{16}), and (e) 3-methyl-1-butene (C_5H_{10}).

$$\left(\frac{\Delta X}{\Delta CO}\right)_t = \left(\frac{\Delta X}{\Delta CO}\right)_0 \exp\{-k_x[OH]t\} \qquad (4.1)$$

where $(\Delta X/\Delta CO)_0$ and $((\Delta X/\Delta CO)_t$ are the CO-normalized excess mixing ratios of X immediately over the fire (t = 0) and after the smoke has aged for time t, respectively, and k_x is the rate coefficient for X reacting with OH. If equation (4.1) is applied to two species X_1 and X_2, the following is obtained:

$$\ln\left(\frac{\Delta X_1}{\Delta X_2}\right)_t = -[OH]\cdot(k_1 - k_2)\cdot t + \ln\left(\frac{\Delta X_1}{\Delta X_2}\right)_0 \qquad (4.2)$$

where, k_1 and k_2 are the rate coefficients for X_1 and X_2, respectively, reacting with OH. Hence, a plot of $\ln(\Delta X_1/\Delta X_2)_t$ versus $(k_1 - k_2)t$ will have slope – [OH], where [OH] is the average concentration of OH in the smoke as it ages over the time interval t.

Results for the average OH concentrations derived in this way using the five best combinations of species (propene, ethene, 1-butene, ethane and CO) that have various reaction rates with OH but negligible competing loss rates due to O_3, are shown in Table 4.7; example plots are shown in Figure 4.16. The average derived concentration of OH, using room temperature rate constants, during the first ~40 min in the Timbavati plume is $(1.7 \pm 0.2)\times10^7$ molecules cm^{-3}.

Noontime, cloud-free, surface OH concentrations at the latitude and in the season of this study were modeled to be only $(3\text{-}4)\times10^6$ molecules cm^{-3} [*Logan et al.*, 1981], or ~4-6 times lower than our estimated value for the OH concentrations in the Timbavati plume. Other models and measurements (including those of polluted urban air) yield maximum OH concentrations ranging from $\sim(2\text{-}10)\times10^6$ molecules cm^{-3} [*Finlayson-Pitts and Pitts,* 2000]. The photochemical model of a smoke plume developed by *Mason et al.* [2001] predicts OH levels a little greater than 1×10^7 molecules cm^{-3} during the first hour of plume evolution when initialized with oxygenated organic compounds and $\Delta NO_x/\Delta CO$ of 0.02 (S. Mason, personal communication). An important implication of the high average OH concentration that we have derived from the Timbavati plume is that the lifetime of reactive species in

Table 4.7. Estimates of average OH concentrations in the Timbavati plume during the first ~40 Minutes of smoke aging. Rate coefficients for the reactions were taken from *Finlayson-Pitts and Pitts* [2000]

Pair	[OH] From Slope of Plot (molecules cm^{-3})	Correlation Coefficient (r^2)	Percentage Loss of Alkene by O_3	[OH] Corrected for Loss by O_3 (molecules cm^{-3})
Propene/ethene	1.5×10^7	0.98	-	1.5×10^7
1-butene/ethene	1.8×10^7	0.99	-	1.8×10^7
Ethene/ethane	1.8×10^7	0.74	3.2	1.8×10^7
Ethene/CO	1.9×10^7	0.97	3.2	1.9×10^7
Propene/ethane	1.6×10^7	0.96	6.6	1.5×10^7
Propene/CO	1.6×10^7	1.00	6.6	1.5×10^7
1-butene/ethane	1.8×10^7	0.99	4.9	1.7×10^7
1-butene/CO	1.9×10^7	0.99	4.9	1.8×10^7
Average	$(1.7\pm0.2)\times10^7$	—	—	$(1.7\pm0.2)10^7$

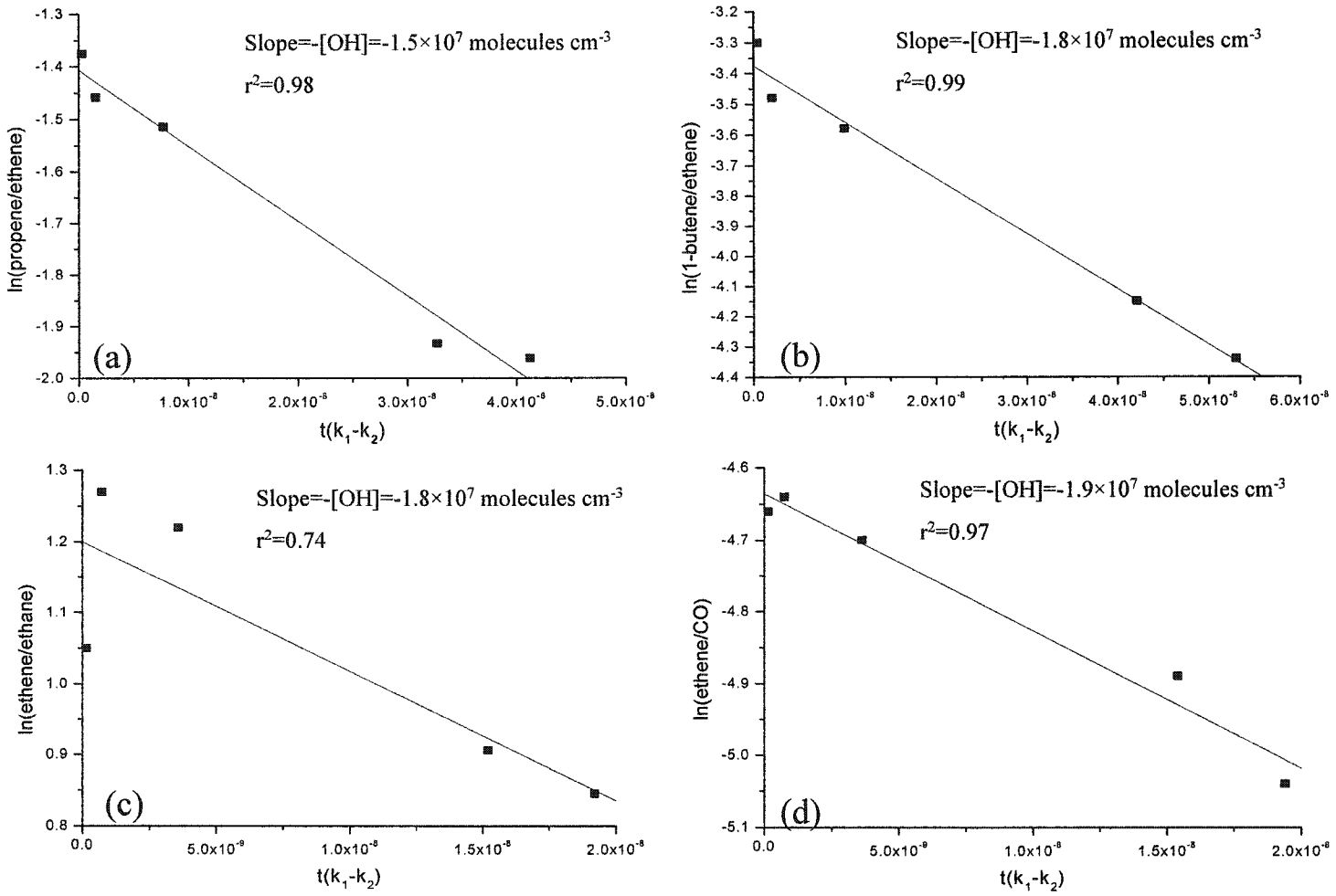

Figure 4.16. Plots of equation (4.2) based on measurements in the Timbavati plume. The slope provides an estimate of the average OH concentration in the plume during the first ~40 min of smoke aging.

biomass-burning plumes is much shorter than suggested by 24-h average lifetimes calculated for ambient conditions.

The short lifetimes of many fire emissions are evident in the data for the Timbavati fire (Table 4.4). For example, Δ1-butene/ΔCO decreased to 35% of its initial value in 31 min; much faster than implied by the average tropical lifetime of 2.2 h calculated by *Mauzerall et al.* [1998] using a 24-hour average OH concentration of 2.7×10^6 molecules cm^{-3}. The Δisoprene/ΔCO ratio fell by a factor of 2 in only 7 min, and Δethene/ΔCO fell by 30% in 39 min. These changes are also much faster than implied by the lifetimes calculated by *Mauzerall et al.* [1998] of 1 and 12 h, respectively.

We conclude that the photochemical environment in young biomass burning plumes differs considerably from ambient or average conditions and requires specialized study, particularly as these young plumes are a major global source of trace gases and particles.

4.8 Transformations of Particles.

The concentrations of CN and accumulation-mode particles (0.1-3 μm diameter) changed as the smoke from the Timbavati fire aged.

Figure 4.17(a) shows the excess CN concentrations measured as the Convair-580 flew along the length of the plume between 0950 and 0955 UTC. The concentrations were high (~500,000 cm^{-3}) in the immediate vicinity of the fire but fell off sharply (to 50,000 cm^{-3}) within about 5.5 km and remained near this value to about 23 km downwind. However, even at 23 km downwind the excess CN concentrations were well over an order of magnitude greater than in the ambient air. To compensate for the effects of plume dilution on the excess CN concentrations we show in Figure 4.17(b) ΔCN/ΔCO along the length of the plume. The normalized excess CN concentrations decrease for about 10 min, but thereafter show an overall increase with aging. We attribute the initial decrease to coagulation of the highly concentrated particles. If we assume monodispersed particles with a diameter of 0.01 μm, the estimated e-folding time for decreasing CN concentrations by particle coagulation is ~9

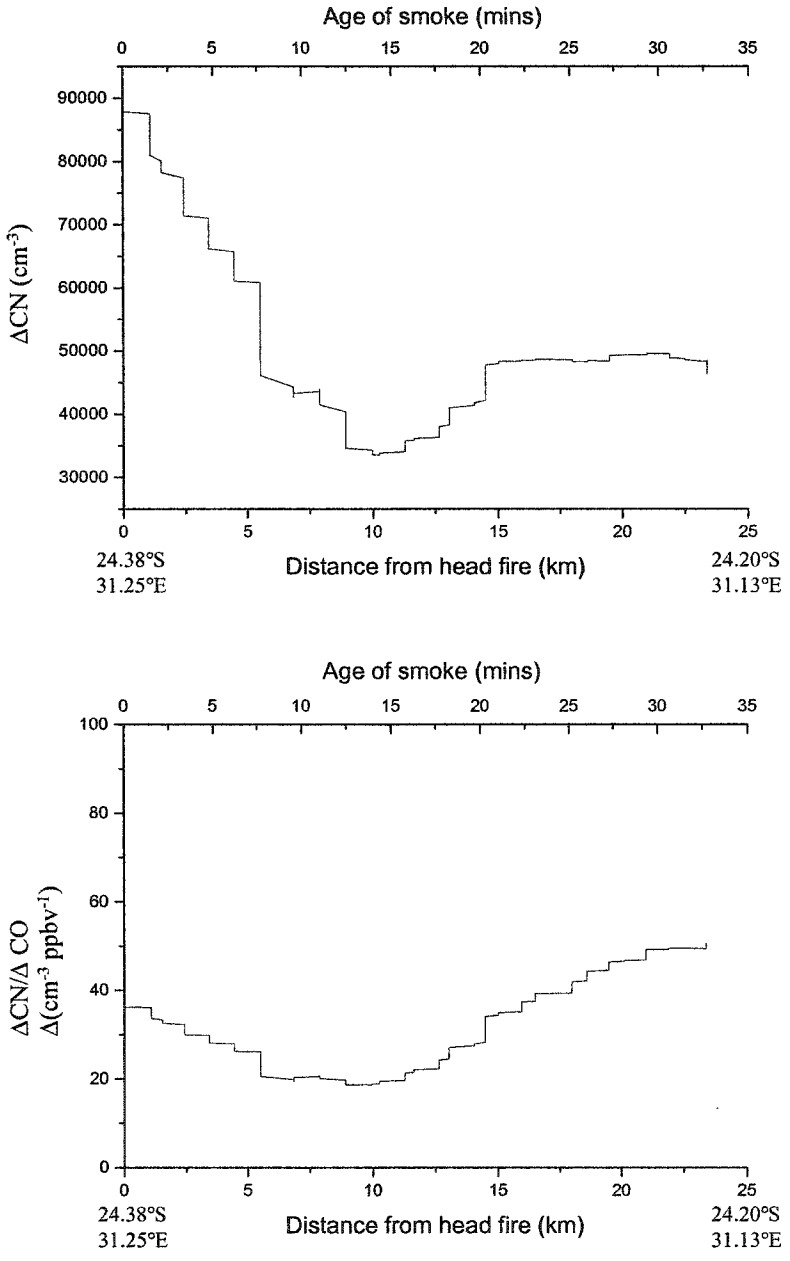

Figure 4.17. (a) Running mean concentration of condensation nuclei (CN) along the length of the Timbavati smoke plume. (b) Excess concentration of CN normalized by excess concentration of CO along the length of the Timbavati smoke plume. The ambient concentration of CN was ~1000 cm^{-3}. The excess concentrations of CO were obtained by interpolating canister measurements.

min up to about 3 km from the fire, but at ~20 km from the fire it is ~170 min. Changing the diameter of the assumed monodispersed particles to 0.003 and 0.1 μm changes the e-folding time up to 3 km from the fire to 2.5 and 70 min, respectively. The increase in the normalized excess CN concentrations beyond ~10 min, seen in Figure 4.17(b), could be due to gas-to-particle (g-to-p) conversion dominating over coagulation. The production of new particles by g-to-p conversion, as opposed to condensation onto existing particles, is favored by smaller surface area concentrations of particles; the aerosol surface area concentration in the Timbavati plume decreased by a factor of about five from 0 to 10 km downwind of the fire. Discussions by *Gao et al.* [2003] on g-to-p conversion of some organic species support this interpretation.

Shown in Figure 4.18 are particle size distributions, measured with the TSI 3320 aerodynamic particle sizer, for smoke samples 0 and 39 min old in the Timbavati plume. The effects of dilution on the particle concentrations due to mixing with the ambient air have been removed from the curves shown in Figure 4.18 by dividing the concentrations by CO. For particles less than about 1.5 μm in diameter, the particle concentrations decreased as the smoke aged, whereas for larger particles the concentrations were greater in the smoke that was 39 min old than in the smoke initially emitted from the fire. These results are consistent with the smaller particles coagulating to form the larger particles.

Sample 5 (see Table 4.1) was the oldest sample (39 min) for which both the excess mixing ratio of CO and the excess mass of particulate nitrate were measured. From the data in Table 4.2, we can compute the excess mass of nitrate (per m^3 of the smoke) in sample 5, which can then be converted to the number of excess NO_3^- molecules per cubic meter of smoke (8×10^{16}) using the molecular mass of nitrate (62) and Avogadro's number (6.022×10^{23} molecules per mole). We can also compute the number of excess CO molecules per cubic meter of smoke in sample 5 (2×10^{19}) from its excess volume-mixing ratio of 0.88 ppmv. These calculations imply that the ratio of excess NO_3^- molecules to excess CO molecules in sample 5 is ~0.004. This ratio is higher than the initial $\Delta NH_3/\Delta CO$ ratio in the smoke (~0.002; see Table 4.5 samples a

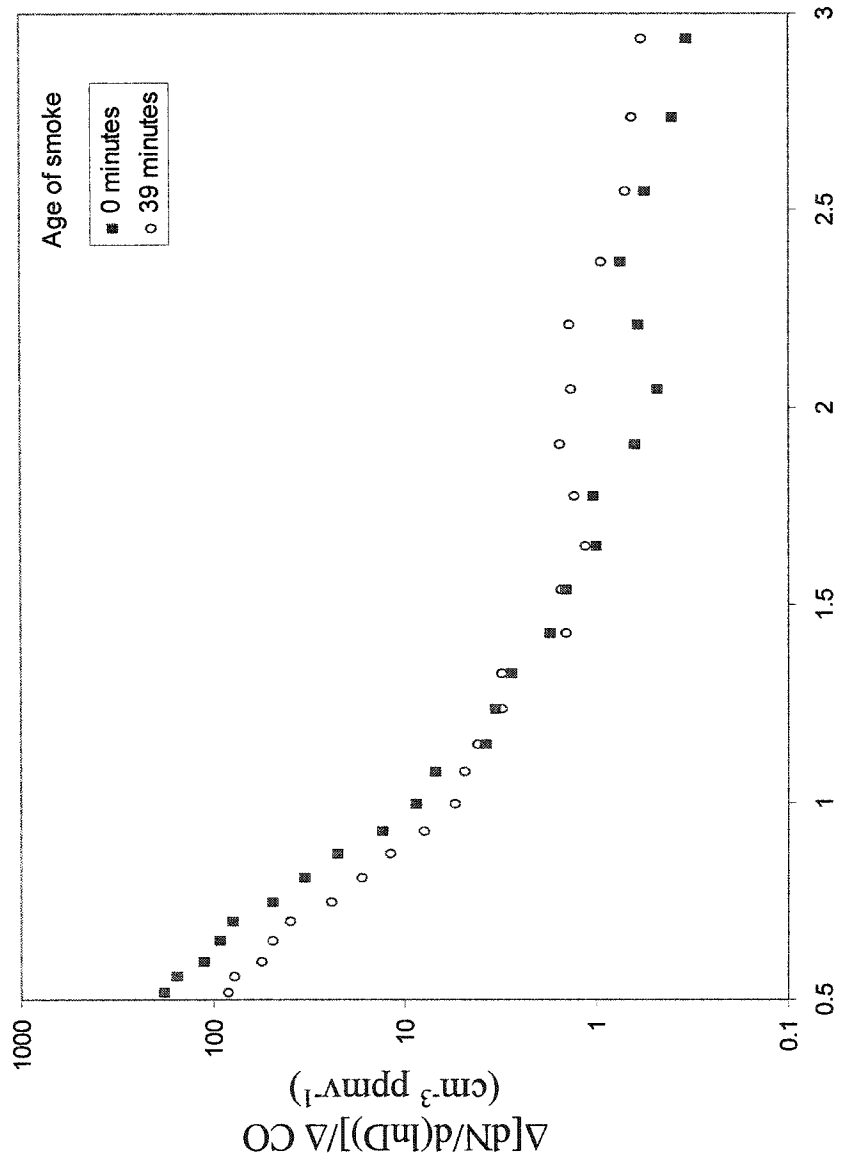

Figure 4.18. Aerosol size distributions of smoke over fire (0 min) and after aging for 39 min. The excess particle concentrations are divided by excess CO concentrations to eliminate the effects of mixing of the smoke with the ambient air.

and b). Therefore, not all of the nitrate can be present as ammonium nitrate. This suggests that some of the NO_3^- may be paired with K^+ or other positive ions rather than ammonium (NH_4^+). Potassium nitrate was observed in older smoke samples by *Li et al.* [2003] using electron microscopy. The $\Delta NO_3^-/\Delta CO$ ratio of 0.004 for sample 5 can also be compared to the initial $\Delta NO_x/\Delta CO$ ratio (see Table 4.5 samples a and b) of ~0.04. The comparison implies that up to ~10% of the initial NO_x was converted to particle nitrate in ~40 min. Much of the rest of the NO_x was probably converted to gas-phase reservoir species, such as PAN, HNO_3(g), alkyl nitrates, etc. (In extratropical fires, the initial $\Delta NH_3/\Delta CO$ and $\Delta NO_x/\Delta CO$ ratios are more nearly equal, which may favor the production of relatively more particle ammonium nitrate [*Goode et al.*, 2000].) A similar analysis for sulfur species suggests that ~10% of the initial SO_2 was converted to SO_4^{2-} in ~40 min.

Four papers in the SAFARI 2000 Special Issue of *Journal of Geophysical Research* provide additional information on the effects of aging on particles in the plume from the Timbavati fire. *Magi and Hobbs* [2003] show that the change in the light-scattering coefficient of the smoke, as the relative humidity was increased from 30 to 80%, was less for smoke aged over 40 min than for smoke just over the fire. Transmission electron microscopy (TEM) was used to study individual particles in the smoke from the Timbavati fire [*Li et al.*, 2003; *Pósfai et al.*, 2003]. In the young smoke just above the fire, potassium chloride (KCl) particles with organic coatings dominated, with lesser amounts of calcium-bearing particles, tar balls, organic particles, sea salt, mineral dust, and minor amounts of soot. The most obvious effect of aging of the smoke was a transformation from KCl particles to potassium sulfate and nitrate particles. The relative number concentration of organic particles was largest in the young smoke, whereas tar balls were dominant in the more aged smoke. *Gao et al.* [2003] discuss the secondary formation of inorganic and organic species in smoke from the Timbavati and other fires. It was found that secondary formation of sulfate, nitrate, levoglucosan, and several organic acids occurred during the initial aging of smoke aerosols, presumably due to condensation.

CHAPTER 5
DISTRIBUTIONS OF TRACE GASES AND AEROSOLS DURING THE DRY BIOMASS BURNING SEASON IN SOUTHERN AFRICA

5.1 Sampling Locations and Vegetative Types

A large body of observations is available from measurements on ambient regional hazes in southern Africa obtained aboard the UW Convair-580 in SAFARI 2000. Figure 5.1 shows a photograph of an ambient regional haze layer in the vicinity of Maun, Botswana, taken aboard the Convair-580 on September 2, 2000.

Vertical profiles were obtained over five sectors of southern Africa that represent four major vegetation classes: the semi-arid savannas of northeast South Africa and northern Botswana, the savanna-forest mosaic of coastal Mozambique, the humid savanna of southern Zambia, and the desert of western Namibia (Figure 5.2a). Most of tropical Africa consists of savanna, which extends from a latitude of ~15°N to ~25°S. Most of the savanna can be broadly classified as humid, extending from ~12°N to ~17°S, while the remainder is semi-arid. Savannas are typically found in hot or warm climates where rainfall ranges from 40-130 cm per year and is concentrated in a few months of the year, followed by a long period of drought. Humid savannas typically receive over 60 cm of annual rainfall and have a dry period of less than 6 months per year. Semi-arid savannas typically receive less than 60 cm of rainfall per year and have a dry period of greater than 6 months per year [*Huntley*, 1982]. The dense forests of northern Congo, which extend west to the Atlantic Ocean, are an exception to the predominant savanna vegetation of tropical Africa. Also, the deserts of southwest and northern Africa have distinct vegetation. The four vegetation classes in this study account for about one-half of the biomass burned in southern Africa during the dry season of 2000 [*Silva et al.*, 2003].

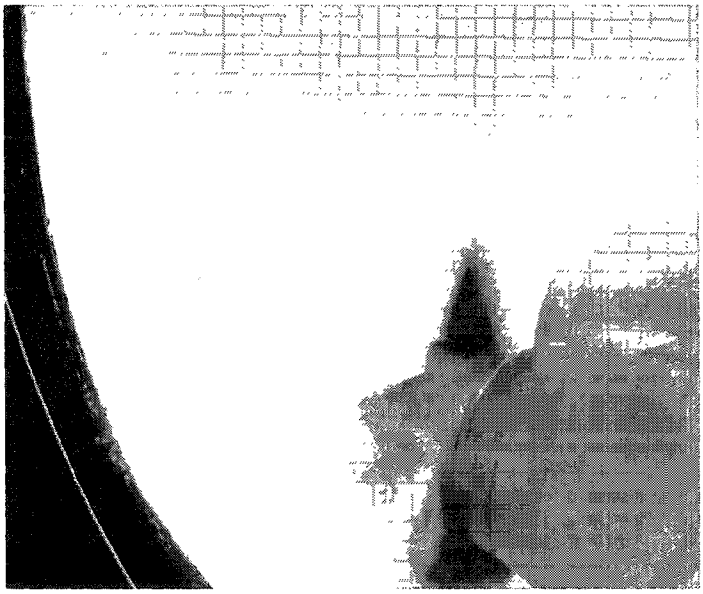

Figure 5.1. Photograph of ambient regional haze over Botswana (19.97 °S, 23.74 °E) at 1124 UTC on 2 September 2000. A stable layer at ~4 km msl separates the haze layer from the free troposphere above. (Photo: Peter V. Hobbs)

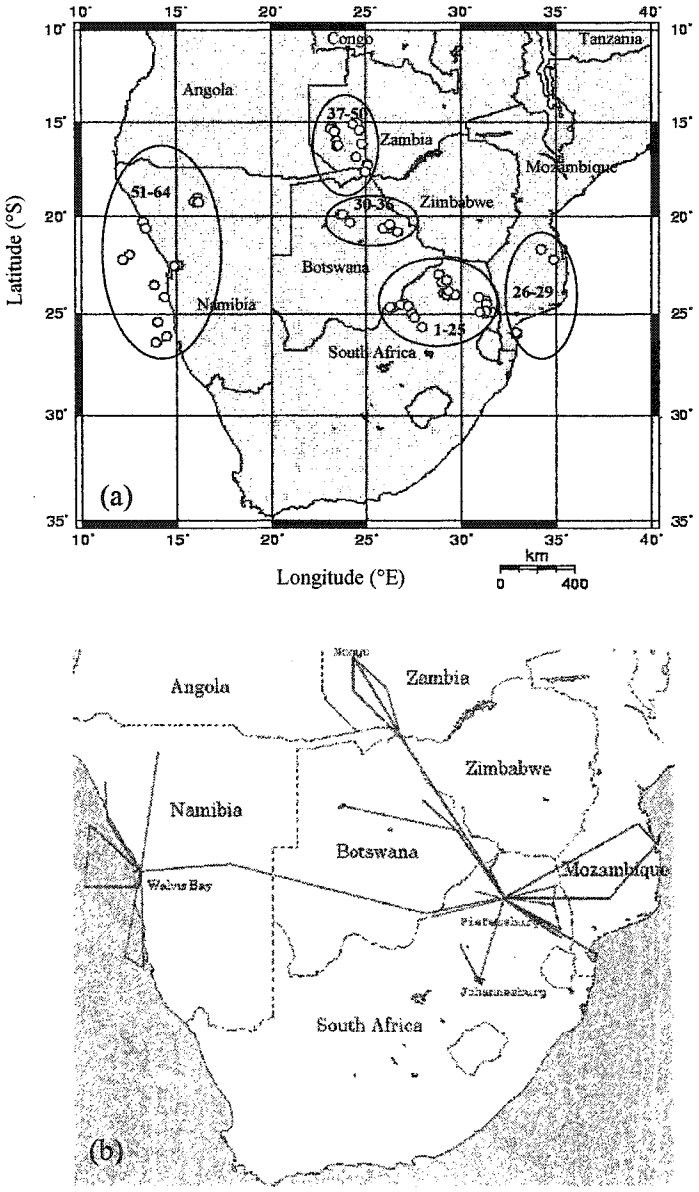

Figure 5.2. (a) Locations of the vertical profiles obtained aboard the University of Washington's Convair-580 research aircraft in southern Africa during the dry biomass burning season of 2000. Profiles were obtained over five major sectors (within the ovals) in South Africa, Mozambique, Botswana, Zambia, and Namibia. The numbers within each oval are the vertical profile numbers listed in Table 5.1; the white circles show the locations of the profiles. Note that some of the vertical profiles listed in Table 5.1 have overlapping locations in this figure. (b) Approximate flight tracks (solid lines) of the UW Convair-580 research aircraft in southern Africa during the dry biomass burning season of 2000. The flying altitude was typically <5 km msl.

Sixty-four vertical profiles were obtained during 30 research flights of the Convair-580 in SAFARI 2000. Twenty-five of these profiles were in South Africa, 4 in Mozambique, 7 in Botswana, 14 in Zambia, and 14 in Namibia (Figure 5.2a, Table 5.1). The altitudes covered by the profiles ranged from close to ground level up to ~5 km above mean sea level (msl). All of the profiles were obtained during daylight hours, and they were all in ambient air, removed from any visible smoke plumes.

The profiles in South Africa were centered around Pietersburg (23.89°S, 29.45°E). The semi-arid savanna of this region, locally known as lowveld and highveld depending on altitude, consists of a combination of woodland and bushland savanna. The profiles in Mozambique were near Maputo (25.97°S, 32.60°E) and Beira (19.79°S, 34.92°E). The coastal mosaic of this region consists of a combination of forest and wooded grassland savanna. The profiles in Botswana were east of Maun (19.83°S, 23.50°E) in a region of mopane woodland savanna that also includes the productive wetlands of the Okavanga delta and the halophytic vegetation of the Sua Pan (an expanse of white salt encrusted clay that is the evaporated remains of a lake). The profiles in Zambia were centered around Kaoma (14.78°S, 24.80°E), a region of primarily miombo woodland savanna dominated by the tree species Brachystegia and related genera. The miombo woodland is one of the most prevalent vegetation classes in Africa, covering much of the continent from ~2-17°S. Interspersed through Zambia's miombo woodlands are dambo grasslands; these are affected by seasonal flooding and are covered with a medium-dense, uniform grass mat. The profiles in Namibia were centered around Walvis Bay (22.83°S, 14.50°E), a desert region with a mean annual rainfall of 1 cm. Fog that forms over the cold offshore Benguela current is brought inland by south-westerly winds during the night, contributing another 4-5 cm of mean annual precipitation from fog deposition. Sand dunes, gravel desert, grasses, and succulents characterize this extremely arid region [*White*, 1981, 1983].

The general locations of the horizontal flight tracks of the UW Convair-580 research aircraft in this study are shown in Figure 5.2b. They cover a wide area of southern Africa from Johannesburg, South Africa, in the south, to Mongu, Zambia, in the north, and from the Indian Ocean in the east to the South Atlantic Ocean in the west.

Table 5.1. Times, locations, and altitudes (msl) for vertical profiles of trace gases and aerosols obtained aboard the University of Washington's Convair-580 aircraft in southern Africa during August and September, 2000. Profiles 1-25 were over the South Africa sector, profiles 26-29 over the Mozambique sector, profiles 30-36 over the Botswana sector, profiles 37-50 over the Zambia sector, and profiles 51-64 over the Namibia sector.

Vertical Profile	Date (mm:dd:yy)	Time (UTC)	Longitude (°E)	Latitude (°S)	Altitude (km)
1	08:14:00	1110-1127	27.95	25.68	1.11-3.64
2	08:14:00	1249-1305	27.40	24.96	1.67-3.45
3	08:14:00	1433-1450	27.53	25.20	0.91-2.74
4	08:14:00	1632-1641	29.26	24.07	1.21-3.29
5	08:17:00	0740-0800	31.23	25.00	0.28-2.99
6	08:17:00	1128-1145	31.28	24.33	0.88-2.99
7	08:18:00	0843-0910	27.01	24.49	0.98-3.33
8	08:18:00	1225-1243	26.42	24.66	1.80-3.98
9	08:18:00	1243-1255	26.82	24.53	2.66-3.97
10	08:18:00	1323-1334	29.16	23.94	1.15-3.34
11	08:20:00	0800-0814	29.06	23.95	1.12-2.86
12	08:20:00	1240-1257	26.23	24.67	1.11-3.12
13	08:20:00	1424-1509	27.20	24.60	1.05-2.86
14	08:20:00	1526-1535	29.21	23.93	1.12-2.89
15	08:22:00	0817-1005	31.65	24.95	0.30-3.60
16	08:22:00	1046-1110	31.30	24.51	0.69-2.49
17	08:22:00	1135-1151	30.90	24.18	0.37-2.50
18	08:22:00	1220-1229	29.63	24.03	1.14-2.49

(Cont.)

Table 5.1 continued

Vertical Profile	Date (mm:dd:yy)	Time (UTC)	Longitude (°E)	Latitude (°S)	Altitude (km)
19	08:23:00	1400-1429	29.21	24.02	1.40-4.53
20	08:29:00	0950-1003	28.80	22.97	1.34-2.65
21	08:29:00	1027-1058	28.99	23.38	1.43-3.74
22	08:29:00	1058-1106	29.31	23.86	1.52-3.74
23	08:29:00	1324-1334	31.28	24.88	0.76-3.32
24	08:29:00	1421-1509	30.95	24.92	0.62-3.06
25	09:06:00	1327-1349	29.21	23.30	1.18-2.72
26	08:24:00	0809-0824	32.95	25.99	0.08-3.90
27	08:24:00	0852-1000	32.88	25.94	0.01-2.53
28	08:31:00	1017-1055	34.84	22.23	0.03-2.78
29	08:31:00	1227-1250	34.20	21.71	0.40-3.72
30	09:02:00	0952-1010	23.62	19.91	0.92-4.29
31	09:02:00	1058-1127	23.74	19.88	2.02-4.27
32	09:02:00	1127-1140	24.13	20.31	2.70-4.30
33	09:03:00	0816-0830	26.65	20.79	2.98-4.44
34	09:03:00	0830-0844	26.21	20.61	1.01-4.40
35	09:03:00	1009-1036	25.90	20.63	0.89-4.44
36	09:03:00	1045-1055	26.25	20.42	2.22-4.41
37	09:01:00	0745-0804	25.03	17.27	1.72-3.00
38	09:01:00	0831-0845	24.52	15.02	2.14-2.99
39	09:01:00	1010-1030	24.63	15.41	1.81-3.62
40	09:01:00	1048-1057	25.06	17.32	1.91-3.67
41	09:05:00	1054-1155	24.76	16.16	1.26-3.97
42	09:05:00	1257-1306	24.28	15.10	1.54-3.11

(Cont.)

Table 5.1 continued

Vertical Profile	Date (mm:dd:yy)	Time (UTC)	Longitude (°E)	Latitude (°S)	Altitude (km)
43	09:05:00	1319-1325	23.43	15.98	1.46-3.03
44	09:05:00	1325-1333	23.45	16.27	1.49-3.48
45	09:05:00	1357-1408	24.94	17.63	1.11-3.41
46	09:06:00	0744-0758	23.51	16.22	1.08-3.61
47	09:06:00	0915-0932	23.16	15.24	1.13-4.54
48	09:06:00	0932-0951	23.11	15.34	1.47-4.55
49	09:06:00	0951-1009	23.32	15.49	1.47-4.75
50	09:06:00	1015-1055	24.47	16.87	1.00-5.05
51	09:10:00	1008-1021	15.04	22.53	0.04-3.58
52	09:11:00	0923-0935	12.52	21.98	0.58-3.62
53	09:11:00	0957-1040	12.15	22.23	0.38-2.88
54	09:11:00	1109-1138	13.78	23.54	0.86-3.50
55	09:13:00	1113-1134	13.20	20.26	0.84-4.89
56	09:13:00	1134-1312	13.33	20.61	0.33-4.91
57	09:14:00	0854-0912	14.42	26.13	1.72-2.96
58	09:14:00	0916-0953	13.86	26.45	0.02-1.92
59	09:14:00	1126-1140	13.96	25.41	0.12-3.59
60	09:14:00	1140-1227	14.32	24.15	0.12-3.58
61	09:16:00	0840-0854	16.07	19.01	1.19-4.24
62	09:16:00	1052-1108	15.90	19.21	1.07-4.59
63	09:16:00	1108-1128	16.14	19.26	1.79-4.52
64	09:16:00	1221-1239	14.84	22.56	0.16-3.07

5.2 Climatic Conditions and Fire Frequency

The months from April to October comprise the dry season in southern Africa. For example, Kafue, Zambia, (15°S, 26°E) receives 800 cm of rainfall from November to March, while from May to September the rainfall is typically less than 1 cm. Evaporative losses result in a water deficit of >10 cm per month during the dry season in Kafue, leading to water stress for biota, and ultimately a dry and withered savanna that can be readily ignited [*Jury*, 2000]. The rate of biomass burning in southern Africa peaks in the northern part of this region in the early dry season, and a peak in local burning moves south over the course of the dry season arriving in South Africa in September [*Justice et al.*, 1996].

Fire count data for the region is provided by the Along Track Scanning Radiometer (ATSR) aboard the European Remote Sensing-2 satellite. Fire-counts are determined at night-time (~10 pm local time) from ATSR measurements in the 3.7 μm thermal channel. Fire-counts are reported as the number of times the 3.7 μm channel exceeds 308 K [*Arino and Rosaz*, 1999]. The ATSR data show an abundance of fires in southern Africa during the period of this study, August 14-September 16 of 2000 (Figure 5.3). The South Africa sector contained numerous local fires in August and September, and the western border of the Mozambique sector was lined with fires in August. There were a number of fires within and surrounding the Zambia sector in September. Depending on the prevailing winds, the vertical distribution of pollutants over the Zambia sector could be strongly influenced by aged emissions from fires in Angola, Congo, and Zimbabwe. Since aged smoke is typically enhanced in oxidation products and oxidation by-products such as organic acids and ozone, the lower atmosphere in Zambia contained large concentrations of these pollutants. As with the Zambia sector, there were abundant fires surrounding the landlocked Botswana sector, with possible transport of fire emissions from Angola, Zambia, Zimbabwe, South Africa, and Mozambique. Transport of emissions into Namibia from the fire-prone area of southern Angola affected the vertical distribution of pollutants in this region.

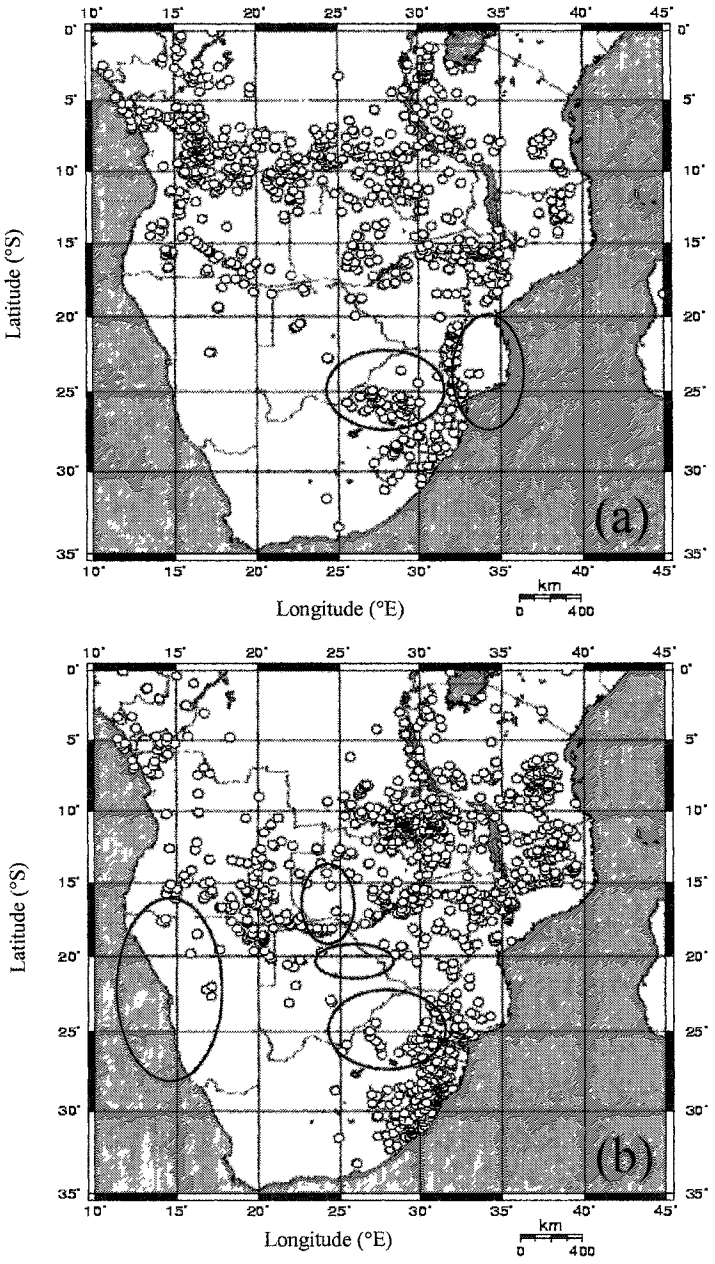

Figure 5.3. Fire counts from the Along Track Scanning Radiometer (ATSR) aboard the European Remote Sensing-2 Satellite at ~10 pm local time in (a) August and (b) September 2000. Locations of the five sets of vertical profiles of the UW Convair-580 aircraft were within the ovals.

The climatological mean atmospheric circulation in southern Africa in the dry season is depicted in Figure 5.4a [*READY*, 2002]. It is characterized by a semipermanent continental gyre with easterly winds in the tropical band (10°-20°S), westerly winds in the temperate band (20°-30°S), and meridional winds over the east and west coasts of Africa around 20°S [*Jury*, 2000]. The transport of smoke from savanna fires under the conditions of the continental gyre are reflected in measurements of the aerosol index from the NASA Total Ozone Mapping Spectrometer (TOMS), which are shown in Figure 5.5a. Smoke from fires in Angola, Congo, and Zambia are transported westward and accumulate over the southern Atlantic Ocean. This long-range transport of pollutants, termed the "great African plume" by *Chatfield et al.* [1998], occurs when biomass burning emissions, which mix into a ~3-4 km deep boundary layer over southern Africa, override cooler air from the rainforests of the central Congo, and then head westward over the south Atlantic Ocean. This plume is a predominant source of pollution in the midtropical southern Atlantic Ocean [*Chatfield et al.*, 1998].

On average, the continental gyre prevails approximately half the time during the dry season and is perturbed by westerly waves with a ~30% frequency [*Jury*, 2000]. For example, a westerly trough in early September 2000 produced the northwesterly flow shown in Figure 5.4b. This resulted in smoke being transported southeastward from central Africa to the Indian Ocean (Figure 5.5b). This event, termed the "river-of-smoke" by *Annegarn et al.* [2002], resulted in heavy haze and reduced visibility over southern Africa for about ten days in early September 2000.

During August 2000 weather conditions were consistent with the climatological mean conditions summarized above, with the continental gyre prevailing about half the time and perturbations by westerly waves present on approximately 1 out of 3 days. However, conditions were more unstable in September 2000, with frequent penetrations by frontal perturbations and unstable air masses, including the river-of-smoke [*Freiman et al.*, 2002].

Vertical air motions over southern Africa during the dry season are driven by sensible heating of the surface by solar radiation, resulting in vigorous vertical fluxes

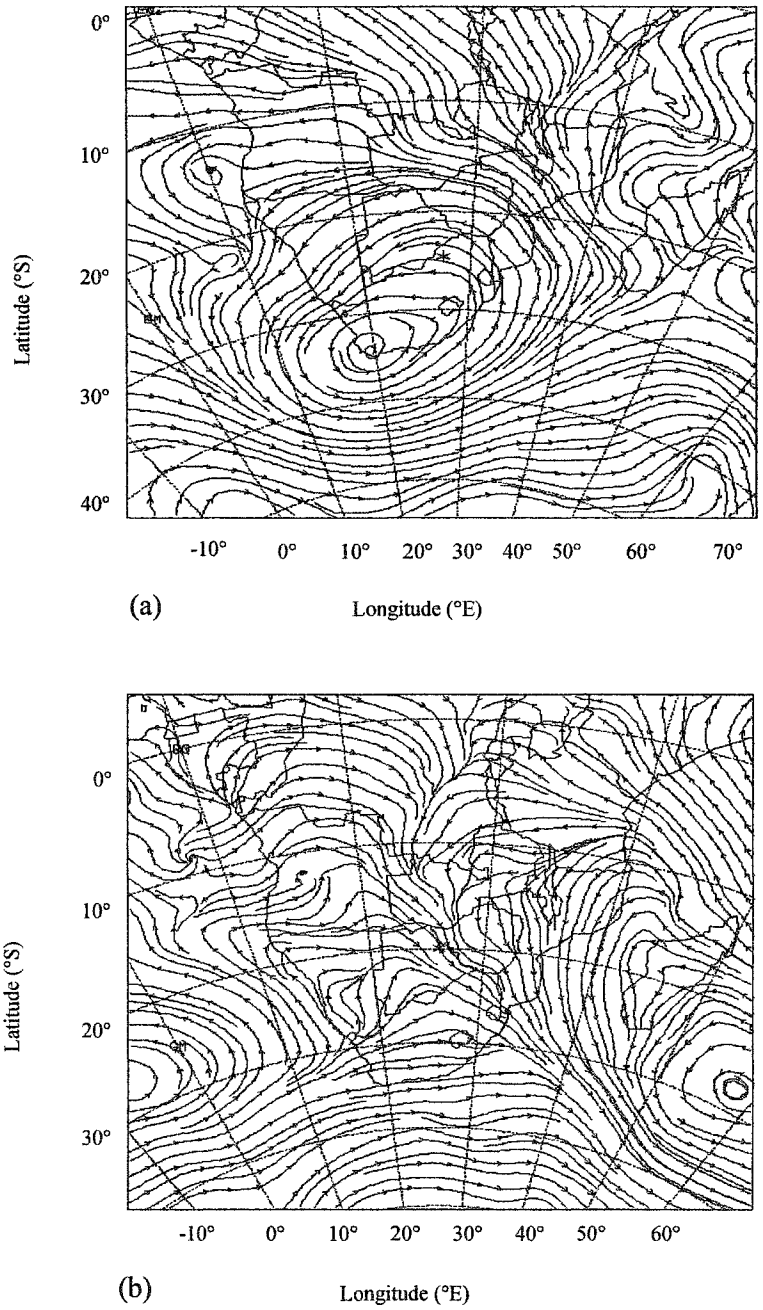

Figure 5.4. The 850 hPa streamlines for (a) 1200 UTC August 14, 2000, and (b) 1200 UTC September 3, 2000. The streamlines in (a) reflect the climatological mean continental gyre, and (b) shows the passage of a westerly trough. From *READY* [2002].

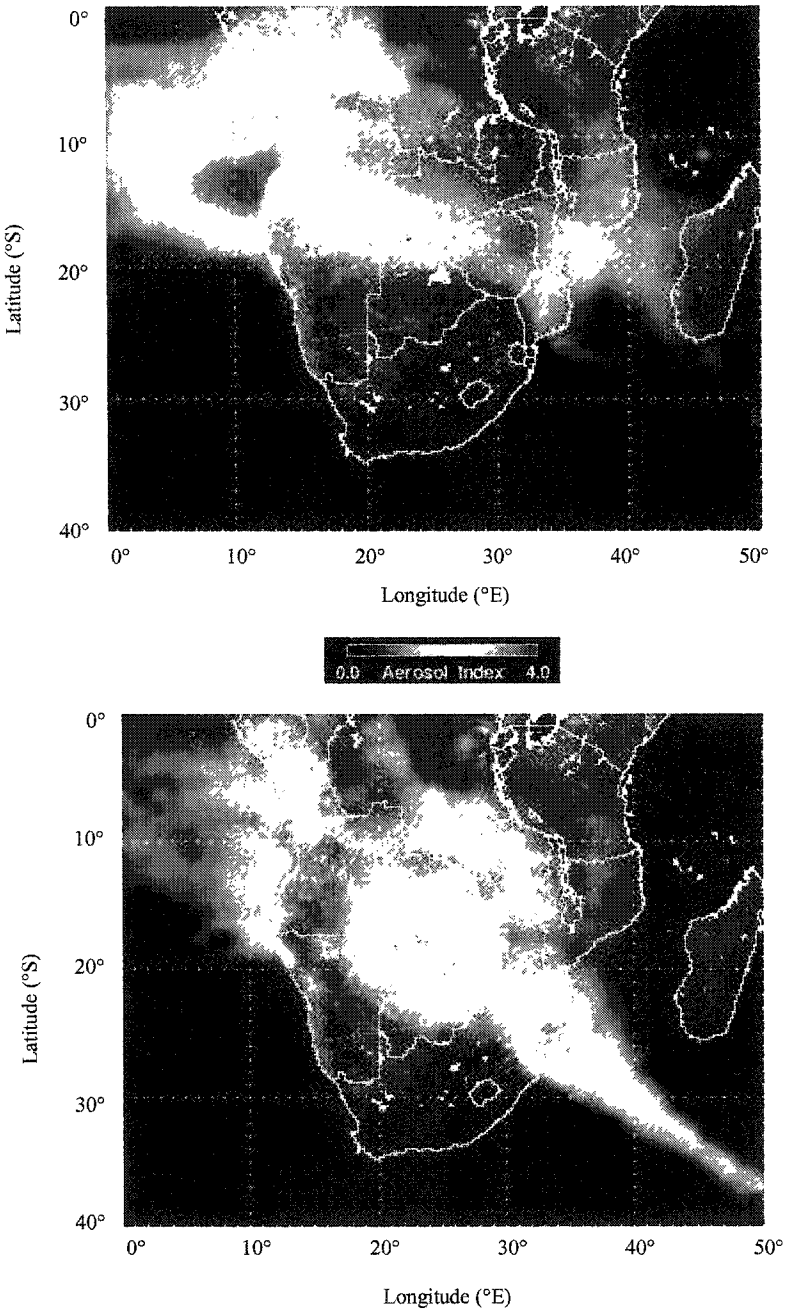

Figure 5.5. TOMS aerosol index for (a) September 7, 2000, under conditions of the continental gyre shown in Figure 5.4a, and for (b) September 4, 2000, during the passage of the westerly trough shown in Figure 5.4b. From *Privette et al.* [2001]. The aerosol index is related to aerosol optical depth; visibility decreases as the aerosol index increases from 0 to 4.

and an atmospheric mixed layer ~3 km in depth over southern Africa during the daytime [*Jury*, 2000]. Above the mixed layer are persistent capping stable layers at ~700 and ~500 hPa (~3 and ~5.5 km msl, respectively), which are produced by strong subsidence. These stable layers are ~0.5-1 km thick and trap pollutants below their bases by inhibiting vertical mixing. Capping stable layers were observed in southern Africa on nine out of ten days during August and September, 2000 [*Freiman et al.*, 2002].

5.3 Industrial Sources and Domestic Burning

The region of northeast South Africa where the vertical profiles 1-25 (Figure 5.2a, Table 5.1) were obtained includes the Kruger National Park and other wildlife preserves, which are characterized by vast tracts of semi-arid savanna. It is also a region of intense power production and mining operations, where some 95% of South Africa's electricity is generated primarily by coal-fired power plants [*EIA*, 2002]. Several of the largest of these plants are located in the Mpumalanga province of South Africa, which includes Kruger National Park. Some of the vertical profiles presented in this chapter were obtained over this region. Many of South Africa's mining operations are also located in northeast South Africa, including 81% of South Africa's coal mines [*EIA*, 2002] and the Palaborwa copper mine, one of the largest copper mines in the world. The heavy machinery required for mining operations are energy intensive and can result in high emissions of pollutants. Airborne measurements obtained in this study in the plume from the Palaborwa mine show an excess of ~15 ppbv of SO_2 above ambient levels. For comparison, an excess of 7-64 ppbv of SO_2 above ambient levels were measured in the smoke plume from the Timbavati fire (Chapter 4).

Profiles 26-29 (Figure 5.2a, Table 5.1) were obtained over the Indian Ocean coast of Mozambique, a region of coastal forest and savanna. With a primarily agricultural society, there are few industrial sources of pollution in this sector, leaving biomass burning as the major local source of air pollution.

Profiles 30-36 (Figure 5.2a, Table 5.1) were obtained over northern Botswana, a region of woodland savanna, wetlands, and salt pans. Botswana is a primarily

agricultural society with a small population (<2 million). Except for diamond mining, there are few industrial sources of pollution in this region.

Profiles 37-50 (Figure 5.2a, Table 5.1) were obtained over the upper Zambezi River Valley, a region of humid savanna where industrial emissions are minor. However, the "copper belt" north of the Zambia sector, situated between Zambia and the Democratic Republic of Congo, is a focus of mining and development activities and contains 34% and 10% of global cobalt and copper reserves, respectively [*Mbendi*, 2003].

Profiles 51-64 (Figure 5.2a, Table 5.1) were obtained over the Namib Desert and the adjacent South Atlantic coast of Namibia. The cold, upwelling waters of the Benguela current off the Namibian coast support a diverse marine ecosystem and a strong fishing industry based out of Walvis Bay, Namibia. Ocean-going vessels are among the world's highest polluting combustion sources per quantity of fuel consumed. For example, emission factors of NO_x (as NO) and SO_2 from ships sampled off the coast of Namibia were 21-69 and 3-56 g per kg fuel burned, respectively [*Sinha et al.*, 2003c], compared to only 3.3±0.6 and 0.43±0.30 g per kg fuel burned, respectively, for savanna fires in southern Africa (Chapter 3). Since relatively few savanna fires occur in Namibia, emissions from ships could have an impact on air quality along the Namibian coast.

In addition to emissions from savanna fires and industrial sources, air quality in southern Africa is substantially affected by biofuel use, since the majority of residential energy for heating and cooking comes from the burning of fuel wood and charcoal. Unlike savanna burning, which is seasonal, biofuel use occurs year-round. Therefore, annual emissions of several important trace gases (e.g., CH_4) from biofuel use rival or even exceed those from savanna fires [*Bertschi et al.*, 2003a]. Biofuel use is commonplace throughout southern Africa, accounting for 75% of total energy consumption in the region [*EIA*, 2002]. Of the five sectors in this study, biofuel use is highest in South Africa, Mozambique, and Zambia where ~8-9 Tg of fuel wood are burned annually per country, compared to <1 Tg yr^{-1} per country for Botswana and Namibia [*Yevich and Logan*, 2003].

5.4 Vertical Profiles

Vertical profiles of temperature, relative humidity (RH), SO_2, O_3, and CN over the South Africa, Mozambique, Botswana, Zambia, and Namibia sectors are summarized in Figures 5.6-5.10. In these figures, the numerous measurements obtained in the profiles over each sector (Table 5.1) are summarized in boxes in which mean, median, and several percentile values are given for various altitudes. In the remainder of this chapter, all altitudes will refer to height above msl.

Before discussing the results shown in Figures 5.6-5.10, we will describe briefly the importance of SO_2, O_3 and CN, and, for comparison, some typical values of these species in various environments.

Sulfur dioxide is the primary anthropogenic sulfur-containing air pollutant. Upon oxidation to sulfate, SO_2 contributes to acidity and light scattering in the atmosphere. The lifetime of SO_2 through oxidation by the hydroxyl radical (OH) is about one week. However, SO_2 in the boundary layer can be removed by dry deposition on a time scale of a day, and even more rapidly by wet deposition. Typical mixing ratios for SO_2 in clean, continental air and in polluted, continental air are ~0.2 and 1.5 ppbv, respectively [*Seinfeld and Pandis*, 1998].

Tropospheric O_3 can damage vegetation and is deleterious to human health. It is an important precursor of OH, the primary oxidant in the troposphere. Ozone is also an important greenhouse gas in the upper troposphere [*Mauzerall et al.*, 1998]. The photochemical lifetime of O_3 is ~10 days and depends on season and latitude. Ozone can also be removed from the troposphere by dry deposition on a time scale of about a month. Typical mixing ratios for O_3 in remote locations range from ~20-40 ppbv; in polluted urban air it can exceed 100 ppbv [*Seinfeld and Pandis*, 1998]. Ozone mixing ratios in smoke from savanna fires are comparable to those in polluted urban air. For example, ~20 km downwind of the Timbavati fire, O_3 mixing ratios in excess of 100 ppbv were measured (Chapter 4).

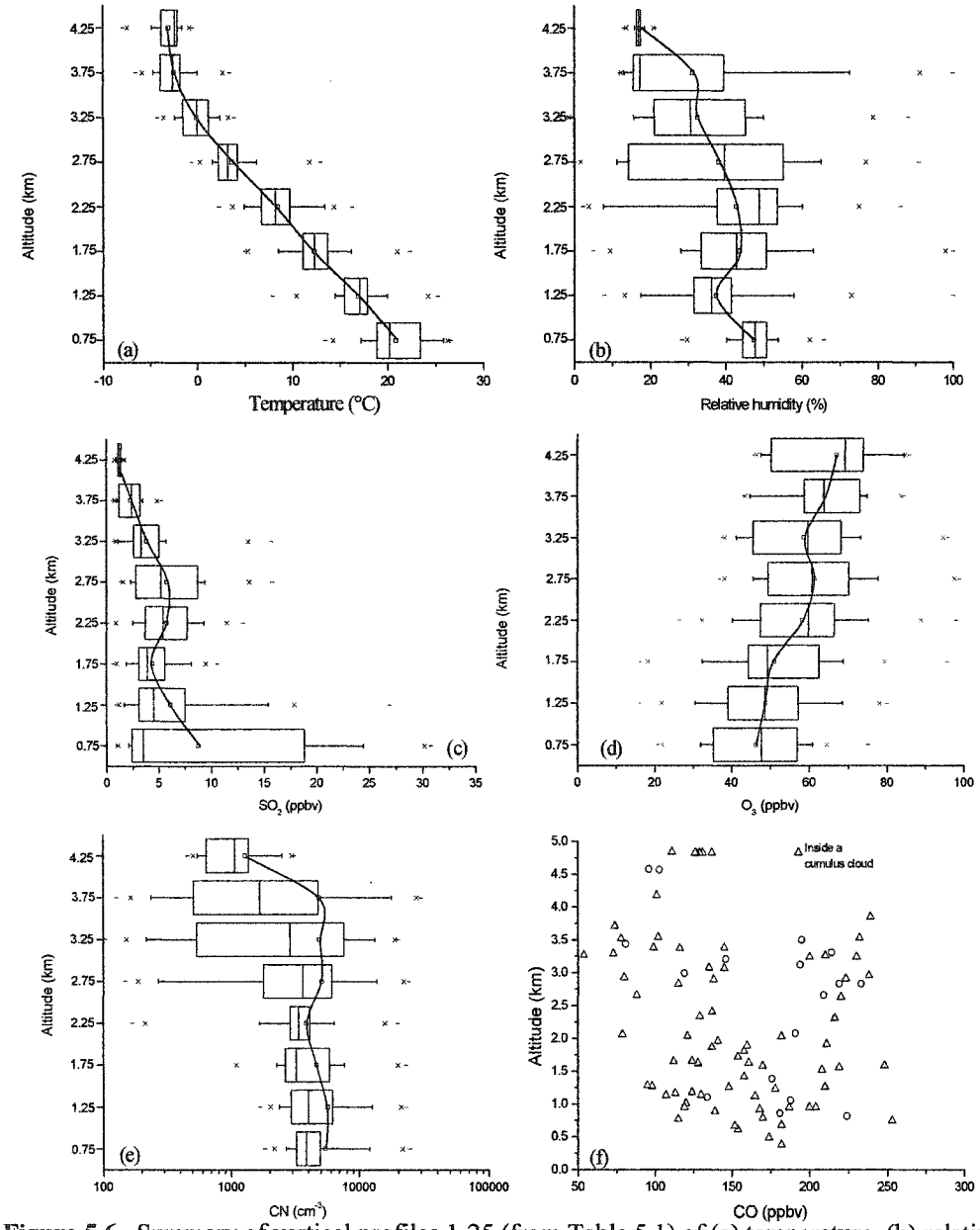

Figure 5.6. Summary of vertical profiles 1-25 (from Table 5.1) of (a) temperature, (b) relative humidity, (c) SO_2, (d) O_3, and (e) CN over the South Africa sector for the period August 14-September 6, 2000. In (a) through (e), the square symbol in each box denotes the mean of the data; the vertical line within each box denotes the 50th percentile value; the left and right sides of each box denote the 25th and 75th percentile values, respectively; and, the error bars denote the 5th and 95th percentile values. The two symbols to the left of the 5th percentile error bar denote the 0th and 1st percentile values, and the two symbols to the right of the 95th percentile error bar denote the 99th and 100th percentiles. Intermittent samples of CO over the South Africa sector are shown in (f), with the circles and triangles indicating measurements by GC/C and AFTIR, respectively.

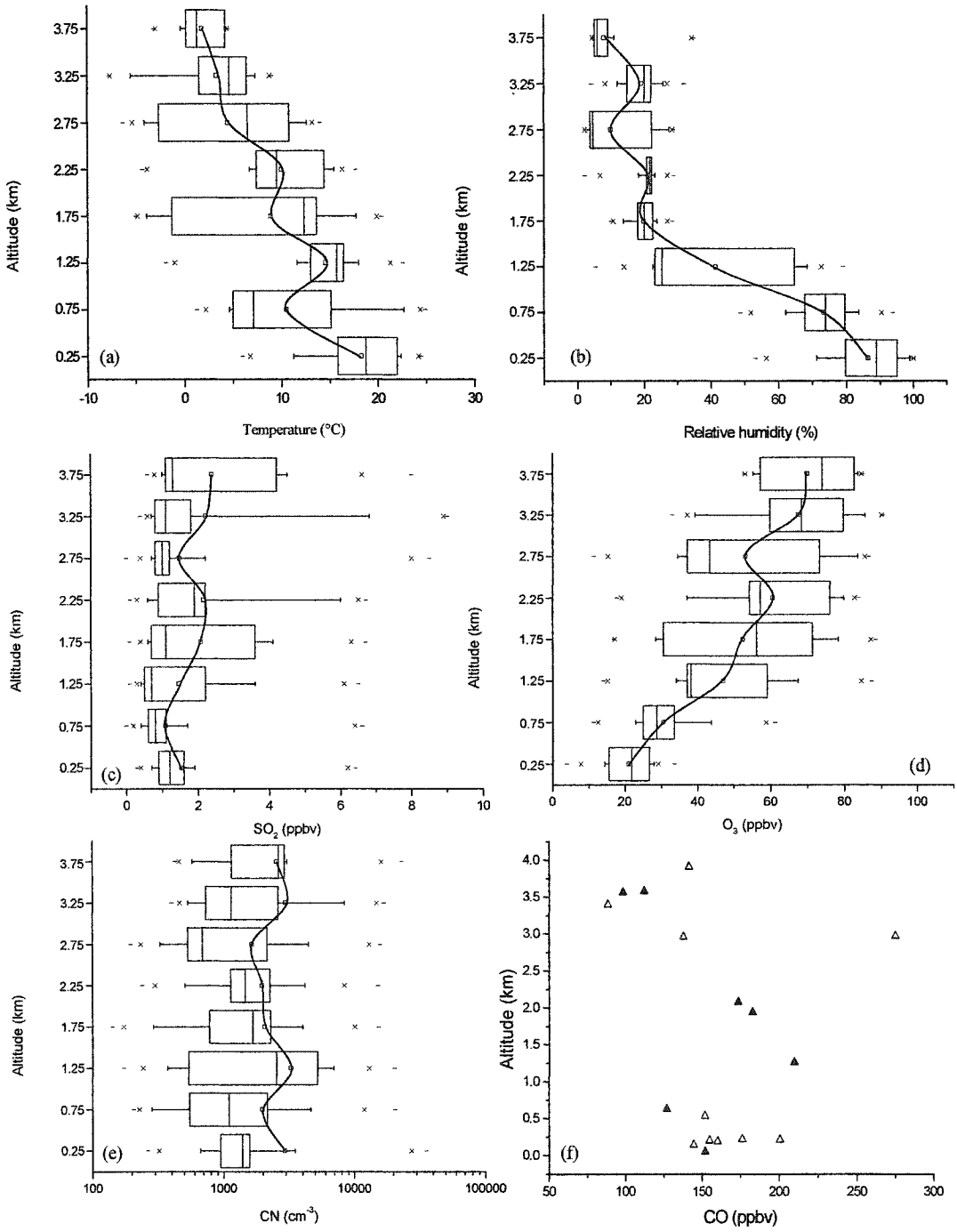

Figure 5.7. (a) through (e) as for Figure 5.6., but for vertical profiles 26-29 (from Table 5.1) over the Mozambique sector for the period of August 24-August 31, 2000. Intermittent samples of CO over the Mozambique sector obtained by AFTIR are shown in (f), with the open and closed triangles indicating continental and maritime measurements, respectively.

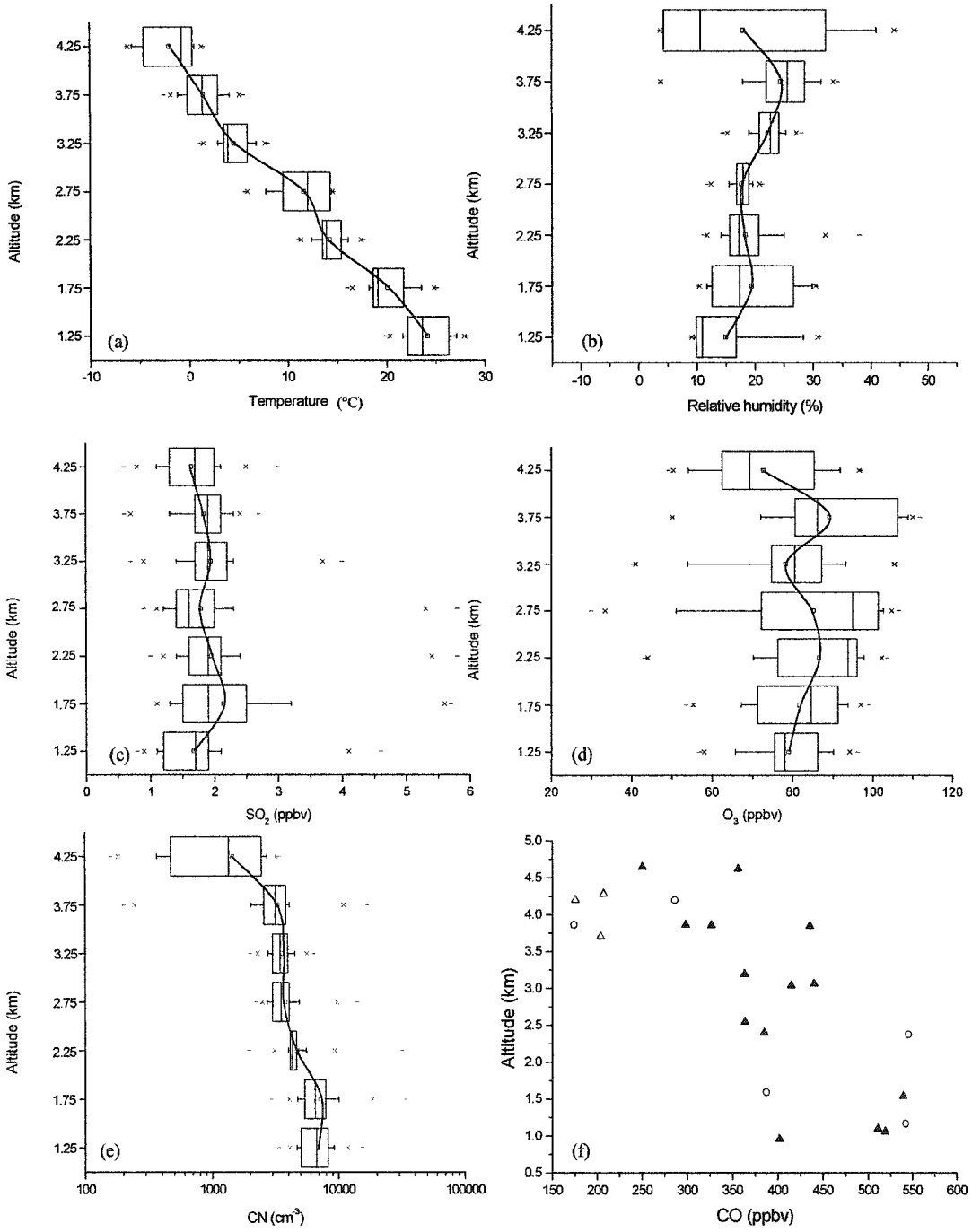

Figure 5.8. (a) through (e) as for Figure 5.6., but for vertical profiles 30-36 (from Table 5.1) over the Botswana sector for the period of September 2-September 3, 2000. Intermittent samples of CO over the Botswana sector are shown in (f), with the open triangles indicating AFTIR measurements obtained on 1 September 2000, the closed triangles indicating AFTIR measurements obtained on 3 and 6 September 2000, and the circles indicating GC/C measurements obtained on 1-3 September 2000.

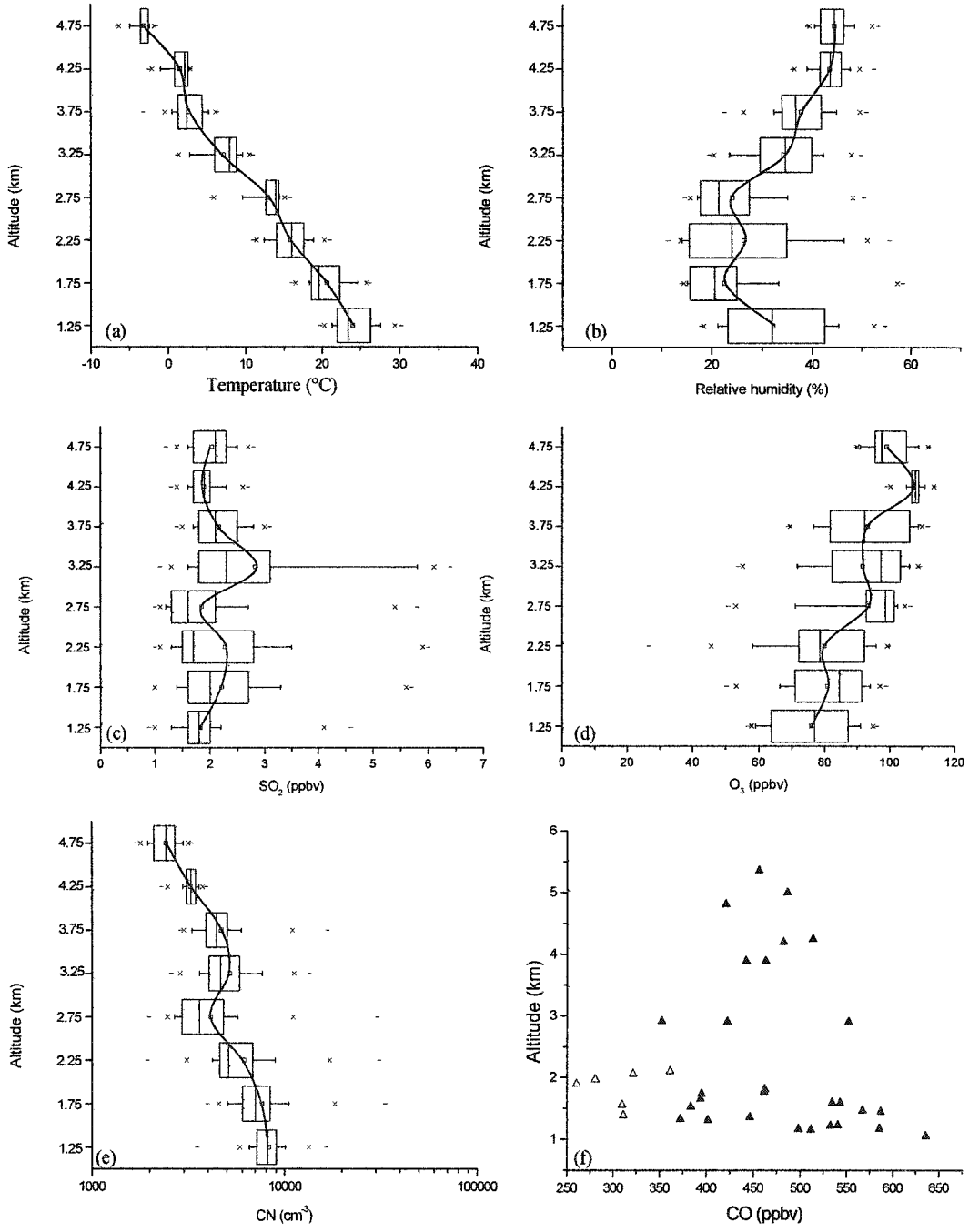

Figure 5.9. (a) through (e) as for Figure 5.6., but for vertical profiles 37-50 (from Table 5.1) over the Zambia sector for the period of September 1-September 6, 2000. Intermittent samples of CO over the Zambia sector are shown in (f), with the open and closed triangles indicating measurements obtained by AFTIR on 1 September 2000 and 5-6 September 2000, respectively.

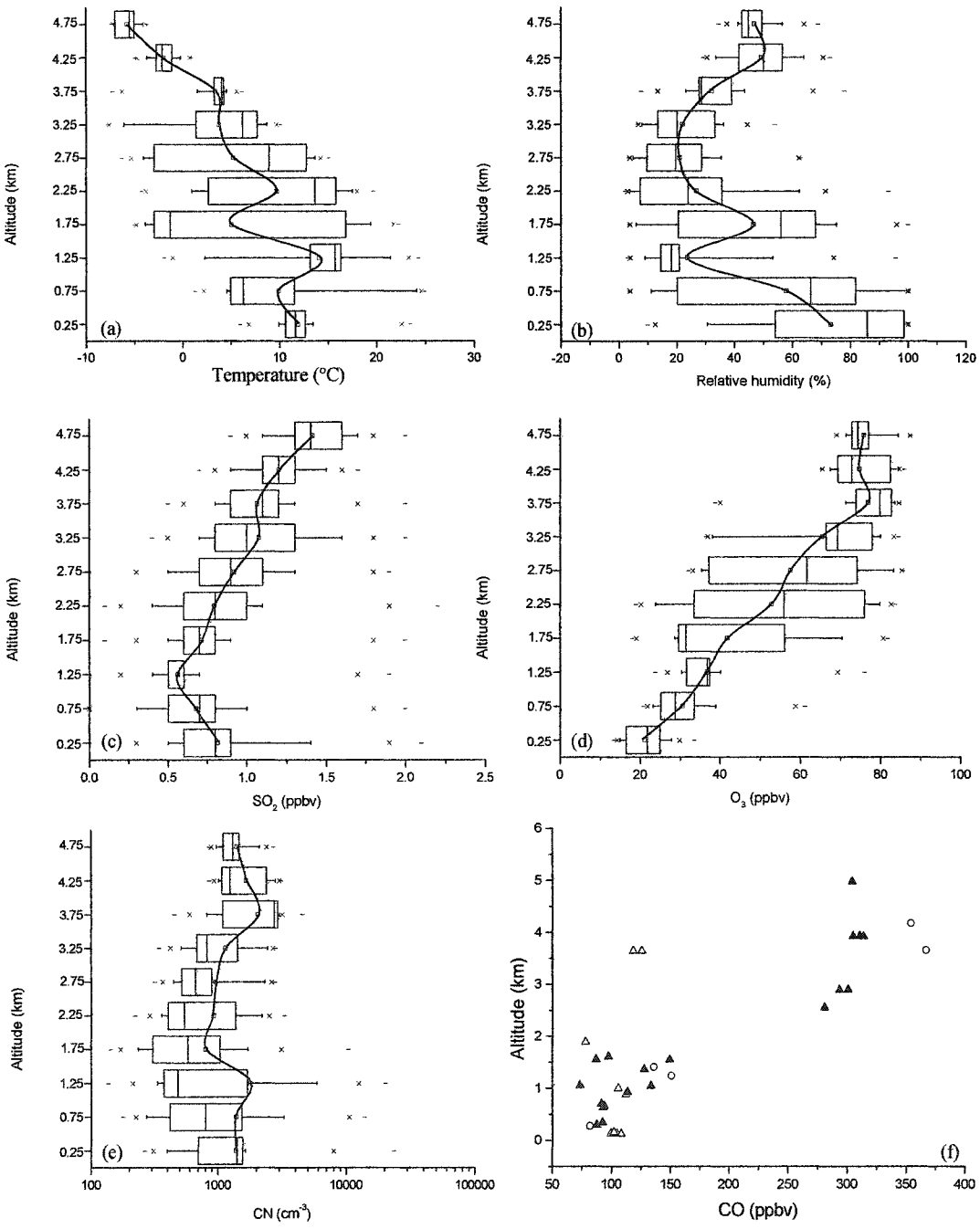

Figure 5.10. (a) through (e) as for Figure 5.6., but for vertical profiles 51-64 (from Table 5.1) over the Namibia sector for the period of September 10-September 16, 2000. Intermittent samples of CO over the Namibia sector are shown in (f), with the open triangles indicating AFTIR measurements obtained on 14 September 2000, the closed triangles indicating AFTIR measurements obtained on 13 September 2000, and the circles indicating GC/C measurements obtained on 13 and 16 September 2000.

Particles in the troposphere reduce visibility, they play a role in heterogeneous chemistry, they are involved in the formation of cloud droplets, and they affect atmospheric radiation. Particles can be removed by coagulation and dry and wet deposition. Particles smaller than ~0.01 μm in diameter and larger than ~20 μm in diameter have lifetimes less than about a day. However, accumulation-mode particles (0.1-3 μm diameter) may reside in the troposphere for weeks or months [*Hobbs*, 2000]. The concentrations of CN typically range from ~10,000-400,000 cm^{-3} for polluted, continental locations, ~2,000-10,000 cm^{-3} for rural sites over continents, ~50-10,000 cm^{-3} for remote, continental sites, and ~100-400 cm^{-3} for marine locations [*Seinfeld and Pandis*, 1998]. The CN concentrations over the Timbavati fire ranged from ~100,000 cm^{-3} over the fire to ~50,000 cm^{-3} 20 km downwind (Chapter 4).

In addition to the vertical profiles of temperature, relative humidity, SO_2, O_3, and CN, we obtained less detailed profiles of CO (from intermittent samples) over South Africa, Mozambique, Botswana, Zambia, and Namibia. The lifetime of CO in the tropics is ~1 month [*Seinfeld and Pandis*, 1998]. In the background troposphere, CO concentrations range from ~50-150 ppbv in remote areas, to ~1000 ppbv in rural-suburban areas, to several ppm in polluted urban areas [*Finlayson-Pitts and Pitts*, 2000]. The mixing ratios of CO in initial smoke from savanna fires are comparable to those in polluted urban air. For example, in the Timbavati plume the CO mixing ratios ranged from ~3.5-5.7 ppmv (Chapter 4).

5.4.1. Temperature and relative humidity

Figures 5.6a, 5.7a, 5.8a, 5.9a, and 5.10a (5.6a-5.10a) summarize the vertical profiles of temperature over the South Africa, Mozambique, Botswana, Zambia, and Namibia sectors, respectively.

Over the South Africa sector, the average lapse rate from 0.5-3 km was ~8.5° km^{-1} (Figure 5.6a), which is intermediate between the dry adiabatic lapse rate of 9.8° km^{-1} and the saturated adiabatic lapse rate of typically 6-7° km^{-1}. Thus, the atmosphere was generally conditionally unstable below 3 km. Above 3.5 km, the average lapse rate over South Africa (~3°C km^{-1}) was less than both the dry and saturated adiabatic lapse

rate, resulting in a stable layer below which pollutants were trapped. Hence, during the period of our measurements, temperature profiles over the South Africa sector were consistent with the climatological average conditions of a mixed layer up to ~3 km, capped by a stable layer.

Over the Mozambique sector, the lapse rate was close to adiabatic near the surface (Figure 5.7a). Above this neutral layer, temperature inversions were present from ~0.75-1.25 km and ~1.75-2.25 km. Above the second inversion was another neutral layer from ~2.25-2.75 km. Above ~2.75 km, the lapse rate was ~3° km^{-1}, less than both the dry and saturated adiabatic lapse rates, resulting in another stable layer below which pollutants were trapped. This last stable layer is consistent with the climatological average conditions of a stable layer at ~3 km. However, the presence of two inversion layers below the 3 km stable layer resulted in increased stratification of the lower atmosphere over the Mozambique sector.

For the Botswana sector, the average lapse rates from ~1.25-2.25 km and from ~2.75-3.25 km were greater than the adiabatic lapse rate, resulting in unstable conditions over these altitudes (Figure 5.8a). Stable layers occurred from ~2.25-2.75 km and from ~3.25-4.25 km, where the lapse rates were only ~6° km^{-1}. Since ground level in this region is at ~1 km, and the first stable layer occurred around 2.5 km, the surface mixed layer was only ~1.5 km deep.

With the exception of two stable layers from ~2.25-2.75 km and from ~3.75-4.25 km, the lapse rate in the Zambia sector was greater than dry adiabatic, which resulted in an unstable atmosphere (Figure 5.9a). The observed stable layers at ~2.5 km and ~4 km were somewhat lower in altitude than the climatological stable layers, which are situated at ~3 km and ~5.5 km. However, the 0.5 km thickness of the observed layers is within the range of the climatological average thickness of ~0.5-1 km.

Over the Namibia sector, a persistent coastal stratus cloud deck was present below ~1 km. Above the cloud deck, distinct temperature inversions were present from ~0.75-1.25 km and ~1.75-2.25 km (Figure 5.10a). Above ~3.5 km, the lapse rate was close to dry adiabatic, resulting in a neutral atmosphere.

Figures 5.6b-5.10b summarize the vertical profiles of relative humidity over the South Africa, Mozambique, Botswana, Zambia, and Namibia sectors, respectively.

Magi and Hobbs [2003] found that over southern Africa during the dry season in 2000 the aerosol total light scattering coefficient increased by a factor of ~1.5-2 when relative humidity increased from 30% to 80%. Relative humidity over the South Africa sector during the period of our study ranged from ~20-60% and generally decreased with increasing altitude. Over the coastal Mozambique sector, RH was high (~60-100%) below 1 km and decreased to <20% above ~1.5 km. There was a local minimum at ~2.75 km, where the median RH was only 4%. Relative humidity over the Botswana sector was low (<30%) and fairly uniform with height. The RH over the Zambia sector ranged from ~15-45%, increasing with increasing height above ~1.5 km.

At the low relative humidities observed in the Botswana and Zambia sectors, the effect of RH on the aerosol light scattering coefficient is small [*Magi and Hobbs*, 2003]. The wide range of RH observed over the Namibia sector derives from differences in RH between the coastal and inland sampling locations. On average, RH in Namibia was highest below ~1 km (~60-75%) with a second peak at the ~1.75 km inversion layer and a third peak in the neutral layer above ~3.5 km. Outside of these layers, RH was low with median values of ~20%.

5.4.2 Sulfur Dioxide

Vertical profiles of SO_2 over the South Africa, Mozambique, Botswana, Zambia, and Namibia sectors are summarized in Figures 5.6c-5.10c, respectively.

The SO_2 mixing ratios over the South Africa sector (~2-25 ppbv; Figure 5.6c) are significantly higher than those typical for polluted continental air. The highest mixing ratios were found near the surface, with a second peak about 1 km below the stable layer. The high mixing ratios of SO_2 near the surface suggest strong local sources, such as biomass burning (Figure 5.3), electric power generation plants, and mining operations. For example, the coal-burning electricity generation plants in the Mpumalanga province in northeastern South Africa emit significant quantities of SO_2. A typical emission factor for coal combustion is given by [*USEPA*, 1998]:

Emitted SO_2 (in g per kg of fuel used) =

19(% of sulfur by weight in fuel).

Since the percentage of sulfur by weight in South African coal is ~1% [*EIA*, 2002], the SO_2 emission factor is ~19 g per kg of fuel burned. This is about a factor of 45 greater than the SO_2 emission factor for savanna burning in southern Africa (Chapter 3).

The SO_2 mixing ratios over the Mozambique sector ranged from ~0.5-6 ppbv (Figure 5.7c), comparable to values typical of polluted, continental air. Concentrations were lowest below ~1 km and around 2.75 km. Concentrations peaked at ~2 km; they were also high above ~3.25 km, where rapid removal by dry or wet deposition was not possible. The elevated SO_2 concentrations aloft suggest transport from the neighboring South Africa sector. The low SO_2 concentrations at ~2.75 km over the Mozambique sector were situated between two, polluted stable layers, suggesting the presence of what *Hobbs* [2002, 2003] called a "clean air slot", namely, a layer of clean, dry air a few hundred of meters thick sandwiched between layers of polluted air. Hobbs describes the presence of a clean air slot from ~2.5-3.4 km in the Mozambique sector at 0813-0815 UTC (Local time = UTC + 2 hr) on August 24, 2000. The average clean air slot seen in Figure 5.7c extends from ~2.5-3 km. On occasion, clean air slots were observed over South Africa and Namibia [*Hobbs*, 2002], but these are not apparent in the average profiles shown in Figures 5.6 and 5.10.

Sulfur dioxide concentrations for the Botswana sector range from ~0.5-3 ppbv (Figure 5.8c), comparable to values typical for polluted, continental air. Concentrations peak in the mixed layer below the 2.5 km stable layer. With a lifetime at the surface of ~1 day due to dry deposition, the high SO_2 surface mixing ratios suggest local sources. Since there were few savanna fires within the region (Figure 5.3), the SO_2 peak near the surface most likely resulted from industrial sources. Botswana is one of the world's leading diamond producers, and two of Botswana's three largest diamond mines, the Letlhakane mine (21.42°S, 25.59°E) and the Orapa mine (21.28°S, 25.37°E), are located in the Botswana sector of this study [*Mbendi*, 2002].

Mixing ratios of SO_2 over the Zambia sector generally ranged from ~1-6 ppbv (Figure 5.9c), comparable to typical polluted continental concentrations. The SO_2 concentrations peaked below the stable layers at ~2.5 and ~4 km, with the highest concentrations around 3.25 km. The location of the SO_2 peak above the first stable layer suggests transport from another location.

Over the Namibia sector, the average SO_2 concentrations below ~3 km were <1 ppbv (Figure 5.10c), with an average value of ~0.5 ppbv at ~1-1.5 km (close to the value of 0.2 ppbv typical for unpolluted air). Above ~3.5 km, where the atmosphere was neutral, the average SO_2 mixing ratios approached 1.5 ppbv, typical of polluted continental air. The high concentrations of SO_2 above ~3.5 km suggest transport from regions of heavy biomass burning in southern Angola (Figure 5.3). Removal of SO_2 by OH has a time scale of ~1 week, long enough to allow transport into the Namibia sector from Angola. Since the high SO_2 concentrations were located above both the cloud deck and the two stable layers, rapid SO_2 removal by dry or wet deposition was not possible.

5.4.3 Ozone

Vertical profiles of O_3 over the South Africa, Mozambique, Botswana, Zambia, and Namibia sectors are summarized in Figures 5.6d-5.10d, respectively.

The concentrations of O_3 for the South Africa sector (Figure 5.6d) ranged from ~35-80 ppbv, which is higher than those typical of remote locations (~20-40 ppbv) but lower than in aged smoke from savanna fires or polluted urban locations, which can exceed 100 ppbv. The O_3 concentrations in the South Africa sector generally increased with altitude, reaching peak values below the stable layer at ~3.5 km.

Over the Mozambique sector, concentrations of O_3 below 1 km were <40 ppbv (Fig 7d), which is typical of remote locations. Above 1 km, the O_3 concentrations ranged from ~30-80 ppbv, with an average of ~70 ppbv above 3 km. As with the South Africa sector, the O_3 concentrations in the Mozambique sector were intermediate between those typical of remote locations and polluted urban air or biomass burning

plumes. As in the case of the SO_2 profile, the O_3 minimum at ~2.75 km in the Mozambique sector suggests the presence of a clean air slot.

Ozone concentrations in the Botswana sector range from ~50-110 ppbv (Figure 5.8d), which is comparable to O_3 concentrations in polluted urban areas and in aged smoke from savanna fires. The O_3 mixing ratios peak within the two stable layers from ~2.25-2.75 km and from ~3.25-4.25 km. The high O_3 concentrations aloft in the Botswana sector suggest the transport of emissions from surrounding regions of biomass burning (Figure 5.3). In fact, back trajectories indicate that air parcels in both stable layers were near ground level in central Zambia only 30-40 h earlier [*HYSPLIT*, 2002].

Ozone concentrations in the Zambia sector generally ranged from ~60-110 ppbv (Figure 5.9d), again typical of polluted urban environments and biomass burning plumes. The concentrations of O_3 in the Zambia sector increased with increasing altitude up to ~2.5 km, above which they were fairly uniform and typically above ~80 ppbv. Ozone concentrations peaked to average values of ~95 and 110 ppbv around the stable layers at ~2.5 and ~4 km, respectively. Since there was considerable biomass burning in the Zambia sector, and it was surrounded by regions of intense biomass burning (Figure 5.3), the high O_3 concentrations aloft in this sector probably resulted from net ozone production in both local and aged transported biomass smoke.

Below ~1.5 km over the Namibia sector, the O_3 mixing ratios ranged from ~15-40 ppbv (Figure 5.10d), which is typical of remote locations. The O_3 concentrations increased with increasing height, stabilizing at ~80 ppbv in the neutral layer above ~3.5 km. This peak O_3 concentration over Namibia is comparable to that in polluted, urban air and in smoke plumes from savanna fires. As with SO_2, the source of O_3 aloft over Namibia was probably intense biomass burning to the north and northeast (Figure 5.3).

5.4.4 Condensation Nuclei

Figures 5.6e-5.10e summarize the vertical profiles of CN over the South Africa, Mozambique, Botswana, Zambia, and Namibia sectors, respectively.

Over the South Africa sector, there was a relatively uniform concentration of CN up to the stable layer at 3.5 km, followed by a sharp decrease above this level (Figure 5.6e). The CN concentrations ranged from ~200-20,000 cm^{-3}, with the variance in the concentrations increasing with increasing altitude. The range in CN concentrations over the South Africa sector overlaps with the lower end of the ~10,000-400,000 cm^{-3} range typically found at polluted, continental sites. The electric generation plants in northeast South Africa burn coal with a high (45%) ash content [*EIA*, 2002], which may contribute to the high CN concentrations in this sector.

Concentrations of CN in the Mozambique sector ranged from ~200-8,000 cm^{-3} (Figure 5.7e), compared to ~50-10,000 cm^{-3} typically found over remote, continental locations, and ~100-400 cm^{-3} typically found over marine locations. At 2.75 km, where minima were present in SO_2 and O_3 concentrations, the median CN concentration over the Mozambique sector was only ~700 cm^{-3}, the lowest at any altitude in the profile, and typical of clean continental air. The relatively low concentrations of particles at 2.75 km over Mozambique, combined with the low relative humidity and SO_2 and O_3 concentrations (Figure 5.7), confirm the presence of a clean air slot at this altitude.

Below ~4 km over the Botswana sector, the CN concentrations were fairly uniform with height, ranging from ~2,000-10,000 cm^{-3} (Figure 5.8e), which is similar to the range typically found over rural, continental locations. Concentrations were highest in the mixed layer below the ~2.5 km stable layer. Above ~4 km, the CN concentration in the Botswana sector decreased. The high CN concentrations lower down could have been due in part to emissions from operations associated with diamond mines.

The CN concentrations in the Zambia sector ranged from ~2,000-10,000 particles cm^{-3} (Figure 5.9e), which is similar to those found in rural, continental sites. The CN concentrations decreased with increasing height, with a local minimum near the ~2.5 km stable layer. The high CN concentrations seen throughout the vertical profile indicate a deep polluted layer to an altitude of at least 5 km. Light-scattering and light-absorption measurements obtained within the Zambia sector from 0746-0755 UTC on September 6, 2000, show a deep polluted layer extending above 5 km and nearly reaching the 500 hPa pressure level [*Magi et al.*, 2003; *Schmid et al.*, 2003].

The measured CN concentrations over the Namibia sector varied from ~200-6,000 cm^{-3} (Figure 5.10e), compared to ~50-10,000 cm^{-3} over remote, continental locations and ~100-400 cm^{-3} typically found over the oceans. The CN concentrations over Namibia peaked at the first stable layer at ~1.25 km, and again at ~3.75 km in the neutral layer.

5.4.5 Intermittent Samples of Carbon Monoxide

Measurements of CO through grab samples of ambient air away from visible plumes were obtained by two independent methods: gas chromatography on 38 canister samples (GC/C), and IR spectroscopy on 203 samples temporarily detained within the AFTIR cell (see section 2). From these data, vertical profiles of CO were constructed for the five sectors, as shown in Figures 5.6f-5.10f.

Of the five sectors, CO concentrations over the Zambia sector were the highest on average, with mixing ratios from ~250-650 ppbv (Figure 5.9f); this is substantially higher than those typical of remote regions (~50-150 ppbv). Since there are few industrial sources of CO in the Zambia sector, the high CO values suggest that biomass burning was the primary source. This is consistent with the fact that the concentrations of CO measured in the Zambia sector almost doubled as the river-of-smoke became increasingly developed. The Zambia sector also had high concentrations of O_3 and CN (Figure 5.9), which are also indicators of smoke from biomass fires.

The second highest average concentrations of CO were over the Botswana sector, where they ranged from ~150-550 ppbv below ~3 km but decreased at higher altitudes (Figure 5.8f). Again, these CO mixing ratios are substantially greater than those typical of remote regions (~50-150 ppbv). Since there were relatively few savanna fires in this sector (Figure 5.3), the high CO concentrations likely resulted from smoke from biomass burning being transported into the sector from surrounding regions of intense savanna burning. This is again consistent with an approximate doubling of the CO concentrations in Botswana as the river-of-smoke transported increasing amounts of smoke from the north. Mining operations within the Botswana sector could

also have contributed to the CO. On one occasion in this sector, we observed a stable layer "break up" during the day and release the CO trapped below it.

The CO concentrations in the South Africa sector ranged from ~50-250 ppbv (Figure 5.6f), significantly lower than those in the Zambia and Botswana sectors. This, together with the moderate O_3 concentrations in the South Africa sector (Figure 5.6d), suggest that this sector was not affected by biomass burning smoke as much as the Zambia and Botswana sectors. In addition, the CO mixing ratios in the South Africa sector never exceeded 150 ppb above 4 km, except for one sample obtained within a high cumulus cloud [*Yokelson et al.*, 2003].

The CO concentrations over the Mozambique sector ranged from ~130-210 ppbv (Figure 5.7f). These concentrations are comparable to those over the South Africa sector, which suggests that both sectors were similarly affected by emissions from biomass burning. In Mozambique, the near-surface CO concentrations were higher over land than just offshore. The highest CO concentration measured offshore was near the top of the first inversion at ~1.25 km, while the highest CO concentration measured over the land was near the top of the third inversion at ~2.75 km. This difference could be due to the fact that the measurements over land were obtained later in the day and over a warmer surface than over the ocean.

The CO concentrations below ~2 km over the Namibia sector ranged from ~50-150 ppbv (Figure 5.10f), which is typical for remote regions. The concentrations of SO_2, O_3, and CN were also low below ~2 km in the Namibia sector. However, above ~2 km and in the vicinity of 21°S, the CO concentrations in the Namibia sector ranged from ~275-375 ppbv, which are greater than the CO concentrations in the South Africa sector and approach those over the Zambia and Botswana sectors. We attribute the high concentrations of CO, as well as O_3 and SO_2 (Figure 5.10), aloft in the northern part of the Namibia sector to the transport of biomass smoke from the regions of heavy biomass burning to the north and northeast of Namibia (Figure 5.3). This is confirmed by HYSPLIT back trajectories (section 7). On 13 September 2000, polluted air aloft at 21°S over Namibia had been over southern Angola 5 days earlier, while the air at the same altitude sampled at 26°S over Namibia on 14 September 2000 had passed over the

Antarctic Ocean 5 days earlier. On both days, the lower, cleaner layer was transported from the remote south Atlantic Ocean.

5.5 Air Mass Trajectories

The *HYSPLIT* [2002] software was used to obtain five-day forward and five-day back air mass trajectories for each of the profiles listed in Table 5.1. The dates, times, and altitudes in Table 5.1 were used to initialize the trajectory runs, with the back trajectories beginning, and the forward trajectories ending, at the center of the altitude range for a given sample profile. Additional trajectories were initialized at the top of the altitude range for a given sample profile. Since these trajectories were generally similar to those initialized at the center of the altitude range for a sample profile, only the latter are discussed here.

A schematic illustrating the results of the back and forward trajectories obtained is shown in Figure 5.11a and 11b, respectively, and is discussed below.

5.5.1 South Africa sector

The back trajectories for the South Africa sector show that about three quarters of the air parcels came from the southeast over the Indian Ocean, corresponding to the southeasterly trade winds, and about a quarter of the trajectories came from the south, passing over areas of savanna burning (Figure 5.3). Since the majority of the back trajectories came from unpolluted areas, the source of the high SO_2 mixing ratios at low altitudes over the South Africa sector (Figure 5.6b) most likely derived from industries and biomass burning within that sector.

Forward trajectories for the South Africa sector show that about 80% of the air parcels exited the continent toward the Indian Ocean. The remaining 20% headed westward toward the Namibia sector. It should be noted that most of the profiles over the South Africa sector (Table 5.1) were obtained in August 2000, prior to the river-of-smoke episode. Therefore, the trajectories generally correspond to the average climatology of the region during the dry season, as depicted in Figure 5.4a.

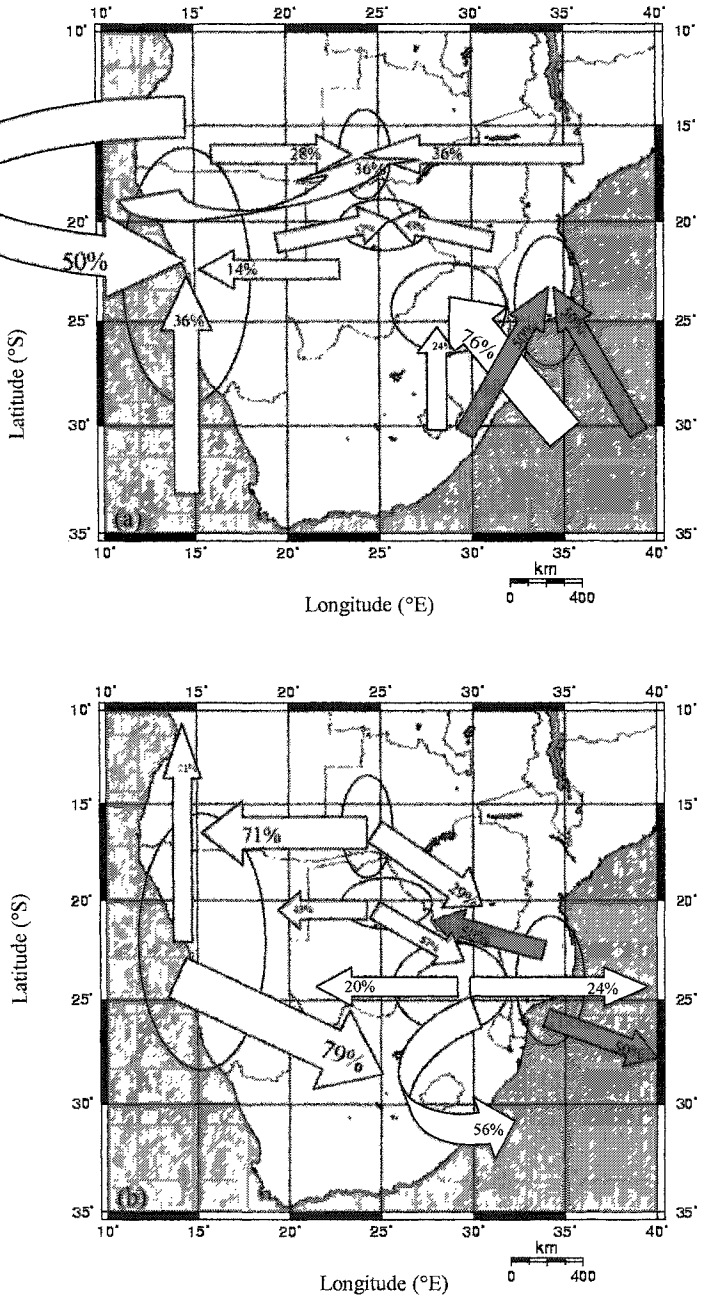

Figure 5.11. Schematic of 5 day (a) back trajectories, and (b) forward trajectories for the South Africa sector (white arrows), Mozambique sector (red arrows), Botswana sector (green arrows), Zambia sector (blue arrows), and Namibia sector (violet arrows). The ovals show the locations of the five sectors. The percentages refer to the fraction of the trajectories that followed the indicated path. One back and one forward trajectory was obtained for each of the vertical profiles listed in Table 5.1. The dates, times, and altitudes in Table 1 were used to initialize the trajectory runs, with the back trajectories beginning, and the forward trajectories ending, at the center of the altitude range for each profile.

5.5.2 Mozambique sector

Back trajectories for the Mozambique sector show that the air parcels that entered this sector were about evenly divided between southeasterly and southwesterly approaches. The southwesterly trajectories passed over abundant savanna fires in northeast South Africa, thereby transporting aged smoke, enhanced in secondary pollutants such as organic acids and O_3, to the Mozambique sector (Chapter 4). These products likely contributed to the high O_3 concentrations above ~3 km in the Mozambique sector (Figure 5.7c). The southeasterly trajectories, corresponding to the general trade wind circulation, passed over the Indian Ocean, bringing generally clean air to the Mozambique sector.

About half of the forward trajectories for the Mozambique sector show westward transport that follows the general subcontinental gyre (Figure 5.4a), which transported aged smoke from Mozambique to Botswana. The remaining trajectories show transport eastward, exiting the continent over the coast of the Indian Ocean.

5.5.3 Botswana sector

Back trajectories for the Botswana sector show air parcels nearly evenly divided between easterly and westerly approaches. Both approaches transported smoke from surrounding areas of intense biomass burning (Figure 5.3). The profiles for the Botswana sector (Table 5.1) were obtained during the transition into the river-of-smoke episode of early September 2000. Therefore, the trajectories for this sector reflect a combination of the typical dry season climatology depicted in Figure 5.4a and the flow that gave rise to the river-of-smoke perturbation shown in Figure 5.4b.

Forward trajectories for the Botswana sector are nearly evenly divided between eastward trajectories heading toward the Indian Ocean and westward trajectories heading for the Atlantic Ocean.

5.5.4 Zambia sector

Back trajectories for the Zambia sector show air parcels nearly evenly divided between southwesterly, westerly and easterly approaches. In view of the abundance of

savanna fires to the south, west and east of the Zambia sector (Figure 5.3), these back trajectories suggest that the impact of local burning in the Zambia sector was augmented by smoke from biomass burning in surrounding regions.

Forward trajectories for this sector show the majority of the parcels following the general trade wind circulation, exiting westward toward the Atlantic Ocean where they contribute to the O_3 anomaly over the southern Atlantic. The remainder of the parcels travel southeastward into South Africa.

Many of the profiles for the Zambia sector (Table 5.1) were obtained during the river-of-smoke episode in early September 2000. Therefore, the trajectories for this sector are a combination of those typical of the dry season climatology depicted in Figure 5.4a and the river-of-smoke perturbation shown in Figure 5.4b. The deep polluted layer over this sector (Figure 5.9) can be attributed to the river-of-smoke perturbation.

5.5.5 Namibia sector

Back trajectories over the Namibia sector show about half the parcels originating over the heavy savanna burning region of Angola, exiting the continent over the Atlantic coast, and then returning to the continent over Namibia. About a third of the back trajectories passed over clean areas to the south of Namibia. The O_3 in the upper polluted layer over the Namibia sector is due to photochemistry in aging biomass burning emissions. Ozone production can occur in biomass burning plumes within ~10 minutes (Chapter 4). Production of O_3 in biomass plumes has been observed to continue for at least 10 days [*Andreae et al.*, 1994]

Forward trajectories for the Namibia sector show most of the air parcels heading southeastward, eventually passing over the Indian Ocean. Since our measurements over Namibia were obtained during September, a month of frequent penetrations by frontal perturbations and unstable air masses, the trajectories resemble a combination of the typical dry season climatology depicted in Figure 5.4a and the river-of-smoke perturbation shown in Figure 5.4b.

5.6 Comparisons of Vertical Profiles with Other Studies

The SAFARI-92 project, which took place in September and October 1992, investigated pyrogenic emissions in southern Africa. Using measurements from ozonesonde launches from Ascension Island, Brazzaville, Okakuejo, and Irene, *Diab et al.* [1996] characterized the vertical distribution of ozone in southern Africa. Irene (25.87°S, 28.22°E) is located within the South Africa sector of the present study, while Okaukuejo (19.18°S,15.92°E) is within the Namibia sector. *Diab et al.* reported O_3 (1 σ) concentration ranges of ~25-55 ppbv at an altitude of 2 km and ~50-65 ppbv at an altitude of 4 km over Irene. Our corresponding O_3 (1 σ) concentrations for the South Africa sector range from ~37-65 ppbv just below 2 km and ~54-74 ppbv just below 4 km. In both the Irene profile and our South Africa sector profile, the O_3 concentrations increase, on average, with increasing altitude. Over Okakuejo, *Diab et al.* report O_3 (1 σ) concentration ranges of ~40-70 ppbv at 2 km and ~45-75 ppbv at 4 km. Our corresponding O_3 (1 σ) concentrations for the Namibia sector are ~25-59 ppbv just below 2 km, and 68-86 ppbv just below 4 km. While both studies show increasing O_3 with increasing altitude in Namibia, our measurements at 21°S show a more pronounced increase in O_3 with increasing altitude.

The TRACE A experiment, which took place in September and October 1992, investigated the effects on the tropical South Atlantic troposphere of biomass burning emissions in the dry season from South America and southern Africa. *Blake et al.* [1996] describe vertical profiles of CO over northeastern Zambia (9.8-11.4°S, 29.0-30.6°W) and western Zimbabwe (18.2-19.0°S, 26.2-27.4°W), near the Zambia and Botswana sectors of the present study. Below 5 km, Blake et al. report CO concentrations ranging from ~100 to 700 ppbv, with the majority between ~200-500 ppbv. Above 5 km, the CO concentrations decreased to a uniform value of ~100 ppbv. In the present study, CO concentrations below 5 km over the Botswana and Zambia sectors range from ~150-650 ppbv (Figures 5.8f-5.9f).

Thompson et al. [2003] describe O_3 profiles obtained from soundings launched from Lusaka, Zambia (15.5 °S, 28.0 °E) and Irene, South Africa (25.87°S, 28.22°E) in

August and September 2000, the same time period as the present study. The Lusaka soundings show O_3 concentrations of ~50-100 ppbv below 2.5 km, and >100 ppbv from 2.5-5 km. Our study shows O_3 concentrations in the Zambia sector, located to the west of Lusaka, of ~60-90 ppbv below 2.5 km and ~70-110 ppbv from 2.5-5 km (Figure 5.9d). A sounding over Irene, located within the South Africa sector, shows O_3 concentrations of ~50-70 ppbv below 5 km. Our study shows O_3 concentrations in the South Africa sector of ~30-80 ppbv below 5 km (Figure 5.6d).

Outside of Africa, significant biomass burning in the tropics occurs in Brazil and Indonesia. For the SCAR-B campaign in August-September 1995, *Reid et al.* [1998] reported average CO and O_3 concentrations of ~500-800 ppbv and ~60-100 ppbv, respectively, below 4 km in regional hazes dominated by emissions from the burning of cerrado and rain-forested regions in Brazil. Average CO and O_3 concentrations below 4 km in the present study range from ~150-450 ppbv and ~50-90 ppbv, respectively. During the PACE-5 campaign in October of 1997, *Sawa et al.* [1999] measured CO concentrations of 3 to 9 ppm below 3 km in thick smoke haze over Kalimantan, Indonesia. These CO concentrations are an order of magnitude greater than those measured by us over southern Africa. The high CO concentrations over Indonesia resulted from extensive forest fires during a long drought associated with a strong El Nino event.

5.7. Horizontal Distributions

In addition to characterizing the vertical distribution of selected pollutants, the horizontal distributions of a larger set of pollutants were measured from the UW Convair-580 aircraft over southern Africa during the dry biomass burning season in SAFARI 2000. Table 5.2 lists the measured average concentrations of twenty gaseous and particulate species below an altitude of 5 km during the period August 14 to September 16, 2000 in the five sectors defined in section 3. The species include long-lived gases (such as CO_2, CO, and CH_4), shorter-lived gases (such as SO_2, O_3, and various non-methane hydrocarbons), halocarbons, carbonaceous and inorganic

Table 5.2. Average background concentrations below 5 km msl of selected gaseous and particulate species over five sectors in southern Africa during the period August 14 to September 16, 2000. n is the number of samples.

			South Africa Sector (29.15°E, 23.99°S)		Mozambique Sector (32.79°E, 26.10°S)		Botswana Sector (26.29°E, 20.68°S)		Zambia Sector (24.00°E, 15.98°S)		Namibia Sector (14.20°E, 19.89°S)		All Sectors
Species*	**Units**	**Measurement Technique†**	**Average**	**n**	**Average**	**n**	**Average**	**n**	**Average**	**n**	**Average**	**n**	**Average**
CO_2	ppmv	GC/C, AFTIR	387±12	102	384±7	7	388±7	22	392±6	36	381±6	34	386±8
CO	ppbv	GC/C, AFTIR	157±47	102	165±43	15	369±120	22	453±101	36	162±96	34	261±81
CH_4	ppbv	GC/C, AFTIR	1736±41	72	1710±55	7	1753±12	22	1758±28	36	1718±32	34	1735±21
Ethane	pptv	GC/C	857±442	18	428	1	1268±442	5	1532±642	2	715±397	5	960±440
Ethene	pptv	GC/C	138±107	18	137	1	320±226	5	271±112	2	35±27	5	180±115
Propane	pptv	GC/C	123±72	18	69	1	216±34	5	188±73	2	67±32	5	133±68
Alkenes ($\geq C_3$)	pptv	GC/C	35±21	18	19	1	33±12	5	34±15	2	12±5	5	27±10
Alkanes ($\geq C_4$)	pptv	GC/C	87±39	18	65	1	87±46	5	60±20	2	24±11	5	65±26
Isoprene	pptv	GC/C	8±9	18	8	1	19±15	5	12±7	2	4±2	5	10±6
SO_2	ppbv	Teco 43S	5.1±2.4	25	2.9±2	4	1.7±0.3	7	2.2±0.7	14	0.8±0.3	14	2.5±1.6
O_3	ppbv	Teco 49C	54±11	25	51±14	4	79±12	7	88±12	14	50±16	14	64±13

(Cont.)

Table 5.2 continued

			South Africa Sector (29.15°E, 23.99°S)		Mozambique Sector (32.79°E, 26.10°S)		Botswana Sector (26.29°E, 20.68°S)		Zambia Sector (24.00°E, 15.98°S)		Namibia Sector (14.20°E, 19.89°S)		All Sectors
Species*	**Units**	**Measurement Technique†**	**Average**	**n**	**Average**	**n**	**Average**	**n**	**Average**	**n**	**Average**	**n**	**Average**
CH_3Br	pptv	GC/C	9±1	18	8	1	10±1	5	9±1	2	9±1	5	9±1
CH_3Cl	pptv	GC/C	634±72	18	575	1	688±60	5	690±48	2	580±60	5	633±56
CN	cm^{-3}	TSI 3025A	$(6.4\pm5.2)\times10^3$	25	$(3.4\pm2.5)\times10^3$	4	$(3.5\pm0.8)\times10^3$	7	$(5.9\pm1.5)\times10^3$	14	$(1.0\pm0.6)\times10^3$	14	$(4.5\pm2.9)\times10^3$
Total particle mass	$\mu g/m^3$	Gravimetric/ Filter	29.6±14.6	16	31.2±23.5	2	20.1±15.0	12	22.3±4.2	4	26.8	1	26.0±4.7
Organic acids	$\mu g/m^3$	IC/Filter	0.6±0.4	16	1.4±1.2	2	1.0±1.0	12	1.0±0.7	4	1.7	1	1.1±0.4
Sulfate	$\mu g/m^3$	IC/Filter	8.3±8.1	16	8.5±5.0	2	1.9±1.5	12	0.9±0.1	4	2.8	1	4.5±3.6
Nitrate	$\mu g/m^3$	IC/Filter	0.3±0.2	16	0.8±0.3	2	1.0±1.0	12	0.9±0.1	4	0.8	1	0.8±0.3
Potassium	$\mu g/m^3$	PAES/Filter	0.3±0.2	16	0.5±0.5	2	0.4±0.4	12	0.2±0.1	4	0.5	1	0.4±0.1
Black carbon (BC)	$\mu g/m^3$	ATN/Filter	1.1±0.4	17	1.0±0.5	2	2.6±1.4	11	5.5±1.4	4	1.0	1	2.3±1.9
Total carbon (TC)	$\mu g/m^3$	EGA/Filter	4.8±1.7	6	5.9±5.1	2	13.2±6.8	11	14.3	1	4.4	1	8.5±4.8

(Cont.)

Table 5.2 continued

			South Africa Sector (29.15°E, 23.99°S)		Mozambique Sector (32.79°E, 26.10°S)		Botswana Sector (26.29°E, 20.68°S)		Zambia Sector (24.00°E, 15.98°S)		Namibia Sector (14.20°E, 19.89°S)		All Sectors
Species*	**Units**	**Measurement Technique†**	**Average**	**n**	**Average**	**n**	**Average**	**n**	**Average**	**n**	**Average**	**n**	**Average**
BC/TC	—	—	0.23	—	0.17	—	0.20	—	0.38	—	0.23	—	0.27
Potassium/BC	—	—	0.27	—	0.50	—	0.15	—	0.04	—	0.50	—	0.17

* Beginning with "total particle mass," the concentrations refer to particles with diameter <3 μm.

† GC/C=gas chromatography via canisters, ATN/Filter = optical attenuation via filters, EGA/Filter = evolved gas analysis via filters, IC = ion chromatography via filters, PAES/Filter = plasma-emission spectrometry via filters.

particulate species, and CN. These species play important roles in global atmospheric chemistry and the earth's radiative balance. The results are summarized below.

5.7.1 Carbon Dioxide, Methane, and Carbon Monoxide

Carbon dioxide, CH_4, and CO are long-lived emission products of biomass burning and other types of combustion. Globally averaged background concentrations of CO_2 and CH_4 in 2000 were ~367 ppmv and ~1.750 ppmv, respectively [*IPCC*, 2001]. The typical background concentration of CO in unpolluted areas is ~40-200 ppbv [*Seinfeld and Pandis*, 1998]. Of the five sectors in this study, the Zambia and Botswana sectors had the highest mixing ratios of these gases (~390 ppmv of CO_2, ~1.75-1.76 ppmv of CH_4, and ~370-450 ppbv of CO) (Table 5.2). There are relatively few industries in the Zambia and Botswana sectors, but there is abundant biomass burning in Zambia. Both sectors are susceptible to smoke transported from intense biomass burning in Angola, Zimbabwe, Mozambique, and South Africa (Figure 5.3). Since CO and CH_4 are the dominant sinks for the OH radical [*Hobbs*, 2000], high concentrations of CO and CH_4 will influence the oxidative capacity of the troposphere in the Zambia and Botswana sectors.

5.7.2 Non-methane Hydrocarbons

Non-methane hydrocarbons are important emission products of biomass burning. Since the lifetime of alkanes in the tropics is on the order of days but the lifetime of alkenes is on the order of hours [*Mauzerall et al.*, 1998], the presence of high concentrations of alkenes suggests local sources, whereas, high concentrations of alkanes could also result from longer range transport.

The Botswana and Zambia sectors had significantly higher concentrations of ethane, ethene, and propane than the other five sectors. *Reid et al.* [1998] reported high alkane concentrations in regional hazes in Brazil (e.g., ethane from 7-11 ppbv). The high alkane levels in Brazil, Botswana, and Zambia could be due to a larger proportion of woody fuels [*Bertschi et al.*, 2003b].

Non-methane hydrocarbons play an important role in atmospheric photochemistry. Oxidation of organic compounds (including hydrocarbons) in the presence of nitrogen oxides leads to formation of O_3. For example, in NO_x-rich, young biomass burning plumes, oxidation of non-methane organic compounds (NMOC, of which ~30% are hydrocarbons) leads to rapid formation of O_3. In the plume from the Timbavati fire, discussed in chapter 4, O_3 mixing ratios exceeded 100 ppbv after only ~30 minutes of plume aging. However, since the lifetime of NO_x is short (~1 day) [*Hobbs*, 2000], NO_x concentrations in the background troposphere over southern Africa are low and dominated by the recycling of NO_x from its oxidation products [*Jacob et al.*, 1996]. In a low NO_x environment, oxidation of CO and NMOC will diminish the concentration of the OH radical. Alkanes are primarily oxidized by the OH radical, whereas, alkenes can also be oxidized by O_3.

Isoprene, which is a by-product of photosynthesis, is the dominant compound emitted by vegetation. With a lifetime of ~1 h, isoprene is quickly oxidized by OH [*Seinfeld and Pandis*, 1998]. In the presence of NO_x, isoprene oxidation results in rapid O_3 formation. However, in a low NO_x environment, isoprene serves as an overall sink for OH. Over the five sectors of the present study, isoprene concentrations were fairly low, ranging from <3 to ~35 pptv (Table 5.2). Isoprene concentrations were highest in the Botswana and Zambia sectors, and lowest in the extremely arid Namibia sector.

5.7.3 Sulfur Dioxide and Ozone

Except for the Namibia sector, average SO_2 concentrations in this study (~1.5-5 ppbv; Table 5.2) were equal to or exceeded the value of ~1.5 ppbv, which is typical of polluted, continental air. The highest average SO_2 concentration was over the South Africa sector (5.1±2.4 ppbv), which was likely due to those coal-burning, electric generation plants and mining operations in northeast South Africa that do not employ pollution controls, and the numerous savanna fires in this sector (Figure 5.3). The average SO_2 concentration in the Namibia sector was 0.8±0.3 ppbv (Table 5.2), which is still considerably greater than that typical of clean continental air (~0.2 ppbv).

Ozone concentrations in all five sectors of this study (~40-100 ppbv; Table 5.2) exceeded the range of ~20-40 ppbv typical of remote locations. This is attributable to extensive biomass burning throughout southern Africa during the dry season (Figure 5.3) and the photochemical transformation/transport of these emissions throughout the region. Ozone concentrations were highest in the Zambia and Botswana sectors (88±12 and 79±12 ppbv, respectively); these values are comparable to those typical of polluted, urban air. We attribute the high concentrations in the Zambia and Botswana sectors to biomass burning in Zambia, and the transport of smoke to these sectors from Angola, Zimbabwe, South Africa, and Mozambique.

5.7.4 Methyl Halides

Halogens in the stratosphere are efficient at catalyzing the rapid destruction of stratospheric ozone; sufficient quantities of methyl halides are emitted by biomass burning to play a role in stratospheric ozone loss [*Mano and Andreae*, 1994]. Due to their long lifetimes (~1 year), methyl halides are fairly well mixed in the troposphere. Average concentrations of methyl chloride for the five sectors in this study ranged from ~575 pptv to 690 pptv (Table 5.2); typical continental background concentrations are ~600 pptv [*Seinfeld and Pandis*, 1998]. The average concentrations of methyl bromide ranged from ~8 pptv to 10 pptv over the five sectors (Table 5.2), compared to typical background continental concentrations in the southern hemisphere of ~7-8 pptv [*Wingenter et al.*, 1998].

5.7.5 Total Particle Mass

Total particle mass is often dominated by particles with diameters >1 μm [*Hobbs*, 2000]. These large particles (e.g., dust, pollen, sea-salt) are often generated by natural, mechanical processes. Typical background concentrations of total particle mass are ~5 μg m^{-3} in remote locations, ~15 μg m^{-3} in rural continental air, and ~32 μg m^{-3} in urban air [*Seinfeld and Pandis*, 1998]. The average total particle mass over the five sectors in this study ranged from ~20-30 μg m^{-3}, which approaches that in polluted, urban air.

5.7.6 Condensation Nuclei

Condensation nucleus concentrations are dominated by particles with diameters <1 μm. Since most of the particles generated by combustion processes have diameters <1 μm, sub-micron particles from combustion should affect the distribution of CN concentrations over southern Africa. In this study, the concentration of CN was, on average, greatest over the South Africa sector (6400±5200 cm^{-3}; Table 5.2) where it overlapped with the range typical of polluted, continental locations (10,000 cm^{-3} to 400,000 cm^{-3}). Again, we attribute this to the extensive biomass burning (Figure 5.3) and mining and electric generation operations in the South Africa sector (section 5). The sector with the lowest average concentration of CN was Namibia (1000±600 cm^{-3}).

5.7.7 Carbonaceous Particles

Carbonaceous particles are composed of black (elemental) carbon and organic carbon. They derive from primary pyrogenic and biogenic emissions and secondary low vapor pressure products of oxidation of organic gases.

Black carbon is produced only by combustion processes; it is the primary light-absorbing aerosol species in the atmosphere. Typical background concentrations of black carbon are ~0.2-2.0 μg m^{-3} in rural and remote continental air, and 1.5-20 μg m^{-3} in urban air [*Seinfeld and Pandis*, 1998]. In this study, black carbon concentrations were highest over the Zambia and Botswana sectors (5.5±1.4 and 2.6±1.4 μg m^{-3}, respectively; Table 5.2), comparable to values in urban air. The concentrations of black carbon in the other three sectors (~0.5-1.5 μg m^{-3}) were within the range typical of rural and remote continental air.

Organic carbon comprises a large and varied class of compounds, including n-alkanes, organic acids, and aromatic species. Unlike black carbon, organic particles tend to scatter solar radiation rather than absorb it. Typical concentrations of organic carbon range from ~4.2-5.6 μg m^{-3} in rural, continental areas to ~6-32 μg m^{-3} in polluted, continental areas [*Seinfeld and Pandis*, 1998]. Concentrations of organic carbon were obtained in the present study by subtracting the measured concentrations of

black carbon from those of total carbon (Table 5.2). The concentrations of organic carbon in the Zambia and Botswana sectors (~8.8 and 10.6 μg m^{-3}, respectively) are comparable to the concentrations present in polluted continental locations. The concentrations of organic carbon in the South Africa, Mozambique, and Namibia sectors (~3-5 μg m^{-3}) lie within the range typical of rural sites.

Samples obtained above and downwind of the Timbavati fire showed that particulate organic acids are generated both directly from savanna burning and by the oxidation of NMOC released from savanna fires and subsequent gas-to-particle conversion [*Gao et al.*, 2003]. Concentrations of organic acids were <2 μg m^{-3} and fairly uniform throughout the five sectors (Table 5.2).

The average concentration of carbonaceous particles (black carbon plus organic carbon) was highest in the Botswana and Zambia sectors (~13-14 μg m^{-3}; Table 5.2), likely due to the emissions from biomass burning. The mass fraction of carbonaceous particles to total particle mass was also highest in the Botswana and Zambia sectors (~65%).

The mass ratio of black carbon to total carbonaceous particles typically ranges from ~0.15-0.20 in rural areas to ~0.2-0.6 in urban areas [*Seinfeld and Pandis*, 1998]. In this study, the ratios of black carbon mass to total carbonaceous particle mass ranged from ~0.18 to 0.40 (Table 5.2), which is comparable to the range in urban environments. Again, this indicates the strong influence of biomass burning on particle properties over southern Africa.

The origin of the high carbonaceous aerosol content over the Zambia sector requires further discussion. The ratios of black carbon to total carbon (BC/TC), black carbon to organic carbon (BC/OC), and potassium to black carbon (K/BC) are ~0.38, 0.63, and 0.04, respectively, for this sector. These ratios differ from those obtained from savanna burning source characterization studies (~0.13, 0.14, 0.71, respectively; *Andreae and Merlet*, 2001), but they are similar to those found in urban environments dominated by fossil fuel burning (BC/TC of ~0.2-0.6, BC/OC of ~0.25-1.5 [*Seinfeld and Pandis*, 1998], and K/BC of ~0.025-0.09 [*Andreae*, 1983]). Although there are few industrial sources of pollution within the Zambia sector of this study, the heavy mining

and development activities of the "copper belt" north of the Zambia sector may contribute carbonaceous aerosol to this sector.

5.7.8 Inorganic Particles

Like organic particles, inorganic particles tend to scatter solar radiation rather than absorb it. Sulfates and nitrates also affect the acidity of the troposphere. Background concentrations of sulfate typically range from ~0.5-2 $\mu g\ m^{-3}$ in unpolluted continental air, >10 $\mu g\ m^{-3}$ in urban air, and ~3 $\mu g\ m^{-3}$ in marine air [*Warneck*, 2000]. In this study, sulfate concentrations were highest over the South Africa and Mozambique sectors (8.27±8.06 and 8.48±5.01, respectively; Table 5.2), where they approached those typical of polluted urban air. The many coal-burning electric generation plants and mining operations in northeast South Africa, and extensive biomass burning in the South Africa and Mozambique sectors, were no doubt responsible for the high sulfate concentrations. Sulfate concentrations in the Botswana, Zambia, and Namibia sectors were <3 $\mu g\ m^{-3}$.

Nitrate is a common component of tropospheric aerosols. It is produced by the oxidation of NO_2 by OH or O_3 to eventually form HNO_3. Typical background concentrations of nitrate range from ~0.4-1.3 $\mu g\ m^{-3}$ in unpolluted continental air, 3-10 $\mu g\ m^{-3}$ in urban air, and <0.1 $\mu g\ m^{-3}$ over oceans [*Warneck*, 2000]. In this study, nitrate concentrations were low and fairly uniform over the five sectors (<2 $\mu g\ m^{-3}$; Table 5.2), which places them in the range of unpolluted continental air. However, the air was, in fact, polluted, but biomass combustion occurs below the threshold for thermal NO_x formation and thus it is often a "low-nitrate" pollution source.

Potassium has been used as an indicator of smoke from savanna burning [*Cachier et al.*, 1995]. Background concentrations of total particulate potassium range from ~0.03-0.12 $\mu g\ m^{-3}$ in unpolluted continental air, ~0.4-0.9 $\mu g\ m^{-3}$ in urban air, and ~0.1 $\mu g\ m^{-3}$ in marine air [*Warneck*, 2000]. Due to extensive biomass burning in southern Africa during the dry season (Figure 5.3), the average particulate potassium

concentrations in this study (~0.3-0.5 μg m^{-3}; Table 5.2) were comparable to the range typical of polluted urban air.

5.7.9 Average Pollutant Concentrations Over All Sectors

The average concentration of a pollutant over all five sectors in this study provides an estimate of the concentration of that pollutant below an altitude of ~5 km in southern Africa from August 14 to September 16 during the dry biomass burning season of 2000. These average concentrations are listed in the last column of Table 5.2. With the exception of the South Africa and Botswana sectors, the measurements in this study were obtained in locations that have few local sources of industrial pollution. Nevertheless, the average concentrations over all five sectors of eight of the species listed in Table 5.2 (CO_2, CO, SO_2, O_3, black particulate carbon, organic particulate carbon, total particle mass, and potassium particles) are greater than those that are typical of remote or rural locations.

The average concentrations over all five sectors of CO_2 and CO (386±8 ppmv and 261±81 ppbv, respectively) exceed their corresponding typical background concentrations in remote or rural regions (~367 ppmv and ~50-150 ppbv, respectively). Since these long-lived trace gases are emitted during combustion, they indicate the impacts of biomass burning on air quality in southern Africa. The average SO_2 concentration over all five sectors (2.5±1.6 ppbv) is comparable to the concentration of SO_2 that is typical of polluted urban air (~1.5 ppbv). This is attributable to emissions from mining, electric power generation, and biomass burning. The average O_3 concentration over all five sectors (64±13 ppbv) exceeds that which is typical of remote locations (~20-40 ppbv). Since O_3 is an oxidant and a precursor to the OH radical, the elevated O_3 concentrations over southern Africa during the biomass burning season will tend to enhance the oxidative capacity of the troposphere in the region.

The average concentrations of black carbon and organic carbon in all five sectors were 2.3±1.9 μg m^{-3} and 6.2±5.2 μg m^{-3}, respectively; the latter value was derived from subtracting black carbon from total carbon in Table 5.2. These average concentrations fall within the range of concentrations of black carbon and organic

carbon that are typical of polluted urban air (~1.5-20 μg m^{-3} and 6-32 μg m^{-3}, respectively). The average ratio of black carbon to total carbonaceous particles over all five sectors (~0.27) is in the range typical of urban areas (~0.2-0.6). The average concentration of total particle mass over all five sectors (26.0±4.7 μg m^{-3}) exceeds the ~15 μg m^{-3} typical of rural locations; indeed, it approaches the concentrations for total particle mass typical of urban air (~32 μg m^{-3}). The high particle mass in the troposphere over southern Africa in the dry season is due primarily to smoke from biomass burning. The average over all five sectors of particulate potassium (0.40±0.12 μg m^{-3}), the sources of which include biomass burning, is comparable to concentrations found in polluted continental air (~0.4-0.9 μg m^{-3}).

CHAPTER 6
TRANSPORT OF BIOMASS BURNING EMISSIONS FROM SOUTHERN AFRICA

6.1. Model Evaluation

In this chapter the transport of biomass burning emissions from southern Africa to the neighboring Atlantic and Indian Oceans during the dry season (May–October) of 2000 is characterized using the GEOS-CHEM three-dimensional model of global tropospheric chemistry. The GEOS-CHEM model was evaluated with ground, ozonesonde, and aircraft measurements obtained in 2000 in and around southern Africa (Figure 6.1a). Measurements of CO, a primary combustion tracer, and O_3, a secondary photochemical product of combustion and natural emissions, are used to assess the model's ability to characterize emissions, photochemistry, and transport in the region. Many of the measurements were obtained in August and September of 2000, during the SAFARI 2000 field campaign. Fire count data for the region in September of 2000 (Figure 6.1b) is provided by the Along Track Scanning Radiometer (ATSR) aboard the European Remote Sensing-2 satellite. Fire counts are determined at night-time (~10 pm local time) from ATSR measurements in the 3.7 μm thermal channel [*Arino and Rosaz*, 1999]. In September of 2000, fires were particularly prevalent in the vicinity of Zambia and in northeast South Africa.

Ground measurements were obtained at four sites (Figure 6.1a): Ascension Island (7.9°S,14.4°W), Crozet (46.5°S,51.9°E), and Seychelles (4.7°S,55.5°E) [*Novelli et al.*, 1998], and Cape Point, South Africa (34.4°S,18.5°E) [*Labuschagne et al.*, 2003] through the World Data Center for Greenhouse Gases (WDCGG, http://gaw.kishou.go.jp/wdcgg.html). Monthly average surface CO concentrations at the four sites (Figures 2a–d), and monthly average O_3 concentrations at Cape Point (Figure 6.2e) for 2000, were compared to monthly average modeled surface concentrations. On average, the model overpredicted CO at the ground sites by 20%, but it captured close to half the variability (r^2=0.43) of the measurements. Agreement

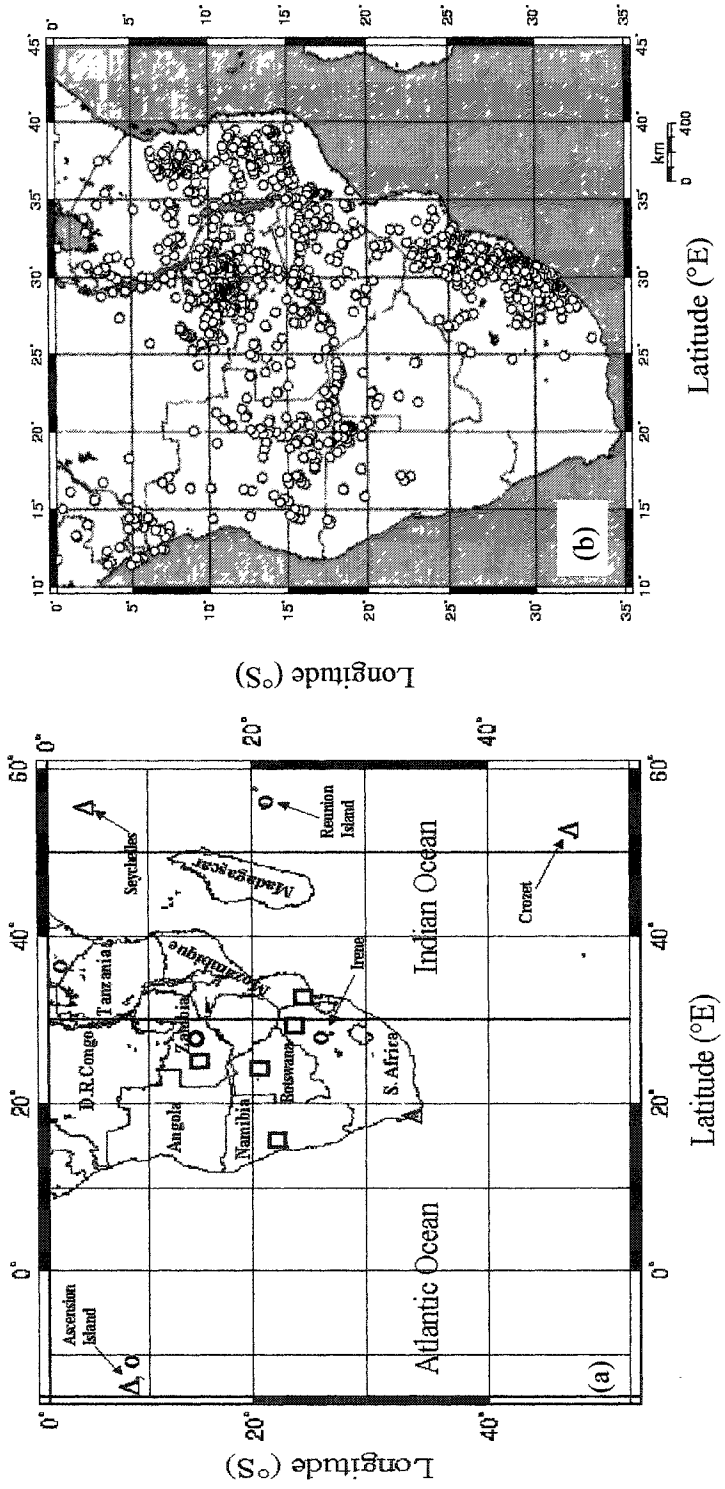

Figure 6.1. (a) Locations of WDCGG surface CO and O_3 measurements (Δ), SHADOZ ozonesonde data (o), and UW CV-580 airborne CO and O_3 measurements (□), used to evaluate the GEOS-CHEM model in the vicinity of southern Africa in 2000. (b) ATSR fire locations for September 2000.

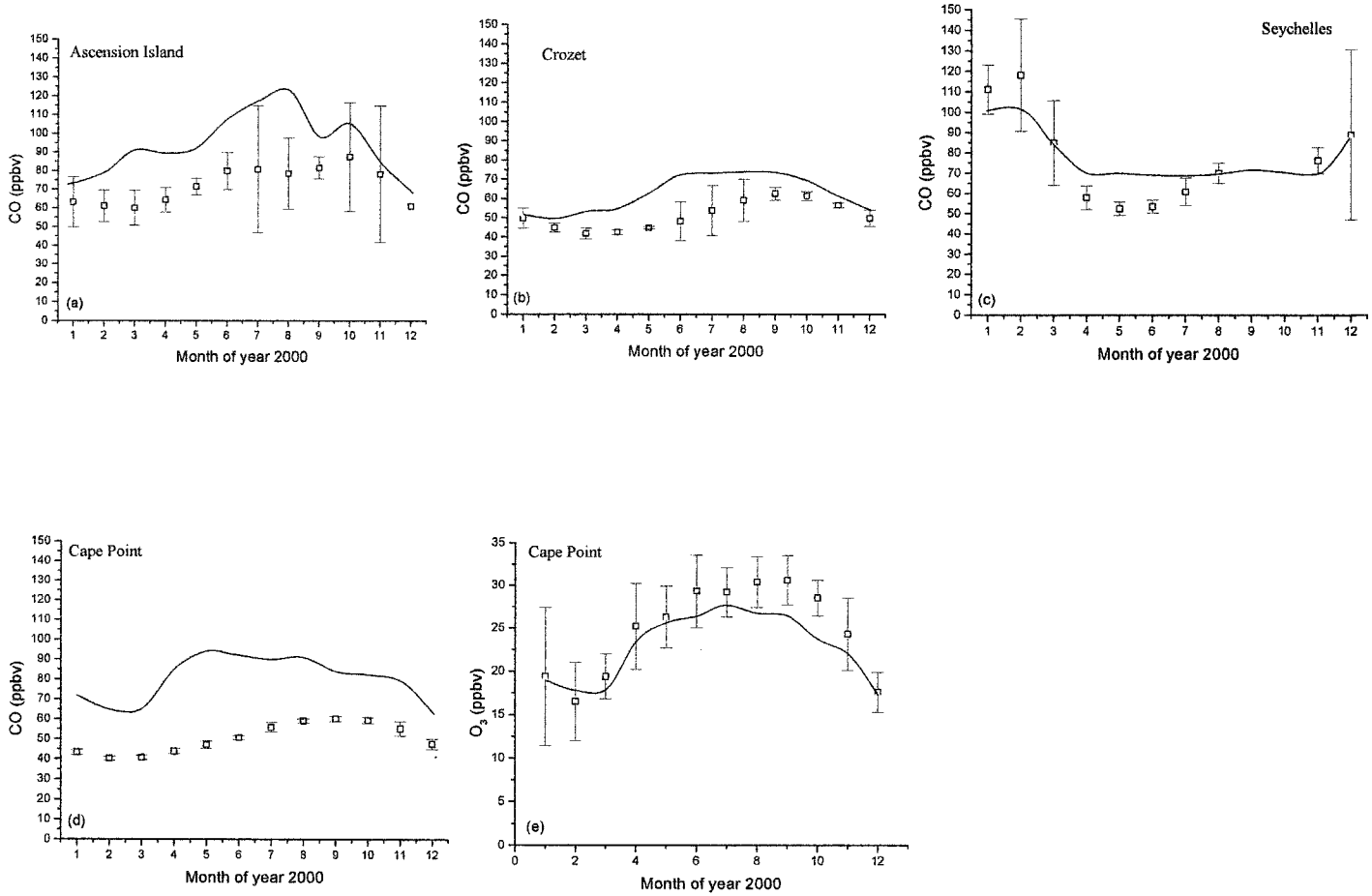

Figure 6.2. Monthly average concentrations of CO in 2000 at (a) Ascension Island (7.9°S, 14.4°W), (b) Crozet (46.5°S, 51.9°E), (c) Seychelles (4.7°S, 55.5°E), and (d) Cape Point (34.4°S, 18.5°E), and monthly average concentrations of O_3 in 2000 at (e) Cape Point. Squares and lines indicate measured and modeled concentrations, respectively. Error bars indicate the standard deviations of the measured monthly average concentrations.

between O_3 surface observations at Cape Point and model is good (r^2=0.93), with the model underpredicting observed O_3 concentrations by only ~7%.

Vertical profiles of O_3 were obtained at five ozonesonde sites maintained by the Southern Hemisphere Additional Ozonesondes (SHADOZ) project [*Thompson et al.*, 2002, 2003a] (Figure 6.1a): Irene, South Africa (25.9°S, 28.2°E), Ascension Island (7.9°S, 14.4°W), Nairobi, Kenya (1.3°S, 36.8°E), Reunion Island (21.1°S, 55.5°E), and Lusaka, Zambia (15.42°S, 28.32°E). Profiles of O_3 from the surface to 10 km above mean sea level (msl) obtained at the first four sites in August 2000 and in Lusaka in September 2000 were averaged and compared to monthly average model O_3 profiles (Figure 6.3). The model underestimates measured O_3 concentrations at Lusaka in the lower troposphere (Figure 6.3e). The ozonesondes at Lusaka were launched from September 6-11, a period influenced by the "river of smoke" event which resulted in a heavily polluted layer from the surface up to ~5 km [*Magi et al.*, 2003; *Schmid et al.*, 2003], whereas the modeled O_3 concentrations were averaged over the entire month of September 2000. In addition, the spatial resolution of the model (2°×2.5°) is coarse relative to the spatial coverage of the ozonesondes. On average over the five sites, the model captured over half of the variability (r^2=0.57) in the observed O_3 profiles, but the model underpredicted the measurements by ~26% (Figure 6.3f).

Airborne measurements of CO and O_3 aboard the University of Washington's (UW) CV-580 research aircraft [*Sinha et al.*, 2003] were obtained in the SAFARI 2000 field project in August and September 2000 in the vicinity of five locations in southern Africa (Figure 6.1a): Pietersburg, South Africa (23.89°S, 29.45°E), Maputo, Mozambique (25.97°S, 32.60°E), Maun, Botswana (19.83°S, 23.50°E), Kaoma, Zambia (14.78°S, 24.80°E), and Walvis Bay, Namibia (22.83°S, 14.50°E). Aircraft measurements from the surface to 5 km were compared to the modeled concentrations along the flight track for these five locations (Figure 6.4). Airborne O_3 measurements were obtained from a continuous O_3 monitor whereas CO measurements were obtained intermittently using canister samples. The model and observations both show a latitudinal gradient of increasing concentrations with decreasing latitude. Concentrations of CO and O_3 were highest in regions of intense savanna burning

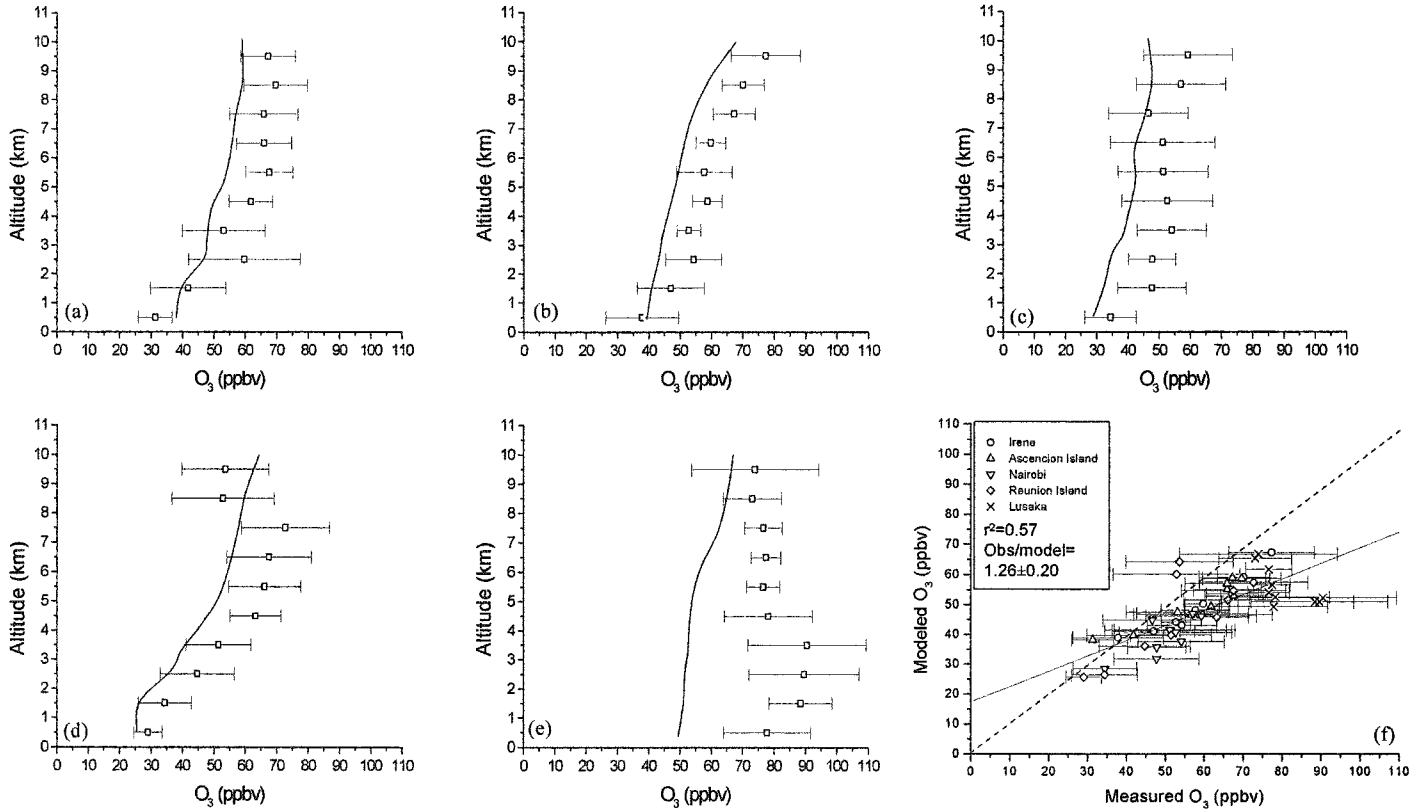

Figure 6.3. Monthly average comparisons of SHADOZ ozonesonde measurements (z = 0-10 km) and GEOS-CHEM modeled O3 at (a) Ascension Island (7.9°S, 14.4°W), (b) Irene, South Africa (25.9°S, 28.2°E), (c) Nairobi, Kenya (1.3°S, 36.8°E), and (d) Reunion Island (21.1°S, 55.5°E) in August 2000, (e) Lusaka, Zambia (15.42°S, 28.32°E) in September 2000, and (f) at all the above sites. Squares and lines indicate measured and modeled concentrations, respectively. Dashed line indicates 1:1 line and error bars indicate the standard deviations of the measured monthly average concentrations.

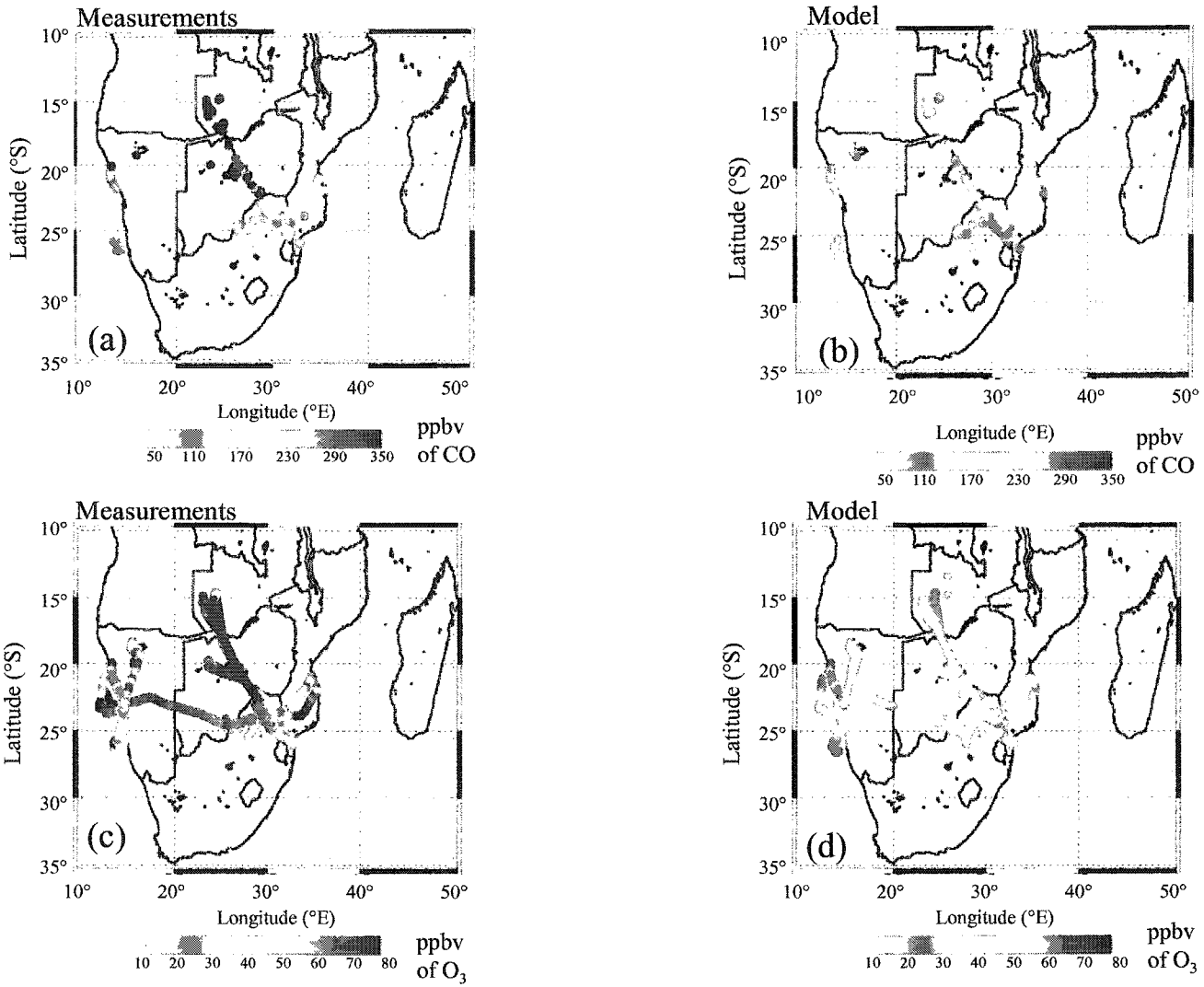

Figure 6.4. Concentrations of CO along the flight track of the UW CV-580 research aircraft obtained from (a) measurements and (b) model. (c) and (d) as for (a) and (b), respectively, but for O_3.

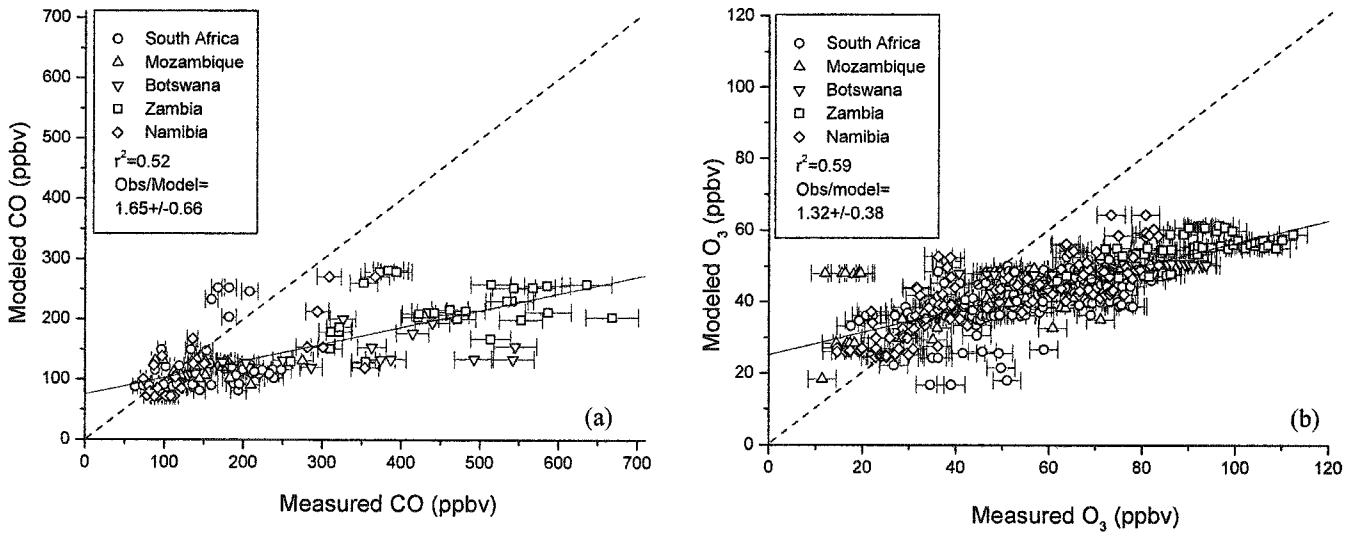

Figure 6.5. (a) Comparisons of UW CV-580 airborne CO measurements and GEOS-CHEM modeled CO along the CV-580 flight track in the vicinity of Pietersburg, South Africa (23,89°S, 29.45°E), Maputo, Mozambique (25.97°S, 32.60°E), Maun, Botswana (19.83°S, 23.50°E), Kaoma, Zambia (14.78°S, 24.80°E), and Walvis Bay, Namibia (22.83°S, 14.50°E) in August and September of 2000. (b) as for (a), but for O_3. Dashed line indicates 1:1 line and error bars indicate instrument precision.

(e.g., Zambia) and lower over coastal regions (Namibia and Mozambique). For CO and O_3, the model captured about half the variability in the observations (r^2=0.52 and 0.59, respectively), but the model underpredicted the measured concentrations by ~60% and ~30%, respectively (Figure 6.5). The underprediction may be partly due to the airborne observing strategy of sampling in the vicinity of active fire emissions, although the airborne measurements used here were not obtained in identifiable smoke plumes. In addition, the spatial resolution of the model (2°×2.5°) is coarse relative to the scale of savanna fires (~0.1°), and modeled biomass burning emissions have a monthly time-resolution despite observed daily variability in savanna fire emissions. The largest disagreements between model and observations occur over Zambia and Botswana, regions of intense biomass burning. Slight errors in the location or timing of emissions can result in large model errors.

6.2. Transport Pathways

In a study of tropospheric air trajectories for the August–September 1992 period, *Garstang et al.* [1996] classified five basic trajectories for the transport of biomass burning emissions from southern Africa (Figure 6.6): direct westward transport, direct eastward transport, anticyclonic circulation and westward transport, anticyclonic circulation and eastward transport, and anticylonic recirculation. The three types of anticylonic circulations were observed to occur on 55% of days during the 1992 study period; direct eastward and westward transport occurred on 41% and 4% of the days, respectively. South of 18°S, the bulk of the trajectories examined showed transport of southern African biomass burning emissions eastward to the Indian Ocean.

During the first week of September 2000, the passage of a westerly trough resulted in direct eastward transport of biomass burning emissions from southern Africa to the Indian Ocean. This "river of smoke" event was visible on the TOMS aerosol index (AI) global imagery [*TOMS*, 2004] with high values of AI (1-3) within the "river of smoke" plume on September 4–6, 2000. TOMS AI is an index ranging from 0-4 measuring the column abundance of ultraviolet absorbing aerosols based on

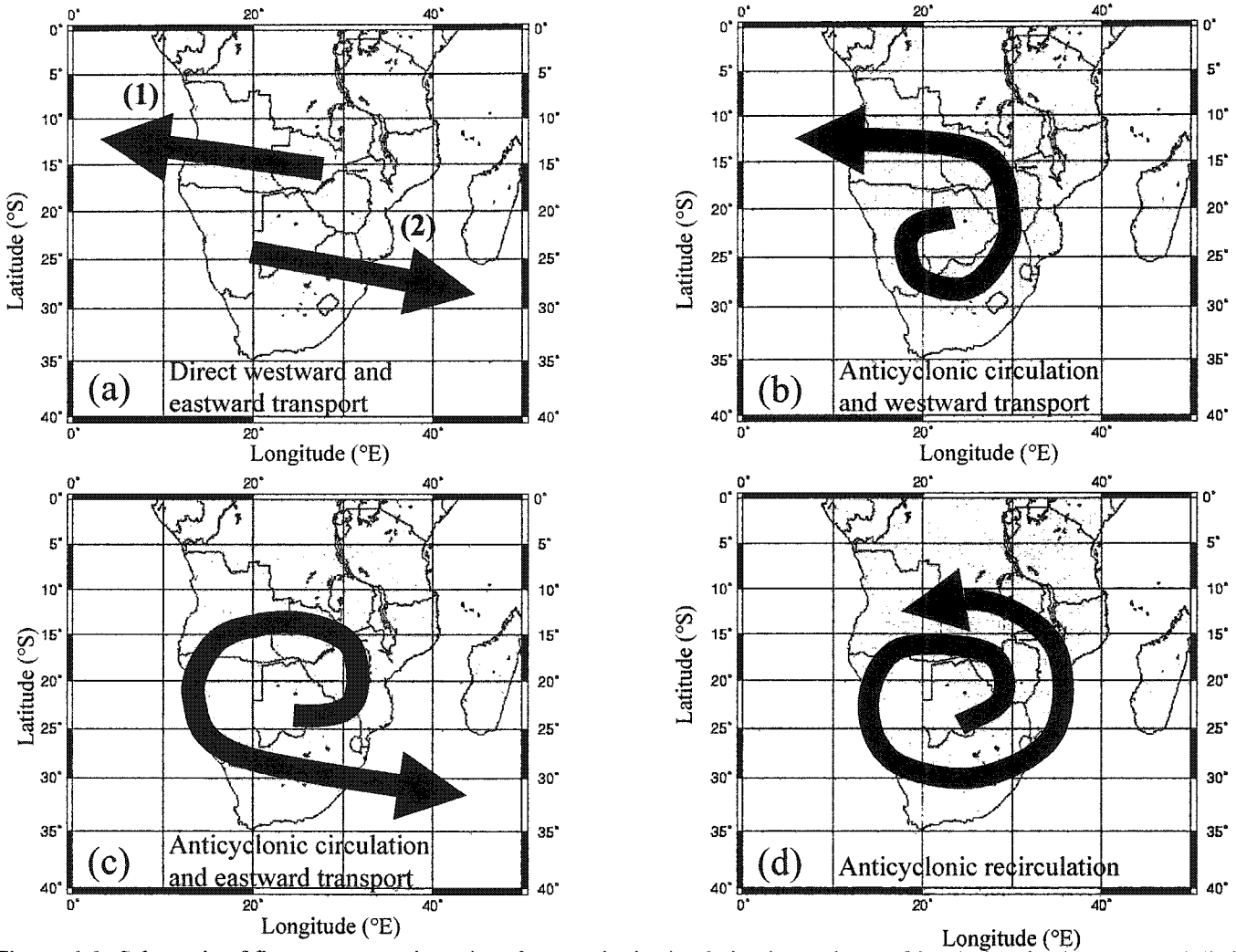

Figure 6.6. Schematic of five common trajectories of tropospheric circulation in southern Africa during the dry season: (a1) direct westward transport, (a2) direct eastward transport, (b) anticyclonic circulation and westward transport, (c) anticyclonic circulation and eastward transport, and (d) anticylonic recirculation. From *Garstang et al.* [1996].

backscattered ultraviolet radiance measurements in the 340-380 nm range [*Herman et al.*, 1997]. We examined the frequency of direct eastward transport events by visually inspecting TOMS AI daily global maps for August and September of the years 1992 and 1996–2003. These events occurred in August 1992, 1996, 2001, and 2003 and September 1992, 1996, 1999, 2000, and 2001, and lasted between 3 and 13 days each. Since eastward transport events, such as the "river of smoke" in 2000, directly transport biomass burning emissions from southern Africa to the Indian Ocean, and since they occur periodically during the dry season months, they are likely an important mechanism for transporting smoke from southern Africa to the Indian Ocean.

6.3. Average Daily CO Flux

To assess the importance of the direct eastward pathway (Figure 6.6a) for transporting biomass burning emissions from southern Africa to the Indian Ocean, we used the GEOS-CHEM model to estimate average daily eastward fluxes of CO from biomass burning in southern Africa (CO_{BBAF}) through a latitude-height cross section (40°E, 0-60°S, 0-11 km) along the eastern coast of southern Africa. Figure 6.7a shows the flux estimates for September 4, 2000, during the "river of smoke" event, and Figure 6.7c shows average model CO concentrations and wind vectors for the same day at an altitude of 5 km. These figures illustrate the direct eastward transport circulation that characterized the "river of smoke" event. The eastward flux of CO_{BBAF} for this event passed through the 40°E latitude-height cross section at ~30°S, with a peak flux (50-100 kg s^{-1}) at ~3-5 km (Figure 6.7a). The integrated average daily eastward flux across the 40°E latitude-height cross section on September 4, 2000 was 0.42 Tg CO_{BBAF} per day.

Figure 6.8 shows the integrated average daily flux of CO_{BBAF} to the east across the 40°E latitude-height cross section in September, 2000. The peak daily flux (~1.15 Tg day^{-1}) occurred in mid-September, rather than the first week of September (0.3-0.5 Tg day^{-1}) when the "river of smoke" event occurred. Figure 6.7b shows model results for September 13, 2000, the beginning of the mid-September period of high CO_{BBAF} fluxes. Average CO concentrations and wind vectors on September 13, 2000, at an altitude of 5 km (Figure 6.7d) illustrate the anticylonic circulation and eastward

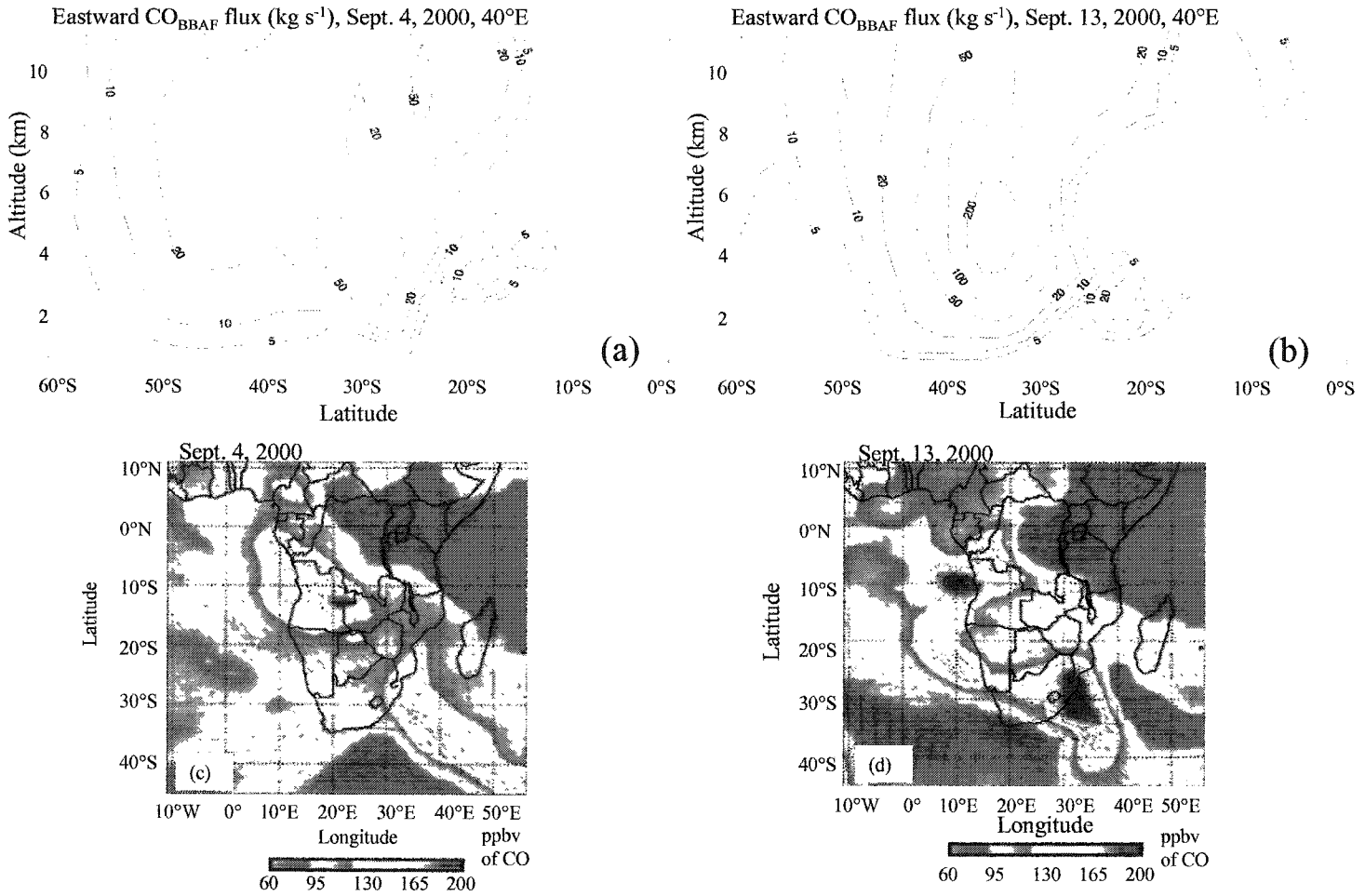

Figure 6.7. (a) Latitude-height cross section (40°E, 0-60°S, z = 0-11 km) along the east coast of southern Africa of eastward flux (kg s^{-1}) of CO_{BBAF} on September 4, 2000, during the "river of smoke" event. (b) as for (a), but on September 13, 2000, during an anticylonic circulation and eastward transport event. (c) CO concentrations (ppbv) and wind vectors at 5 km over southern Africa on September 4, 2000. (d) as for (c), but on September 13, 2000.

transport that prevailed in mid-September, 2000 (Figure 6.6c). The core of high CO_{BBAF} flux along the 40°E latitude-height cross section is located further south (~35°S, Figure 6.7b) relative to the core of high CO_{BBAF} flux in the September 4 "river of smoke" latitude-height cross section (~30°S, Figure 6.7a). The core of high CO_{BBAF} flux on September 13 is also located at a higher altitude (~4-6 km, Figure 6.7b) relative to that on September 4 (~3-5 km, Figure 6.7a). Thirdly, CO_{BBAF} fluxes peak at 200-300 kg s^{-1} on September 13, 2000 (Figure 6.7b) compared to 50-100 kg s^{-1} on September 4, 2000 (Figure 6.7a). The integrated average daily eastward flux along the 40°E latitude-height cross section on September 13, 2000, was 0.72 Tg CO_{BBAF} day^{-1}, 70% higher than that for September 4, 2000 (0.42 Tg CO day^{-1}). Based on average daily eastward flux estimates in September 2000 (Figure 6.8), the anticyclonic circulation and eastward transport observed in mid-September 2000 appears to be the most effective transport pathway for transporting biomass burning emissions from southern Africa to the Indian Ocean. In this pathway, emissions from central southern Africa (Angola, D. R. Congo, and Zambia) are transported westward before returning eastward and combining with emissions from South Africa and Mozambique (Figure 6.7d). In contrast, emissions from central southern Africa do not appear to be transported eastward during the "river of smoke" event (Figure 6.7c). However, Figure 6.7c shows only CO concentrations and wind vectors at 5 km. Below 4 km, emissions from central southern Africa are part of the "river of smoke" that moves eastward to the Indian Ocean.

To evaluate model performance for the direct eastward transport (September 4, 2000) and for the anticyclonic circulation with eastward transport (September 13, 2000) events described above, SHADOZ ozonesonde observations on September 4, 2000, and UW CV-580 airborne CO measurements on September 13, 2000, are compared to model results (Figure 6.9). SHADOZ ozonesondes were launched on September 1 and September 4–7, 2000, during the "river of smoke" event in Irene, South Africa (25.9°S, 28.2°E), a location impacted by the "river of smoke". The model reproduced the observed O_3 concentrations on September 1 (Figure 6.9a), just prior to the arrival of the "river of smoke" plume over Irene. During the river of smoke event on September 4, the model predicted an O_3 enhancement of 10 ppbv between 2 and 4 km, much smaller

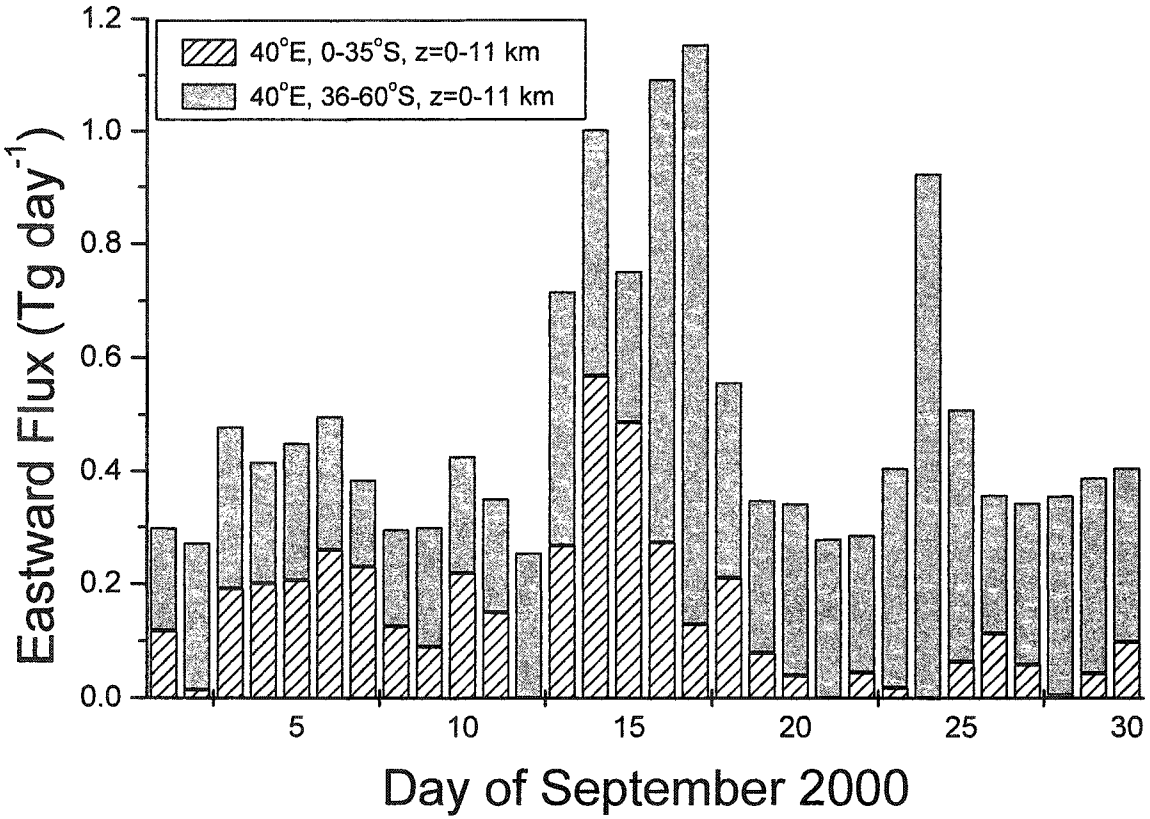

Figure 6.8. Average daily eastward fluxes (Tg per day) of CO_{BBAF} across the 40°E latitude-height cross section (z = 0-11 km) from 0-35°S and 36-60°S in September 2000.

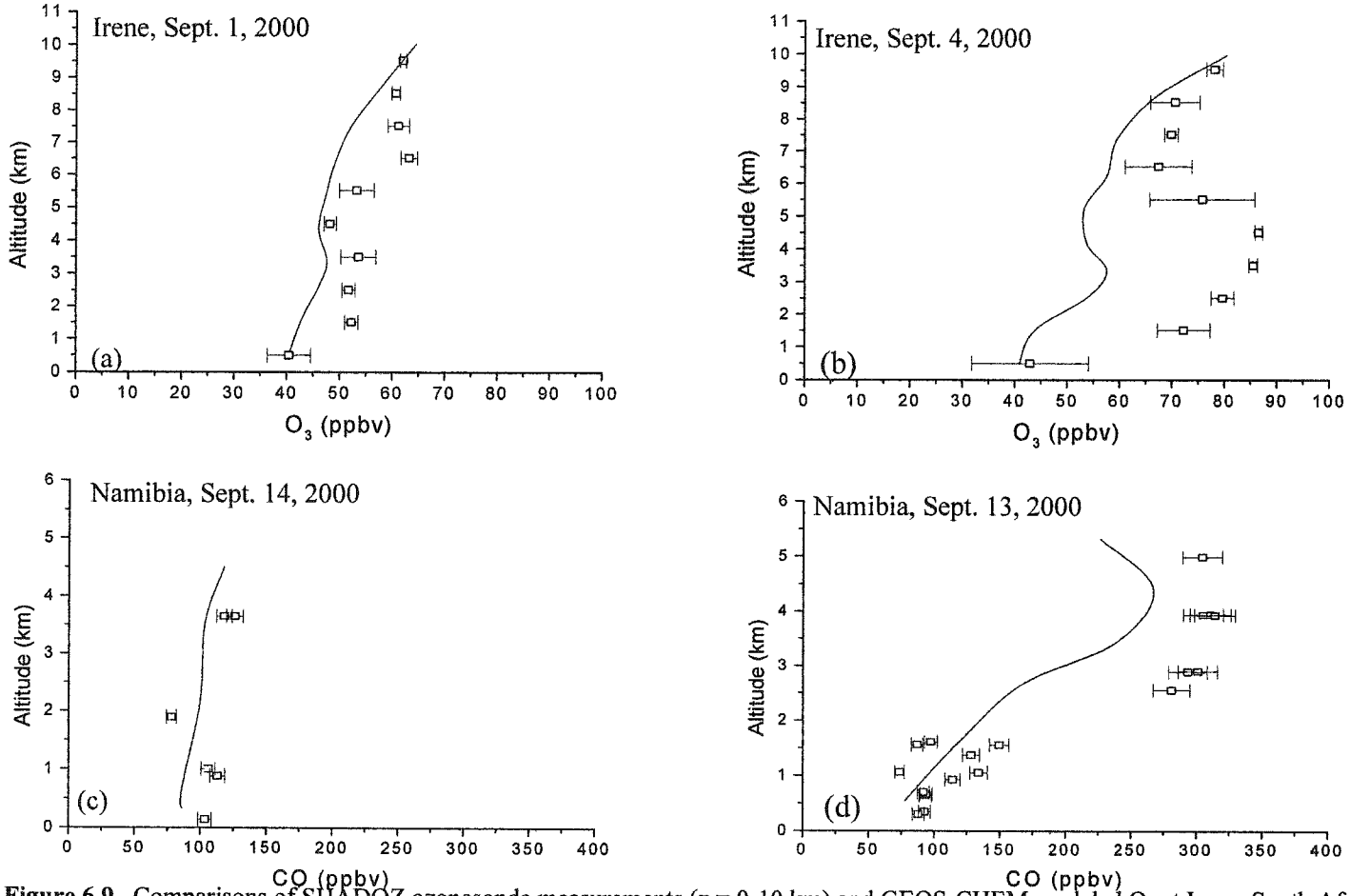

Figure 6.9. Comparisons of SHADOZ ozonesonde measurements (z = 0-10 km) and GEOS-CHEM modeled O_3 at Irene, South Africa (25.9°S, 28.2°E) on (a) September 1, 2000, just prior to the "river of smoke" event, and (b) September 4, 2000, during the "river of smoke" event. Comparisons of UW CV-580 airborne CO measurements and GEOS-CHEM modeled CO along the CV-580 flight track off the coast of Namibia on (c) September 14, 2000 at 26.0°S, 13.8°E, south of an anticylonic circulation and eastward transport event, and on (d) September 13, 2000 at 20.4°S, 13.3°E within an anticylonic circulation and eastward transport event. Squares and lines indicate measured and modeled concentrations, respectively. Error bars indicate instrument precision.

than the observed 30-40 ppbv enhancement (Figure 6.9b). On average, the model underpredicted observed O_3 concentrations from the surface to 10 km by ~40% on September 4–6, the days of peak "river of smoke" outflow.

On September 13 and 14, 2000, CO was measured aboard the UW CV-580 off the coast of Namibia [*Sinha et al.*, 2003]. On September 14, measurements were made at 26.0°S, 13.8°E, just south of an anticyclonic circulation and eastward transport event. Measured and modeled CO concentrations were low (~100 ppbv) throughout the profile on September 14 (Figure 6.9c). On September 13, CO measurements were made at 20.4°S, 13.3°E, within an anticyclonic circulation and eastward transport event. Low CO concentrations (100-150 ppbv) were measured below 2 km and high concentrations (~300 ppbv) from 2-5 km (Figure 6.9d). The model reproduced this split structure, with CO concentrations of 75-125 ppbv below 2 km and 225-275 ppbv above 3 km (Figure 6.9d). The high CO aloft is a consequence of the anticyclonic flow that transported biomass burning emissions from Zambia and Angola initially westward to the Atlantic Ocean and then back eastward to eventually reach the Indian Ocean (Figure 6.7d). To summarize, the model accurately represented features of the anticyclonic circulation and the eastward transport outflow in mid-September, 2000. Since large eastward fluxes (~1 Tg CO_{BBAF} day^{-1}) were modeled under this circulation pattern (Figure 6.8), anticylonic circulation and eastward transport is likely a significant pathway for transporting biomass burning emissions from southern Africa to the Indian Ocean. The GEOS-CHEM model underestimated outflow during the "river of smoke" direct eastward transport event in early September, 2000. Therefore, direct eastward transport events like the "river of smoke" could be a more significant source of southern African biomass burning smoke to the Indian Ocean than indicated by Figure 6.8.

6.4. Average Monthly CO Flux

By summing average daily eastward CO_{BBAF} fluxes from Figure 6.8, we derive an eastward flux of 13.7 Tg per month of CO_{BBAF} transported eastward to the Indian Ocean in September 2000. Of this amount, only about one-third (4.3 Tg) is transported across 0-35°S (Figure 6.8), the latitudes over which direct eastward transport of biomass

burning emissions from southern Africa occur (Figure 6.7a). Therefore, two-thirds of the CO_{BBAF} transported to the Indian Ocean results from indirect eastward transport pathways, such as anticyclonic circulation and eastward flow. Outflow modeled during direct eastward transport events may be underestimated, as it was for the "river of smoke" direct eastward transport event in early September, 2000. Therefore, the apportionment of CO flux between direct and indirect eastward transport pathways is uncertain.

A flux of 12.5 Tg per month of CO_{BBAF} from southern African biomass burning was transported westward to the Atlantic Ocean over the latitude-height cross section (10°E, 0-60°S, 0-11 km) in September 2000. The westward CO_{BBAF} flux from southern African biomass burning was concentrated over the latitudes 0-20°S (Figure 6.10); this contributed to the annual dry season South Atlantic pollution anomaly [*Fishman et al.*, 1996]. However, over the latitude band 21-60°S along the 10°E latitude-height cross section, 9.7 Tg per month of CO_{BBAF} was transported eastward (Figure 6.10). Therefore, approximately three-quarters of the 12.5 Tg per month of CO_{BBAF} that was transported westward from southern Africa to the Atlantic Ocean over the latitude band 0-20°S later returned eastward over higher latitudes (21-60°S), indicating an anticyclonic circulation similar to that shown in Figure 6.7d. Integrating over the entire 10°E latitude-height cross section (0-60°S, z = 0-11 km), the net westward CO_{BBAF} flux to the Atlantic Ocean was only 2.8 Tg $month^{-1}$ in September 2000.

Modeled CO emissions from southern African biomass burning was ~16 Tg per month in September 2000. Since the net eastward flux of CO_{BBAF} to the Indian Ocean (13.7 Tg $month^{-1}$) greatly exceeded the net westward flux to the Atlantic Ocean (2.8 Tg $month^{-1}$), the Indian Ocean appears to be the primary net recipient of CO from southern African biomass burning. A considerable quantity of CO_{BBAF} (12.5 Tg $month^{-1}$) reached the Atlantic Ocean over the latitudes 0-20°S, but most of it returned eastward over higher latitudes eventually reaching the Indian Ocean.

The large westward flux of CO_{BBAF} across 10°E, 0-20°S affects CO concentrations at these latitudes over the southern Atlantic Ocean west of Africa. Global CO maps from the Measurements of Pollution in the Troposphere (MOPITT)

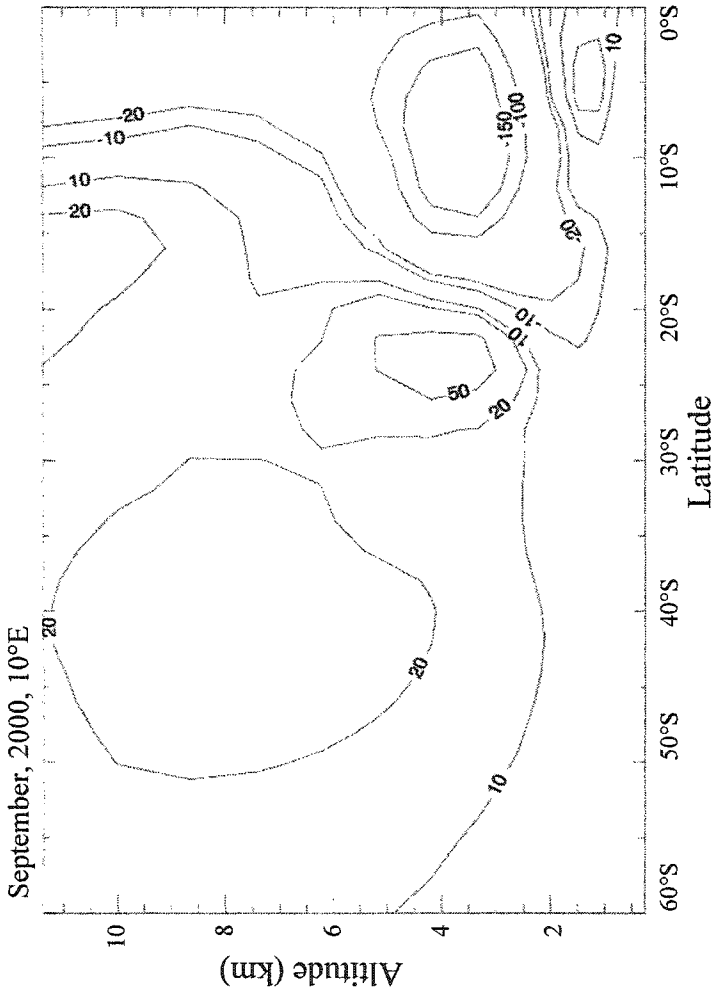

Figure 6.10. Latitude-height cross section (10°E, 0-60°S, z = 0-11 km) along the west coast of southern Africa of average monthly zonal flux (kg s^{-1}) of CO_{BBAF} in September 2000. Positive and negative values indicate eastward and westward flux, respectively.

nadir infrared correlation radiometer instrument [*MOPITT*, 2004] aboard the Terra satellite show elevated concentrations of CO (175-200 ppbv) west of Angola at 700 hPa. Nevertheless, over the course of the dry season, tropospheric CO concentrations are enhanced not only over the southern Atlantic Ocean but over most of the southern hemisphere subtropics [*MOPITT*, 2004]. Biomass burning in southern Africa has also been shown to contribute to the accumulation of O_3 over the southern Atlantic Ocean [*Fishman et al.*, 1991]. Like CO, tropospheric O_3 columns are enhanced over most of the southern hemisphere subtropics by the end of the dry season [*Fishman et al.*, 2003].

6.5. Seasonal and Interannual CO Fluxes

Average monthly fluxes of CO_{BBAF} during the dry season (May–October) from 1994–2000 were modeled across four latitude-height cross sections: the eastern coast of southern Africa from 40°E, 0-35°S, and z = 0-11 km (Figure 6.11a) and from 40°E, 36-60°S, and z = 0-11 km (Figure 6.11b), and the western coast of southern Africa from 10°E, 0-20°S, and z = 0-11 km (Figure 6.11c) and from 10°E, 21-60°S, and z = 0-11 km (Figure 6.11d). Eastward fluxes, which transport CO_{BBAF} to the Indian Ocean (Figures 11a,b), and westward fluxes in Figure 6.11c, which transport CO_{BBAF} to the Atlantic Ocean, increase as the dry season progresses, peaking in September at 15.8±2.1 Tg per month and 9.1±2.4 Tg month^{-1}, respectively. Two-thirds of the eastward flux across 40°E occurs south of the African continent from 36-60°S (Figure 6.11b) due to indirect eastward transport pathways such as anticylonic circulation and eastward transport.

Eastward fluxes across 10°E, which recirculate CO_{BBAF} from the Atlantic Ocean back toward southern Africa, steadily increase as the dry season progresses (Figure 6.11d). In October, the eastward flux of CO_{BBAF} (11.0±0.6 Tg month^{-1}; Figure 6.11d) across the 10°E latitude-height cross section (21-60°S, z = 0-11 km) exceeds the westward flux (6.1±1.6; Figure 6.11c) across 10°E (0-20°S, z = 0-11 km). Therefore, not all of the eastward flux at 10°E (21-60°S, z = 0-11 km) derived from recirculated westward flux. Some of the eastward flux at 10°E in October must originate from CO_{BBAF} that passes eastward through the 40°E latitude-height cross-section and

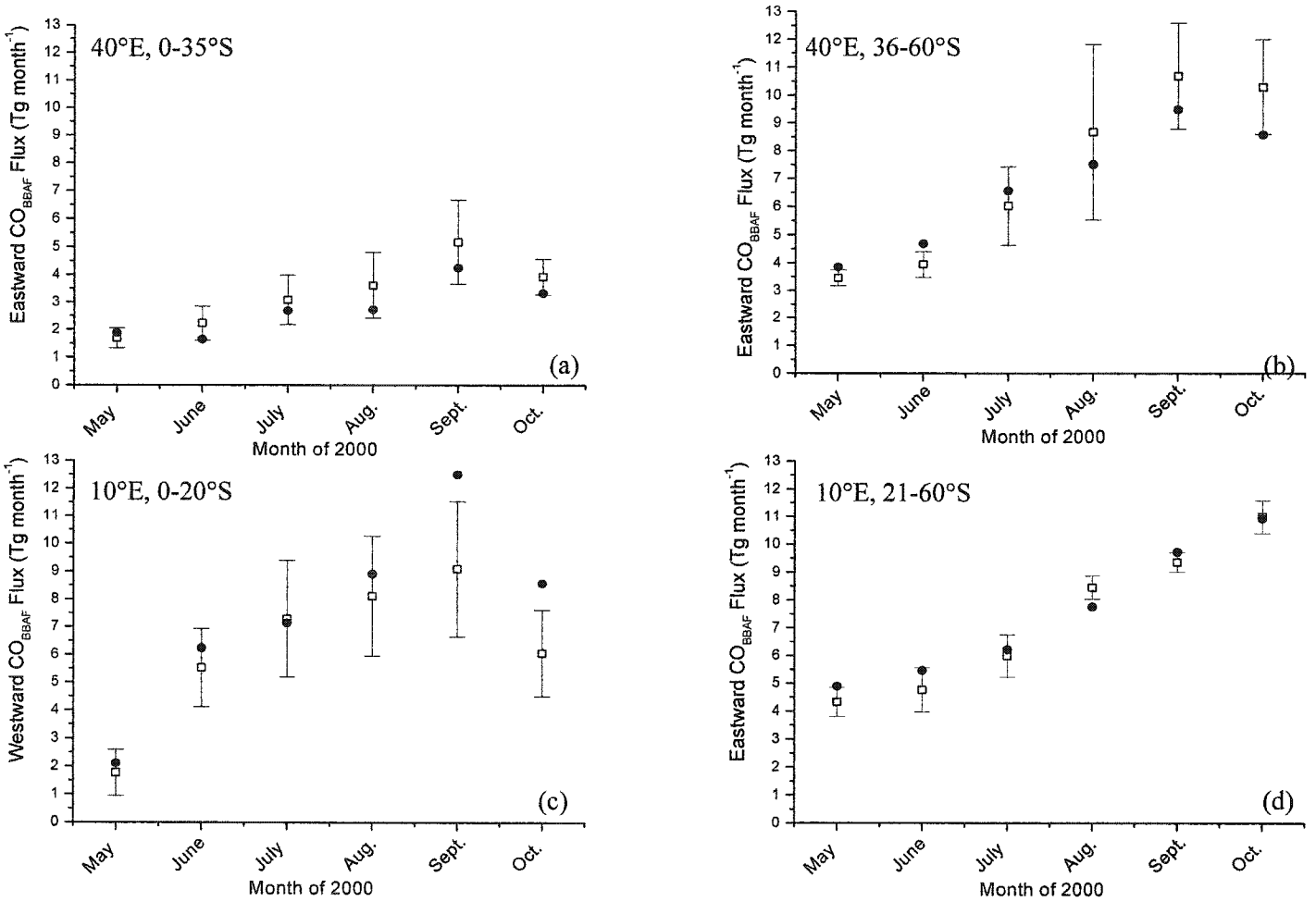

Figure 6.11. (a) Monthly eastward flux of CO_{BBAF} during the dry season (May–October) averaged over 1994–2000 (squares) and for 2000 (circles) across the latitude-height cross section (40°E, 0-35°S, z = 0-11 km). (b) as for (a), but for the latitude-height cross section (40°E, 36-60°S, z = 0-11 km). (c) as for (a), but for westward flux across the latitude-height cross section (10°E, 0-20°S, z = 0-11 km). (d) as for (a), but for the latitude-height cross section (10°E, 21-60°S, z = 0-11 km). Error bars indicate standard deviation of model fluxes averaged over 1994–2000.

travels around the globe as part of the southern subtropical global CO plume that forms by the end of the dry season [*Chatfield et al.*, 2002] before being eventually transported back over southern Africa.

Along with fluxes averaged over the period 1994–2000, Figure 6.11 shows fluxes specific for the 2000 dry season. Westward fluxes across 10°E (0-20°S, z = 0-11 km) were above-average in September and October 2000 (Figure 6.11c), and eastward fluxes were somewhat below average across 40°E (0-60°S, z = 0-11 km) in September and October 2000 (Figures 11a,b). Therefore, the eastward flux of CO_{BBAF} to the Indian Ocean in September 2000 (13.7 Tg month^{-1}) estimated in section 6 is conservative with respect to typical September eastward CO fluxes. Apart from September and October, CO_{BBAF} fluxes in 2000 were within the range of variability observed during the 1994–2000 period (Figure 6.11). Fluxes were determined using climatological average biomass burning emissions. Therefore, interannual variability in fluxes reflect year-to-year changes in meteorological fields. *Swap et al.* [2003] proposed that biomass combustion in southern Africa during the 2000 dry season was above average because of above-average rainfall in the preceding wet season. Above-average rainfall enhances fuel loading, but changes in combustion factors and burned area also have to be considered to determine interannual variability in biomass combustion. In a study of interannual variability of biomass burning emissions constrained by satellite observations, *Duncan et al.* [2003] found that emissions of CO from biomass burning in southern Africa in 2000 were not above average with respect to the 1979–2000 period.

Summing the average 1994–2000 monthly CO_{BBAF} fluxes from Figure 6.11 over the months of the dry season (May–October), yields ~60 Tg of CO_{BBAF} transported eastward to the Indian Ocean across the 40°E latitude-height cross-section (0-60°S, z = 0-11 km) during the dry season (Figures 11a,b). Of this amount, ~20 Tg of CO_{BBAF} is transported across 0-35°S (Figure 6.11a), the latitudes over which direct eastward transport of biomass burning emissions from southern Africa occur. The remaining ~40 Tg of eastward CO_{BBAF} flux occur south of the African continent from 36-60°S due to indirect eastward transport pathways, such as anticyclonic circulation and eastward flow.

Along the 10°E latitude-height cross-section, ~40 Tg of CO_{BBAF} (Figure 6.11b) from southern African biomass burning is transported westward to the Atlantic Ocean from 0-20°S (z = 0-11 km) during the dry season, and a roughly equal amount (~40 Tg) is transported back eastward over 21-60°S (z = 0-11 km) during the dry season. For reference, total annual anthropogenic CO emissions from the United States is ~80 Tg yr^{-1} [*USEPA*, 1997].

6.6. Carbon Monoxide Over the Southern Indian Ocean

Due to the substantial eastward flux (~60 Tg) of CO from biomass burning in southern Africa during the course of an average dry season (Figures 11a,b), CO concentrations in the troposphere over the southern Indian Ocean should be higher by the end of the dry season (September and October) than at the beginning (May). Global CO maps from MOPITT show the development of a planetary-scale band of elevated CO forming in the southern hemisphere subtropics by the end of the biomass burning season. At 700 hPa over the subtropical southern Indian Ocean, CO concentrations in September 2000 are elevated by ~20-40 ppbv above those observed in May (60 ppbv) [*MOPITT*, 2004].

In this study, modeled CO concentrations over the southern Indian Ocean show a similar trend to that observed by MOPITT. Modeled CO concentrations over a latitude-height cross-section in the central southern Indian Ocean (75°E, 0-60°S, z = 0-11 km) show an increase in mid-tropospheric CO concentrations from ~65 ppbv in May (Figure 6.12a) to ~90 ppbv CO by September (Figure 6.12b). This increase of ~25 ppbv can be further described by plotting CO concentrations along the 75°E latitude-height cross section from two major sources of biomass burning, namely, southern Africa and South America. Figures 12c and 12d show that up to ~13 and ~18 ppbv of CO over the central southern Indian Ocean in September of 2000 originates from southern African and South American biomass burning, respectively. Average monthly contributions to CO concentrations over a central region in the 75°E latitude-height cross section (30-40°S, z = 5-7 km) from biomass burning in southern Africa and South America during the 2000 dry season are shown in Figure 6.13. The contributions from southern Africa and South America were ~4-13 and 2-16 ppbv, respectively, peaking in

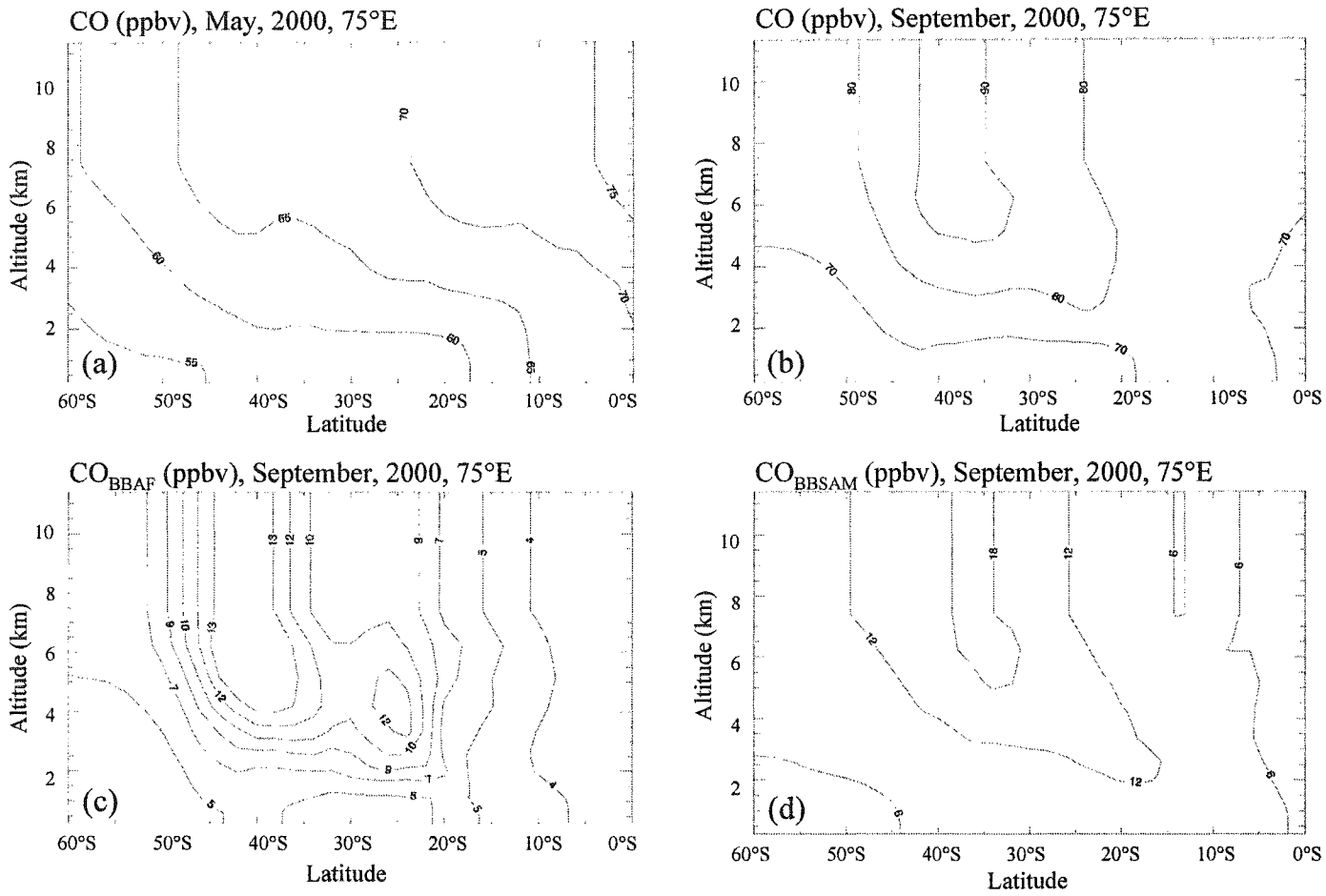

Figure 6.12. Latitude-height cross section (75°E, 0-60°S, z = 0-11 km) over the central southern Indian Ocean of (a) monthly average CO concentrations (ppbv) in May 2000, (b) monthly average CO concentrations (ppbv) in September 2000 (c) monthly average concentrations (ppbv) of CO from biomass burning in southern Africa in September 2000, and (d) monthly average concentrations (ppbv) of CO from biomass burning in South America in September 2000.

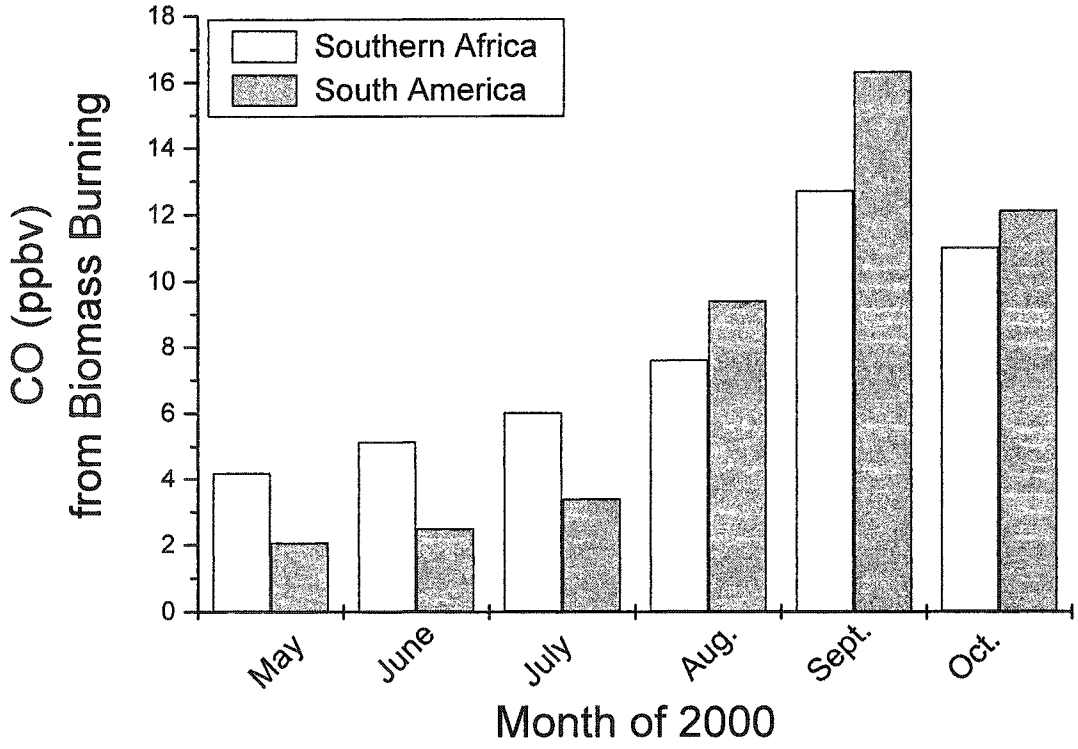

Figure 6.13. Average monthly contributions of CO (ppbv) from biomass burning in southern Africa and South America to the mid-troposphere over the central southern Indian Ocean (75°E, 30-40°S, z = 5-7 km).

September. During the dry season of 2000, modeled emissions of CO from biomass burning in southern Africa and South America were ~80 and ~40 Tg, respectively. Emissions from South America occurred primarily in August, September, and October 2000, whereas emissions from southern Africa were more evenly distributed over the period June–October 2000.

6.7 Long-Range Transport

To evaluate the ability of the GEOS-CHEM model to characterize long-range transport of biomass burning emissions, we can compare output from the model with aircraft measurements made over Australia in mid-September 2000 [*Pak et al.* 2003]. Figure 6.14a shows a large meandering plume of CO (~100-120 ppbv) on September 13, 2000, ranging across the mid-troposphere (z = 5 km) over the southern Indian Ocean and reaching southern Australia. Pak et al. describe airborne measurements of CO_2, CO, CH_4, VOCs, and O_3 made at 38°S, 145°E near Melbourne, Australia, on September 13, 2000, about 1 week after the "river of smoke" event in southern Africa. The measured background concentration of CO in the sampling location was ~60 ppbv. However, on September 13, 2000, the measured concentration of CO was 80-85 pbbv from 3-7 km, indicating an enhancement of 20-25 ppbv above background. Modeled CO at this location on September 13, 2000, is ~80-83 ppbv from 3-7 km, similar to the aircraft measurements. At the location of the aircraft measurements, modeled CO concentrations from biomass burning in southern Africa and South America are ~6-9 and 6-15 ppbv, respectively. Thus, these two sources account for most of the measured ~20-25 ppbv CO enhancement at this location (Figure 6.14b).

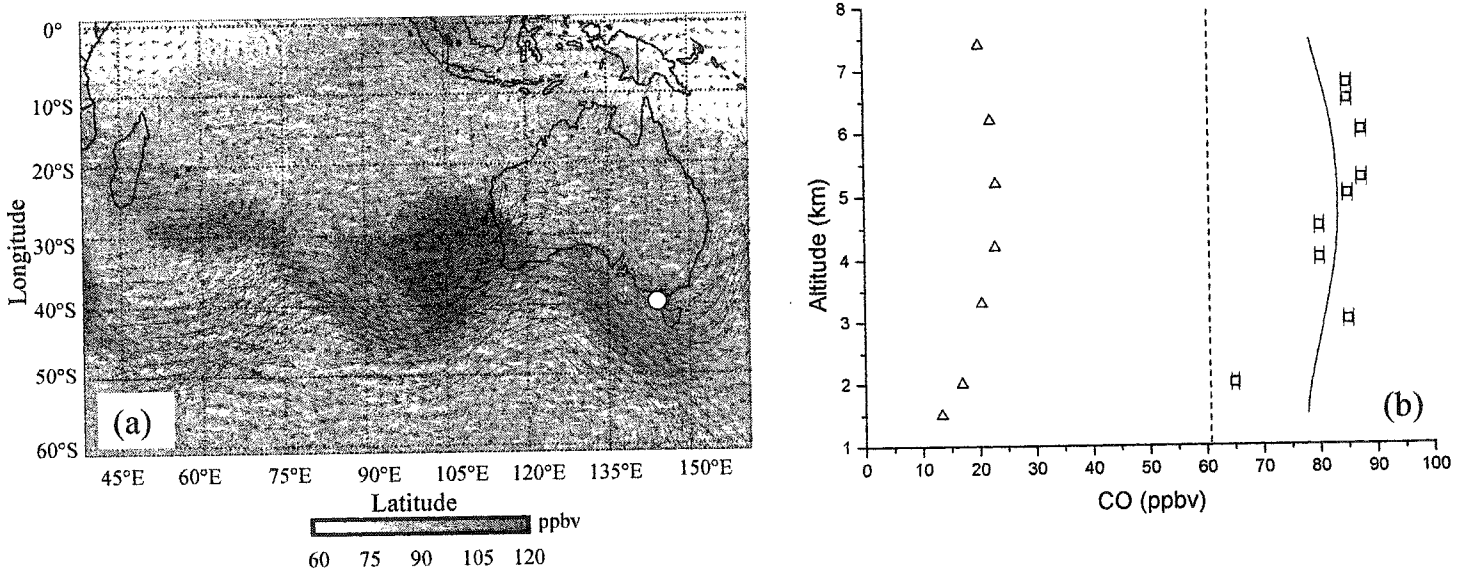

Figure 6.14. (a) CO concentrations (ppbv) and wind vectors at 5 km over the southern Indian Ocean and Australia on September 13, 2000. Location of airborne CO measurements [*Pak et al.*, 2003] is indicated by white circle. (b) Comparisons of airborne CO measurements and GEOS-CHEM modeled CO in the mid-troposphere near Melbourne, Australia (38°S, 145°E) on September 13, 2000. Squares and solid line indicate total measured CO and total modeled CO, respectively. Triangles indicate the sum of modeled CO from biomass burning in southern Africa and South America. Dashed line indicates measured background CO concentrations at this location and error bars indicate instrument precision.

CHAPTER 7
SUMMARY AND CONCLUSIONS

This dissertation has characterized the emissions, evolution, distribution, and transport of trace gases and particles from savanna fires in southern Africa during the dry biomass burning season. The analysis has been based on measurements obtained aboard the UW Convair-580 research aircraft in the SAFARI 2000 field project in August and September 2000, and on chemical transport modeling using the GEOS-CHEM model. This chapter contains a summary of the main results presented and some recommendations for future research.

7.1 Emissions from Savanna Fires

Emission ratios and emission factors have been reported for fifty species in initial smoke from savanna fires in southern Africa. The correlation coefficients (r^2) of the excess mixing ratio of these species versus the excess mixing ratio of CO or CO_2 were all ≥ 0.5; accordingly, these species were considered to be emitted by the fires. The fuels burned in the fires sampled represent vegetation types from the lowveld to the highveld in South Africa, to dambo and miombo woodlands in Zambia, to east African coastal mosaic in Mozambique.

For most species, there is good agreement between the emission ratios and emission factors reported here for initial smoke from savanna fires in southern Africa and those given by *Ferek et al.* [1998] for initial smoke from fires in Brazil and (for stable compounds) by *Blake et al.* [1996] for mainly aged smoke from savanna fires in southern Africa, as well as with a recent compilation of measured and estimated emission factors for savanna burning worldwide by *Andreae and Merlet* [2001]. However, this study provides the first measurements of numerous species in initial

smoke from savanna fires in southern Africa, and the first measurements for eight species that have not been reported previously. In some cases, the emission ratios and emission factors given here differ significantly from the measured or estimated emission factors reported in previous studies.

The completely new emission ratios and emission factors given in this dissertation for young smoke from savanna fires in southern Africa are for dimethyl sulfide, methyl nitrate, five hydrocarbons (3-methyl-1-butene, *c*-2-pentene, *t*-2-pentene, 2-methyl-1-pentene, and *n*-heptane), and particles with diameters from 0.1 to 3 μm. For all of these species the correlation coefficients (r^2) of the excess mixing ratio versus the excess mixing ratio of CO was ≥0.5, indicating that they were emitted by the fires. Of particular interest are methyl nitrate, which can redistribute active nitrogen species and lead to ozone formation; the hydrocarbons, which will reduce the concentrations of OH in smoke plumes; and, particles in the accumulation mode, which have long residence times in the atmosphere, can act as cloud condensation nuclei and promote heterogeneous reactions.

The emission factors reported here that differ significantly from those given for savanna fires by *Andreae and Merlet* [2001] are ammonia, formaldehyde, hydrogen cyanide, and condensation nuclei. Our emission factor for ammonia is about one-fourth that given by Andreae and Merlet, and our emission factors for formaldehyde, hydrogen cyanide, and condensation nuclei are greater by factors of about 3, 20 and 3-15, respectively, than those of Andreae and Merlet. Emissions of formaldehyde, and other oxygenated organic compounds, should increase regional ozone production [*Mason et al.,* 2001]. Abundant hydrogen cyanide emissions support the proposed use of this species, which can be monitored from satellites, for detecting smoke from biomass burning [*Li et al.,* 2000]. Multiplying the average emission factor given here for condensation nuclei, namely, $(3.0\pm1.7)\times10^{16}$ particles per kilogram of fuel burned by

the estimate of *Hao and Liu* [1994] of 1600 Tg yr^{-1} for savanna burned in Africa, yields ~2×10^{28} to 8×10^{28} particles per year emitted from African savanna fires. This estimate is about a factor of ten greater than that given by *Le Canut et al.* [1996] for particles emitted worldwide by savanna fires.

The emission factors reported here for total particulate matter, total particulate carbon, organic particulate carbon, and black carbon show large variations from one fire to another. However, our average values for these species do not differ significantly from those given by *Andreae and Merlet* [2001] for savanna fires.

Emission ratios and emission factors for five species (CO_2, CO, CH_4, C_2H_2, and C_2H_4) were obtained by gas chromatography and Fourier transform infrared spectroscopy. This provided a unique opportunity to compare measurements from two independent techniques under field conditions. Except for C_2H_4, study-average emission ratios and emission factors obtained by these two methods were not significantly different.

Finally, it should be emphasized that the emission ratios and emission factors given in this dissertation are for initial smoke, that is, for smoke less than a few minutes old. Many species are transformed as smoke ages, as discussed in chapter 4.

Woodland and grassland savanna fires in southern Africa during the 2000 dry season were estimated to account for ~12.3%, 12.6%, 5.9%, 10.3%, 4.0%, and 7.5% of annual emissions of CO_2, CO, total hydrocarbons, NO_x (as NO), NH_3, and SO_2, respectively, from all types of savanna fires worldwide. For total particulate matter, black carbon, organic carbon, and potassium, the corresponding percentages are ~17.5%, 11.1%, 9.9%, and 12.2%, respectively. For oxygenated species, such as formaldehyde, acetic acid, formic acid, and methanol, the percentages are ~24.2%, 18.4%, 9.8%, and 9.2%, respectively. For CH_3Br, CH_3Cl, and CH_3I they are ~2.8%,

4.3%, and 0.5%, respectively. Our emissions estimates for woodland and grassland savanna fires during the 2000 dry season in southern Africa are uncertain to ~70%.

Average annual emissions of CH_4, ethane, ethene, acetylene, propene, formaldehyde, methanol, and acetic acid from the use of biofuels in Zambia are comparable to or exceed dry season emissions from miombo woodland and dambo grassland fires in Zambia. Average annual emissions of methane from the use of biofuels in southern Africa are nearly three times higher than those from woodland and grassland savanna fires in southern Africa during the dry season of 2000.

7.2 Evolution of Smoke from Savanna Fires

Airborne measurements have been presented of the emissions and initial evolution of particles and gases from a 1000 ha prescribed burn of savanna vegetation in South Africa. This study has provided excess mixing ratios and downwind changes in normalized excess mixing ratios for forty-two trace gases, total particulate matter, organic carbon, black carbon, and particulate Cl^-, NO_3^-, SO_4^{2-} and K^+. Average OH concentrations in the young smoke plume have been estimated. Downwelling and upwelling UV fluxes (300-390 nm) have been reported within the smoke along the length of the plume, and the spectral depletion of solar radiation by the smoke has been measured. This study has also provided measurements of the light-scattering coefficient, and condensation nucleus (CN) concentrations across the width of the smoke plume at various distances downwind of the fire (Figures 5 and 6), CN measurements along the length of the plume, and the evolution of the particle size spectra during ~40 min of aging.

The CO-normalized excess mixing ratios of nitrate, ozone, and gaseous acetic acid increased significantly as the smoke aged over ~40-45 min, indicating that these species were produced by chemical reactions in the plume (Tables 4-6 and Figure 12).

The CO-normalized excess mixing ratio of seventeen species decreased significantly as the smoke aged over ~40-45 min, indicating that they were consumed by chemical reactions (Tables 4-6 and Figures 13-15). The downwelling UV flux near the center of the smoke plume was about two-thirds of that near the top of the plume. Despite this, the average OH concentration in the relatively young smoke, estimated to be $(1.7\pm0.2)\times10^7$ molecules cm^{-3}, was high enough to significantly shorten the lifetimes of reactive species. The transformations of species in the smoke were faster than observed in extratropical regions. The CO-normalized excess CN concentrations decreased rapidly during the first ~10 min of aging and thereafter increased relatively slowly. We attribute this to particle coagulation initially dominating gas-to-particle conversion, and then vice versa at longer times. The CO-normalized concentrations of particles <1.5 μm diameter decreased as the smoke aged over ~40 min, whereas, for larger particles, the concentrations were greater in the aged smoke.

7.3 Distribution of Smoke in Southern Africa

Measurements have been presented of the vertical distributions of temperature, relative humidity, SO_2, O_3, CN, and CO (Figures 6-10), and the horizontal distributions of twenty gaseous and particulate species (Table 2), over five sectors of southern Africa (Figure 2a) from August 14 to September 16 of 2000 during the dry biomass burning season. The Zambia and Botswana sectors had the highest concentrations of CO_2, CO, CH_4, ethane, propane, O_3, black particulate carbon, and total particulate carbon. We attribute this primarily to the transport of smoke from biomass burning in Angola, Zimbabwe, South Africa, and Mozambique, as well as to local biomass burning.

The South Africa sector had the highest concentrations of SO_2, sulfate, and CN. The SO_2 concentrations were particularly high at the surface, which we attribute to

electric power generating plants, mining operations and biomass burning within this sector.

Air quality in the Mozambique sector was similar to the neighboring South Africa sector, with comparable concentrations of CO_2, CO, CH_4, O_3, organic particles, and inorganic particles. Since there are few industrial sources of pollution in Mozambique, air quality was likely dominated by biomass burning within the sector and the transport of pollutants from South Africa.

The vertical distribution of pollutants over the arid Namibia sector can show a split structure, with a clean layer below ~2.5 km, and a polluted layer above ~2.5 km. Coastal stratus clouds are often located at about 1 km. In the polluted layer the mixing ratios of SO_2, O_3, and CO reached ~1.5 ppbv, ~80 ppbv, and ~275-375 ppbv, respectively. Back trajectories and pollutant lifetimes indicate that transport of biomass smoke into the Namibia sector from intense savanna burning in southern Angola was responsible for the pollution aloft.

When pollutant concentrations were averaged over all five sectors of this study, the concentrations of eight species (CO_2, CO, SO_2, O_3, black carbon, organic particulate carbon, total particle mass, and potassium) were elevated above the concentrations typical of remote or rural continental locations. For several of these species, the average concentrations over all five sectors approached values typical of polluted, urban air. Since most of the measurements in this study took place in locations well removed from industrial sources of pollution, the high average concentrations of pollutants in the lower troposphere reflect the impact of biomass burning (savanna fires and domestic) on the air quality of the region.

Even locations with few biomass fires and industrial emissions, such as Namibia, can attain pollution levels comparable to those found in polluted urban air or in plumes from fires.

7.4 Transport of Smoke from Southern Africa

The transport of emissions from biomass burning in southern Africa has been characterized using the GEOS-CHEM global model of tropospheric chemistry driven by assimilated meteorological data. The model is compared to ground, ozonesonde, and aircraft measurements of CO and O_3 obtained in and around southern Africa in 2000. The model shows a negative bias of ~20% for CO and a positive bias of ~10-20% for O_3 in oceanic sites downwind of fire emissions. Near areas of active fire emissions, the model underpredicts observed concentrations of CO and O_3 by ~60% and ~40%, respectively, likely due to the coarse spatial (2°×2.5°) and temporal (monthly) resolution of the model compared to that of active fires.

Two pathways dominate the eastward transport of biomass burning emissions from southern Africa to the Indian Ocean: a) direct eastward transport, and b) anticyclonic circulation and eastward transport. During the "river of smoke" episode [*Annegarn et al.*, 2002] in early September, 2000, the average daily eastward flux of CO_{BBAF} across the 40°E latitude-height cross section (0-60°S, z = 0-11 km) was ~0.3-0.5 Tg per day. During an anticyclonic circulation and eastward transport event in mid-September, the corresponding flux was ~0.7-1.15 Tg per day. The model reproduced the concentrations of CO measured off the coast of Namibia in mid-September during the anticyclonic circulation and eastward transport event, but the model underpredicted ozonesonde profile measurements over Irene, South Africa, by ~40% in early September during the direct eastward transport event.

In September 2000 comparable amounts of CO_{BBAF} were transported eastward to the Indian Ocean (13.7 Tg per month) and westward to the Atlantic Ocean (12.5 Tg per month). However, approximately three-quarters of the 12.5 Tg per month of CO_{BBAF} transported westward from southern Africa to the Atlantic Ocean over the latitude band

0-20°S returned eastward over the latitude band 21-60°S, resulting in a net westward flux of only ~2.8 Tg per month of CO_{BBAF} to the Atlantic Ocean. Therefore, the Indian Ocean appears to be the primary net recipient of CO emitted by biomass burning in southern Africa.

The model simulations indicate that during an average dry season (May–October) from 1994–2000, ~60 Tg of CO_{BBAF} is transported eastward to the Indian Ocean across the 40°E latitude-height cross-section (0-60°S, z = 0-11 km). Two-thirds of the eastward flux of CO_{BBAF} across 40°E occurs south of the African continent from 36-60°S, due to indirect eastward transport pathways such as anticylonic circulation and eastward transport. In an average dry season, a considerable quantity of CO_{BBAF} (~40 Tg) is transported westward to the Atlantic Ocean across the 10°E latitude-height cross-section (0-20°S, z = 0-11 km), but a roughly equal amount (~40 Tg) is transported back to the east at higher latitudes (21-60°S). On average over the period 1994–2000, both eastward fluxes of CO_{BBAF} to the Indian Ocean and westward fluxes to the Atlantic Ocean peak in September at 15.8±2.1 Tg per month and 9.1±2.4 Tg per month, respectively.

The model simulations indicate that the ~60 Tg of CO from biomass burning in southern Africa transported eastward during an average dry season affects CO concentrations over the southern Indian Ocean. By the end of the 2000 dry season (September and October), CO concentrations in the mid-troposphere over the subtropical southern Indian Ocean were ~25 ppbv higher than at the beginning of the dry season (May). Carbon monoxide from biomass burning in southern Africa and South America accounted for most of this enhancement, contributing ~4-13 and 2-16 ppbv per month, respectively, during the dry season with peak contributions in September. The model reproduced a ~20-25 ppbv enhancement of CO over Melbourne, Australia, that was measured on September 13, 2000. This enhancement was due to

long-range transport of biomass burning emissions from southern Africa and South America. These two source regions contributed ~6-9 and 6-15 ppbv CO, respectively, to midtropospheric CO concentrations over Melbourne on September 13, 2000.

7.5 Recommendations for Future Work

Regional emission estimates from biomass burning in southern Africa have large uncertainties (e.g., ~70% in this study). Remote sensing should be used to constrain these estimates and provide a consistent and complete time series of emissions data. The four major terms in an emissions calculation (area burned, fuel load, combustion factor, and emission factor) can be related to land surface properties measured by remote sensing.

Area burned can be measured directly with the Moderate Resolution Imaging Spectroradiometer (MODIS) [*Roy et al.*, 2002] and the Systeme Pour l'Observation de la Terre (SPOT) Vegetation instrument [*Grégoire et al.*, 2003] aboard the Terra and SPOT 4 satellites, respectively. Fuel load is related to net primary productivity (NPP), which in turn depends on the fraction of photosynthetically active radiation (FPAR) absorbed by vegetation [*Van der Werf et al.*, 2003]. FPAR is a variable that can be measured by remote sensing instruments such as MODIS and the SPOT Vegetation instrument. *Hoffa et al.* [1999] related combustion factors to the percentage of green vegetation (PGREEN) in total vegetation. PGREEN is a term that is related to the normalized difference vegetation index (NDVI) which can be measured by MODIS and the SPOT-Vegetation instrument. Lastly, statistical relations between emission factors and the modified combustion efficiency (MCE) for 50 trace gas and particle species have been given in Chapter 3 of this dissertation. MCE is in turn related to PGREEN, because dead vegetation is more flammable and burns more efficiently than live green vegetation. As stated above, PGREEN is related to NDVI which can be measured by remote sensing (MODIS and the SPOT Vegetation instrument).

To summarize, the MODIS and SPOT Vegetation remote sensing instruments measure land surface properties such as NDVI, FPAR, and burned area which can help to constrain regional emissions calculations. Such constraints should improve the

accuracy of emissions estimates for biomass burning in southern Africa and provide the means to obtain a time series of emissions for the region over the time period of the satellite measurements. Such a time series could be used to assess seasonal and interannual variability in biomass burning emissions. Successful coupling of remote sensing with emissions estimates for biomass burning in southern Africa could also serve as a template for constraining global biomass burning emissions, which are even more uncertain than regional estimates.

REFERENCES

Anderson, B. E., W. B. Grant, G. L. Gregory, E. V. Browell, J. E. Collins Jr., G. W. Sachse, D. R. Bagwell, C. H. Hudgins, D. R. Blake, and N. J. Blake, Aerosols from biomass burning over the tropical South Atlantic region: Distributions and impacts, *J. Geophys. Res., 101*, 24,117-24,138, 1996.

Andreae, M. O., Soot carbon and excess fine potassium: Long-range transport of combustion-derived aerosols, *Science, 220*, 1148-1151, 1983.

Andreae, M. O., Biomass burning: its history, use, and distribution and its impact on environmental quality and global climate, in *Global Biomass Burning: Atmospheric, Climactic, and Biospheric Implications*, edited by J. S. Levine, pp. 3-21, MIT Press, Cambridge, Mass, 1991.

Andreae, M. O., B. E. Anderson, D. R. Blake, J. D. Bradshaw, J. E. Collins, G. L. Gregory, G. W. Sachse, and M. C. Shipman, Influence of plumes from biomass burning on atmospheric chemistry over the equatorial and tropical Atlantic during CITE 3, *J. Geophys. Res., 99,* 12,793-12,808, 1994.

Andreae, M. O., T. W. Andreae, H. Annegarn, J. Beer, H. Cachier, P. Le Canut, W. Elbert, W. Maenhart, J. Salma, F. G. Wiehold, and T. Zerker, Airborne studies of aerosol emissions from savanna fires in southern Africa: Aerosol chemical composition, *J. Geophys. Res., 103,* 32,114-32,128, 1998.

Andreae, M. O., E. Atlas, H. Cachier, W. R. Cofer III, G. W. Harris, G. Helas, R. Koppmann, J. Lacaux, and D. Ward, Trace gas and aerosol emissions from savanna fires, in *Biomass Burning and Global Change, Volume 1*, edited by J. S. Levine, pp. 278-295, MIT Press, Cambridge, Mass., 1996.

Andreae, M. O., and P. Merlet, Emission of trace gases and aerosols from biomass burning, *Global Biochem. Cycles, 15,* 955-966, 2001.

Annegarn, H. J., L. Otter, R. J. Swap, and R. J. Scholes, Southern Africa's ecosystem in a test-tube: A perspective on the Southern African Regional Science Initiative (SAFARI 2000), *S. Afr. J. Sci., 98,* 111–113, 2002.

Arino, O., and J.-M. Rosaz, 1997 and 1998 World ATSR Fire Atlas using ERS-2 ATSR-2 data, in *Proc. Joint Fire Science Conf.*, Boise, Idaho, Published by the University of Idaho and the International Association of Wildland Fire, pp. 177-182, 1999.

Bergstrom, R., P. B. Russell, and P. Hignett, Wavelength dependence of the absorption of black carbon particles: Predictions and results from the TARFOX experiment and implications for the aerosol single-scattering albedo, *J. Atmos. Sci., 59,* 567-577, 2002.

Bergstrom, R., P. Pilewskie, B. Schmid, and P. B. Russell, Comparison of measured and predicted aerosol radiative effects during SAFARI 2000, *J. Geophys. Res., 108,* 8474, doi:10.1029/2002JD002435, 2003.

Bertschi, I., R. J. Yokelson, D. E. Ward, T. J. Christian, and W-M. Hao, Trace gas emissions from the production and use of domestic biofuels in Zambia measured

by open-path Fourier transform infrared (FTIR) spectroscopy, *J. Geophys. Res.*, *108*, 8469, doi:10.1029/2002JD002158, 2003a.

Bertschi, I., R. J. Yokelson, D. E. Ward, R. E. Babbitt, R. A. Susott, J. G. Goode, and W. M. Hao, Trace gas and particle emissions from fires in large diameter and belowground biomass fuels, *J. Geophys. Res., 108*, 8472, doi:10.1029/2002JD002100, 2003b.

Bey, I., D. J. Jacob, R. M. Yantosca, J. A. Logan, B. D. Field, A. M. Fiore, Q. Li, H. Y. Liu, L. J. Mickley, and M. G. Schultz, Global modeling of tropospheric chemistry with assimilated meteorology: Model description and evaluation, *J. Geophys. Res., 106*, 23,073–23,095, 2001.

Blake, N. J., D. R. Blake, B. C. Sieve, T.-Y. Chen, F. S. Rowland, J. E. Collins Jr., G. W. Sachse, and B. E. Anderson, Biomass burning emissions and vertical distribution of atmospheric methyl halides and other reduced carbon gases in the South Atlantic region, *J. Geophys. Res., 101,* 24,151-24,164, 1996.

Cachier, H., C. Liousse, P. Buatmenard, and A. Gaudichet, Particulate content of savanna fire emissions, *J. Atmos. Chem., 22*, 123-148, 1995.

Cachier, H., C. Liousse, M. Pertuisot, A. Gaudichet, F. Echalar, and J. Lacaux, African fire particulate emissions and atmospheric influence, in *Biomass Burning and Global Change, Volume 1*, edited by J. S. Levine, pp. 428-440, MIT Press, Cambridge, Mass., 1996.

Chatfield, R. B., J. A. Vastano, L. Li, G. W. Sachse, and V. S. Connors, The Great African plume from biomass burning: Generalizations from a three-dimensional study of TRACE A carbon monoxide, *J. Geophys. Res., 103*, 28,059-28,077, 1998.

Chatfield, R. B., Z. Guo, G. W. Sachse, D. R. Blake, and N. J. Blake, The subtropical global plume in the Pacific Exploratory Mission-Tropics A (PEM-Tropics A), PEM-Tropics B, and the Global Atmospheric Sampling Program (GASP): How tropical emissions affect the remote Pacific, *J. Geophys. Res., 107*, 4278, 10.1029/2001JD000497, 2002.

Chatfield, R. B., H. Guan, A. M. Thompson, and J. C. Witte, Convective lofting links Indian Ocean air pollution to paradoxical South Atlantic ozone maxima, *Geophys. Res. Lett., 31*, L06103, doi: 10.129/2003GL018866, 2004.

Cofer, W. R. III, J. S. Levine, E. L. Winstead, D. R. Cahoon, D. I. Sebacher, J. P. Pinto, and B. J. Stocks, Source composition of trace gases released during African savanna fires, *J. Geophys. Res., 101,* 23,597-23,602, 1996.

Colman, J. J., A. L. Swanson, S. Meinardi, B. C. Sive, D. R. Blake, and F. S. Rowland, Description of the analysis of a wide range of volatile organic compounds in whole air samples collected during PEM-Tropics A and B, *Anal. Chem., 73,* 3723-3731, 2001.

Crutzen, P. J., and M. O. Andreae, Biomass burning in the tropics: Impact on atmospheric chemistry and biogeochemical cycles, *Science, 250,* 1669-1678, 1990.

Delmas, R., On the emission of carbon, nitrogen and sulfur in the atmosphere during bushfires in intertropical savannah zones, *Geophys. Res. Lett., 9,* 761-764, 1982.

Diab, R. D., A. M. Thompson, M. Zunckel, G. J. R. Coetzee, J. Combrink, G. E. Bodeker, J. Fishman, F. Sokolic, D. P. McNamara, C. B. Archer, and D. Nganga, Vertical ozone distribution over southern Africa and adjacent oceans during SAFARI-92, *J. Geophys. Res., 101*, 23,823-23,833, 1996.

Duncan, B. N., R. V. Martin, A. C. Stoudt, R. Yevich, and J. A. Logan, Interannual and seasonal variability of biomass burning emissions constrained by satellite observations, *J. Geophys. Res., 108*, 4100, doi:10.1029/2002JD002378, 2003.

Eagan, R. C., P. V. Hobbs, and L. F. Radke, Measurements of cloud condensation nuclei and cloud droplet size distributions in the vicinity of forest fires, *J. Appl. Meteor., 13*, 553-557, 1974.

Eck, T. F., B. N. Holben, D. E. Ward, M. M. Mukelabai, O. Dubovik, A. Smirnov, J. S. Schafer, N. C. Hsu, S. J. Piketh, A. Queface, J. Le Roux, R. J. Swap, and I. Slutsker, Variability of biomass burning aerosol optical characteristics in southern Africa during the SAFARI 2000 dry season campaign and a comparison of single scattering albedo estimates from radiometric measurements, *J. Geophys. Res., 108*, 8477, doi:10.1029/2002JD002321, 2003.

Edwards, D. P., J. F. Lamarque, J. L. Attie, L. K. Emmons, A. Richter, J. P. Cammas, J. C. Gille, G. L. Francis, M. N. Deeter, J. Warner, D. C. Ziskin, L. V. Lyjak, J. R. Drummond, J. P. Burrows, Tropospheric ozone over the tropical Atlantic: A satellite perspective, *J. Geophys. Res.,108,* 4237, doi:10.1029/2002JD002927, 2003.

Energy Information Administration (EIA), *Southern Africa and the Southern African Development Community*, www.eia.doe.gov/emeu/cabs/sadc.html, 2002.

Ferek, R. J., J. S. Reid, P. V. Hobbs, D. R. Blake, and C. Liousse, Emission factors of hydrocarbons, halocarbons, trace gases and particles from biomass burning in Brazil, *J. Geophys. Res., 103*, 32,107-32,118, 1998.

Finlayson-Pitts, B. J., and J. W. Pitts Jr., *Chemistry of the Upper and Lower Atmosphere,* Academic Press, San Francisco, 2000.

Fishman, J., K. Fakhruzzaman, B. Cros, and D. Nganga, Identification of widespread pollution in the southern hemisphere deduced from satellite analyses, *Science, 252,* 1693-1696, 1991.

Fishman, J., J. M. Hoell, R. D. Bendura, R. J. McNeil, and V. W. J. H. Kirchhoff, NASA GTE TRACE A experiment (Sept.-Oct. 1992): Overview, *J. Geophys. Res., 101,* 23,869-23,879, 1996.

Fishman, J., A. E. Wozniak, and J. K. Creilson, Global distribution of tropospheric ozone from satellite measurements using the empirically corrected tropospheric ozone residual technique: Identification of the regional aspects of air pollution, *Atmos. Chem. Phys., 3*, 893–907, 2003.

Food and Agriculture Organization (FAO), The role of wood energy in Africa, FAO Working Paper FOPW/99/3, Rome, Italy, 1999.

Freiman, M. T., M. R. Jury, and S. Medcalf, The state of the atmosphere over South Africa during the Southern African Regional Science Initiative (SAFARI 2000), *S. Afr. J. Sci., 98*, 91-96, 2002.

Gao, S., D. A. Hegg, P. V. Hobbs, T. W. Kirchstetter, B. Magi, and M. Sadelik, Water-soluble organic components in aerosols associated with savanna fires in southern

Africa: Identification, evolution and distribution, *J. Geophys. Res.*, *108*, 8491, doi:10.1029/2002JD002324, 2003.

Garstang, M., P. D. Tyson, R. Swap, M. Edwards, P. Kallberg, and J.A. Lindesay, Horizontal and vertical transport of air over southern Africa, *J. Geophys. Res.*, *101*, 23,721–23,736, 1996.

Goode, J. G., R. J. Yokelson, R. A. Susott, and D. E. Ward, Trace gas emissions from laboratory biomass fires measured by open-path Fourier transform infrared spectroscopy: Fires in grass and surface fuels, *J. Geophys. Res., 104,* 21,237-21,245, 1999.

Goode, J. G., R. J. Yokelson, D. E. Ward, R. A. Susott, R. E. Babbitt, M. A. Davis, and W. M. Hao, Measurements of excess O_3, CO_2, CO, CH_4, C_2H_4, C_2H_2, HCN, NO, NH_3, HCOOH, CH_3COOH, HCHO and CH_3OH in 1997 Alaskan biomass burning plumes by airborne Fourier transform infrared spectroscopy (AFTIR), *J. Geophys. Res., 105,* 22,147-22,166, 2000.

Grégoire, J-M., K. Tansey, and J. M. N. Silva, The GBA2000 initiative: Developing a global burned area database from SPOT-VEGETATION imagery, *Int. J. Remote Sens.*, *24*, 1369-1376, 2003.

Gundel, L. A., R. L. Dod, H. Rosen, and T. Novakov, The relationship between optical attenuation and black carbon concentrations for ambient and source particles, *Sci. Total Environ., 36*, 197-202, 1984.

Hao, W. M., and M. H. Liu, Spatial and temporal distribution of tropical biomass burning, *Global Biochem. Cycles*, *8*, 495-503, 1994.

Hegg, D. A., L. F. Radke, P. V. Hobbs, R. A. Rasmussen, and P. J. Riggan, Emissions of some trace gases from biomass fires, *J. Geophys. Res., 95*, 5669-5675, 1990.

Herman, J. R., P. K. Bhartia, O. Torres, C. Hsu, and C. Seftor, and E. Celarier, Global distribution of UV-absorbing aerosols from Nimbus 7/TOMS data, *J. of Geophys. Res., 102*, 16,911–16,922, 1997.

Hobbs, P. V., *Introduction to Atmospheric Chemistry,* Camb. Univ. Press, Cambridge, England, 2000.

Hobbs, P. V., Atmosphere science: Clean air slots amid atmospheric pollution, *Nature, 415*, 861, 2002.

Hobbs, P. V., Clean air slots amid dense atmospheric pollution in southern Africa, *J. Geophys. Res., 108*, 8490, doi:10.1029/2002JD002156, 2003.

Hobbs, P. V., and L. F. Radke, Cloud condensation nuclei from a simulated forest fire, *Science, 163*, 279-280, 1969.

Hobbs, P.V., and J. D. Locatelli, Ice nuclei from a natural forest fire, *J. Appl. Meteor., 8*, 833-834, 1969.

Hobbs, P. V., J. S. Reid, J. A. Herring, J. D. Nance, R. E. Weiss, J. L. Ross, D. A. Hegg, R. D. Ottmar, and C. Liousse, Particle and trace-gas measurements in the smoke from prescribed burns of forest products in the Pacific northwest, in *Biomass Burning and Global Change, Vol. 2,* edited by J. S. Levine, pp. 697-715, MIT Press, Cambridge, Mass., 1996.

Hobbs, P. V., J. S. Reid, R. A. Kotchenruther, R. J. Ferek, and R. Weiss, Direct radiative forcing by smoke from biomass burning, *Science, 275*, 1776-1778, 1997.

Hoell, J. M., D. D. Davis, D. J. Jacob, M. O. Rodgers, R. E. Newell, H. E. Fuelberg, R. J. McNeal, J. L. Raper, and R. J. Bendura, Pacific Exploratory Mission in the tropical Pacific: PEM Tropics A, August–September 1996, *J. Geophys. Res., 104*, 5567–5584, 1999.

Hoffa, E. A., D. E. Ward, W. M. Hao, R. A. Susott, and R.H. Wakimoto, Seasonality of carbon emissions from biomass burning in a Zambian savanna, *J. Geophys. Res., 104*, 13,841-13,853, 1999.

Huntley, B. J., Southern African Savannas, in *Ecology of Tropical Savannas*, edited by B. J. Huntley and B. H. Walker, pp.101-119, Springer-Verlag, New York, 1982.

Hurst, D. F., D. W. T. Griffith, J. N. Carras, D. J. Williams, and P. J. Fraser, Measurements of trace gases emitted by Australian savanna fires during the 1990 dry season, *J. Atmos. Chem., 18,* 33-56, 1994.

Hybrid Single-Particle Lagrangian Integrated Trajectory (HYSPLIT) Model, National Oceanic and Atmospheric Administration (NOAA) Air Resources Lab (ARL), www.arl.noaa.gov/ready/hysplit4.html, 2002.

Intergovernmental Panel on Climate Change (IPCC), *Climate Change 2001: The Scientific Basis*, Cambridge University Press, Cambridge, England, 2001.

International Geosphere-Biosphere Programme (IGBP) Report 41, The miombo network: Framework for a terrestrial transect study of land-use and land-cover change in the miombo ecosystems of central Africa, edited by P. V. Desanker, P. G. H. Frost, C. O. Justice, and R. J. Scholes, Stockholm, Sweden, 1997.

Jacob, D. J., B. G. Heikes, S.-M. Fan, J. A. Logan, D. L. Mauzerall, J. D. Bradshaw, H. B. Singh, G. L. Gregory, R. W. Talbot, D. R. Blake, and G. W. Sachse, The origin of ozone and NO_x in the tropical troposphere: A photochemical analysis of aircraft observations over the South Atlantic Basin, *J. Geophys. Res., 101*, 24,235-24,250, 1996.

Jenkins, G. S., J. H. Ryu, A. M. Thompson, and J. C. Witte, Linking horizontal and vertical transports of biomass fire emissions to the Tropical Atlantic Ozone Paradox during the Northern Hemisphere winter season: 1999, *J. Geophys. Res.,108*, 4745, doi:10.1029/2002JD003297, 2003.

Joint Research Centre (JRC), Global Burnt Area 2000 Project, Ispra, Italy, 2003. (Available at www.grid.unep.ch/activities/earlywarning/preview/ims/gba)

Jury, M. R., The dry season climate of tropical southern Africa and implications for pyrogenic emissions, *S. Afr. J. Sci., 96*, 387-390, 2000.

Justice, C. O., J. D. Kendall, P. R. Dowty, and R. J. Scholes, Satellite remote sensing of fires during the SAFARI campaign using NOAA advanced very high-resolution radiometer data, *J. Geophys. Res., 101*, 23851-23863, 1996.

Kirchstetter, T. W., C. E. Corrigan, and T. Novakov, Laboratory and field investigation of the adsorption of gaseous organic compounds onto quartz filters, *Atmos. Environ., 35*, 1663-1671, 2001.

Kirchstetter, T. W., T. Novakov, P. V. Hobbs, and B. Magi, Airborne measurements of carbonaceous aerosols in southern Africa during the biomass burning season, *J. Geophys. Res., 108*, 8476, doi:10.1029/2002JD002171, 2003.

Korontzi, S., D. P. Roy, C. O. Justice, and D. E. Ward, Modeling and sensitivity analysis of fire emissions in southern Africa during SAFARI 2000, *Remote Sensing Environ.*, in press, 2004.

Labuschagne, C., E.-G. Brunke, and G. Coetzee, Atmospheric CO and O_3 monthly mean concentrations, Cape Point, WMO WDCGG, SAWS, Tokyo, 2003. (Available at http://gaw.kishou.go.jp/wdcgg.html)

Laursen, K. K., P. V. Hobbs, L. F. Radke, and R. A. Rasmussen, Some trace gas emissions from north American biomass fires with an assessment of regional and global fluxes from biomass burning, *J. Geophys. Res., 97*, 20,687-20,701, 1992.

Lacaux, J., R. A. Delmas, B. Cros, B. Lefeivre, and M. O. Andreae, Influence of biomass burning on precipitation chemistry in the equatorial forests of Africa, in *Global Biomass Burning*, edited by J. S. Levine, pp. 167-173, MIT Press, Cambridge, Mass., 1991.

Landmann, T., Characterizing sub-pixel landsat ETM plus fire severity on experimental fires in the Kruger National Park, South Africa, *S. Afr. J. Sci, 99*, 357-360, 2003.

Le Canut, P., M. O. Andreae, G. W. Harris, F. G. Wienhold, and T. Zenker, Airborne studies of emissions from savanna fires in southern Africa, 1. Aerosol emissions measured with a laser optical particle counter, *J. Geophys. Res., 101,* 23,615-23,630, 1996.

Li, Q. B, D. J. Jacob, I. Bey, R. M. Yantosca, Y. J. Zhao, Y. Kondo, J. Notholt, Atmospheric hydrogen cyanide (HCN): Biomass burning source, ocean sink?, *Geophys. Res. Lett., 27*, 357-360, 2000.

Li, J., M. Pósfai, P. V. Hobbs, and P. R. Buseck, Individual aerosol particles from biomass burning in southern Africa: 2. Compositions and aging of inorganic particles, *J. Geophys. Res., 108*, 8484, doi:10.1029/2002JD002310, 2003.

Liu, H., D.J. Jacob, I. Bey, and R.M. Yantosca, Constraints from ^{210}Pb and ^{7}Be on wet deposition and transport in a global three-dimensional chemical tracer model driven by assimilated meteorological fields, *J. Geophys. Res., 106* , 12,109–12,128, 2001.

Lobert, J., W. Keene, J. Logan, and R. Yevich, Global chlorine emissions from biomass burning: Reactive Chlorine Emissions Inventory, *J. Geophys. Res., 104*, 8373–8389, 1999.

Logan, J. A., M. J. Prather, S. C. Wofsy, and M. B. McElroy, Tropospheric chemistry: A global perspective, *J. Geophys. Res., 86,* 7210-7254, 1981.

Magi, B., and P. V. Hobbs, Effects of humidity on light scattering by aerosols in southern Africa during the biomass burning season, *J. Geophys. Res., 108*, 8495, doi:10.1029/2002JD002144, 2003.

Magi, B. I., P. V. Hobbs, B. Schmid, and J. Redemann, Vertical Profiles of light, scattering, light absorption, and single scattering albedo during the dry, biomass burning season in southern Africa and comparisons of in situ and remote sensing measurements of aerosol optical depths, *J. Geophys. Res., 108*, 8504, doi:10.1029/2002JD002361, 2003.

Mano, S., and M. O. Andreae, Methyl bromide from biomass burning, *Science, 263*, 1255-1256, 1994.

Martin, R. V., D. J. Jacob, J. A. Logan, I. Bey, R. M. Yantosca, A. C. Staudt, Q. B. Li, A. M. Fiore, B. N. Duncan, H. Y. Liu, P. Ginoux, and V. Thouret, Interpretation of TOMS observations of tropical tropospheric ozone with a global model and in situ observations, *J. Geophys. Res.*, *107*, 4351, doi:10.1029/2001JD001480, 2002.

Mason, S. A., R. J. Field, R. J. Yokelson, M. A. Kochivar, M. R. Tinsley, D. E. Ward, and W. M. Hao, Complex effects arising in smoke plume simulations due to inclusion of direct emissions of oxygenated organic species from biomass combustion, *J. Geophys. Res., 106,* 12,527-12,539, 2001.

Mauzerall, D. L., J. A. Logan, D. J. Jacob, B. E. Anderson, D. R. Blake, J. D. Bradshaw, B. Heikes, G. W. Sachse, H. Singh, and B. Talbot, Photochemistry in biomass burning plumes and implications for tropospheric ozone over the tropical South Atlantic, *J. Geophys. Res., 103,* 8401-8423, 1998.

Mazurek, M. A., W. R. Cofer III, and J. S. Levine, Carbonaceous aerosols from prescribed burning of a boreal forest ecosystem, in *Global Biomass Burning: Atmospheric, Climatic and Biospheric Implications,* edited by J. S. Levine, pp. 258-263, MIT Press, Cambridge, Mass., 1991.

Mbendi, Information for Africa, http://www.mbendi.co.za/index.htm, 2003.

McKenzie, L. M., D. E Ward, and W. M. Hao, Chlorine and bromine in the biomass of tropical and temperate ecosystems, in *Biomass Burning and Global Change, Volume 1*, edited by J. S. Levine, pp. 240-248, MIT Press, Cambridge, Mass., 1996.

Measurements of Pollution in the Troposphere (MOPITT), MOPITT CO Retrievals Monthly Average Plots, Hampton, VA, 2004. (Available at http://www.eos.ucar.edu/mopitt/data/plots/mapsv3_mon.html)

Meinardi, S., I. J. Simpson, N. J. Blake, D. R. Blake, and F. S. Rowland, Dimethyl disulfide (DMDS) and dimethyl sulfide (DMS) emissions from biomass burning in Australia, *Geophys. Res. Lett., 30,* doi:10.1029/2003GL016967, 2003.

Moxim, W. J., and H. Levy, A model analysis of the tropical South Atlantic Ocean tropospheric ozone maximum: The interaction of transport and chemistry, *J. Geophys. Res.*, *105*, 17,393-17,415, 2000.

Novakov, T., Microchemical characterization of aerosols, in *Nature, Aim and Methods of Microchemistry*, edited by H. Malissa, M. Grasserbaure, and R. Belcher, pp. 141-165, Springer-Verlag, New York, 1981.

Novakov, T., Soot in the atmosphere, in *Particulate Carbon: Atmospheric Life Cycle*, edited by G. T. Wolff and R. L. Klimish, pp. 19-41, Plenum, New York, 1982.

Novelli, P. C., K. A. Masarie, and P. M. Lang, Distributions and recent changes of carbon monoxide in the lower troposphere, *J. Geophys. Res., 103,* 19,015–19,033, 1998.

Pak, B. C., R. L. Langenfelds, S. A. Young, R. J. Francey, C. P. Meyer, L. M. Kivlighon, L. N. Cooper, B. L. Dunse, C. E. Allison, L. P. Steele, I. E. Galbally, and I. A. Weeks, Measurements of biomass burning influences in the troposphere over southeast Australia during the SAFARI 2000 dry season campaign, *J. Geophys. Res., 108*, 8480, doi:10.1029/2002JD002343, 2003.

Pilewskie, P., J. Pommier, R. Bergstrom, W. Gore, S. Howard, M. Robbette, B. Schmid, P. V. Hobbs, and S.-C. Tsay, Solar spectral radiative forcing during the Southern African Regional Science Initiative, *J. Geophys. Res., 108*, 8486, doi:10.1029/2002JD002411, 2003.

Pósfai, M., R. Simonics, J. Li, P. V. Hobbs, and P. B. Buseck, Individual aerosol particles from biomass burning in southern Africa: 1. Compositions and size distributions of carbonaceous particles, *J. Geophys. Res., 108,* 8483, doi: 10.1029/2002JD002291, 2003.

Privette, J., D. Landis, J. Nickeson, and J. Morisette, *SAFARI 2000 CD-ROM Series, Volume 1*, NASA Goddard Space Flight Center, July 2001.

Quay, P. D., S. L. King, J. Strutsman, D. O. Wilbur, P. L. Steele, I. Fung, R. H. Gammon, T. A. Brown, G. W. Farwell, P. M. Grootes, and F. H. Schmidt, Carbon isotopic composition of atmospheric methane: Fossil and biomass burning strengths, *Global Biogeochem. Cycles, 5,* 25-47, 1991.

Radke, L. F., J. L. Stith, D. A. Hegg, P. V. Hobbs, Airborne studies of particles and gases from forest fires, *J. Air Poll. Control Assoc., 28*, 30-34, 1978.

Realtime Environmental Applications Display System (READY), *FNL archive*, www.arl.noaa.gov/ready.html, 2002.

Reid, J. S., P. V. Hobbs, R. J. Ferek, D. R. Blake, J. V. Martins, M. R. Dunlap, and C. Liousse, Physical, chemical, and optical properties of regional hazes dominated by smoke in Brazil, *J. Geophys. Res., 103,* 32,059-32,080, 1998.

Rodgers, C. F., J. G. Hudson, B. Zielinska, R. L. Tanner J. Hallett, and J. G. Watson, Cloud condensation nuclei from biomass burning, in *Global Biomass Burning*, edited by J. S. Levine, pp. 431-438, MIT Press, Cambridge, Mass., 1991.

Rosen, H., and T. Novakov, Optical-transmission through aerosol deposits on diffusely reflective filters—a method for measuring the absorbing component of aerosol-particles, *Appl. Opt., 22,* 1265-1267, 1983.

Ross, J. L., P. V. Hobbs, and B. Holben, Radiative characteristics of regional hazes dominated by smoke from biomass burning in Brazil: Closure tests and direct radiative forcing, *J. Geophys. Res., 103*, 31,925-31,942, 1998.

Roy, D. P., P. E. Lewis, and C. O. Justice, Burned area mapping using multi-temporal moderate spatial resolution data – a bi-directional reflectance model-based expectation approach, *Remote Sens. Env., 83*, 263-286, 2002.

Sawa, Y., H. Matsueda, Y. Tsutsumi, J. B. Jensen, H. Y. Inoue, and Y. Makino, Tropospheric carbon monoxide and hydrogen measurements over Kalimantan in Indonesia and northern Australia during October, 1997, *Geophys. Res. Lett., 26*, 1389-1392, 1999.

Schmid, B., J. Redemann, P. B. Russell, P. V. Hobbs, D. L. Hlavka, M. McGill, B. N. Holben, E. J. Welton, J. Campbell, O. Torres, R. Kahn, D. Diner, M. Helmlinger, D. A. Chu, C. R. Gonzalez, and G. de Leeuw, Coordinated airborne, spaceborne, and ground-based measurements of massive, thick aerosol layers during the dry season in southern Africa, *J. Geophys. Res., 8496,* doi:10.1029/2002JD002297, 2003.

Scholes, R. J., J. Kendall, and C. O. Justice, The quantity of biomass burned in southern Africa, *J. Geophys. Res., 101,* 23,667–23,676, 1996.

Seinfeld, J. H., and S. N. Pandis, *Atmospheric Chemistry and Physics*, John Wiley, New York, 1998.

Shea, R. W., B. W. Shea, J. B. Kauffman, D. E. Ward, C. I. Haskins, and M. C. Scholes, Fuel biomass and combustion factors associated with fires in savanna ecosystems of South Africa and Zambia, *J. Geophys. Res., 101,* 23,551-23,568, 1996.

Silva, J. M. N., J. M. C. Pereira, A. I. Cabral, A. C. L. Sá, M. J. P. Vasconcelos, B. Mota, and J.-M. Grégoire, An estimate of the area burned in southern Africa during the 2000 dry season using SPOT-VEGETATION satellite data, *J. Geophys. Res., 108*, 8498, doi:10.1029/2002JD002320, 2003.

Sinha, P., P. V. Hobbs, R. J. Yokelson, I. T. Bertschi, D. R. Blake, I. J. Simpson, S. Gao, T. W. Kirchstetter, and T. Novakov, Emissions of trace gases and particles from savanna fires in southern Africa, *J. Geophys. Res., 108*, 8487, doi:10.1029/2002JD002325, 2003a.

Sinha, P., P. V. Hobbs, R. J. Yokelson, D. R. Blake, S. Gao, and T. W. Kirchstetter, Distributions of trace gases and aerosols during the dry biomass burning season in southern Africa, *J. Geophys. Res., 108*, 4536, doi:10.1029/2003JD003691, 2003b.

Sinha, P., P. V. Hobbs, R. J. Yokelson, T. J. Christian, T. W. Kirchstetter, and R. Bruintjes, Emissions of trace gases and particles from two ships in the southern Atlantic Ocean, *Atmos. Environ., 37*, 2139-2148, 2003c.

Sinha, P., P. V. Hobbs, R. J. Yokelson, D. R. Blake, S. Gao, and T. W. Kirchstetter, Emissions from miombo woodland and dambo grassland savanna fires, *J. Geophys. Res., 109*, D11305, doi:10.1029/2004JD004521, 2004a.

Sinha, P., L. Jaegle, P. V. Hobbs, and Q. Liang, Transport of biomass burning emissions from southern Africa, *J. Geophys. Res.*, in press, 2004b.

Staudt, A. C., D. J. Jacob, J. A. Logan, D. Bachiochi, T. N. Krishnamurti, and N. Poisson, Global chemical model analysis of biomass burning and lightning influences over the South Pacific in austral spring, *J. Geophys. Res., 107*, 10.1029/2000JD000296, 2002.

Swap, R. J., H. J. Annegarn, J. T. Suttles, M. D. King, S. Platnick, J. L. Privette, and R. J. Scholes, Africa burning: A thematic analyses of the Southern African Regional Science Initiative (SAFARI 2000), *J. Geophys. Res., 108*, 8465, doi:10.1029/2003JD003747, 2003.

Thompson, A. M., K. E. Pickering, D. P. McNamara, M. R. Schoeberl, R. D. Hudson, J. H. Kim, E. V. Browell, V. W. J. H. Kirchhoff, and D. Nganga, Where did tropospheric ozone over southern Africa and the tropical Atlantic come from in October 1992? Insights from TOMS, GTE TRACE A, and SAFARI 1992, *U. Geophys. Res., 101,* 24,251-24,278, 1996.

Thompson, A. M., B. G. Doddridge, J. C. Witte, R. D. Hudson, W. T. Luke, J. E. Johnson, B. J. Johnson, S. J. Oltmans, R. Weller, A tropical Atlantic paradox: Shipboard and satellite views of a tropospheric ozone maximum and wave-one in January-February 1999, *Geophys. Res. Lett., 27*, 3317-3320, 2000.

Thompson, A. M., J. C. Witte, M. T. Freiman, N. A. Phahlane, and G. J. R. Coetzee, Lusaka, Zambia, during SAFARI-2000: Convergence of local and imported

ozone pollution, *Geophys. Res. Lett., 20*, 1976, doi:10.1029/2002GL015399, 2002.

Thompson, A.M., J.C. Witte, R.D. McPeters, S.J. Oltmans, F.J. Schmidlin, J.A. Logan, M.Fujiwara, V.W.J.H. Kirchhoff, F. Posny, G.J.R. Coetzee, B. Hoegger, S. Kawakami, T. Ogawa, B.J. Johnson, H. Vömel and G. Labow, Southern Hemisphere Additional Ozonesondes (SHADOZ) 1998–2000 tropical ozone climatology 1. Comparison with Total Ozone Mapping Spectrometer (TOMS) and ground-based measurements, *J. Geophys. Res., 108*, 8238, doi:10.1029/2001JD000967, 2003a.

Thompson, A. M., J. C. Witte, S. J. Oltmans, F. J. Schmidlin, J. A. Logan, M. Fujiwara, V. W. J. H. Kirchhoff, F. Posny, G. J. R. Coetzee, B. Hoegger, S. J. Kawakami, T. Ogawa, J. P. F. Fortuin, H. M. Kelder, Southern Hemisphere Additional Ozonesondes (SHADOZ) 1998-2000 tropical ozone climatology - 2. Tropospheric variability and the zonal wave-one, *J. Geophys. Res., 108*, 8241, doi:10.1029/2002JD002241, 2003b.

Total Ozone Mapping Spectrometer (TOMS), Aerosol Index, Greenbelt, MD, 2004. (Available at http://toms.gsfc.nasa.gov/aerosols/aerosols.html)

Turpin, B. J., J. J. Huntzicker, and S. V. Hering, Investigation of the organic aerosol sampling artifacts in the Los Angeles basin, *Atmos. Environ., 28*, 3061-3071, 1994.

United States Environmental Protection Agency (USEPA), Latest Findings on National Air Quality: 1997 Status and Trends, Washington D.C., 1997. (Available at http://www.epa.gov/air/aqtrnd97/brochure/index.html)

United States Environmental Protection Agency (USEPA), *Compilation of Air Pollutant Emission Factors, AP-42,* Fifth Edition, Vol. 1, Ch. 1, Final Section - Supplement E: External Combustion Sources, 1998.

Van der Werf, G., J. T. Randerson, G. J. Collatz, and L. Giglio, Carbon emissions from fires in tropical and subtropical ecosystems, *Global Change Biol.*, 9, 547-562, 2003.

Ward, D. E., and W. M. Hao, Air toxic emissions from burning of biomass globally—Preliminary estimates, *Proceedings of 85th Annual Meeting and Exhibition, Air & Waste Manage. Assoc.,* Vancouver, British Columbia, 1992.

Ward, D. E., and C. C. Hardy, Smoke emissions from wildland fires, *Environ. Int., 17*, 117-134, 1991.

Ward, D. E., and L. F. Radke, Emissions measurements from vegetation fires: A comparative evaluation of methods and results, in *Fire in the Environment: The Ecological, Atmospheric, and Climatic Importance of Vegetation Fires,* edited by P. J. Crutzen and J. G. Goldammer, pp. 53-76, Wiley, New York, 1993.

Warneck, P., *Chemistry of the Natural Atmosphere,* Academic Press, San Francisco, 2000.

White, F., *UNESCO/AETFAT/UNSO Vegetation Map of Africa*, Paris: UNESCO, 1981.

White, F., *Vegetation of Africa*, Paris: UNESCO, 1983.

Wingenter, O. W., C. J.-L. Wang, D. R. Blake, and F. S. Rowland, Seasonal variation of tropospheric methyl bromide concentrations: Constraints on anthropogenic input, *Geophys. Res. Lett., 25*, 2797-2800, 1998.

Yevich, R., and J. A. Logan, An assessment of biofuel use and burning of agricultural waste in the developing world, *Glob. Biogeochem. Cycles, 17*, 1095, doi:10.1029/2002GB001952, 2003.

Yokelson, R. J., D. W. T. Griffith, and D. W. Ward, Open-path Fourier transform infrared studies of large-scale laboratory biomass fires, *J. Geophys. Res., 101,* 21,067-21,080, 1996.

Yokelson, R. J., J. G. Goode, D. E. Ward, R. A. Susott, R. E. Babbitt, D. D. Wade, I. Bertschi, W.W. T. Griffith, and W. M. Hao, Emissions of formaldehyde, acetic acid, methanol, and other trace gases from biomass fires in North Carolina measured by airborne Fourier transform infrared spectroscopy, *J. Geophys. Res., 104*, 30,109-32,125, 1999.

Yokelson, R. J., I. T. Bertschi, T. J. Christian, P. V. Hobbs, D. E. Ward, and W. M. Hao, Trace gas measurements in nascent, aged, and cloud-processed smoke from African savanna fires by airborne Fourier transform infrared (AFTIR) spectroscopy, *J. Geophys. Res.*, *108*, 8478, doi:10.1029/2002JD002322, 2003.

VITA

Parikhit Sinha was born in Siligury, India, on April 13, 1975 at the foothills of the Himalayan mountains. In 1979, he immigrated with his family to the United States and was raised in Randolph, New Jersey. After graduating as salutatorian from Randolph High School in 1993, he attended Harvard University in Cambridge, Massachusetts, graduating with a degree in environmental engineering, cum laude, in 1997. After working for two years in the risk assessment group of the environmental consulting firm, Gradient Corporation in Cambridge, Massachusetts, he joined the Cloud and Aerosol Research Group in the Department of Atmospheric Sciences at the University of Washington in Seattle, Washington in 1999. In August and September of 2000, he participated as a flight chemist aboard the UW Convair-580 research aircraft in the SAFARI 2000 field project in southern Africa. On February 3, 2002, Parikhit was married to Amanda Elizabeth Moses, a graduate student in the department of chemistry at the University of Washington. From 2000-2004, Parikhit has been a member of the viola section of *Orchestra Seattle.* From 2002-2004, he has been a gardener at the Picardo and Magnuson Park community P-patches in Seattle.

Parikhit's graduate research on emissions from savanna fires in southern Africa and related work has led to the following publications:

Sinha, P., P. V. Hobbs, R. J. Yokelson, I. T. Bertschi, D. R. Blake, I. J. Simpson, S. Gao, T. W. Kirchstetter, and T. Novakov, Emissions of trace gases and particles from savanna fires in southern Africa, *J. Geophys. Res., 108*, 8487, doi:10.1029/2002JD002325, 2003.

Hobbs, P. V., P. Sinha, R. J. Yokelson, T. J. Christian, D. R. Blake, S. Gao, T. W. Kirchstetter, T. Novakov, and P. Pilewskie, Evolution of gases and particles from a savanna fire in South Africa, *J. Geophys. Res., 108*, 8485, doi:10.1029/2002JD002352, 2003.

Sinha, P., P. V. Hobbs, R. J. Yokelson, T. J. Christian, T. W. Kirchstetter, and R. Bruintjes, Emissions of trace gases and particles from two ships in the southern Atlantic Ocean, *Atmospheric Environment, 37,* 2139-2148, 2003.

Sinha, P., P. V. Hobbs, R. J. Yokelson, D. R. Blake, S. Gao, and T. W. Kirchstetter, Distributions of trace gases and aerosols during the dry biomass burning season

in southern Africa, *J. Geophys. Res., 108*, 4536, doi:10.1029/2003JD003691, 2003.

Friedli, H. R., L. F. Radke, R. Prescott, P. V. Hobbs, and P. Sinha, Mercury emission measurements from the August 2001 wildfires and an agricultural waste fire in Washington and Oregon State and the resulting atmospheric mercury budget estimates, *Glob. Biogeoch. Cycles, 17*, 1039, doi:10.1029/2002GB001972, 2003.

Sinha, P., P. V. Hobbs, R. J. Yokelson, D. R. Blake, S. Gao, and T. W. Kirchstetter, Emissions from miombo woodland and dambo grassland savanna fires, *J. Geophys. Res.*, *109*, D11305, doi:10.1029/2004JD004521, 2004.

Sinha, P., L. Jaegle, P. V. Hobbs, and Q. Liang, Transport of biomass burning emissions from southern Africa, *J. Geophys. Res.*, in press, 2004.